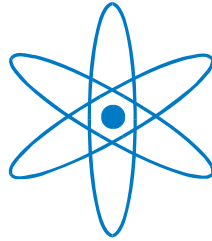


# PHYSIK-DEPARTMENT



## High-Energy Emission from Bright Gamma-Ray Bursts using Fermi

Dissertation

von

Elisabetta Bissaldi



TECHNISCHE UNIVERSITÄT  
MÜNCHEN



MAX-PLANCK-INSTITUT  
FÜR EXTRATERRESTRICHE PHYSIK



# TECHNISCHE UNIVERSITÄT MÜNCHEN

Max–Planck–Institut für extraterrestrische Physik

## **High–Energy Emission from Bright Gamma–Ray Bursts using Fermi**

**Elisabetta Bissaldi**

Vollständiger Abdruck der von der Fakultät für Physik der Technischen Universität  
München zur Erlangung des akademischen Grades eines

**Doktors der Naturwissenschaften**

genehmigten Dissertation.

Vorsitzender: Univ.–Prof. Dr. A. Ibarra

Prüfer der Dissertation: 1. Hon.–Prof. Dr. G. Hasinger  
2. Univ.–Prof. Dr. L. Oberauer

Die Dissertation wurde am 08.04.2010 bei der Technischen Universität München  
eingereicht und durch die Fakultät für Physik am 25.05.2010 angenommen.



*To my dad*



# Contents

<b>List of Figures</b>	<b>IV</b>
<b>List of Tables</b>	<b>VIII</b>
<b>Summary and Dissertation Outline</b>	<b>1</b>
<b>Zusammenfassung</b>	<b>3</b>
<b>1 Gamma-Ray Bursts: An Overview</b>	<b>7</b>
1.1 The “Dark” Era . . . . .	8
1.2 The BATSE Era . . . . .	11
1.2.1 GRB Global Properties . . . . .	12
1.2.2 EGRET and the High-Energy GRB Emission . . . . .	19
1.3 The Afterglow Era . . . . .	22
1.3.1 Important Observational Progress . . . . .	23
1.3.2 Theoretical GRB Models . . . . .	25
1.3.3 GRB Relationships . . . . .	30
1.4 The Pre- <i>Fermi</i> Era . . . . .	33
1.4.1 The <i>Swift</i> Mission . . . . .	34
<b>2 The Fermi Observatory</b>	<b>37</b>
2.1 The Large Area Telescope . . . . .	38
2.1.1 Precision Converter-Tracker . . . . .	41
2.1.2 Calorimeter . . . . .	42
2.1.3 Anticoincidence Detector . . . . .	43
2.1.4 LAT and GRBs . . . . .	45
2.2 The Gamma-Ray Burst Monitor . . . . .	48
2.2.1 NaI(Tl) Detectors . . . . .	48
2.2.2 BGO Detectors . . . . .	50
2.2.3 PMTs and FEE . . . . .	52

## CONTENTS

---

2.2.4	Data System . . . . .	54
2.3	GBM Triggers . . . . .	56
2.3.1	Trigger localization . . . . .	56
2.3.2	Spacecraft Reorientations . . . . .	58
2.3.3	TRIGDAT . . . . .	61
2.3.4	The RMFIT Analysis Software . . . . .	62
<b>3</b>	<b>GBM Performance</b>	<b>63</b>
3.1	Calibration Campaigns . . . . .	64
3.1.1	MPE Laboratory Setup and Instrumentation . . . . .	66
3.1.2	NaI Low–Energy Calibration at PTB/BESSY . . . . .	68
3.1.3	BGO High–Energy Calibration at SLAC . . . . .	69
3.1.4	Simulation of the Laboratory and the Calibration Setup . . . . .	71
3.2	Calibration Data Analysis . . . . .	73
3.2.1	Database and software . . . . .	73
3.2.2	Processing of Calibration Runs . . . . .	73
3.3	Calibration Results . . . . .	87
3.3.1	Channel–to–Energy (CE) Relation . . . . .	87
3.3.2	Energy Resolution . . . . .	109
3.3.3	Full–Energy Peak Effective Area and Angular Response . . . . .	116
3.3.4	QDE and Spatial Uniformity of NaI Detectors . . . . .	121
3.3.5	NaI Detectors High–Voltage dependence . . . . .	125
3.3.6	NaI EQM Thermal Test . . . . .	127
3.4	Detector Calibration at System Level . . . . .	128
3.4.1	Channel–to–Energy Conversion . . . . .	130
3.5	On–Orbit Performance and Operations . . . . .	131
<b>4</b>	<b>First Year of GBM Scientific Results</b>	<b>135</b>
4.1	GRB 090323 and GRB 090328 . . . . .	136
4.1.1	Observations of GRB 090323 . . . . .	137
4.1.2	Observations of GRB 090328 . . . . .	139
4.1.3	Time–Resolved Spectral Analysis . . . . .	141
4.2	Joint GBM–LAT Observations . . . . .	144
4.3	GRB 090902B . . . . .	157
4.3.1	Observations and Light Curves . . . . .	157
4.3.2	Time–resolved Spectral Analysis . . . . .	159
4.3.3	Discussion and Interpretation . . . . .	162

---

4.4	GBM and BAT Observations of GRB 080810 . . . . .	165
4.4.1	Observations and Analyses . . . . .	166
<b>5</b>	<b>BGO–Bright GRBs</b>	<b>173</b>
5.1	Selection Methodology . . . . .	174
5.1.1	Event Selection . . . . .	174
5.1.2	Detector Selection . . . . .	176
5.1.3	Data Type Selection . . . . .	176
5.1.4	Time and Energy Interval Selections . . . . .	177
5.2	Analysis of the BGO Peak Count Rate . . . . .	180
5.2.1	LAT Detections . . . . .	187
5.2.2	BGO Effective–Area Correction . . . . .	189
5.3	Spectral Analysis . . . . .	190
5.3.1	Photon Models . . . . .	190
5.4	Spectral Analysis Results . . . . .	193
5.4.1	Spectral Parameter Distribution . . . . .	198
5.4.2	Correlation Among Spectral Parameters . . . . .	207
	<b>Conclusions</b>	<b>215</b>
	<b>Bibliography</b>	<b>217</b>

# List of Figures

1.1	Light curve of the first Gamma-Ray Burst . . . . .	9
1.2	Temporal variations in GRB 821104 . . . . .	10
1.3	Isotropic distribution of 2704 BATSE GRBs . . . . .	13
1.4	Bimodal distribution of BATSE GRBs . . . . .	14
1.5	Distribution of hardness ratio versus $T_{90}$ . . . . .	15
1.6	GRB light curves from the first BATSE Catalog . . . . .	15
1.7	Deconvolved spectra of GRB 990123 . . . . .	16
1.8	Spectral parameter distributions from BATSE GRBs . . . . .	18
1.9	High-energy emission from GRB 940217 . . . . .	19
1.10	Energy fluxes for GRB 941017 . . . . .	21
1.11	<i>Beppo-SAX</i> observation of GRB 970228 . . . . .	24
1.12	V-band images of the GRB 970228 optical afterglow . . . . .	24
1.13	Schematic diagram of the fireball shock model . . . . .	29
1.14	$E_p$ - $E_{\text{iso}}$ distribution . . . . .	31
1.15	Energy fluence- $E_{\text{peak}}$ distribution . . . . .	32
1.16	Effective areas for <i>Swift</i> and <i>Fermi</i> detectors . . . . .	35
2.1	The launch of the Fermi Observatory . . . . .	38
2.2	Schematic diagram of the Large Area Telescope . . . . .	39
2.3	The LAT tracker . . . . .	41
2.4	LAT calorimeter module . . . . .	43
2.5	LAT ACD . . . . .	44
2.6	GRB localization with the LAT . . . . .	46
2.7	Model-dependent LAT GRB sensitivity . . . . .	47
2.8	GBM NaI detector . . . . .	49
2.9	X-ray transmission of the NaI detector entrance window . . . . .	51
2.10	The Fermi spacecraft . . . . .	51
2.11	GBM BGO detector . . . . .	53
2.12	Functional block diagram of GBM . . . . .	55

LIST OF FIGURES

2.13	GBM location maps . . . . .	57
2.14	LAT exposure for GRB 090323 and GRB 090328 . . . . .	59
2.15	General scheme of GBM actions taken upon triggering . . . . .	61
3.1	Calibration at the MPE laboratory . . . . .	67
3.2	Calibration at the BESSY II electron storage ring . . . . .	68
3.3	High-energy calibration campaign at SLAC . . . . .	70
3.4	Simulation of the laboratory environment . . . . .	71
3.5	Spectra measured at PTB/BESSY . . . . .	74
3.6	Spectra measured at MPE (1) . . . . .	75
3.7	Spectra measured at MPE (2) . . . . .	76
3.8	Spectra measured at MPE and SLAC . . . . .	77
3.9	Full-energy peak analysis of NaI lines (1) . . . . .	83
3.10	Full-energy peak analysis of NaI lines (2) . . . . .	84
3.11	Full-energy peak analysis of BGO lines (1) . . . . .	85
3.12	Full-energy peak analysis of BGO lines (2) . . . . .	86
3.13	The differential linearity measured for NaI FM04 . . . . .	87
3.14	CE relation for NaI FM01–FM04 below the K-edge . . . . .	95
3.15	CE relation for NaI FM05–FM09 below the K-edge . . . . .	96
3.16	CE relation for NaI FM10–FM13 below the K-edge . . . . .	97
3.17	CE relation for NaI FM01–FM04 above the K-edge . . . . .	98
3.18	CE relation for NaI FM05–FM09 above the K-edge . . . . .	99
3.19	CE relation for NaI FM10–FM13 above the K-edge . . . . .	100
3.20	Schematic representation of the CE relation . . . . .	101
3.21	CE relation at the K-edge for NaI FM01–04 . . . . .	102
3.22	CE relation at the K-edge for NaI FM05–09 . . . . .	103
3.23	CE relation at the K-edge for NaI FM10–13 . . . . .	104
3.24	Comparison between real and simulated spectra (1) . . . . .	106
3.25	Comparison between real and simulated spectra (2) . . . . .	107
3.26	BGO CE relation . . . . .	108
3.27	Energy resolution of all BGO detectors . . . . .	111
3.28	FWHM for the NaI and BGO FM detectors . . . . .	111
3.29	Energy resolution of the NaI detectors FM01–FM07 . . . . .	114
3.30	Energy resolution of the NaI detectors FM08–FM13 . . . . .	115
3.31	Effective area of the NaI and BGO FM detectors . . . . .	116
3.32	Off-axis effective area for NaI FM04 and BGO EQM . . . . .	118
3.33	Off-axis effective area for BGO FM01 and FM02 . . . . .	119

## LIST OF FIGURES

---

3.34	BGO spectra measured at different angles . . . . .	120
3.35	Comparison of GBM and BATSE effective area . . . . .	120
3.36	NaI FM04 effective area between 10 and 60 keV . . . . .	122
3.37	Contour plots at 10, 36 and 60 keV for detector NaI FM04 . . .	123
3.38	QDE contour plots at 10 and 60 keV . . . . .	124
3.39	HV fit results for NaI detector FM04 . . . . .	126
3.40	Spectra recorded during the NaI thermal test . . . . .	128
3.41	Temporal evolution of the photo-peak center and resolution . .	129
3.42	NaI FM04 spline fit . . . . .	130
3.43	NaI and BGO background spectra (1) . . . . .	132
3.44	NaI and BGO background spectra (2) . . . . .	133
4.1	GBM source-to-detector angle evolution for GRB 090323 . . .	138
4.2	NaI light curve of GRB 090323 . . . . .	138
4.3	GBM light curves for GRB 090323 . . . . .	139
4.4	GBM light curves for GRB 0903238 . . . . .	140
4.5	Spectral fits to GRB 090323 and GRB 090328 . . . . .	142
4.6	Sky map of <i>Fermi</i> -GBM detected GRBs . . . . .	146
4.7	Light curves of GRB 080825C . . . . .	147
4.8	Spectral analysis results for GRB080825C . . . . .	148
4.9	Light curves of GRB 080916C . . . . .	150
4.10	Fit parameters evolution of GRB 080916C . . . . .	151
4.11	Light curves of GRB 081024B . . . . .	153
4.12	Light curves of GRB 090510 . . . . .	155
4.13	Spectral analysis results for GRB 090510 . . . . .	156
4.14	Light curves of GRB 090902B . . . . .	158
4.15	Light curve of GRB 090902B between 0.1 and 300 GeV . . .	160
4.16	Joint fit to <i>interval b</i> of GRB 090902B . . . . .	161
4.17	GRB 080810 <i>Swift</i> -BAT and <i>Fermi</i> -GBM light curves . . . .	167
4.18	GRB 080810 $E_{\text{peak}}$ evolution . . . . .	170
4.19	GBM, BAT and XRT spectra of GRB 080810 . . . . .	171
5.1	GBM NaI vs. BGO durations . . . . .	178
5.2	GBM NaI and BGO duration distributions . . . . .	178
5.3	GBM light curves of GRB 090227B and GRB 090228 . . . .	182
5.4	GBM light curves of GRB 081215 and GRB 090510 . . . . .	183
5.5	Distribution of the measured BGO peak count rate . . . . .	186
5.6	Distribution of BGO count rates . . . . .	186

## LIST OF FIGURES

---

5.7	BGO peak count rate measured in channel 1 . . . . .	188
5.8	Effective area correction . . . . .	189
5.9	Effective area correction . . . . .	191
5.10	Spectral parameter distributions from bright GRBs . . . . .	200
5.11	BATSE vs GBM spectral parameter distributions . . . . .	201
5.12	Spectral parameters vs. fluence (8–1000 keV) . . . . .	202
5.13	Spectral parameters vs. fluence (1–40 MeV) . . . . .	203
5.14	Spectral parameters vs. fluence (BATSE/GBM, 20–2000 keV) . . . . .	204
5.15	Duration vs. fluence distribution . . . . .	205
5.16	Distribution of hardness ratio versus $T_{90}$ . . . . .	206
5.17	Peak Photon Flux Distribution . . . . .	206
5.18	Energy fluence distributions . . . . .	207
5.19	Scatter plots of parameter pairs . . . . .	208
5.20	Scatter plots of BATSE vs GBM parameter pairs . . . . .	209
5.21	Predicted values of the Amati and Ghirlanda relation energy ratios . . . . .	211
5.22	$E_{\text{peak}}$ vs Fluence (8 keV–40 MeV) distribution . . . . .	212

# List of Tables

2.1	Summary of LAT parameters and estimated performance . . . . .	40
2.2	Orientations of NaI Detectors in Spacecraft Coordinates . . . . .	50
2.3	GBM vs. BATSE comparison . . . . .	52
2.4	GBM Science Data Types . . . . .	54
3.1	Properties of radioactive nuclides . . . . .	65
3.2	List of all calibrated GBM detectors . . . . .	66
3.3	Contribution of simulated laboratory components . . . . .	72
3.4	Double peak fit constraints . . . . .	79
3.5	Determination of the systematic errors . . . . .	80
3.6	Standard deviations of the NaI fit parameters . . . . .	81
3.7	Standard deviations of the BGO fit parameters . . . . .	81
3.8	Fit parameters for PTB/BESSY data . . . . .	89
3.9	CE relation below the K-edge for PTB/BESSY data . . . . .	89
3.10	Scaling factors between PTB/BESSY and MPE data . . . . .	89
3.11	Fit parameters for the NaI FM detectors below the K-edge . . . . .	90
3.12	Fit parameters for the NaI FM detectors above the K-edge . . . . .	90
3.13	CE relation for NaI FM01–FM07 below the K-edge . . . . .	91
3.14	CE relation for NaI FM08–FM13 below the K-edge . . . . .	92
3.15	CE relation for NaI FM01–FM07 above the K-edge . . . . .	93
3.16	CE relation for NaI FM08–FM13 above the K-edge . . . . .	94
3.17	Fit parameters for the BGO detectors . . . . .	108
3.18	CE relation for BGO detectors . . . . .	109
3.19	Energy resolution of the NaI detectors FM01–FM07 . . . . .	112
3.20	Energy resolution of the NaI detectors FM08–FM13 . . . . .	113
3.21	HV values for each NaI FM detector . . . . .	125
3.22	HV power-law fit results . . . . .	126
3.23	Parameters for the thermal test campaign . . . . .	127
4.1	Spectral fit parameters for GRB 090323 and GRB 090328 . . . . .	143

## LIST OF TABLES

---

4.2	Properties of joint GBM–LAT detected bursts . . . . .	145
4.3	Spectral fit parameters for GRB 090902B . . . . .	163
4.4	GRB 080810 BAT and GBM $T_{90}$ measurements . . . . .	168
4.5	Fits to GRB 080810 time-sliced spectra from GBM and BAT . . . . .	169
5.1	Properties of 56 bright GRBs . . . . .	175
5.2	NaI and BGO burst duration . . . . .	179
5.3	BGO CTIME energy channels . . . . .	180
5.4	Peak count rates of the <i>MAIN</i> sample . . . . .	184
5.5	GRBs located inside or at the edge of the LAT FoV . . . . .	187
5.6	Time–integrated fit results . . . . .	194
5.7	Fluence results . . . . .	197



# Summary and Dissertation Outline

Gamma-Ray Bursts (GRBs) represent the most explosive events in the Universe after the Big Bang. They are sudden, intense flashes of gamma-rays, which, for a few blinding seconds, become the brightest objects in the Universe. This reflects extreme conditions which are fascinating and worth exploring.

During the last two decades, the understanding of GRBs has been revolutionized more by observational progress rather than by theoretical predictions. A first major advance in the comprehension of the GRB phenomenon occurred in 1991 with the launch of the Compton Gamma-Ray Observatory (CGRO). The all-sky survey from the Burst and Transient Experiment on-board CGRO measured about 3000 bursts and showed that they were isotropically distributed, thus suggesting a cosmological origin. A better understanding of the physics of GRBs has been made possible by precise localizations in the late '90s, which discovered that the prompt emission in  $\gamma$ -rays is followed by a longer-lasting afterglow, which can be detected in all wavelength ranges from radio, optical, to X- and  $\gamma$ -rays up to several days after the explosion. The huge energy and power releases required by cosmological distances supported what has become a “standard” model in the theoretical framework of GRBs, according to which the observed radiation arises as the outcome of a relativistically expanding “fireball”.

Among the scientific objectives of one of the present NASA missions, the *Fermi* Gamma-ray Space Telescope (FGST), is the study GRBs. *Fermi*'s payload comprises two science instruments, the Large Area Telescope (LAT) and the Gamma-Ray Burst Monitor (GBM). GBM was designed to detect and localize bursts for the *Fermi* mission. By means of an array of 12 NaI(Tl) (8 keV to 1 MeV) and two BGO (0.2 to 40 MeV) scintillation detectors, GBM extends the energy range (20 MeV to  $> 300$  GeV) of the LAT instrument into the traditional range of current GRB databases. The physical detector response of the GBM instrument to GRBs has been determined with the help of Monte Carlo simulations, which are supported and verified by on-ground individual detector calibration measure-

## SUMMARY AND DISSERTATION OUTLINE

---

ments. The GBM detectors have been calibrated from 10 keV to 17.5 MeV using various gamma sources, and the detector response has been derived by simulations over the entire energy range (8 keV to 40 MeV) using GEANT.

The GBM instrument has been operating successfully in orbit since June 11, 2008. The total trigger count from the time GBM triggering was enabled in July 2008 through December 2009 is 655, and about 380 of these triggers were classified as GRBs. Moreover, GBM detected several bursts in common with the LAT. These amazing detections mainly fulfill the primary science goal of GBM, which is the joint analysis of spectra and time histories of GRBs observed by both *Fermi* instruments. For every trigger, GBM provides near-real time on-board burst locations to permit repointing of the spacecraft and to obtain LAT observations of delayed emission from bursts. GBM and LAT refined locations are rapidly disseminated to the scientific community, often permitting extensive multiwavelength follow-up observations by NASA's *Swift* mission or other space-based observatories, and by numerous ground-based telescopes, thus allowing redshift determinations.

Calculations of LAT upper limits are mainly based on the brightest bursts detected by GBM inside the LAT field-of-view. The determination of a consistent sample for upper-limit calculations can be established by selecting those bursts which have a strong signal in the GBM BGO detectors. The careful preparation of a sample of BGO-bright bursts detected by GBM during its first year is fundamental to look into the most interesting burst characteristics. This is mainly possible thanks to a detailed spectral analysis of the selected sample, and the successive investigation of correlations among spectral parameters.

The structure of this thesis can be summarized as follows: The first chapter introduces the basic concepts and scientific background of GRB physics. Afterwards, instrumental details about the *Fermi* instruments LAT and GBM, as well as LAT performance and capabilities for GRB science are presented in chapter 2. Chapter 3 focuses on the detector-level calibration of the GBM instrument, and in particular on the analysis methods and results, which crucially support the development of a consistent GBM instrument response. The main GBM scientific results collected during the first year of operation are then presented in chapter 4. Particular emphasis is given to the description of joint GBM-LAT and GBM-*Swift* observations and analysis results. The last chapter presents the selection methodology and detailed spectral analysis of a sample of well-defined BGO-bright bursts detected by GBM during its first year. Using these results, correlations among spectral parameters are finally discussed.

# Zusammenfassung

Gammastrahlenblitze (GRBs) stehen für die explosivsten Ereignisse im Universum nach dem Urknall. Sie sind plötzliche, starke Blitze von Gammastrahlen, die für ein paar Sekunden die hellsten Objekte im Universum werden. Dies spiegelt die extremen Entstehungsbedingungen dieser Ereignisse wieder, die faszinierend und erforschungswert sind.

In den letzten zwei Jahrzehnten hat sich das Verständnis von GRBs mehr dank der Fortschritte bei den Beobachtungstechniken als durch theoretische Vorhersagen erweitert. Ein erster wichtiger Schritt zum Verständnis des GRB-Phänomens erfolgte im Jahr 1991 mit dem Start des Compton Gamma-Ray Observatory (CGRO). Durch den All-Sky Survey des Burst and Transient Experiments an Bord des CGROs wurden etwa 3000 GRBs beobachtet. Es konnte so gezeigt werden, dass ihre Positionen am Himmel isotrop verteilt sind und somit einen kosmologischen Ursprung nahelegen. Ein besseres Verständnis der Physik der GRBs wurde durch genauere Lokalisierungen in den späten 90er Jahren ermöglicht, welche zu der Entdeckung führten, dass die Anfangsemission im Gamma-Bereich von einer längeren Emission, später Nachleuchten genannt, begleitet wird. Das Nachleuchten wurde in allen Wellenlängen entdeckt, und zwar vom Radio bis in den optischen, Röntgen und Gamma-Bereich hinein. Dieses Nachleuchten kann bis zu mehreren Tagen nach der Explosion beobachtet werden. Die durch die kosmologische Entfernung erforderliche und extrem hohe Energiefreisetzung resultierte in dem heute bekannten "Standard" Modell der GRB-Theorien. Bei diesem Modell entsteht die beobachtete Strahlung als Ergebnis eines relativistisch expandierenden "Fireball".

Zu den wissenschaftlichen Zielen einer der derzeitigen NASA-Missionen, nämlich des *Fermi* Gamma-Ray Space Telescope (FGST), zählt auch das Studium der GRBs. *Fermis* Nutzlast besteht aus zwei wissenschaftlichen Instrumenten, dem Large Area Telescope (LAT) und dem Gamma-Ray Burst Monitor (GBM). Die GBM-Detektoren wurden entwickelt, um GRBs für die *Fermi*-Mission zu

entdecken und zu lokalisieren. Durch eine Anordnung von 12 NaI (Tl) (8 keV bis 1 MeV) und zwei BGO (0,2 bis 40 MeV) Szintillatoren erweitert GBM den Energiebereich (20 MeV bis > 300 GeV) des LAT-Instruments in den traditionellen GRB-Energiebereich. Die charakteristischen Eigenschaften der GBM-Detektoren wurden mit Hilfe von Monte-Carlo-Simulationen ermittelt, die durch detaillierte Messungen während mehrerer Eichungskampagnen unterstützt wurden. Die GBM-Detektoren wurden von 10 keV bis 17.5 MeV mit verschiedenen radioaktiven Gammaquellen kalibriert, und Simulationen wurden später über den gesamten Energiebereich (8 keV bis 40 MeV) mit GEANT durchgeführt.

Das GBM-Instrument ist seit dem 11. Juni 2008 erfolgreich in Betrieb. Die gesamte Anzahl der getriggerten Ereignisse seit Aktivierung des "on-board Triggers" im Juli 2008 bis Dezember 2009 ist 655. Rund 380 dieser Trigger wurden als GRBs identifiziert. Ausserdem entdeckte der GBM mehrere GRBs gemeinsam mit dem LAT. Diese herausragenden Entdeckungen erfüllen vor allem das primäre Ziel des GBMs, nämlich die gemeinsame Analyse der Spektren und des zeitlichen Verlaufs der GRBs, die von beiden *Fermi*-Instrumenten beobachtet werden. Für jeden Trigger bestimmt der GBM eine Echtzeitposition, die möglicherweise zu einer Weiterbeobachtung des Objektes durch das LAT-Instrument führen kann mit dem Ziel, die Entdeckung verzögerter hochenergetischer GRB-Emission zu ermöglichen. Die mit dem LAT gemessenen genaueren Positionen werden dann in kürzest-möglicher Zeit an die GRB-Gemeinschaft weitergegeben, damit andere Satellitenmissionen, wie z. B. die NASA *Swift* Mission, und Bodenteleskope den GRB in anderen Wellenlängenbereichen weiterbeobachten können. Diese Beobachtungen können dann in günstigen Fällen zu einer Bestimmung der Rotverschiebung führen.

Falls ein GRB nur vom GBM gemessen wird, ist die Berechnung der oberen Grenze der Emission für das LAT extrem interessant und basiert im Wesentlichen auf den hellsten GBM Bursts, die auch im LAT Sichtfeld sichtbar sind. Um Berechnungen solcher Obergrenzen durchführen zu können, benötigt man eine sinnvolle Untermenge von GRBs. Für diese Untermenge wurden die Bursts ausgewählt, die ein starkes Signal in den BGO-Detektoren hatten. Eine sorgfältige Auswahl ist sehr wichtig, um später einen Einblick in die Burst-Emissionsprozesse geben zu können. Dies ist vor allem dank einer detaillierten spektralen Analyse der ausgewählten GRB-Liste und der nachfolgenden Untersuchung von Korrelationen zwischen den spektralen Parametern möglich.

Die vorliegende Arbeit gliedert sich in zwei Teile. Der erste behandelt mehr die technischen Eigenschaften der GBM-Detektoren, während sich der zweite im

Wesentlichen auf die wissenschaftlichen Ergebnisse konzentriert. Kapitel 1 führt in die physikalischen Grundlagen und wissenschaftlichen Zusammenhänge von GRB–Theorie und Beobachtungen ein. Im Kapitel 2 werden die Instrumente der *Fermi*–Mission LAT und GBM vorgestellt. Kapitel 3 befasst sich mit der Kalibrierung des GBM–Instruments, und insbesondere mit den Analysemethoden und –ergebnissen, welche zur Entwicklung und Unterstützung eines leistungsfähigen Instruments nötig sind. Die wichtigsten wissenschaftlichen Ergebnisse, die der GBM während des ersten Jahres der *Fermi*–Mission erhalten hat werden dann in Kapitel 4 vorgestellt. Besonderer Wert wird auf die gemeinsamen GBM–LAT und GBM–*Swift* Ergebnisse und Analysen gelegt. Das letzte Kapitel behandelt die Selektionskriterien einer wohl definierten Liste von BGO–hellen Bursts. Zur Analyse der zeitintegrierten Spektren werden verschiedene Modelle verwendet. Die erhaltenen Ergebnisse werden zuletzt im Rahmen empirischer GRB–Korrelationen zwischen spektralen Parametern diskutiert.

## ZUSAMMENFASSUNG

---

# Chapter 1

## Gamma-Ray Bursts: An Overview

GRBs are, by definition, electromagnetic signals in the hard X-ray band with short durations, having most of their electromagnetic output typically at sub-MeV energies. Most of it is concentrated into a brief episode, which, for a few seconds, outshines every other gamma-ray source in the sky.

The GRB field is almost unique in astrophysics in its multidisciplinary nature. Involving stellar-scale events located at cosmological distances, GRBs straddle the traditional distance scales, and represent a high-energy phenomenon emitting a broad-band electromagnetic spectrum, which extends over at least fifteen decades, as well as some possible non-electromagnetic signals, such as cosmic rays, neutrinos and gravitational waves. This makes the GRB field an intersection of many branches in astrophysics.

GRBs have been studied since 1963, and were not predicted by any theory prior their serendipitous discovery. Since then, astronomers have performed 40 years of studies and observations, starting to converge on a model that has successfully explained and predicted their emission at different wavelengths, at least for bursts lasting longer than 2 s. However, there are still observations that puzzle and challenge the concept of GRBs.

Experimental observation led the developments in the GRB field more than theoretical modeling. Many key results were obtained with the launch of new satellites, opening new areas of research. This chapter describes the observational and theoretical progress in the GRB study which followed the main GRB-dedicated space missions.

### 1.1 The “Dark” Era

In 1950, the *Treaty Banning Nuclear Weapon Tests in the Atmosphere, in Outer Space and Under Water* was negotiated by USA, USSR and Great Britain (France joined in 1960 and China in 1964). To assure that the treaty was not being violated, the US started a project called VELA (from Spanish “Watchman”). The VELA project was a series of satellites carrying X-ray detectors to observe the X-ray blast of a nuclear explosion. Even if those small detectors were good enough for the detection of nuclear bombs exploding on Earth, it was thought that the Russians could have the technology to let a bomb explode on the dark side of the moon. In this case the X-rays are completely shielded, but the radioactive blast triggered by the bomb and expanding beyond the lunar dish produces detectable gamma-rays. This was the reason for having small gamma-ray and neutron detectors on board.

The first VELA satellite was launched in 1963. On July 2, 1967, VELA 4 (launched in 1965) detected a flash of mysterious gamma-rays, but it was not able to deduce the exact origin of this radiation. Only VELA 5A & B (launched in 1969) and VELA 6A & B (launched in 1970) had the timing accuracy necessary to reconstruct the source direction through differences in the arrival of the measured photons via triangulation. A detailed analysis of the recorded gamma-ray flashes started in 1972, the main conclusion being that they were of extraterrestrial origin. The discovery was finally published in 1973 (Klebesadel et al., 1973) with a total of 16 GRBs observed between 1969 and 1972. All events were within an energy range of 0.2–1.5 MeV, and the time-integrated flux densities varied between  $\sim 10^{-5}$  to  $\sim 2 \times 10^{-4}$  erg cm $^{-2}$ .

It was immediately realized that the light curves of GRBs are quiet variable from one burst to the next, and that the timescales can vary from few milliseconds to hundreds of seconds. Some had light curves with no structure while others had clearly resolved peaks as observed in the first GRB (Figure 1.1). The large variety of shapes has been tentatively used to classify GRBs, but without much success. The only exception was the possible bimodal distribution of GRB durations, which was already evidenced by the first experiments (Mazets et al., 1981b).

The detection of bursts of gamma-rays was soon confirmed by other satellites (*IMP-6* and Russian *Konus*) and new space missions were dedicated to gamma-ray and X-ray observations. Most of these experiments were sensitive to a decade of energy in the keV regime and, unlike the VELA satellites, were equipped to do spectroscopy of the gamma-ray events. Cline et al. (1973) reported spectral

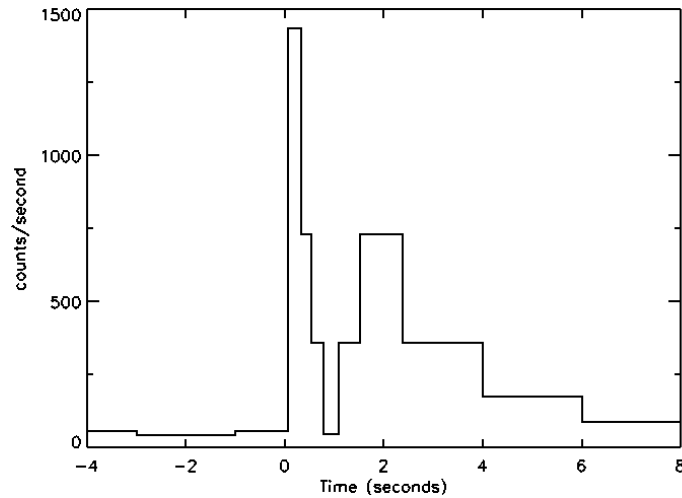


**Figure 1.1:** Light curve of the first Gamma-Ray Burst observed by VELA 4A on July 2nd, 1967. The VELA 4A & B data was used to construct a time history of this event which was published in *Scientific American* in 1976. The light curve shows two well defined peaks at  $\sim 0.3$  s and  $\sim 2$  s presenting evidence of structured GRB concaves, later observed in other GRBs. From Strong & Klebesadel (1976)

measurements of six GRBs using a semi-omnidirectional X-ray detector on IMP-6. These spectra appeared to be well represented by an exponential of the form  $dn/dE = I_0 \exp(-E/E_0)$  photon/( $\text{cm}^2 \text{ keV s}$ ) with a characteristic energy  $E_0$  of 150 keV. Quickly, other results were reported: a significant contribution was made e.g. by Mazets et al. (1981b), who measured the spectra of 143 bursts between 30 keV and 2 MeV from September 1978 to February 1980. An important property of GRB's spectra which was discovered very early is the spectral variability: very often, the spectrum was observed to soften during the evolution of the burst. The Gamma-Ray Spectrometer (GRS) on board the Solar Maximum Mission (SMM) illustrated this kind of evolution, quantified by a hardness ratio (see Fig. 1.2, Norris et al. (1986)).

Independently of the precise shape of the spectra, a general property of GRBs is the non-thermal nature of their emission, with the maximum of their energy emitted in the hard X-ray or soft gamma-ray domain (100 keV to 1 MeV). The paucity of soft X-rays is another general property of GRBs. Various thermal and non-thermal radiation processes have been considered to fit the continuum of GRB spectra obtained with a large diversity of instruments (see e.g. Lamb, 1984). For the 20 years following the publication of the GRB discovery, this mysterious phenomenon led to a huge interest and to numerous conferences and publications on the subject, as well as the proliferation of theories. In one famous review

## 1. GAMMA-RAY BURSTS: AN OVERVIEW

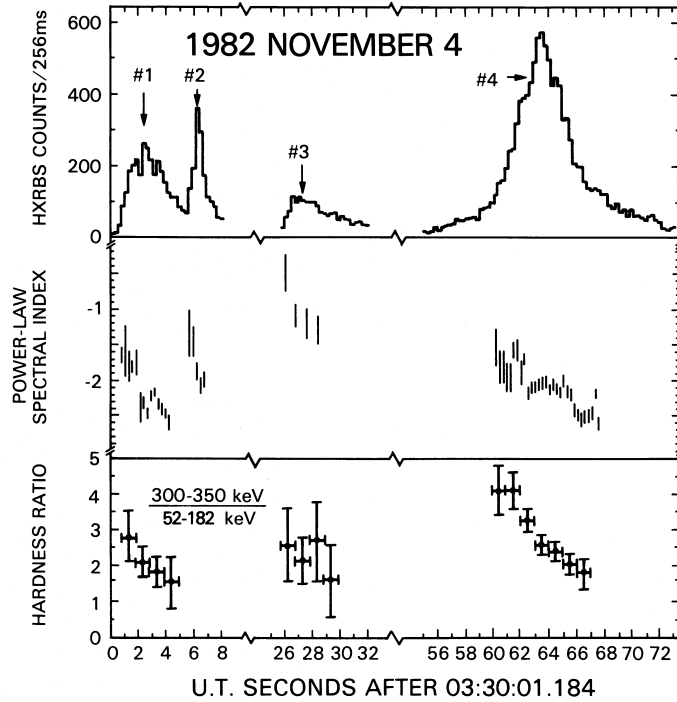


**Figure 1.2:** Temporal variations in GRB 821104. Principal pulse structures are labeled 1 through 4 in the *top panel*. Spectral power-law indices are obtained from fits between 144 and 440 keV (*middle panel*). The ratio of the count rates in the 300–350 keV band and 52–182 keV band are plotted in the *bottom panel*. From Norris et al. (1986)

article at the 1975 Texas Symposium on Relativistic Astrophysics, no fewer than 100 different possible theoretical models of GRB were listed (Ruderman, 1975).

For several years it was believed that GRBs originate from Galactic neutron stars on the basis of the low-energy absorption features, explained as cyclotron resonance lines (indicating strong magnetic fields), seen by the *Konus* and later by the *Ginga* satellites and of high-energy emission features, interpreted as the 511 keV annihilation line originating near the surface of a solar-mass neutron star (Mazets et al., 1981a; Murakami et al., 1988). The later demonstration that the majority of GRBs lie at cosmological distances and the no-detection of these features by other instruments except *Ginga* made these explanations very unlikely.

The mystery around GRBs lasted nearly 30 years although observations already pointed to some of the now well known properties of GRBs. However they were not sufficiently conclusive because it was not possible to detect any counterpart of the GRB phenomenon at any wavelength, due to the large error boxes of the positions given by the gamma-ray instruments.

## 1.2 The BATSE Era

After the discovery phase and the confirmation by the other small satellites, the next major advance occurred with the launch of the *Compton Gamma-Ray Observatory* (CGRO). CGRO was a sophisticated satellite observatory dedicated to observe the high-energy Universe, operating from April 5, 1991 to June 3, 2000. It was so big (17 tons) that it had to be launched with the space shuttle. Compton carried a collection of four instruments which together could detect an unprecedented broad range of six decades in energy, from 20 keV to 30 GeV, and which were much larger and more sensitive than any gamma-ray telescope previously flown in space. These instruments were the *Burst And Transient Source Experiment* (BATSE), monitoring the sky in the 20 to 1000 keV band; the *Oriented Scintillation Spectrometer Experiment* (OSSE) in the 0.05 to 10 MeV band; the *Imaging Compton Telescope* (COMPTEL) in the 0.8 to 30 MeV band; and the *Energetic Gamma-Ray Experiment Telescope* (EGRET), operating between 20 MeV and 30 GeV.

### The Burst And Transient Source Experiment

Thanks to its full sky coverage and to its sensitivity, BATSE was a very successful instrument which detected nearly 3000 GRBs in nine years. BATSE consisted of eight detector modules that were located at the corners of the spacecraft at an angle of  $54.7^\circ$  with respect to the spacecraft's z-axis. This allowed a burst to be observed with four BATSE detectors, thus enabling subsequent localizations of the events to a few degrees. Each module comprised two types of detectors, a Large Area Detector (LAD) and a Spectroscopy Detector (SD). The LAD was the primary detector of BATSE and was made of a disc-shaped NaI(Tl) crystal of 50.8 cm diameter and 1.27 cm thickness, uncollimated for a large field-of-view. The scintillation light was collected by three PMTs. In front of the LAD a plastic scintillator was used as an active shield against charged particles (charged-particle detector or CPD). Events registered in both the LAD and the CPD were rejected.

The large detection area of the LAD provided much higher sensitivity than the SD, thus offering a fine temporal resolution with a sufficiently high energy resolution. The Full-Width at Half-Maximum (FWHM) energy resolutions of the LAD at 88, 511, 662, and 1275 keV were, on average, 27%, 17%, 16% and 19%, respectively (Horack, 1991). The LAD used automatic gain control to stabilize the energy gain by adjusting the high voltage applied to the PMTs so that the 511 keV electron annihilation line position in the detector's channel space stayed

## 1. GAMMA-RAY BURSTS: AN OVERVIEW

---

constant. Therefore, the energy ranges of all eight LADs were nearly fixed to 30–2000 keV throughout the mission. The SD was also an un-collimated NaI(Tl) scintillation detector, but with a cylindrical shape of 12.7 cm diameter and 7.62 cm thickness. It was directly coupled to a single PMT, identical to those used for the LADs. On the BATSE module, the SD was mounted under the LAD. Because of its thickness, the SD provided much finer energy resolution than the LAD. The FWHM energy resolutions of the SD at 88, 511, 662, and 1275 keV were, on average, 15%, 8%, 7% and 6%, respectively (Horack, 1991). The gains of the SDs were commandable from ground to allow broader energy coverage extending from  $\sim 5$  keV with high gain, to  $\sim 20$  MeV, with low gain. BATSE sensitivity and good time resolution allowed the study of the detailed energy and temporal evolution of the GRB spectra, providing information on the nature of GRBs that constitutes the basis of our knowledge of these phenomena. A comparison of the BATSE instrument performances with the GBM ones is given in chapter 3. Hereafter, the main solid results achieved during the CGRO era concerning the GRB prompt emission, i.e. what is usually identified as the gamma-ray burst itself, are briefly reviewed.

### 1.2.1 GRB Global Properties

#### Angular Distribution

BATSE observations proved with high level of accuracy that GRBs are isotropically distributed across the sky. Figure 1.3 shows the position of the 2704 bursts detected by BATSE, and it can be seen that their locations are distributed completely isotropically in the sky. This is true both for short as for long bursts. Isotropy suggested a cosmological distribution, with no dipole or quadrupole components (Meegan et al., 1992). Furthermore, the number counts distribution of the BATSE bursts displayed a paucity of faint bursts relative to the number expected in an Euclidean space. This provided another piece of evidence for the cosmological origin of the sources (Fenimore et al., 1993b).

#### Temporal Properties

The large diversity of GRB morphology was of course confirmed. GRB durations span 5 orders of magnitude, while their time histories can have diverse morphologies, from single-peaked to multiple-peaked events with a complicated structure. Four main temporal properties of GRBs are listed below.

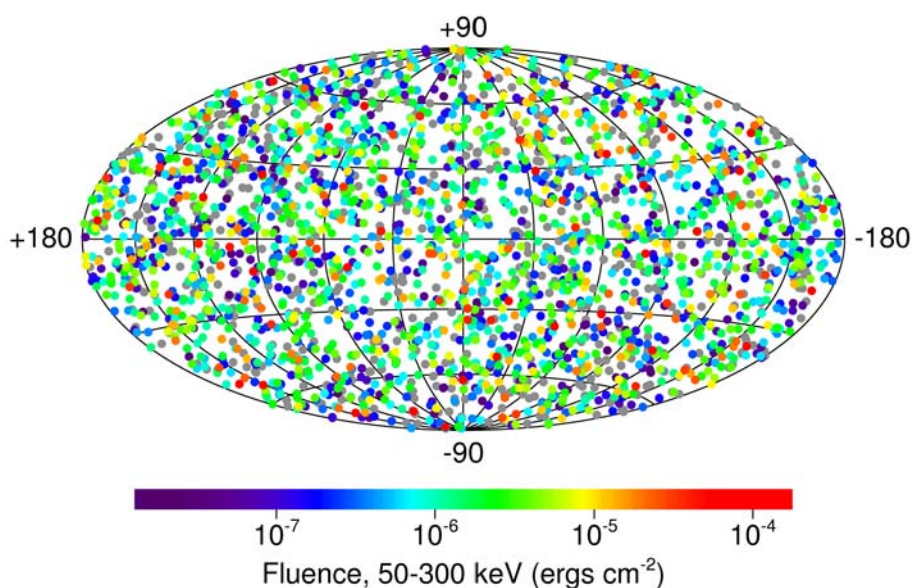


**Figure 1.3:** Isotropic all-sky distribution of 2704 GRBs recorded with BATSE during the nine-year mission. The projection is in Galactic coordinates. The burst locations are color-coded based on the fluence: Bright bursts appear in red, and weak bursts appear in purple. Grey is used for bursts for which the fluence cannot be calculated due to incomplete data. From <http://www.batse.msfc.nasa.gov/batse/grb/skymap/>

1. Several attempts have been made to categorize the bursts by their temporal morphologies. Finally, the burst duration appeared as the main characteristic for the identification of two distinct classes of GRBs. The distribution of burst durations can be technically expressed in terms of  $T_{90}$  or  $T_{50}$ , i.e. the time interval within which 90% or 50% of the burst fluence is detected. Figure 1.4 shows that the distribution of GRB durations appears bimodal, the majority of them lasting more than 2 s (“long GRBs”), while about one third is shorter (“short GRBs”) (Kouveliotou et al., 1993). Typical values are represented by  $\sim 20$  s for long bursts and  $\sim 0.2$  s for short bursts. The hardness of GRBs has also been calculated and represented as a function of their duration. Figure 1.5 shows that shorter bursts tend to have harder spectra than the long ones.
2. The GRB light curves are very irregular (see Figure 1.6), consisting of single or multiple peaks that may be distinct and well-separated or overlap with each other. Some bursts consist of very erratic, spiky components, while others are smooth with one or a few components. The time intervals between the peaks vary (during the burst itself) and sometimes the intervals

## 1. GAMMA-RAY BURSTS: AN OVERVIEW

---

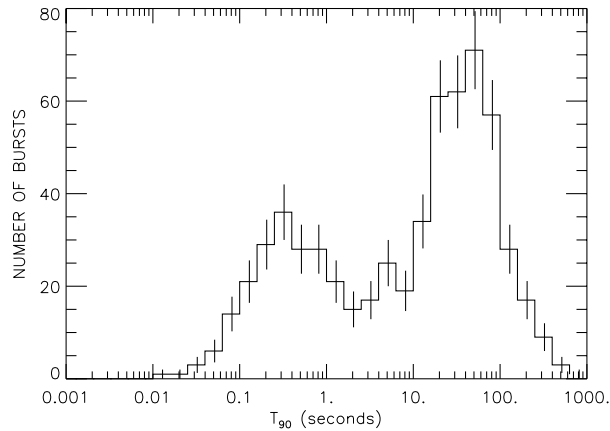


**Figure 1.4:** Bimodal burst distribution created with the BATSE  $T_{90}$  times from the BATSE 4B Catalog. Light curves used for the calculation of  $T_{90}$  are integrated over all 4 channels ( $E > 20$  keV). From Paciesas et al. (1999)

of emission alternate with long quiescent periods. Bursts with a large number of pulses in the time history are found to have larger fluences and longer durations (Quilligan et al., 2002).

3. The light curves display rapid variability, down to the millisecond time-scale (Bhat et al., 1992). The width of individual pulses ( $\Delta t$ ) varies in a wide range. The shortest spikes have millisecond or even sub-millisecond widths, and  $\Delta t/T$  could reach as low as  $10^{-3}$ – $10^{-4}$ . Historically, the fast varying flux has provided the key justification for the compact size of the emitting region of GRBs. Cavallo & Rees (1978) examined the processes taking place in a fireball of high-energy (MeV) photons, pointing out that a source with the energy content and sizes inferred for GRBs would be highly opaque. This was formulated as the “compactness problem” (see §1.3.2) and invoking relativistic motion of the source to overcome it was decisive in understanding GRB events.
4. The vast majority of individual pulses are asymmetric, with leading edges steeper than the trailing ones, although only a small fraction can be visually discerned. Smooth single peak bursts are generally described by a FRED-like profile (Fast Rise Exponential Decay) (Norris et al., 1996). Time histories are different in different energy bands and at higher energies the overall burst duration as well as the rise and decay time scales are shorter than those at lower energies (Link et al., 1993).

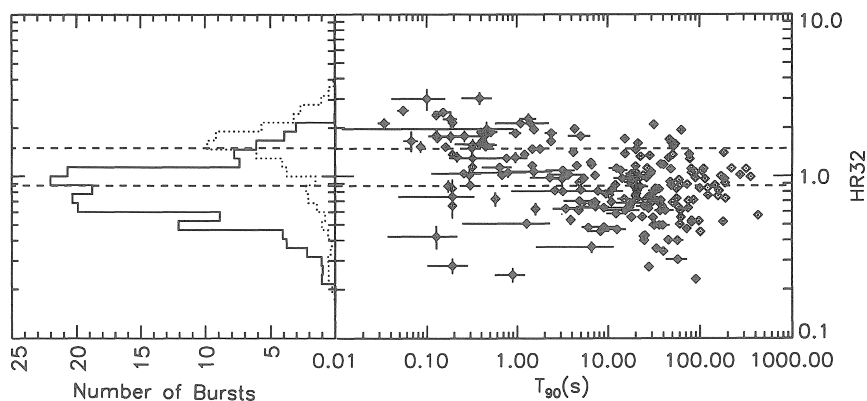


**Figure 1.5:** Distribution of hardness ratio versus  $T_{90}$  for 222 BATSE GRBs. The hardness ratio is defined by the ratio of counts in the energy ranges [100–300]/[50–100].  
From Kouveliotou et al. (1993)

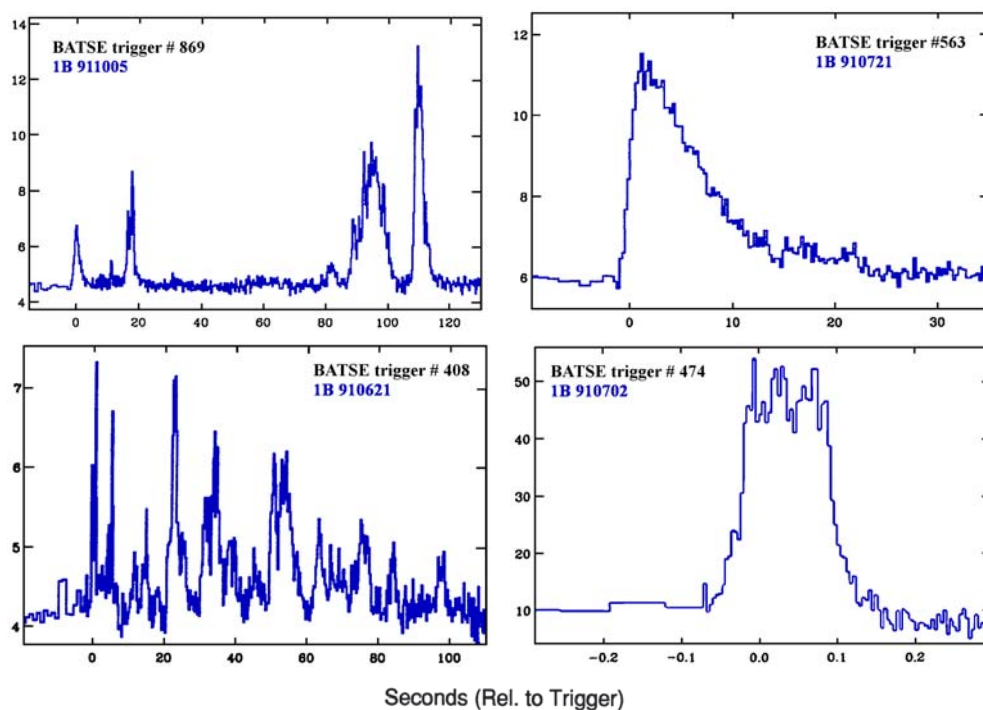


**Figure 1.6:** An assortment of light curves from the first BATSE Catalog illustrating the variety evident in burst temporal profiles: from the *top left panel* (clockwise) multi-episode, FRED, short and erratic. From Fishman et al. (1994)

## 1. GAMMA-RAY BURSTS: AN OVERVIEW

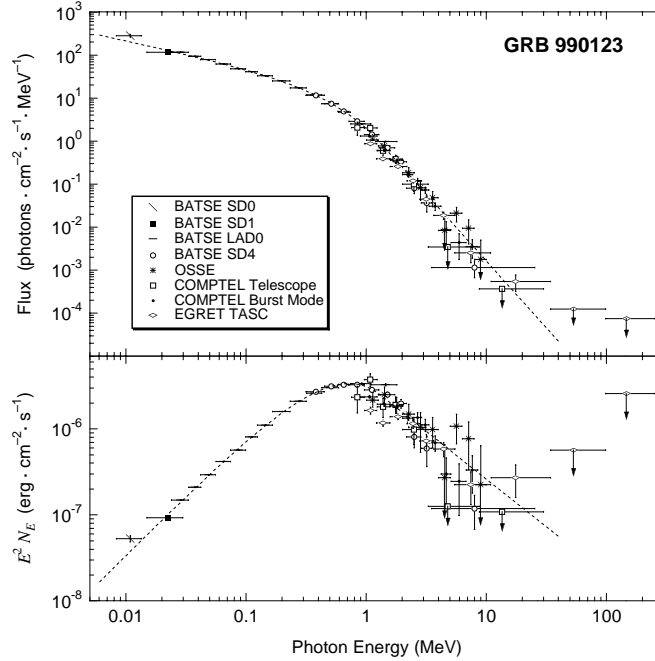


**Figure 1.7:** Deconvolved spectra of GRB 990123 from the CGRO detectors, shown both as photon flux  $N_E$  (*upper panel*) and in  $E^2 N_E = \nu f_\nu$  (*lower panel*) units. The spectra have been re-binned into wider bins for clarity. From Briggs et al. (1999a)

### Spectral Properties

The GRB continuum spectrum is non-thermal, with almost all of the luminosity emitted as gamma-ray photons, from  $\sim 100$  keV to  $\sim 1$  MeV (however this spectral range may suffer from selection effects due to instrumental sensitivity, see e. g. Lloyd & Petrosian, 1999). Thermal (Planck-like) spectra are ruled out for the great majority of bursts. The main characteristics of GRB spectra appear more clearly when  $E^2 N_E$  is plotted versus  $E$  (see Figure 1.7, *bottom panel*). This representation shows a maximum around a few hundred keV, which has been called  $E_{\text{peak}}$  or  $E_p$  and is a fundamental characteristic of GRBs.

1. GRB spectra observed by BATSE were investigated by Band et al. (1993), who characterized them by a smoothly-joining broken power law, known as the “Band function” (see Figure 1.7, *upper panel*). At low energies, this empirical function is characterized by a power-law continuum with an exponential cutoff:

$$N_E(E) = A E^\alpha \exp\left(-\frac{E}{E_0}\right) \quad (1.1)$$

at high energy, a steeper power-law:

$$N_E(E) = B E^\beta \text{ with } \alpha > \beta, \quad (1.2)$$

where  $\alpha$  and  $\beta$  represent the low and high-energy indices, respectively. The transition between the two functions occurs at  $E_{\text{break}} = E_0(\alpha - \beta)$ , while  $E_p$  is defined by  $E_p = E_0(2 + \alpha)$ . The three spectral parameters,  $\alpha$ ,  $\beta$  and  $E_0$ , are independent and vary from burst to burst with no universal values.  $E_0$  ranges from below 100 keV to more than 1 MeV for BATSE bursts, peaking below 200 keV, with only a small fraction of the spectra breaking above 400 keV. The “Band” spectral shape is valid both for the integrated emission over the whole burst duration, and for the emission during a certain temporal segment of the burst.

2. A sample of 350 bright BATSE bursts with fine time resolution was analyzed by Kaneko et al. (2006), who considered several spectral shapes including the “Band function”. They reported the distributions of the observed sets of parameters. The peak energy of the  $\nu F_\nu$  GRB spectrum,  $E_p$ , ranges from 150 keV to 400 keV, showing a *log-normal* distribution centered around 225 keV (Figure 1.8, *bottom panel*) with a full-width at half-maximum less than a decade in energy. Also for the spectral parameters  $\alpha$  and  $\beta$  there is no universal value, but their distributions peak around  $\sim -1$  (Figure 1.8, *top left panel*) and  $\sim -2.3$  (Figure 1.8, *top right panel*), respectively. The “narrow”  $E_p$  distribution among different bursts is likely to be influenced by selection effects. Furthermore, various investigations indicate that the lack of high  $E_p$  bursts is likely intrinsic (Harris & Share, 1998). The observed spectral parameter diversity must be addressed by the physical model of the emission processes. In the standard model (see §1.3), the observed radiation in a GRB is produced when shock-heated plasma loses its internal energy through synchrotron and inverse Compton emission (Mészáros & Rees, 1993). The peak energy and the high-energy photon index  $\beta$  are associated to the characteristics of the particle energy distribution, while the low-energy photon index  $\alpha$ , and in particular its harder limit, depends significantly on the radiation process at work, and thus gives the possibility of distinguishing between the different scenarios for the GRB emission (Lloyd & Petrosian, 2000).
3. Ford et al. (1995) examined the spectral evolution of the peak energy of the  $\nu F_\nu$  distribution for long and bright GRBs, finding that  $E_p$  decreases with

## 1. GAMMA-RAY BURSTS: AN OVERVIEW

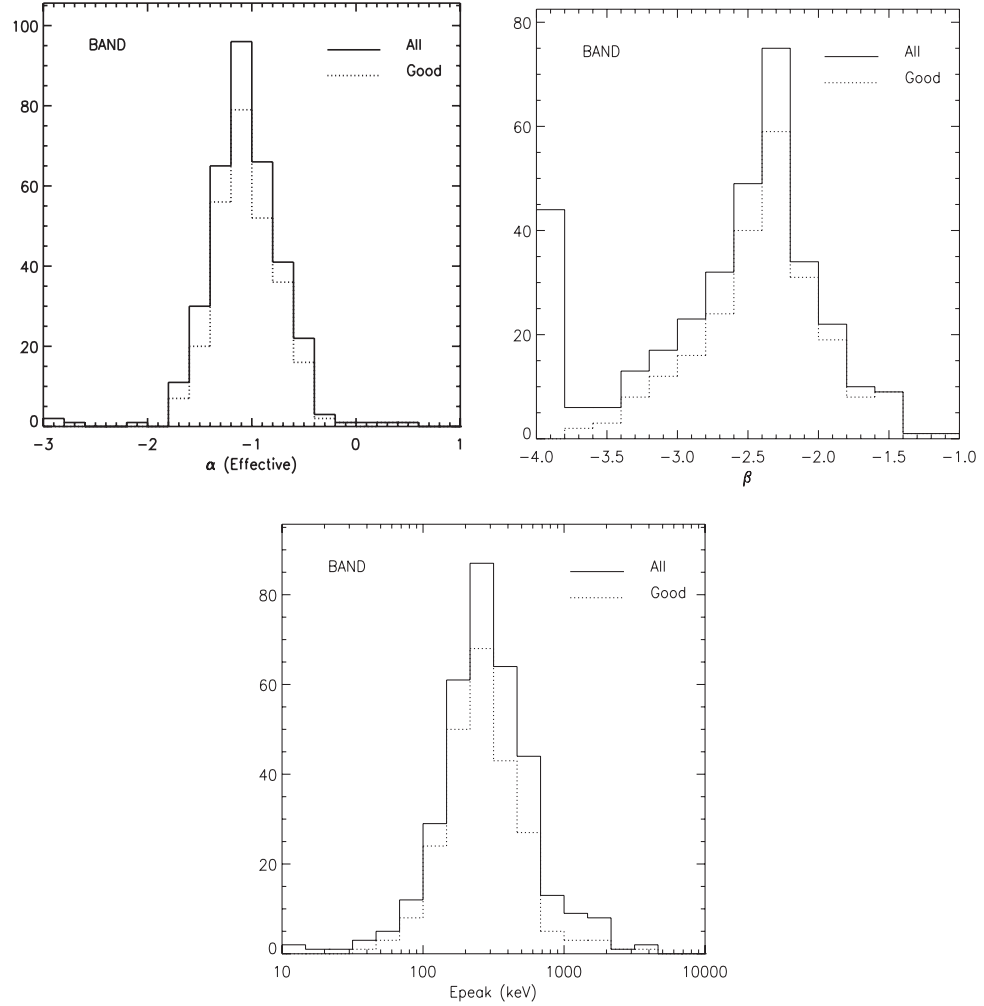


**Figure 1.8:** Low-energy index (*top left panel*), high energy index (*top right panel*) and  $E_p$  (*bottom panel*) distribution of time-integrated spectra from 350 bright BATSE GRBs fitted with a “Band” model. The distribution of the well-constrained parameters is referred to as “good” (*dotted line*). From Kaneko et al. (2006)

time. This ‘hard-to-soft’ evolution was found also within individual pulses. The study of spectral evolution of the lower energy photon spectra in GRBs (Crider et al., 1997) revealed that in the flux-rise phase the spectrum can be harder than  $E^{-2/3}$ , which is the limiting photon spectral slope predicted by the optically thin synchrotron model (see e. g. Tavani, 1996). Further details regarding different GRB emission models can be found in §1.3.2.

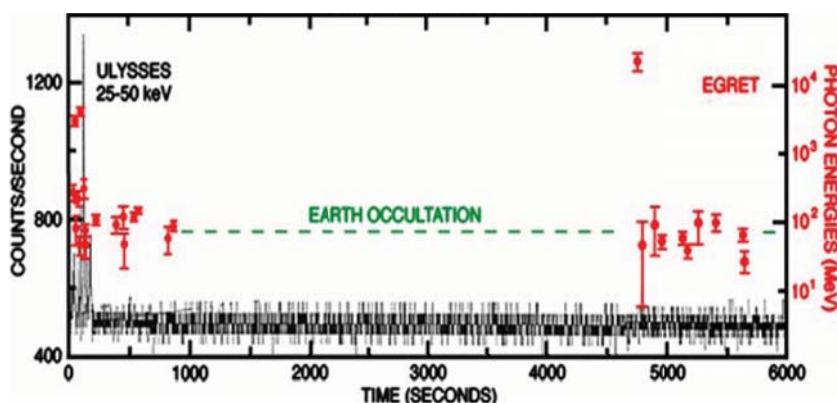


**Figure 1.9:** Prompt and delayed high-energy emission from GRB 940217. The prompt emission as observed by Ulysses in the energy range 25–50 keV is shown as *solid black line*. It lasted 150 s. The *red symbols* represent every photon observed by EGRET. In the right side, the energy for each photon is given. Unfortunately, the Earth occultation did not allow to follow the high energy emission for  $\sim 4000$  s. From Hurley et al. (1994)

## 1.2.2 EGRET and the High-Energy GRB Emission

The first survey of the sky in the 30 MeV–10 GeV range was performed by another experiment on board the CGRO: EGRET. It was a spark chamber equipped with an anti-coincidence counter and a calorimeter, the Total Absorption Shower Counter (TASC), located at the bottom of the module. Although the field of view of the EGRET spark chamber was very limited, the TASC was capable of accumulating data for BATSE-triggered GRBs from all directions, independently from the spark-chamber events. Like the BATSE detectors, the TASC was also a NaI(Tl) scintillation detector with much larger dimension of 76 cm  $\times$  76 cm and 20 cm thickness. The FWHM energy resolution of the TASC was about 20 % over the entire energy range. The response was highly dependent on the incident direction of the event photons, because of the block shape of the TASC NaI crystal, as well as the presence of intervening spacecraft materials surrounding the detector. The TASC was not capable of localizing events; therefore, for GRB observations, the locations determined by BATSE were used to obtain detector response for each event.

The EGRET observed different types of high-energy burst phenomena. Emission above 100 MeV was detected in five bright bursts, namely GRB 910503 (Schneid et al., 1993), GRB 910601 (Dingus, 1995), GRB 930131 (Sommer et al., 1994), GRB 940217 (Hurley et al., 1994) and GRB 940301 (Schneid et al., 1994). One of this sources, GRB 930131, had high-energy emission that was consis-

## 1. GAMMA–RAY BURSTS: AN OVERVIEW

---

tent with an extrapolation from its spectrum obtained by BATSE between 25 keV and 4 MeV (see also Dingus, 2003). However, the correlation with the prompt phase pulses was hampered by the severe EGRET spark chamber dead time ( $\sim 100$  ms/event) that was comparable or longer than the pulse timescales. The EGRET observations of these bursts suggested that the  $\sim 1$  GeV emission would last longer than the lower–energy emission, thus resulting in part from a different physical origin. In GRB 940217, an 18 GeV photon was detected  $\sim 75$  minutes post–trigger (see Figure 1.9). Also 18 events with an energy  $> 30$  MeV were detected in the time interval from the end of the prompt emission until the end of the observation. More recently, a similar behavior was observed only in GRB 080514B by AGILE (Giuliani et al., 2008). In this case, 10 high–energy events with energies up to 300 MeV were detected by the GRID instrument extending for a longer duration (at least 13 s) than the hard X–ray emission observed by SuperAGILE (Tavani et al., 2008), which lasted about 7 s.

The four bursts with high–energy emission detected by EGRET were all long bursts, although GRB 930131 is an interesting case since the BATSE light curve is dominated by a hard initial emission lasting 1 s and followed by a soft extended emission. The discussion whether high–energy emission is present in both long and short bursts remained open until the recent observations made by *Fermi*. *Fermi* is greatly expanding the catalog of high–energy burst detections, thus giving us the possibility to better understand bursts and the environment in which they occur. These new discoveries will be discussed in detail in chapter 4.

Another interesting feature observed during the BATSE era is a high–energy (up to 200 MeV) temporally–resolved spectral component in addition to the Band function, which is clearly present in GRB 941017 (Gonzalez et al., 2003). This component is harder than the low–energy prompt component, and continues after the low–energy component fades into the background, as shown in Figure 1.10, with a single spectral component being ruled out. Recently, Kaneko et al. (2008) presented a detailed study of the time–integrated spectra of GRB 941017 and of another burst, GRB 980923, which shows this additional spectral component, too.

At even higher energies, a tentative  $\gtrsim 0.1$  TeV detection at the  $3\sigma$  level of GRB 970417a has been reported with the water Cherenkov detector Milagro (Atkins et al., 2000). Better sensitivity is expected from atmospheric Cherenkov telescopes such as MAGIC, VERITAS and HESS. Since 2005, MAGIC–I followed up 51 GRBs up to now. However, no significant emission of very–high–energy (VHE) gamma–rays could be detected. For some of the bursts preliminary

### 1.2.2. EGRET and the High-Energy GRB Emission

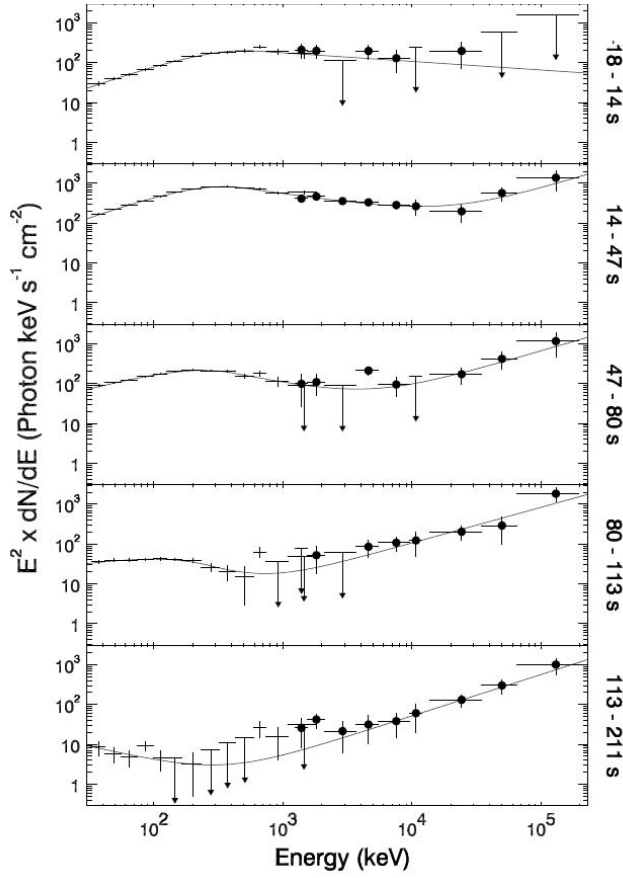


**Figure 1.10:** Energy fluxes for GRB 941017 during 5 different time intervals. *Crosses* and *circles* correspond to BATSE–LAD (Large Area Detector) and EGRET–TASC (Total Absorption Shower Calorimeter), respectively. The *solid lines* represent the best fit to the joint LAD–TASC data using a Band function. The upper limits correspond to  $2\sigma$  deviation from the background. From Gonzalez et al. (2003)

upper limit results were published. In the case of GRB 050713a (Albert et al., 2006) the flux upper limits estimated by MAGIC are compatible with the assumption of an unbroken power-law spectrum extending from a few hundred keV up to hundreds of GeV.

From the theoretical point of view, the few EGRET detections of high-energy gamma-ray emission from the prompt phase require high bulk Lorentz factors of at least several hundreds, due to the lower bounds imposed by the compactness problem later described in §1.3.2.

A natural source for high-energy gamma-rays is the Self-Synchrotron Compton (SSC) component produced by Inverse Compton (IC) from the burst itself or from the afterglow (Mészáros et al., 1994). Typical random Lorentz factors of

## 1. GAMMA–RAY BURSTS: AN OVERVIEW

---

electrons,  $\gamma_e$ , within internal shocks are of order a thousand (in the fluid’s rest frame). The SSC photons energy should be  $\gamma_e^2$  higher than the synchrotron photons. This implies that if the observed gamma–ray emission is produced by synchrotron in internal shocks then the IC emission would produce a second peak around a few hundred GeV. The SSC component would be even higher from the early afterglow. The synchrotron emission from the forward shock is expected to be around 10 keV (if the observed early afterglow is indeed produced by the external shocks). With a Lorentz factor of a typical electron around  $10^5$ , the expected SSC component should be around 100 TeV. Finally the reverse shock emission is expected to produce 100 eV photons (Sari & Piran, 1999). With typical electron Lorentz factors of a few thousand this should correspond to SSC photons with typical energy of 100 MeV. The fluxes of these high energy components should be comparable or even larger than the prompt GRB gamma–rays fluxes. This emission should be simultaneous with the GRB emission. Observations by *Fermi* of the evolution of spectral energy distributions over the full range of a few keV to GeV–TeV energies are currently helping in distinguishing among the possible mechanisms.

### 1.3 The Afterglow Era

One of the most important observational breakthroughs in the study of GRBs was due to innovative discoveries by the Italian–Dutch satellite *Beppo-SAX*. *SAX* was a program of the Italian Space Agency (ASI) with participation of the Netherlands Agency for Aerospace programs (NIVR), and the acronym *SAX* stands for “Satellite per Astronomia X” (X–ray Astronomy Satellite). Launched on April 30, 1996, the satellite was renamed *Beppo-SAX* in honor of the Italian Nobel–Prize winner Giuseppe Occhialini (nicknamed “Beppo”) and remained operative for 6 years, until April 30, 2002. The scientific payload of the satellite was composed by four narrow–field X–ray telescopes (NFI), covering the energy range from 0.1 to 300 keV, two coded–mask Wide Field Cameras (WFCs), sensitive at medium to hard X–ray energies, i.e. 2–26 keV, and the Gamma–Ray Burst Monitor (GRBM), operating in the 40–700 keV energy band. *Beppo-SAX* was able to trigger bursts with the GRBM and to observe them with a position error of arc–minutes due to the WFCs (aligned with GRBM); This made possible to promptly slew the satellite in the found direction and to observe the region with the NFI.

### 1.3.1 Important Observational Progress

#### GRB 970228 & GRB 970508

In February 1997, *Beppo-SAX* pinpointed a new fading X-ray source occurring on longer timescales with respect to the prompt emission of GRB 970228 (see Figure 1.11, Costa et al., 1997). The detection of this radiation, which was called “afterglow”, led to follow-ups at other wavelengths after a delay of a few hours for processing. Thanks to the dissemination of the burst coordinates through the Gamma-ray burst Coordinates Network (i.e. the GCN system, Barthelmy et al., 1998), ground-based telescopes pointed the target and enabled the discovery of an optical afterglow (van Paradijs et al., 1997). The afterglow of GRB 970228 was the first to be detected both in the X-ray band and in the optical band (see Figure 1.12). Ground-based observations of this burst revealed a close proximity of the afterglow with the optical light of a faint galaxy (van Paradijs et al., 1997), later confirmed by HST imaging. Given the low probability of a coincidence with a random field galaxy, it was identified as the likely host of GRB 970228.

The first radio afterglow was detected for GRB 970508 by Frail et al. (1997), who reported a variable radio source within WFCs error box and coincident with the optical transient. This radio afterglow showed strong fluctuations at early times, which vanished at later times (Frail et al., 2000) and which were interpreted as a result of scintillation by the irregularities in the ionized Galactic interstellar gas, thus allowing the determination of the angular size of the source (Goodman, 1997).

#### Redshift Determination

GRB 970508 also represented the first burst for which a direct redshift measurement was obtained. Metzger et al. (1997) inferred a value of  $z \geq 0.835$  from the absorption features imposed on the afterglow continuum. Usually, GRB redshifts can be also derived from the emission features of the host galaxies. The host galaxy of 970508 was identified with the Keck Telescope when the afterglow faded below detection, several months after the GRB (Bloom et al., 1998). This redshift measurements finally confirmed the cosmological distance of the source and marked the end of a 25-year long debate on the distance scale of GRBs and on the amount of energy released in these events, which is of the order of  $\sim 10^{50}$ – $10^{55}$  erg.

## 1. GAMMA-RAY BURSTS: AN OVERVIEW

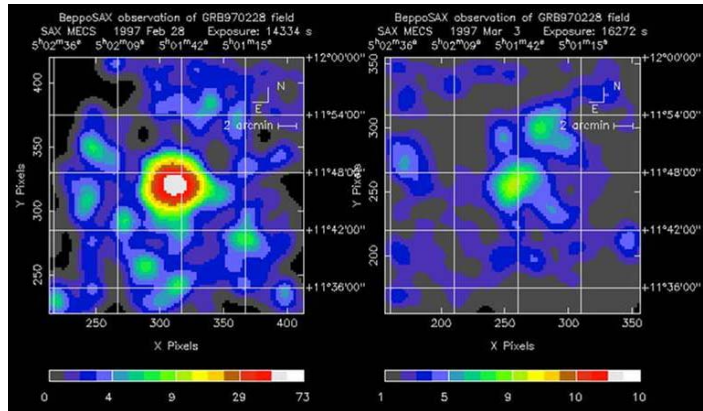


**Figure 1.11:** *Beppo-SAX* observation of the GRB 970228 field on February 28, 1997 (*left panel*) and on March 3, 1997 (*right panel*). It is evident that the X-ray source that is clearly visible during the first day of GRB monitoring fades away after some days. From Costa et al. (1997)

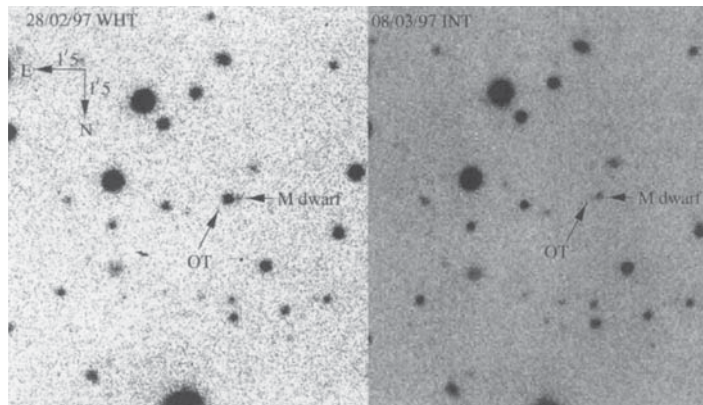


**Figure 1.12:** V-band images of a  $1.5' \times 1.5'$  region of the sky which contains the optical transient (OT) associated with GRB 970228. The *left* image was obtained with the William Herschel Telescope (WHT) on la Palma on February 28, 1997, at 23:48 UT, less than 21 h after the burst. The *right* image was taken with the Isaac Newton Telescope (INT) on March 8, 1997, at 20:42 UT. A large brightness variation is seen between the two images. From van Paradijs et al. (1997)

### Beaming

In some bursts, a clear steepening in the optical light curve was seen after some time  $t_{break}$  of the order of days. Achromatic breaks over different bands were often observed and were typically attributed to the presence of a jet. Therefore such feature was termed the “jet break”. At later times, the decay rate gradually slows down until finally reaching a constant level due to the contribution of the host galaxy.

### The GRB–SN Connection

The connection of GRBs with stellar explosions was first proposed theoretically (Colgate, 1968). A likely GRB–Supernova association was discovered for GRB 980425 vs. SN 1998bw (Galama et al., 1998). SN 1998bw was a peculiar, energetic Type Ic supernova. Independent of the reality of this association, these observations triggered much interest about the possibility that GRBs are in some way connected to some rare kind of supernovae. The main evidences in favor of it were the identifications of rebrightenings of the late optical/IR light curve observed in some afterglows. More examples of the spectroscopic SN–GRB connection include SN 2003dh/GRB 030329 (Stanek et al., 2003; Hjorth et al., 2003), SN 2003lw/GRB 031203 (Malesani et al., 2004), and SN 2006aj/GRB 060218 (Campana et al., 2006; Modjaz et al., 2006).

In 2007, Bissaldi et al. tested whether the hypothesis of type Ib/c SNe from different massive progenitors could reproduce the local GRB rate as well as the GRB rate as a function of redshift. They found an excellent agreement between the observed GRB local rate and the predicted type Ib/c SN rate in irregular galaxies, when a range for single Wolf–Rayet stars of 40–100  $M_{\odot}$  is adopted. They also predicted the cosmic type Ib/c SN rate by taking into account all the galaxy types in a unitary volume of the Universe and compared it with the observed cosmic GRB rate as a function of redshift. By assuming the formation of spheroids at high redshift, they predicted a cosmic type Ib/c SN rate, which is always higher than the GRB rate, suggesting that only a small fraction (0.1–1%) of type Ib/c SNe become GRBs. In particular, they find a ratio between the cosmic GRB rate and the cosmic type Ib/c rate in the range  $10^{-2}$ – $10^{-3}$ , in agreement with previous estimates. Due to the high rate of star formation in spheroids at high redshift, which represented their preferred scenario for galaxy formation, they predicted more GRBs at high redshift than in the hierarchical scenario for galaxy formation, a prediction which remains to be proved by future observations.

### 1.3.2 Theoretical GRB Models

The afterglow emission in the X–ray, optical/infrared and radio bands following the GRB on longer timescales was predicted before its discovery as a consequence of the evolution of the physical conditions responsible for the GRB event (Katz, 1994; Mészáros & Rees, 1997). In the standard GRB emission model, the so-called “fireball” model, the afterglow is produced when the relativistic ejecta interact with the surrounding medium and decelerate. Therefore, the emission is

## 1. GAMMA–RAY BURSTS: AN OVERVIEW

---

expected to shift progressively toward softer energy bands as the burst remnant evolves. In order to better understand the GRB phenomenon, a description of some of the physical processes that follow from observations and of the theoretical structure of the fireball model is essential for further discussions.

### The Compactness Problem

Phenomenological considerations have led to the general agreement that, independently of the mechanism responsible for the primary energy production in GRBs, the emitting material producing the prompt and afterglow emission must be moving relativistically. There are three main characteristics resulting from BATSE GRBs that led to this conclusion:

- The fluences and typical durations, connected to high temporal variability;
- The detection (by EGRET) of photons with an energy above  $\sim 1$  GeV;
- The observed non–thermal spectrum.

For a typical GRB gamma–ray fluence  $F \sim 10^{-6} \text{erg cm}^{-2}$  and a typical GRB duration  $\sim 10$  s, the total isotropic gamma–ray energy released is typically

$$E = 4\pi D^2 F \sim 10^{51} \left( \frac{D}{1 \text{Gpc}} \right)^2 \left( \frac{F}{10^{-6} \text{erg cm}^{-2}} \right) \text{erg}. \quad (1.3)$$

This huge amount of energy has to be released within the short variability time scale, which for many GRBs is of the order of  $\Delta t \sim 10$  ms. Naively (without relativistic motion), the scale of the emission area is  $r_{rad} \sim c\Delta t = 3 \times 10^8$  cm ( $\sim 3000$  km). Assuming that a fraction  $f_p$  of photons is above the energy threshold for the electron–positron pair production,  $E_{th} \sim 2m_e c^2$ , where  $m_e$  is the electron mass and  $c$  the speed of light, there is the possibility that these photons interact with lower energy photons through the process  $\gamma\gamma \rightarrow e^+e^-$ . The pair–production optical depth is huge:

$$\tau_{\gamma\gamma} = \frac{f_p \sigma_T F D^2}{r_{rad}^2 m_e c^2} \simeq 10^{13} f_p \left( \frac{F}{10^{-7} \text{erg cm}^{-2}} \right) \left( \frac{D}{10^{28} \text{cm}} \right)^2 \left( \frac{\Delta t}{10^{-2} \text{s}} \right)^{-2}, \quad (1.4)$$

where  $\sigma_T$  is the Thompson cross section. Such a copious pair production would generate an optically thick fireball, leading to thermalization of the photons. This is inconsistent with the observed non–thermal spectrum of GRBs. The gamma–rays should have been attenuated in the source before traveling through the Universe and reaching the Earth. The only way to get rid of this apparent paradox

is by invoking the relativistic motion of the emitting plasma, characterized by a Lorentz factor  $\Gamma$ , i.e., the GRB emitting region as a whole moves toward the observer at relativistic speed.

The relativistic motion eases the ‘‘compactness problem’’ in two ways (Lithwick & Sari, 2001): first, the observed photons are emitted in the source co-moving frame with a frequency  $\nu' \simeq \nu_{obs}/\Gamma$ . Therefore, a smaller fraction  $f_p$  of photons is above the pair production threshold.  $f_p$  is modified by a factor  $\Gamma^{-2\alpha}$ , where  $\alpha$  is the photon number spectral index ( $N(E)dE \propto E^{-\alpha}dE$ ). Second, the real physical scale of the emission site moving toward the observer is  $r' \sim \Gamma^2 c \Delta t$ . This effect modifies the optical depth by a factor of  $\Gamma^{-4}$ . The combination of these two effects reduces the optical depth to by a factor  $\Gamma^{2\alpha+4}$ . This is only a rough estimate; more sophisticated analyses result in various lower limits of  $\Gamma$  in different bursts (e.g. Woosley & Loeb, 1995; Baring & Harding, 1997). For a typically observed spectral index  $\alpha \sim 2$ , the lower limit to the Lorentz factor  $\Gamma$  required to satisfy the demand of an optically thin source is  $\Gamma > 10^{13/(2\alpha+4)} \simeq 100$ . Hence, GRBs involve the fastest bulk motions known so far in the Universe.

EGRET observations of high-energy photons also contributed to this conclusion. Indeed the energy threshold for pair production depends on the angle between the two interacting photons, having energies  $\epsilon_{th}$  and  $\epsilon_{ta}$  respectively:

$$\epsilon_{th} > 2(m_e c^2)^2 [\epsilon_{ta}(1 - \cos \Theta)]^{-1} \simeq 4(m_e c^2)^2 \epsilon_{ta}^{-1} \Theta^{-2}, \quad (1.5)$$

where  $\Theta$  is the angle between the two photons in the observer’s frame. In the same frame, the causality condition implies  $\Theta \leq \Gamma^{-1}$ . So, in order to get  $\Theta \leq 2m_e c^2 / \sqrt{\epsilon_{th} \epsilon_{ta}}$ , the condition  $\Gamma^{-1} \leq 2m_e c^2 / \sqrt{\epsilon_{th} \epsilon_{ta}}$  has to be fulfilled. Considering an energy of the interacting photon  $\epsilon_{ta} \sim 1$  MeV, it implies  $\epsilon_{th} \leq 10^4 \epsilon_{ta}^{-1} \Gamma_2^2$  MeV, where  $\Gamma_2$  is the Lorentz factor in units of  $10^2$ . Therefore  $\Gamma$  must be  $\gg 1$ . Observations of radio scintillation are also supporting evidence for relativistic motion, if the scintillation is due to scattering off of interstellar gas. In that case, the inferred size of the emitting region and the measured elapsed time lead to an estimate of the bulk velocity.

Moreover, the highly relativistic motion implies unavoidable considerations regarding the fireball composition. A pure photon fireball fails to account for the duration and time structure observed in GRBs, that is, it would result in a very short burst, with a quasi-thermal spectrum emitted after the expanding fireball becomes optically thin (Goodman, 1986; Paczyński, 1986). If the initial energy deposition is accompanied by a baryon-polluted flow (Mészáros & Rees, 1992),

## 1. GAMMA-RAY BURSTS: AN OVERVIEW

---

during the expansion of the fireball the radiative energy is converted into the kinetic energy of the entrained baryons. In this case baryons carry essentially all of the energy of the initial fireball, and the main emission of the observed gamma-ray radiation occurs when the bulk of the kinetic energy of the baryons is re-randomized and radiated away.

Assuming that GRBs result from the slowing down of ultra-relativistic matter, the total amount of the allowed baryonic mass (in order to obtain high Lorentz factors) is  $M_0 = E_0/(\Gamma c^2) \leq 10^{-5} M_\odot$ . The value of the initial baryon loading parameter,  $\eta = E_0/M_0 c^2$ , thus determines the dynamics of the fireball, in particular the relative amount of energy in the bulk kinetic form and in the electron-positron radiation form. From the dynamical point of view, initially the bulk Lorentz factor  $\Gamma$  increases linearly with distance/radius  $r$ , and as the fireball expansion occurs at the expense of the co-moving thermal energy, the temperature  $T$  drops as  $r^{-1}$ . After the maximum bulk Lorentz factor  $\Gamma \sim \eta$  is reached, the fireball reaches a radius  $r_{sat} \propto r_0 \eta$ , where  $r_0$  is the original size of the fireball. The deceleration of the fireball by a factor  $\Gamma \simeq 10^2 \Gamma_2$  takes place at a radius that is greater with respect to the radius where the fireball becomes optically thin. The characteristic duration of GRBs is determined by the temporal interval between photons produced in different regions of the shock wave resulting from the fireball deceleration,  $t_{obs} \sim \Delta R'/(c \eta)$  where  $\Delta R'$  is the co-moving size of the shell formed by the shock wave,  $\Delta R' \sim r_{dec}/\eta$ . Therefore  $t_{obs} \sim r_{dec}/(\eta^2 c)$ . The non-thermal spectrum observed for GRBs is a result of the impact of the fireball with the interstellar medium (ISM). This produces two shocks, a *forward shock* that moves toward the observer, and a *reverse shock*, propagating backward through the fireball. The observed spectrum may be therefore interpreted as the synchrotron radiation produced by shock-accelerated electrons in presence of a magnetic field. These electrons may belong either to the fireball ejected material or to the ISM. The efficiency of such processes depends on the shocks structure, on the presence of magnetic fields and on the efficiency of the electron acceleration by the fireball.

### Internal/External Shocks

Figure 1.13 shows a schematic representation of the fireball shock model. *Internal shocks* form as shells of different Lorentz factors collide with each other, producing the prompt burst emission, while *external shocks* cause an X-ray through radio afterglow as they interact with the local medium. Internal shocks are expected to arise in the flow if e.g. the initial distribution of Lorentz factors (i.e. the time

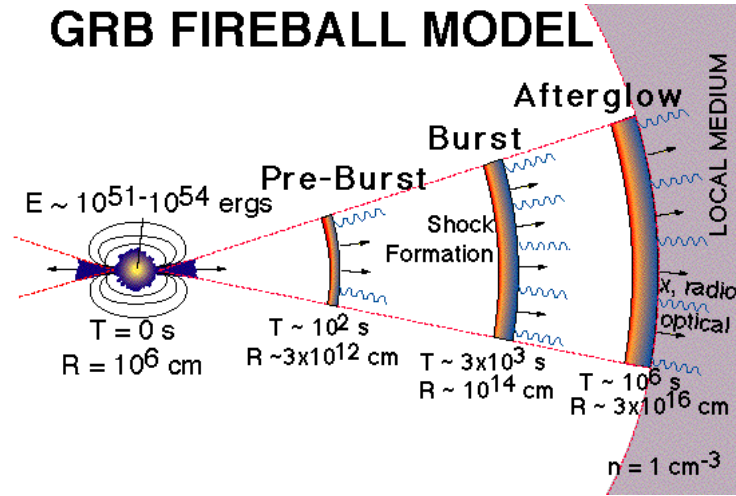


**Figure 1.13:** Schematic diagram of the fireball shock model. Jets are shown exiting from a central engine. Internal shocks form as shells of different Lorentz factors collide, while external shocks arise when shells interact with the external medium, producing the X-ray through radio afterglow. From <http://heasarc.gsfc.nasa.gov/>

dependence of the ejection velocity of the outflow) is highly variable. The flow is usually modeled by a succession of relativistic shells of different Lorentz factors, mimicking the time dependence of the properties of a wind, and the shocks take place when faster-moving shells catch up with slower ones. A collision of two shells is the elementary process that produces a single pulse in gamma-rays. Thus, in the internal shock scenario, the temporal structure (e.g. pulse durations) directly reflects the temporal behavior of the inner engine (Ramirez-Ruiz & Fenimore, 2000).

In the standard scenario, one considers an inner engine with a variability time scale  $\Delta t$  that can be down to the order of ms, and a typical distance between adjacent shells  $c\Delta t$ . If we suppose that a rear shell moves faster than a leading one, i.e.  $\Gamma_2 \gg \Gamma_1 \sim \Gamma$ , the internal shock takes place at a typical radius  $r_{IS} \simeq 2c\Delta t\Gamma^2 \simeq 6 \times 10^{13} \text{ cm} \simeq 4 \text{ AU}$ . In internal shocks the relative kinetic energy of the shells is converted into random/internal energy. The observed prompt gamma-ray burst spectrum is generally considered to be due to the synchrotron/IC emission from leptons accelerated in such shocks. The main difficulties of this model are:

- A rather low efficiency for the conversion of the kinetic energy of the flow into internal energy as only the relative energy of the shells can be randomized;

## 1. GAMMA–RAY BURSTS: AN OVERVIEW

---

- The synchrotron emission process cannot simply account for the hardness of the low–energy part of the spectrum observed in some GRBs.

The afterglow is produced when the relativistic flow interacts with the ambient medium after most shells have merged and thus decelerates. For a short–enough fireball duration, the deceleration radius corresponds approximately to the distance where the ISM mass collected by the fireball is equal to  $(1/\Gamma)$  of its rest mass and is of the order of  $\simeq 5 \times 10^{16}$  cm ( $\simeq 4 \times 10^3$  AU). Sari et al. (1998) calculated the broadband spectrum and corresponding light curve of synchrotron radiation from the electrons accelerated by the shock into a power–law distribution ( $N(\gamma_e) \propto \gamma_e^{-p}$ ). Both the spectrum and the light curve consist of several power–law segments with related indices,  $F(\nu, t) \propto \nu^{-\beta} t^{-\delta}$ ; the breaks correspond to the critical frequencies of transition between different regimes of emission (see e.g. van Paradijs et al., 2000).

The simplest model is derived under the assumptions of: 1) isotropic fireball; 2) uniform ambient density; 3) synchrotron emission of the electrons; 4) constraints on the micro–physical parameters. It predicts that the evolution of the fireball with radius  $r$  and with the observer’s time  $t$  follows the relation  $\Gamma \propto r^{-3/2} \propto t^{-3/8}$ . This scaling is valid for an adiabatic evolution of the fireball, i.e. in which the energy  $E \propto n r^3 \Gamma^2$  remains constant. This is generally valid at late epochs (later than hours) in all afterglows and at early epochs for many afterglows.

### 1.3.3 GRB Relationships

The detection of GRB afterglows and the redshift determination yielded a small sample of bursts for which the observed properties could be translated into intrinsic ones. This initiated a search for relations between the various intrinsic properties, which could have far–reaching implications both for the theoretical understanding of GRBs and for the application of GRBs as a cosmological tool.

Even before a large sample of bursts with redshifts was available, it was suggested that the intrinsic peak energy  $E_{\text{peak}}$  and isotropic energy  $E_{\text{iso}}$  are correlated (Lloyd et al., 2000). The systematic analysis of spectral and energetics properties of a dozen *Beppo-SAX* GRBs with measured redshift by Amati et al. (2002) showed that a tight correlation is present between the *intrinsic* peak energy of the  $\nu F_\nu$  spectrum (in the burst frame),  $E_p$ , and the isotropic equivalent bolometric energy (in the 1–10000 keV energy range),  $E_{\text{iso}}$  (usually expressed in units of  $10^{51}$  erg):

$$E_p = K_1 \times E_{\text{iso}}^{m_1}, \quad (1.6)$$

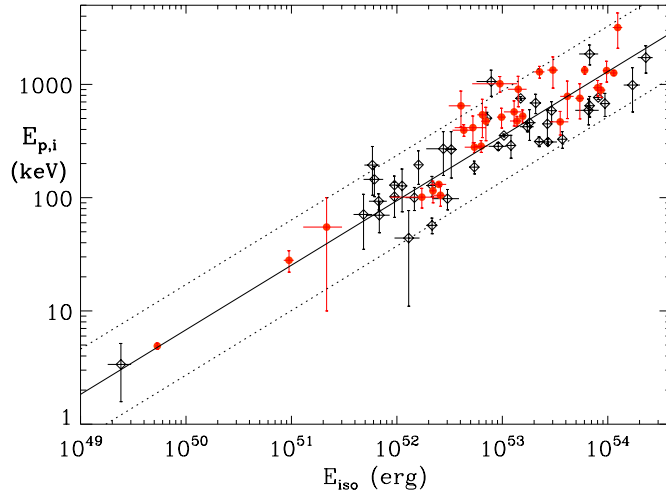


**Figure 1.14:** Location in the  $E_p$ – $E_{\text{iso}}$  plane of the 70 GRBs and XRFs with firm estimates of redshift. Red dots are *Swift* GRBs. Black dots are GRBs discovered by other satellites. The best-fitting power law is the continuous line ( $\pm 2\sigma$  region). From Amati et al. (2008)

where  $K_1$  is a constant (in keV) and  $m_1 \sim 0.5$ . This represents the so-called Amati relation. Subsequently, Ghirlanda et al. (2004) found that  $E_p$  and the actual emitted energy  $E_{\text{iso}}$  are even more tightly correlated: this is the Ghirlanda relation. In this relation the energy is determined from  $E_{\text{iso}}$  with corrections for the beaming of the gamma-ray emission:

$$E_\gamma = E_{\text{iso}} (1 - \cos \theta_j) = f_B E_{\text{iso}} , \quad (1.7)$$

where  $\theta_j$  is the jet opening angle,  $f_B$  is the beaming fraction, which is determined observationally from modeling the evolution of the afterglow, and  $E_\gamma$  is the total energy actually radiated. The Ghirlanda relation can then be expressed as follows:

$$E_p = K_2 \times E_\gamma^{m_2} . \quad (1.8)$$

Figure 1.14 shows the pre-*Fermi* Amati relation, which includes 70 long GRBs (Amati et al., 2008). The power-law fit (see equation 1.6) to the data gives an index  $m_1 = 0.57 \pm 0.01$  and a normalization  $K_1 = 94 \pm 2$  keV. A study by Friedman & Bloom (2005) lead to the values  $m_2 = 0.70 \pm 0.07$  and  $K_2 = 512 \pm 15$  keV for the Ghirlanda relation. However, both relations suffer from very large dispersions and seem to be not tight enough to serve as a standard candle for precision cosmology.

## 1. GAMMA-RAY BURSTS: AN OVERVIEW

---

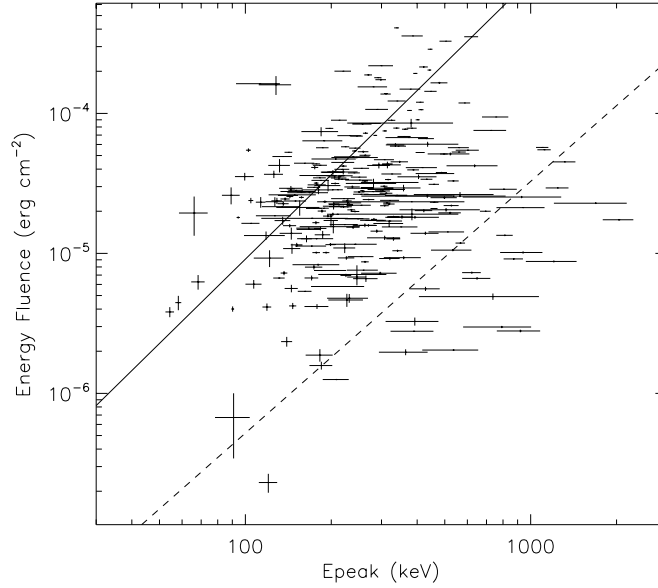


**Figure 1.15:** Energy fluence in 25–2000 keV vs.  $E_{\text{peak}}$  plot. The Amati relation limit is shown as a *solid line*, and the Ghirlanda  $3\sigma$  limit is shown as a *dashed line*. Bursts below these lines are inconsistent with the relation. The uncertainties are  $1\sigma$ . From Kaneko et al. (2006)

A discussion of the possible sources of scattering around the Amati relation is given by Amati et al. (2008).

Several authors (Nakar & Piran, 2005a; Band & Preece, 2005; Kaneko et al., 2006) point out that the Amati relation, and to a lesser extent the Ghirlanda relation, result from selection effects affecting the burst sample used to discover and calibrate this relation. The calibrating sample could fall on the high-fluence, low- $E_p$  edge of the BATSE sample. In particular, Nakar & Piran (2005a) pointed out that while larger burst databases lack the redshifts necessary to calibrate the Amati relation, these databases can test the validity of this relation because the ratio  $E_p/E_{\text{iso}}$  cannot exceed a maximum value for all redshifts. They found that a large fraction of the bursts in the databases they considered cannot satisfy the Amati relation. Building on this analysis by Nakar & Piran (2005a), Band & Preece (2005) tested these relations for consistency with a subset of 760 bursts observed by BATSE. They demonstrated that in the most rigorous test, where the bursts may be at any redshift and have any beaming fraction for which these relations are satisfied, the Amati relation could not be satisfied by 88% of the bursts, consistent with the results of Nakar & Piran (2005a), while the Ghirlanda relation would not be satisfied by only 1.6% of the bursts.

The correlation between  $E_{\text{peak}}$  and energy fluence values was tested also with the 350 bright GRBs analysed by Kaneko et al. (2006). On the scatter plot of Figure 1.15, the limit on the Amati relation and the maximum  $3\sigma$  limit derived by Ghirlanda et al. (2005) are shown as *solid* and *dashed lines*, respectively. The bursts below these lines are inconsistent with the relation. Note that the GRB sample used to test the consistency in Band & Preece (2005) includes many more dimmer bursts than bursts in the Kaneko sample. Despite the fact that this sample only consists of bright GRBs, most of the bursts are significantly inconsistent with the Amati limit. Even for the  $3\sigma$  Ghirlanda limit, there appear to be more outliers than they found in their work. The well-constrained parameters of the Kaneko catalog strongly indicate that the Amati relation is only valid for a small sample of selected bursts. This relations will be further discussed and tested with the BGO bright burst sample presented in chapter 5.

## 1.4 The Pre-*Fermi* Era

A consolidation of the progress achieved by *Beppo-SAX* was possible through a series of satellites, comprising HETE-2, INTEGRAL and *Swift*. Launched on October 9, 2000, the High-Energy Transient Explorer or HETE-2 was equipped with three instruments (Atteia et al., 1995; Kawai et al., 1999; Vanderspek et al., 1999) which were sensitive to gamma- and X-radiation, shared a common field of view of  $\sim 1.5$  steradians, spanning a detectable energy range of about 3 decades (from  $\sim 0.5$  to  $\sim 500$  keV), and were capable of immediate inter-instrument communication. Each HETE-2 instrument operated independently of the others; however, if a burst was detected by one of the instruments, the others were notified and began collecting data at higher temporal and energy resolution. New features of HETE-2 were the fast alerts to the ground which unraveled the previously unexplored early optical afterglows and permitted high-resolution spectroscopy of some very bright optical afterglows. With its broad energy range, HETE-2 was able to trigger on X-ray flashes (XRFs), which were first discovered by *Beppo-SAX* as a new subclass of GRBs (Heise et al., 2001). They represented a rare transient detectable only in hard X-rays less than 100 keV. with peak spectral energies less than 40 keV.

Another satellite which is currently providing interesting GRB observations is the International Gamma Ray Astrophysics Laboratory (INTEGRAL). This European multi-purpose gamma-ray mission launched in October 2002 is dedicated

to the fine spectroscopy and imaging of celestial gamma-ray sources in the energy range 15 keV–10 MeV. Even though INTEGRAL is not a GRB-dedicated mission, it can detect many GRBs thanks to the anticoincidence system (ACS) of its spectrometer SPI (Lichti et al., 1996; von Kienlin et al., 2003), however with no spectral or localization capability. On the contrary, the IBIS on-board imager detects about one GRB per month. Unlike HETE-2 and *Swift*, which are in Low Earth Orbit (LEO), INTEGRAL is in a highly elliptical orbit allowing an almost continuous monitoring from the ground.

### 1.4.1 The *Swift* Mission

A great step forward in the comprehension of the GRB phenomenon has been made with the successful launch of the *Swift* Gamma-ray Burst Explorer (Gehrels et al., 2004) on November 20, 2004. *Swift* is a medium-sized explorer (MIDEX) which has been developed by a NASA-led international collaboration and was designed specifically to study GRBs and their afterglows in multiple wavebands. The payload consists of three instruments:

1. The Burst Alert Telescope (BAT), which represents a new-generation wide-field gamma-ray detector in the 15–150 keV energy band with a higher sensitivity than for the corresponding predecessors BATSE and *Beppo-SAX*, and triggers autonomous spacecraft slews in less than 100 s;
2. A narrow-field X-ray Telescope (XRT) that gives 5 arcsec positions and performs detailed spectroscopy in the 0.2–10 keV band;
3. A narrow-field UV/Optical Telescope (UVOT) that operates in the 170–600 nm band, providing 0.3 arcsec positions and optical finding charts.

At the present time, *Swift* is collecting a large amount of new data, with seemingly every burst displaying its own peculiar characteristics. Indeed, with every new prompt XRT observation of a burst, new details are emerging. Prior to the launch of *Swift*, the long time needed to accurately determine the GRB position limited most afterglow measurements, which have been performed only hours after the burst. Thanks to its fast-pointing capabilities, *Swift* achieved the goal of accurately localized afterglows starting a minute or so after the burst trigger, at gamma-ray, X-ray and optical wavelengths. Moreover, a canonical X-ray afterglow light curve is emerging from the first comprehensive observations of the early afterglow phase of GRBs. The multiwavelength *Swift* light curves are bringing invaluable information to understand prompt emission–afterglow transition, GRB emission site, central engine activity, forward–reverse shock physics, and

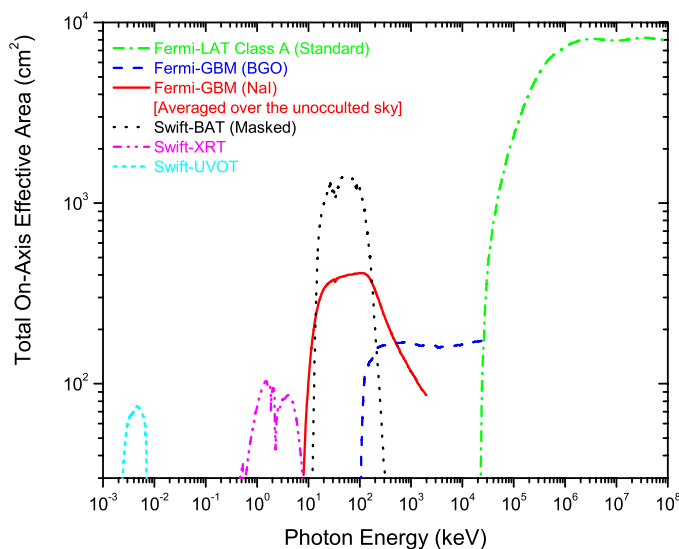


**Figure 1.16:** Effective areas for the three *Swift* instruments BAT, XRT and UVOT and for the *Fermi* instruments GBM and LAT. Exceptional bursts can be detected over 11 energy decades facilitating broad-band temporal and spectral evolution studies (see chapter 4 for such examples). From Stamatikos (2009)

immediate environment. *Swift* also achieved the long-awaited discovery of the afterglows of “short” gamma-ray bursts.

A large fraction of GRBs also displays X-ray “flares” during the first few hours superimposed on the declining light curves. Most of these flares are energetically small, but a few are very powerful (Burrows et al., 2005b) with a fluence comparable to that of the prompt phase. Late flares are also occasionally seen. The detection of delayed X-ray flares suggests an inner-engine origin, at radii inside the deceleration radius characterizing the beginning of the forward shock afterglow emission. Given the observed temporal overlapping between the flares and afterglows, Wang et al. (2006) invoke IC emission arising from such flare photons scattered by forward shock afterglow electrons and find that this IC emission produces GeV–TeV flares, which could be detected by *Fermi* and ground-based TeV telescopes. The detection of GeV–TeV flares combined with low energy observations may help to constrain the poorly known magnetic field in afterglow shocks.

As of December 2009, *Swift* has detected around 450 GRBs of which ~85% have X-ray afterglow detections by XRT and ~60% have UVOT optical and/or UV afterglow detections. *Swift* localizes ~95 GRBs per year, with an average rate of 2 bursts detected per week, over the four years of on-orbit observations

## 1. GAMMA–RAY BURSTS: AN OVERVIEW

---

(Barthelmy et al., 2009). *Swift* has also vastly increased the number of GRBs for which a redshift is known or inferred. For the first 409 bursts that triggered *Swift* (Krimm et al., 2009), 135 have a published redshift, compared with 42 redshifts before the advent of *Swift* (Jakobsson et al., 2006). Furthermore *Swift* broke through the symbolic redshift  $z = 6$  barrier, beyond which very few objects of any kind have been measured. On April 23 2009 the highest spectroscopic redshift ever was measured: the event was GRB 090423 at  $z = 8.2$  (Tanvir et al., 2009) Also in March 2008 the brightest source ever was recorded. This was GRB 080319B at  $z = 1.9$ , nicknamed the “naked eye” GRB because it had an optical magnitude  $m = 5.6$  at its maximum (Cwiok et al., 2008). In September 2008, the at-the-time second most distant object ever was detected, GRB 080913B at  $z = 6.7$  (Greiner et al., 2009a). Thanks to this rich phenomenology and the large redshift range spanned, there is no doubt that GRBs are very effectively probing, among other things, the chemical evolution of the Universe (see e. g. Savaglio, 2010), all the way from the local Universe to the epoch of first stars, more than 13 Gyr ago.

Although *Swift* has detected a very large number of GRBs, the majority of  $E_{\text{peak}}$  values lie beyond BAT’s canonical energy range. Thus, correlated *Swift*–BAT/*Fermi*–GBM GRB observations would simultaneously augment *Fermi*’s low energy response while increasing the number of  $E_{\text{peak}}$  values for BAT GRBs also observed by GBM (see Figure 1.16). Additionally, since *Swift*’s high–fidelity localization precision surpasses GBM’s by over  $\sim 2$ – $3$  orders of magnitude, joint fits help in guiding the selections for GRB follow–up campaigns. In this manner, 35% of bursts in the joint BAT–GBM analysis are expected to be accompanied by panchromatic ground–based follow–up observations resulting in spectroscopic redshift determinations and host galaxy identifications. Results from the BAT/GBM cross–calibration analysis for the first GRB jointly detected after the launch of *Fermi* (GRB 080810) are presented in chapter 4. and more details regarding the on–going BAT/GBM cross–calibration project can be found in Stamatikos (2009).

## Chapter 2

# The Fermi Observatory

The *Fermi* mission was conceived to address important open questions in high-energy astrophysics, many of which were raised but not answered by results from EGRET. In particular, regarding the GRB science, *Fermi* opens a completely new era of multiwavelength observations enabling their study over an unprecedentedly broad energy band. This ranges from the typical GRB energies, i.e. 10 keV–1 MeV Band, which are fully covered by *Fermi*'s secondary instrument, the Gamma-Ray Burst Monitor (GBM), up to 300 GeV, which represent the upper energy limit of the main instrument, the Large Area Telescope (LAT). The synergy of these two instruments with other currently operating missions and with the numerous ground-based optical/IR telescopes underlines the great interest in unveiling the mysteries which still puzzle the GRB community.

The GBM detectors fit in this overall picture by providing a higher trigger energy range (50–300 keV) than e.g. Swift-BAT (15–150 keV) and a spectral coverage up to 40 MeV, an energy limit which can only be investigated with the LAT and the Mini-Calorimeter on-board AGILE (Tavani et al., 2006). New insights into the GRB properties are therefore expected from GBM, thus advancing the study of GRB physics.

The project of *Fermi* began while its predecessor EGRET was still in flight. It has been designed to extend the detection range an order of magnitude beyond EGRET's upper limit of 30 GeV and is currently expanding the catalogue of high-energy burst detections. With its 4527 kg and a volume of  $< 3 \text{ m}^3$  (the LAT contributes 3000 kg to the total mass) *Fermi* was still small enough to be successfully launched on a Delta II 7920H-1 rocket. Launch occurred successfully on June 11, 2008, at 16:05 GMT<sup>1</sup> from the Cape Canaveral Air Force Station

---

<sup>1</sup>Greenwich Mean Time

## 2. THE FERMI OBSERVATORY

---



**Figure 2.1:** *Left Panel:* the *Fermi* spacecraft is integrated onto the Delta II second stage in the mobile service tower. The first half of the payload fairing is moved into place around the telescope. The fairing is a molded structure that fits flush with the outside surface of the Delta II upper stage booster and forms an aerodynamically smooth nose cone, protecting the spacecraft during launch and ascent. *Right Panel:* On Cape Canaveral Air Force Station's Launch Pad 17-B, flame and smoke mark the launch of the Delta II rocket. Photo credit: NASA/Kim Shiflett (<http://mediaarchive.ksc.nasa.gov/>)

Space Launch Complex 17-B (see Figure 2.1). The spacecraft resides in a LEO (96.5 min circular) at an altitude of 550 km (340 mi), and at an inclination of  $28.5^\circ$  to the Earth's equator. During the South Atlantic Anomaly (SAA) passages (approximately 17% of the time, on average) the Fermi detectors do not take scientific data. This chapter is dedicated to the description of the *Fermi* instruments, briefly presenting the LAT hardware and instrument performance, and then focusing mainly on the GBM detectors and overall performances.

### 2.1 The Large Area Telescope

LAT owes much of its design inspiration to precedent gamma-ray instruments, such as EGRET and earlier pair-conversion telescopes (such as the SAS-2 and COS-B missions from NASA and ESA, respectively). However, LAT is more

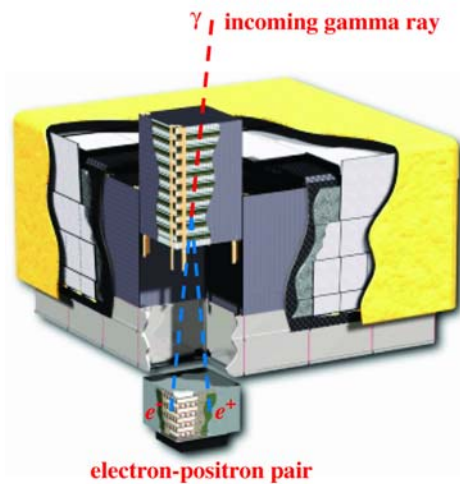


**Figure 2.2:** Schematic diagram of the Large Area Telescope. The telescope's dimensions are  $1.8 \text{ m} \times 1.8 \text{ m} \times 0.72 \text{ m}$ . The power required and the mass are 650 W and 2,789 kg, respectively. From Atwood et al. (2009)

than simply a larger version of previous space telescopes. It was specifically designed to avoid some of the limitations of EGRET, and it incorporates new technology and advanced on-board software that will allow it to achieve scientific goals greater than obtained with previous space experiments. LAT is a product of an international collaboration between NASA, DOE, and many scientific institutions across France, Italy, Japan, and Sweden.

LAT operates in the energy range between 20 MeV and 300 GeV. This detector is based on solid-state technology, obviating the need for consumables (as was the case for EGRET's spark chamber, whose detector gas needed to be periodically replenished) and greatly decreasing ( $< 10 \mu\text{s}$ ) dead time (EGRET's high dead time was due to the length of time required to re-charge the HV power supplies after event detection). These features, combined with the large effective area and excellent background rejection, allow the LAT to detect both faint sources and transient signals in the gamma-ray sky. The scientific objectives addressed by the LAT include:

1. Determining the nature of the unidentified sources and the origins of the diffuse emission revealed by EGRET;
2. Understanding the mechanisms of particle acceleration operating in celestial sources, particularly in active galactic nuclei (AGNs), pulsars, supernovae remnants, and the Sun;
3. Understanding the high-energy behavior of GRBs and transients;

## 2. THE FERMI OBSERVATORY

**Table 2.1:** Summary of Large Area Telescope Instrument parameters and estimated performance. From Atwood et al. (2009)

Parameter	Value or Range
Energy range	20 MeV–300 GeV
Effective area at normal incidence <sup>a</sup>	9,500 cm <sup>2</sup>
Energy resolution (equivalent Gaussian 1 $\sigma$ ):	
100 MeV – 1 GeV (on axis)	9%–15%
1 GeV – 10 GeV (on axis)	8%–9%
10 GeV – 300 GeV (on-axis)	8.5%–18%
>10 GeV (>60° incidence)	≤6%
Single photon angular resolution (space angle)	
on-axis, 68% containment radius:	
>10 GeV	≤0.15°
1 GeV	0.6°
100 MeV	3.5°
on-axis, 95% containment radius	< 3 × $\theta_{68\%}$
off-axis containment radius at 55°	< 1.7 × on-axis value
Field of View (FoV)	2.4 sr
Timing accuracy	< 10 $\mu$ sec
Event readout time (dead time)	26.5 $\mu$ sec
GRB location accuracy on-board <sup>b</sup>	< 10'
GRB notification time to spacecraft <sup>c</sup>	<5 sec
Point source location determination <sup>d</sup>	< 0.5'
Point source sensitivity (>100 MeV) <sup>e</sup>	$3 \times 10^{-9}$ ph cm <sup>-2</sup> s <sup>-1</sup>

<sup>a</sup> Maximum (as function of energy) effective area at normal incidence. Includes inefficiencies necessary to achieve required background rejection. Effective area peak is typically in the 1 to 10 GeV range

<sup>b</sup> For burst (<20 sec duration) with >100 photons above 1 GeV. This corresponds to a burst of  $\sim 5$  cm<sup>-2</sup> s<sup>-1</sup> peak rate in the 50–300 keV band assuming a spectrum of broken power law at 200 keV from photon index of -0.9 to -2.0. Such bursts are estimated to occur in the LAT FoV  $\sim 10$  times per year

<sup>c</sup> Time relative to detection of GRB

<sup>d</sup> High latitude source of  $10^{-7}$  cm<sup>-2</sup> s<sup>-1</sup> flux at >100 MeV with a photon spectral index of -2.0 above a flat background and assuming no spectral cut-off at high-energy; 1 $\sigma$  radius; 1-year survey

<sup>e</sup> For a steady source after 1 year sky survey, assuming a high-latitude diffuse flux of  $1.5 \times 10^{-5}$  cm<sup>-2</sup> s<sup>-1</sup> sr<sup>-1</sup> (>100 MeV) and a photon spectral index of -2.1, with no spectral cut-off

4. Using gamma-ray observations as a probe of dark matter;
5. Using high-energy gamma-rays to probe the early Universe and the cosmic evolution of high-energy sources to  $z \geq 6$ .

To make significant progress in understanding the high-energy sky, the LAT has good angular resolution for source localization and multi-wavelength studies, high sensitivity over a broad FoV to monitor variability and detect transients, good calorimetry over an extended energy band to study spectral breaks and cut-offs and good calibration and stability for absolute, long-term flux measurement. The LAT measures the tracks of the electron (e-) and positron (e+) that result when an incident gamma-ray undergoes pair-conversion (see Figure 2.2), preferentially in a thin, high-Z material foil, and measures the energy of the subsequent electromagnetic shower that develops in the telescope's calorimeter. Table 2.1

summarizes the scientific performance capabilities of the LAT. To take full advantage of the LAT’s large FoV, the primary observing mode of *Fermi* is the so–called “scanning” mode in which the normal to the front of the instrument ( $z$ -axis) on alternate orbits is pointed to  $+35^\circ$  from the direction perpendicular to the orbital plane and to  $-35^\circ$  from that direction on the subsequent orbit. In this way, after two orbits (about 3 hr), the sky exposure is almost uniform. This uniformity is increased by the 54 days precession of the orbital plane. For particularly interesting targets of opportunity, the observatory can be inertially pointed.

The LAT is a pair–conversion telescope with a precision converter–tracker and calorimeter, each consisting of a  $4 \times 4$  array of 16 modules supported by a low–mass aluminum grid structure. A segmented anticoincidence detector (ACD), covers the tracker array, and a programmable trigger and data acquisition system (DAQ) utilizes prompt signals available from the tracker, calorimeter, and anticoincidence detector subsystems to form a trigger. A brief technical description of the LAT’s main components is presented in the following sections.

### 2.1.1 Precision Converter–Tracker

The converter–tracker has 16 planes of high– $Z$  material in which gamma–rays incident on the LAT can convert to an  $e^+e^-$  pair. The converter planes are interleaved with position–sensitive detectors that record the passage of charged particles, thus

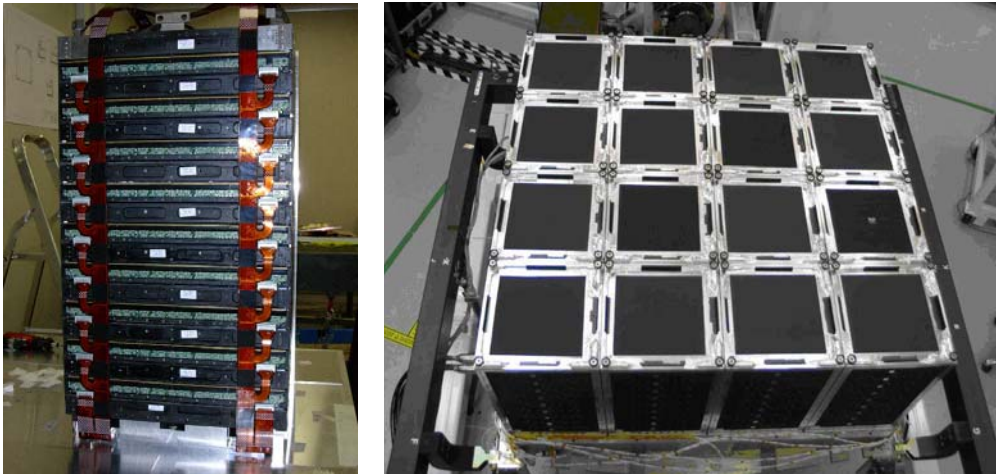


**Figure 2.3:** *Left Panel:* Completed tracker module with one sidewall removed. *Right Panel:* Completed tracker array integrated in the grid at the end of 2005 at the Stanford Linear Accelerator Center (SLAC). From Atwood et al. (2009)

## 2. THE FERMI OBSERVATORY

---

measuring the tracks of the particles resulting from pair conversion. This information is used to reconstruct the directions of the incident gamma-rays. Each tracker module has 18  $x, y$  tracking planes, consisting of 2 layers ( $x$  and  $y$ ) of single-sided silicon strip detectors. The 16 planes at the top of the tracker are interleaved with high- $Z$  converter material (tungsten). A complete tracker module is shown in the *left panel* of Figure 2.3, while the *right panel* shows the completed 16 module tracker array before integration with the ACD. See Atwood et al. (2007) for a more complete discussion of the tracker design and performance.

One of the most complex LAT design trades was the balance between the need for thin converters, to achieve a good Point Spread Function (PSF) at low energy, where the PSF is determined primarily by the  $\sim 1/E$  dependence of multiple scattering, versus the need for converter material to maximize the effective area, important at high energy. The resolution was to divide the tracker into 2 regions, “front” and “back.” The front region (first 12  $x, y$  tracking planes) has thin converters, each 0.03 radiation lengths thick, to optimize the PSF at low energy, while the converters in the back (4  $x, y$  planes after the front tracker section) are  $\sim 6$  times thicker, to maximize the effective area at the expense of less than a factor of two in angular resolution (at 1 GeV) for photons converting in that region. Instrument simulations show that the sensitivity of the LAT to point-sources is approximately balanced between the front and back tracker sections, although this depends on the source spectral characteristics (see Atwood et al. (2009) for more details).

### 2.1.2 Calorimeter

The primary purposes of the calorimeter are twofold:

1. To measure the energy deposition due to the electromagnetic particle shower that results from the  $e^+e^-$  pair produced by the incident photon;
2. To image the shower development profile, thereby providing an important background discriminator and an estimator of the shower energy leakage fluctuations.

Each calorimeter module has 96 CsI(Tl) crystals, with each crystal of size  $2.7\text{ cm} \times 2.0\text{ cm} \times 32.6\text{ cm}$ . CsI(Tl) has very good stopping power, a fast response, and a little less light output than the NaI(Tl) used in EGRET. The crystals are optically isolated from each other and are arranged horizontally in 8 layers of 12 crystals each. The total vertical depth of the calorimeter is 8.6 radiation lengths (for a total instrument depth of 10.1 radiation lengths). Each calorimeter module

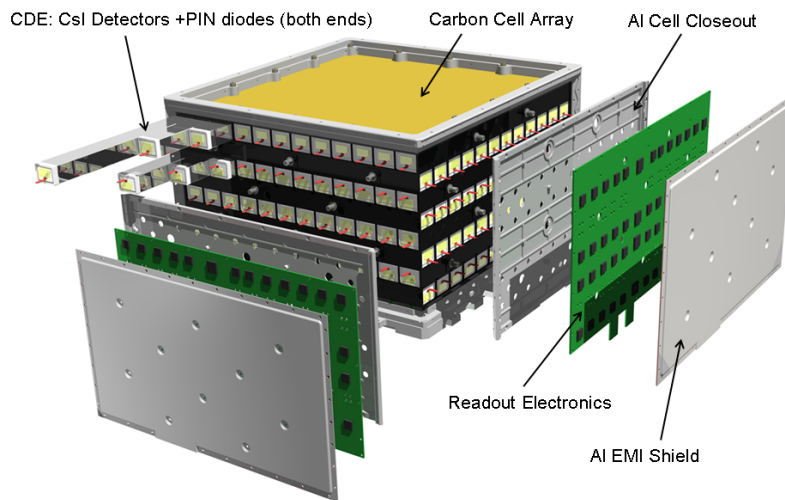


**Figure 2.4:** LAT calorimeter module. The 96 CsI(Tl) scintillator crystal detector elements are arranged in 8 layers, with the orientation of the crystals in adjacent layers rotated by  $90^\circ$ . The total calorimeter depth (at normal incidence) is 8.6 radiation lengths. From Atwood et al. (2009)

layer is aligned  $90^\circ$  with respect to its neighbors, forming an  $x, y$  (hodoscopic) array (Carson et al., 1996). Figure 2.4 shows schematically the configuration of a calorimeter module. Before sending digitized data to the DAQ, the CAL sends its trigger primitives to the trigger system. These primitives consist of two logic signals from each tower. If a predetermined low-energy ( $>100$  MeV, CAL-LO) or high-energy ( $>1$  GeV, CAL-HI) threshold is exceeded for any crystal in the calorimeter module, a trigger request is produced. These signals are also known as CAL triggers.

### 2.1.3 Anticoincidence Detector

A problem affecting EGRET was the “self-veto” effect. High-energy gamma-rays interacting in the rest of the instrument (e.g. the TASC) produced a shower of secondary particles, which splashed back up (“backsplash” effect) into the ACD, causing the event to be mistaken for a background cosmic-ray. Because the EGRET veto conditions were hard-wired into the triggering system, they could not be changed after launch. In contrast, if it is necessary to alter the LAT veto conditions, it is possible to update the on-board software. LAT’s ACD is required to provide at least 0.9997 efficiency (averaged over the ACD area) for detection of singly charged particles entering the field-of-view of the LAT.

## 2. THE FERMI OBSERVATORY

---

The solution developed for LAT was to segment the ACD into 89 separate tiles that are read out individually (Figure 2.5, *right panel*). The ACD tiles are plastic scintillator ones, arranged in a  $5 \times 5$  grid on the top, or “front” face, and then in 3 rows of 5 columns on each side face, with one long tile at the bottom. Attaching a photomultiplier tube (PMT) to each of 89 ACD tiles would have presented difficulty, so wavelength shifting fibers (WLS) were embedded every 0.5 cm in each tile and then run to PMTs located along the base of the ACD. Each tile has two PMTs for redundancy. To minimize the chance of light leaks due to penetrations of the light-tight wrapping by micrometeoroids and space debris, the ACD is completely surrounded by a low-mass micrometeoroid shield ( $0.39 \text{ g cm}^{-2}$ ). All ACD electronics and PMTs are positioned around the bottom perimeter of the ACD, and light is delivered from the tiles and WLS fibers by a combination of wavelength-shifting and clear fibers. The electronics are divided into 12 groups of 18 channels, with each group on a single circuit board. Each of the 12 circuit boards is independent of the other 11, and has a separate interface to the LAT central electronics. Further details of the ACD design, fabrication, testing, and performance are given by Moiseev et al. (2007).

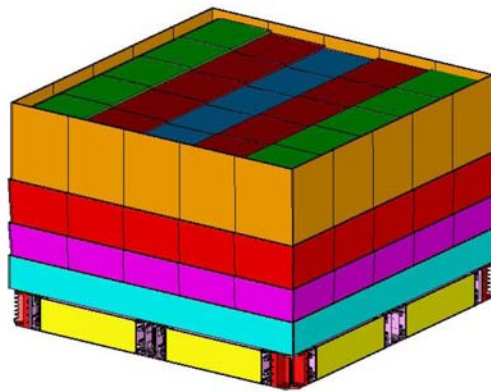


**Figure 2.5:** *Left Panel:* Schematic view of the LAT ACD (false color). The top, or front, is composed of 25 tiles in a  $5 \times 5$  grid, and each side is composed of 4 rows of 5 tiles, except for the bottom row, which is monolithic. Some of the mechanical and electrical assembly is visible at the base. From Atwood et al. (2009) *Right Panel:* ACD tile with wave shifting fibers. The tile is 1 cm thick organic plastic scintillator, with embedded waveshifting fibers to collect the light. Two sets of fibers transmit scintillation light to separate PMTs. From Thompson & Thompson (2003)

## 2.1.4 LAT and GRBs

The key points of the LAT, i.e. its wide field of view effective area and excellent PSF, short dead time and good energy resolution, make this instrument the most sensitive high-energy gamma-ray detector ever flown. The study of GRBs takes particular advantage of the improvement in angular resolution, while the reduced dead time allows the study of the substructure of the GRB pulses, typically of the order of milliseconds, with a time resolution that has never before been accessible at GeV energies.

The LAT data telemetered to ground consist of the signals from different parts of the detector; from these signals the ground software must “reconstruct” the events and filter out events that are unlikely to be gamma rays. Therefore, the Instrument Response Functions (IRFs) depend not only on the hardware but also on the reconstruction and event-selection software. For the same set of reconstructed events trade-offs in the event selection between retaining gamma rays and rejecting background result in different event classes. There are currently three standard event classes, the *transient*, *source* and *diffuse* event classes, that are appropriate for different scientific analyses (as their names suggest). Less severe cuts increase the photon signal (and hence the effective area) at the expense of an increase in the non-photon background and a degradation of the PSF and the energy resolution. The least restrictive class, the transient event class, is designed for bright, transitory sources that are not background limited. The on-ground event rate over the whole FOV above 100 MeV is about 2 counts/s for the transient class and 0.4 counts/s for the source class. There should be essentially no background during the prompt emission (with a typical duration of less than a minute) so that the transient class is the most appropriate for burst prompt emission analysis. On the other hand, the analysis of afterglows, which may linger for a few hours, will need to account for the non-burst background, at least in the low region of the energy spectrum, where the PSF is larger. The on-board flight software also performs event reconstructions for the burst trigger. Because of the available computer resources, the on-board event selection is not as discriminating as the on-ground event selection, and therefore the on-board burst trigger is not as sensitive because the astrophysical photons are diluted by a larger background flux. Similarly, larger localization uncertainties result from the larger on-board PSF.

To estimate the LAT sensitivity to GRB, a phenomenological GRB model is adopted that assumes the spectrum of the GRB is described by the Band function, and the high-energy power law extends up to LAT energies. Figure 2.6 shows

## 2. THE FERMI OBSERVATORY

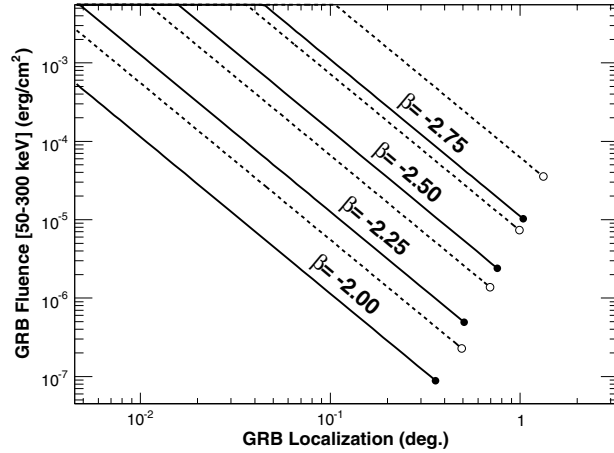


**Figure 2.6:** GRB localization with the LAT. The lines correspond to the scaling law between the location accuracy (at  $1\sigma$ ) and the intensity of the burst, expressed as fluence in the 50–300 keV band. Solid lines correspond to GRB at normal incidence, and dashed lines to  $60^\circ$  off-axis. Different sets of lines are for different high-energy spectral indices (assuming the Band function describes the GRB SED). The starting points of the lines (filled circles for on-axis, and empty for off-axis) correspond to the minimum fluence required to detect a burst (at least 10 counts in the LAT detector).  
From Atwood et al. (2009)

the minimum detectable fluence as a function of the localization accuracy, for two viewing angles and for different high-energy spectral indices keeping the peak energy and the low-energy spectral index of the Band model fixed (to 500 keV and -1, respectively). The plot shows the expected relation between the fluence and the localization accuracy, which scales as the inverse of the square root of the burst fluence.

Recently, Band et al. (2009) simulated approximately 10 years of observations in scanning mode. Figure 2.7 shows the number of expected bursts per year as a function of the number of photons per burst detected by the LAT. The GRB spectrum is extrapolated from BATSE to LAT energies. The all-sky burst rate is assumed to be  $50 \text{ GRB yr}^{-1}$  full sky (above the peak flux in 256 ms of  $10 \text{ ph s}^{-1} \text{ cm}^{-3}$  in the 50–300 keV or with an energy flux in the 20–2000 keV band greater than  $2 \times 10^{-5} \text{ erg cm}^{-2}$ ), based on BATSE catalog of bright bursts (Kaneko et al., 2006). The effect of the Extragalactic Background Light (EBL; Kneiske et al., 2004; Metcalfe et al., 2003; Stecker et al., 2006; Franceschini et al., 2008) absorption is included. The different couples of lines refer to different energy thresholds (100 MeV, 1 GeV, and 10 GeV). Dashed lines are the same computation but using only the subsample of GRBs with beta more negative than -2. For

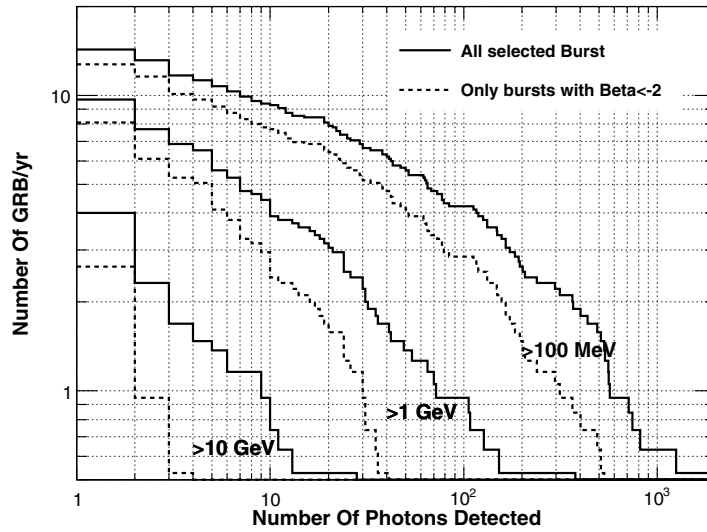


**Figure 2.7:** Model-dependent LAT GRB sensitivity. Different curves refer to different energy thresholds. *Dashed curves* are the result of the analysis excluding very hard bursts, with a beta greater than -2. From Band et al. (2009)

example one can see that 9 GRBs/yr are expected having 10 photons with energy  $> 100$  MeV (*top curve*), while only 4 GRBs are expected having 10 photons with energy  $> 1$  GeV (*middle curve*) plus a photon with energy  $> 10$  GeV. This consideration emphasizes how the EBL attenuation only the high-energy curve, as expected from the theory, leaving the sensitivities almost unchanged below 10 GeV. Assuming that the emission component observed in the 10–1000 MeV band continues unbroken into the LAT energy band, they estimated that the LAT will independently detect approximately 10 bursts per year, depending on the sensitivity of the detection algorithm; approximately one burst every three months will have more than a hundred counts in the LAT detector above 100 MeV: these are the bursts for which a detailed spectral or even time resolved spectral analysis will be possible. By restricting the analysis to the subsample of bursts with beta more negative than -2, these numbers decrease. Nevertheless, even if we adopt this conservative approach, the LAT should be able to detect independently approximately 1 burst every two months, and will be able to detect radiation up to tens of GeV. With the assumed high-energy emission model a few bursts per year will show high-energy prompt emission, with photons above 10 GeV. These rates are in agreement with the number of bursts detected in the LAT data after few months of operations (see chapter 4), but the statistics is still low for any strong constraint on the burst population.

### 2.2 The Gamma-Ray Burst Monitor

The primary role of the GBM is to augment the science return from *Fermi* in the study of GRBs by making observations at lower energies ( $\sim 8$  keV to  $\sim 40$  MeV) than the LAT. The GBM-LAT combination thus provides burst spectra over seven decades in energy. Secondary objectives are to provide near-real time burst locations on board to permit repointing of the spacecraft to obtain LAT observations of delayed emission from bursts, and to disseminate burst locations rapidly to the community of ground-based observatories. Since GBM is also able to trigger on solar flares, terrestrial gamma-ray flashes (TGFs) and soft gamma-ray repeaters (SGRs), a large amount of data are available for studies of these sources as well. When not processing a burst trigger, GBM transmits background data useful for a number of other studies, enabling a wide range of guest investigations. These data is used to monitor variable X-ray sources using the Earth-occultation technique, as was done using BATSE (Harmon et. al, 2002). Hard X-ray pulsars with periods greater than a few seconds will be monitored using Fourier transforms and epoch folding (Bildstein et al., 1997).

The GBM instrument was built and is currently operated by a collaboration involving scientists at the NASA Marshall Space Flight Center, the University of Alabama in Huntsville, the Max Planck Institute for Extraterrestrial Physics in Garching, Germany, and the Los Alamos National Laboratory. The flight hardware comprises a set of 12 Thallium-activated Sodium Iodide crystals (NaI(Tl), hereafter NaI), two Bismuth Germanate crystals ( $\text{Bi}_4\text{Ge}_3\text{O}_{13}$ , commonly abbreviated as BGO), a Data Processing Unit (DPU), and a Power Supply Box (PSB). In total, 17 scintillation detectors were built: 12 flight module (FM) NaI detectors, two FM BGO detectors, one spare NaI detector and two engineering qualification models (EQM), one for each detector type. Since detector NaI FM 06 immediately showed low-level performances, it was decided to replace it with the spare detector, which was consequently numbered FM 13.

#### 2.2.1 NaI(Tl) Detectors

The cylindrical NaI crystals (see Fig. 2.8) have a diameter of 12.7 cm (5") and a thickness of 1.27 cm (0.5"). For light tightness and for sealing the crystals against atmospheric moisture (NaI(Tl) is very hygroscopic) each crystal is packed light-tight in a hermetically sealed aluminum housing (with the exception of the glass window to which the PMT is attached, which is of the type NBK-7). In

## 2.2.1. NaI(Tl) Detectors

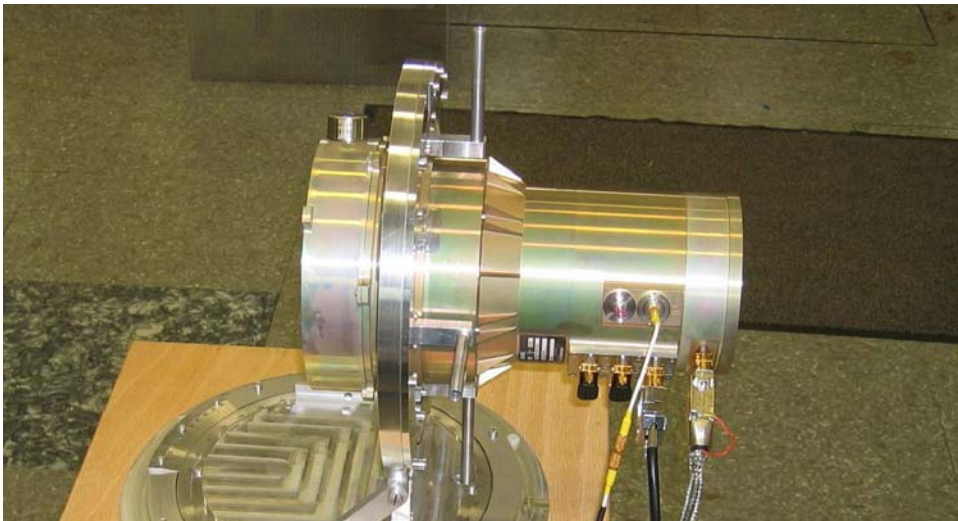
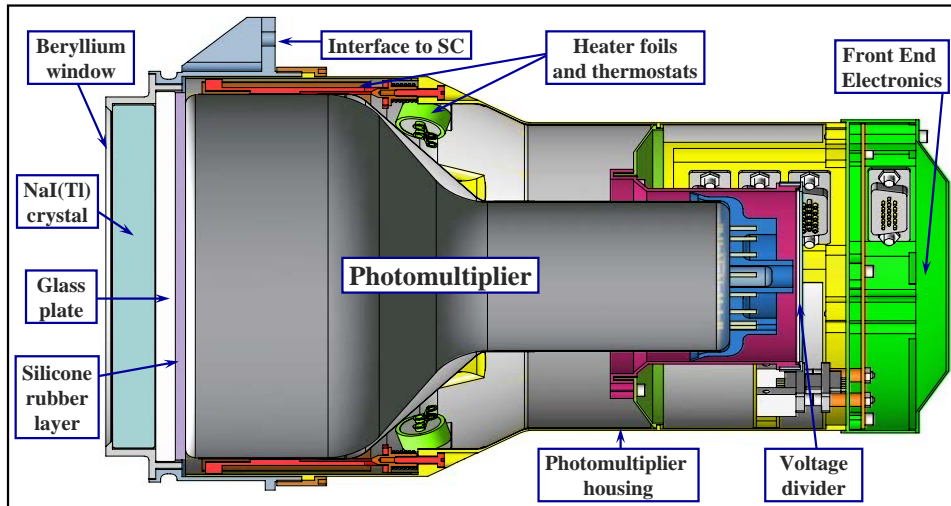


**Figure 2.8:** *Top panel:* Schematic cross-section of a GBM NaI detector showing the main components. A picture of a detector flight unit mounted on the calibration stand was taken in the laboratory during detector level calibration measurements and is shown in the *bottom panel*

## 2. THE FERMI OBSERVATORY

---

**Table 2.2:** NaI Detector Measured Orientations in Spacecraft Coordinates.  
From Meegan et al. (2009)

Detector #	Azimuth	Zenith	Detector #	Azimuth	Zenith
n0	45.9°	20.6°	n6	224.9°	20.4°
n1	45.1°	45.3°	n7	224.6°	46.2°
n2	58.4°	90.2°	n8	236.6°	90.0°
n3	314.9°	45.2°	n9	135.2°	45.6°
n4	303.2°	90.3°	na	123.7°	90.4°
n5	3.4°	89.8°	nb	183.7°	90.3°

order to allow measurements of X-rays down to 5 keV (original project goal of the GBM Proposal, 1999) the radiation entrance window is made of a 0.2 mm thick Beryllium sheet. However, due to mechanical stability reasons, an additional 0.7 mm thick Silicone layer had to be mounted between the Be window and the crystal, causing a slight increase of the low-energy detection threshold. Moreover, an 0.5 mm thick Tetracel layer (on the front-window side) and a Teflon layer (on the circumference) were used in order to increase the light output of the crystals.

The transmission probability as a function of energy for all components of the detector window's system is shown in Figure 2.9. Consequently, NaI detectors are able to detect gamma-rays in the energy range between  $\sim 8$  keV and  $\sim 1$  MeV. The individual detectors are mounted around the spacecraft and are oriented as shown schematically in Figure 2.10 (*left panel*). This arrangement results in an exposure of the whole sky unoccluded by the Earth in orbit. A table of the direction angles of the NaI crystals in spacecraft coordinates is given in Table 2.2. The zenith angle is measured from the spacecraft +Z axis, (nominally aligned with the maximum effective area of the LAT), and the azimuth is measured clockwise from the +X (sun-facing) side of the spacecraft.

### 2.2.2 BGO Detectors

With their energy range extending between  $\sim 0.2$  and  $\sim 40$  MeV, two BGO detectors provide the overlap in energy with the LAT instrument and are crucial for in-flight inter-instrument calibration. The two cylindrical BGO crystals (see Fig. 2.11) have a diameter and a length of 12.7 cm (5") and are mounted on opposite sides of the *Fermi* spacecraft (see Fig. 2.10), providing nearly a  $4\pi$  sr FoV. The BGO housings are made of CFRP (Carbon Fibre Reinforced Plastic), which provides the light tightness and improves the mechanical stability of the BGO unit.

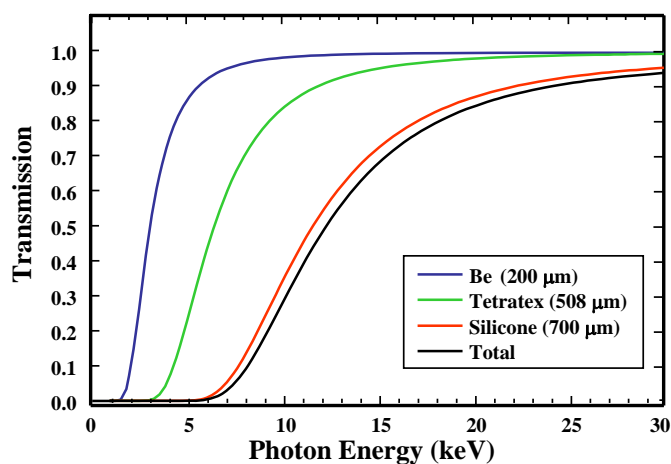


**Figure 2.9:** X-ray transmission of all individual layers of a NaI detector entrance window (the 0.2 mm thick Beryllium sheet in *blue*, the 0.5 mm thick Tetratex layer in *green*, the 0.7 mm thick Silicone layer in *red* and the sum of all components in *black*). The transmission at 10 keV is  $\sim 30\%$

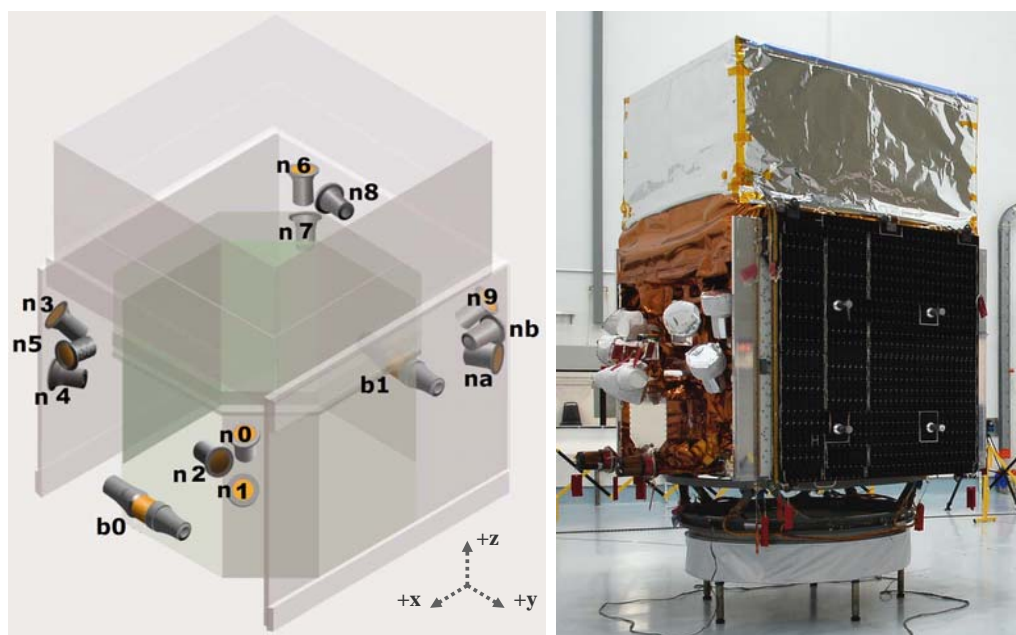


**Figure 2.10:** *Left panel:* Schematic representation of the *Fermi* spacecraft, showing the placement of the 14 GBM detectors: 12 NaI detectors (from  $n0$  to  $nb$ ) are located in groups of three on the spacecraft edges, while two BGOs ( $b0$  and  $b1$ ) are positioned on opposite sides of the spacecraft. *Right panel:* Picture of *Fermi* taken at Cape Canaveral few days before the launch. Here, six NaIs and one BGO are visible on the spacecraft's side. Photo credit: NASA/Kim Shiflett (<http://mediaarchive.ksc.nasa.gov>)

## 2. THE FERMI OBSERVATORY

**Table 2.3:** Comparison of the GBM instrument characteristics with the BATSE detectors

	<b>BATSE</b>	<b>GBM</b>
Total Mass	850 kg	115 kg
Trigger threshold	$\sim 0.2$ ph/(cm <sup>2</sup> s)	$\sim 0.61$ ph/ (cm <sup>2</sup> s)
Telemetry rate	3.55 kbps	15–25 kbps
GRB Rate	260 GRB/yr	300 GRB/yr
	<b>Large Area Detectors</b>	<b>Low–energy Detectors</b>
Material	NaI	NaI
Number	8	12
Area	2025 cm <sup>2</sup>	126 cm <sup>2</sup>
Thickness	1.27 cm	1.27 cm
Energy range	25–1800 keV	8–1000 keV
	<b>Spectroscopy Detectors</b>	<b>High–energy Detectors</b>
Material	NaI	BGO
Number	8	2
Area	126 cm <sup>2</sup>	126 cm <sup>2</sup>
Thickness	7.62 cm	12.7 cm
Energy range	30 keV to 10 MeV	120 keV to 30 MeV

For thermal reasons, the interface parts are fabricated of Titanium. On each end, the circular side windows of the crystal are polished in mirror quality and are viewed by a PMT (same type as used for the NaI detectors). Viewing the crystal by two PMTs guarantees a better light collection and a higher level of redundancy. A detailed comparison of the GBM NaI and BGO detector characteristics with the BATSE detectors is given in Table 2.3.

### 2.2.3 PMTs and FEE

The Hamamatsu R877 photomultiplier tube (PMT) is used for all the GBM detectors. This is a 10–stage 5–inch phototube made from borosilicate glass with a bialkali (CsSb) photocathode, which has been modified (R877RG–105) in order to fulfill the GBM mechanical load–requirements. The high voltage supplied to the PMTs is adjustable by command between 735 V and 1243 V in steps of 2 V. The PMT housing includes a Front–End Electronics (FEE) board that shapes the PMT pulses. The output signals of all PMTs (for both NaIs and BGOs) are first amplified via linear charge–sensitive amplifiers. The preamplifier gains and the HVs are adjusted so that they produce a  $\sim 5$  V signal for a 1 MeV gamma–ray incident on a NaI detector and for a 30 MeV gamma–ray incident on a BGO de-

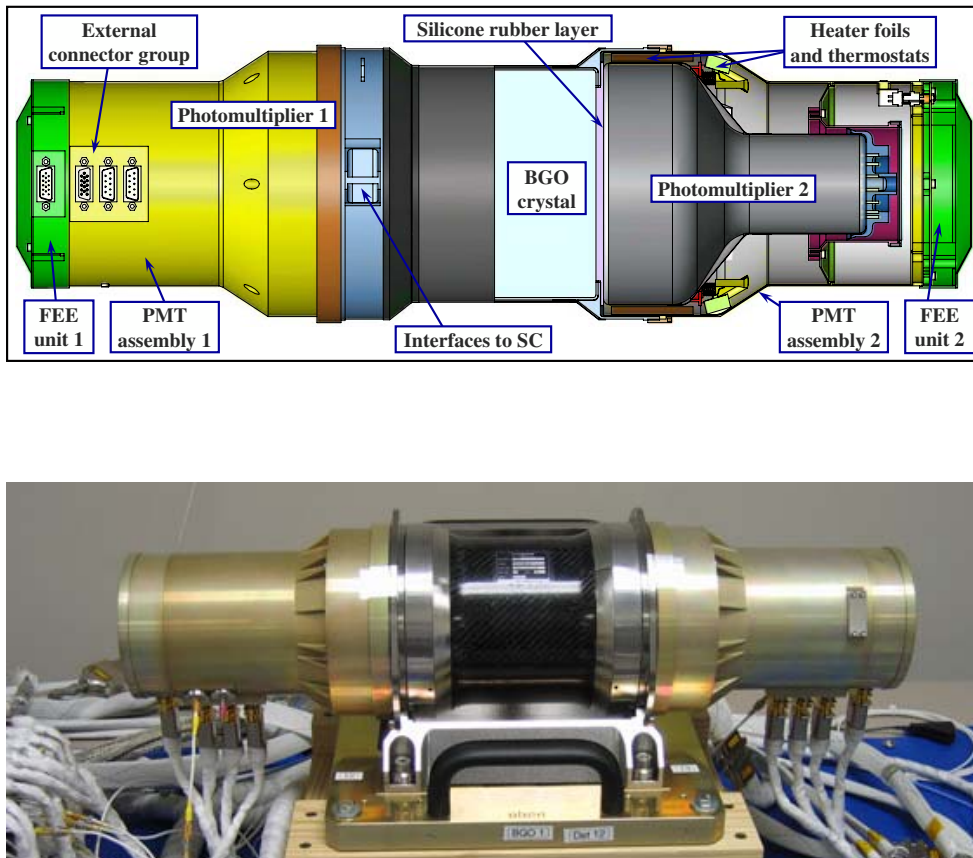


**Figure 2.11:** *Top Panel:* Schematic cross-section of a GBM BGO detector. The right hand side of the schematic is a cut away view, whereas the left hand side is an external view. The central portion contains the BGO crystal (*light blue*), which is partially covered by the outer surface of the detector's assembly. A picture of a BGO detector flight unit taken in the laboratory during system level calibration measurements is shown in the *bottom panel*

## 2. THE FERMI OBSERVATORY

---

ector. Due to a change of the BGO HV settings after launch, this value changed to 40 MeV, thus extending the original BGO energy range (GBM Proposal, 1999). Signals are then sent through pulse shaping stages to an output amplifier supplying differential signals to the input stage of the DPU, which are combined by a unity gain operational amplifier in the DPU before digitizing. In the particular case of BGO detectors, outputs from the two PMTs are divided by two and then added at the preamplifier stage in the DPU.

### 2.2.4 Data System

In the DPU, the detector pulses are continuously digitized by a separate flash ADC at a speed of  $0.1 \mu\text{s}$ . The pulse peak is measured by a separate software running in a Field Programmable Gate Array (FPGA). This scheme allows a fixed energy-independent dead-time for digitization. An adjustable dead time after peak detection allows the bipolar signal to return to ground. The net dead time per event is nominally  $2.6 \mu\text{s}$ . The signal processor digitizes the amplified PMT anode signals into 4096 linear channels. Due to telemetry limitations, these channels are mapped (pseudo-logarithmic compression) on-board into (1) 128-channel resolution spectra (Continuous High SPECTral resolution or **CSPEC** data) and (2) spectra with a poorer spectral resolution of eight channels and better temporal resolution (Continuous high TIME resolution or **CTIME** data) by using uploaded look-up tables (LUTs). The CSPEC and CTIME accumulation intervals are controlled by the flight software. The range for CSPEC is from 1.024 s to 32.768 s, in multiples of 1.024 s (default value of 4.096 s), while for CTIME the range is from

**Table 2.4:** GBM Science Data Types

<b>Name</b>	<b>Purpose</b>	<b>Temporal Resolution</b>	<b>Energy Resolution</b>
<b>CSPEC</b>	Continuous high SPECTral resolution	Nominal: 4.096 s During bursts: 1.024 s Adjustable range: 1.024–32.768 s	128 energy channels (adjustable channel boundaries)
<b>CTIME</b>	Continuous high TIME resolution	Nominal: 0.256 s During bursts: 0.064 s Adjustable range: 0.064–1.024 s	8 energy channels (adjustable channel boundaries)
<b>TTE</b>	Time-tagged events during bursts	$2 \mu\text{s}$ time tags for 300 s after trigger 500 K events before trigger. Max. rate, all detectors: 375 kHz.	128 energy channels (same as CSPEC)

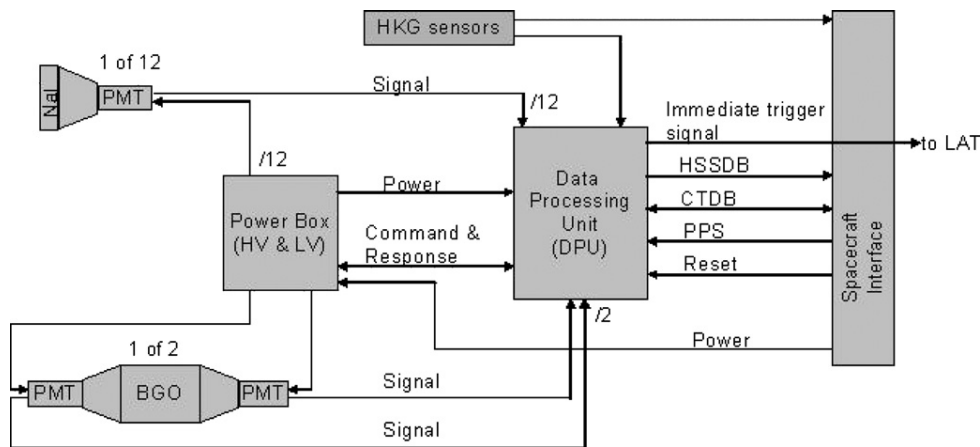


**Figure 2.12:** Functional block diagram of GBM. From Meegan et al. (2009)

64 to 1024 ms, in multiples of 64 ms, with a default value of 256 ms. The current LUTs are pseudo-logarithmic so that the spectral channel widths are commensurate with the detector resolution as a function of energy. Moreover, time-tagged event (TTE) data are continuously stored by the DPU. These data consist of individually digitized pulse height events from the GBM detectors which have the same channel boundaries as CSPEC and 2 microsecond resolution. TTE data are transmitted only when a burst trigger occurs or by command and have a nominal duration of  $\sim 300$  s, including at least 10 s of pre-trigger data. Table 2.4 summarizes the GBM science data types.

Besides processing signals from the detectors, the DPU processes commands, formats data for transmission to the spacecraft and controls high and low voltage (HV and LV) to the detectors. Changes in the detector gains can be due to several effects, such as temperature changes of the detectors and of the HV power supply, variations in the magnetic field at the PMT, and PMT aging. GBM adopts a technique previously employed on BATSE, that is an Automatic Gain Control (AGC). In this way, long timescale gain changes are compensated by the GBM flight software by adjusting the PMT HV to keep the background 511 keV line at a specified energy channel.

The absolute time is synchronized once per second using the spacecraft GPS time, which is accurate to  $\pm 1.5 \mu\text{s}$ . The timing agreement between LAT and GBM has been verified to be within  $2 \mu\text{s}$  in ground testing using muons that traverse both the LAT detector and one of the GBM BGO detectors.

Figure 2.12 shows a functional block diagram of the GBM. The High Speed Science Data Bus (HSSDB) is the primary channel for sending GBM science data

to the spacecraft for transmission to the ground. The Command and Telemetry Data Bus (CTDB) transmits commands from the spacecraft to GBM and house-keeping data from GBM to the spacecraft. The CTDB is also used to send immediate notifications of GRBs to the ground and for communications between the GBM and LAT. The pulse per second (PPS) signal provides a timing pulse to GBM every second. The immediate trigger signal provides a prompt notification to the LAT that GBM has triggered.

### 2.3 GBM Triggers

The trigger scheme for the GBM is similar to that used with BATSE. A burst trigger occurs when the flight software detects an increase in the count rates of two or more NaI detectors above an adjustable threshold specified in units of the standard deviation of the background rate. The background rate is an average rate accumulated over the previous  $T$  seconds (nominally 17), excluding the most recent 4 s. Energy ranges are confined to combinations of the eight channels of the CTIME data. Trigger timescales may be defined as any multiple of 16 ms up to 8.192 s. Except for the 16 ms timescale, all triggers include two phases offset by half of the accumulation time. A total of 120 different triggers can be specified, each with a distinct threshold. The trigger algorithms currently implemented include four energy ranges: the BATSE standard 50–300 keV range, 25–50 keV to increase sensitivity for SGRs and GRBs with soft spectra, >100 keV, and >300 keV to increase sensitivity for hard GRBs and TGFs. When a burst trigger occurs, the flight software makes several changes to the data output. TTE data are rerouted from the pre-burst ring buffer to the spacecraft. The CTIME and CSPEC integration times are decreased, nominally to 64 ms and 1.024 s, respectively. After a set time, nominally 300 s, the direct output of TTE data is terminated, and the pre-burst TTE buffer is dumped and restarted. Accelerated CTIME and CSPEC data rates continue for an additional time, nominally 600 s after the trigger.

#### 2.3.1 Trigger localization

One of the goals of GBM is to provide information to allow reorienting the *Fermi* observatory to position strong bursts near the center of the LAT field of view (FoV) for extended observations. The GBM flight software contains algorithms to determine approximate locations of trigger events and to evaluate the probability that a trigger arises from a GRB. Three types of locations are produced: automatic

### 2.3.1. Trigger localization

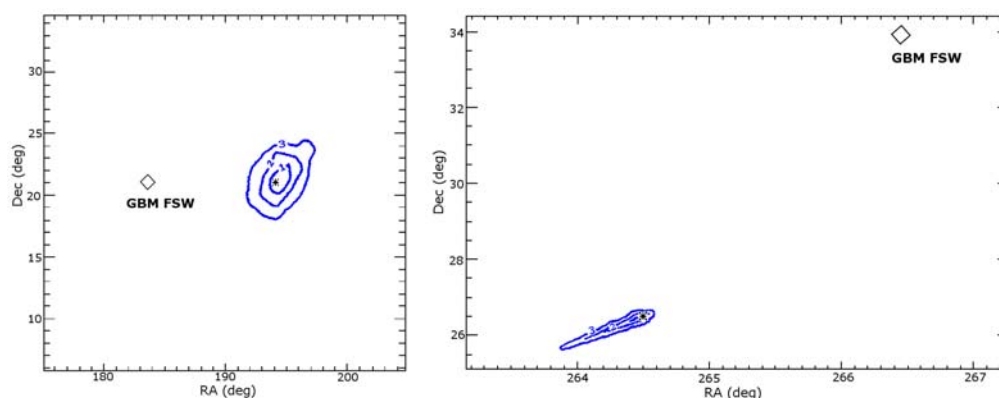


**Figure 2.13:** GBM location maps of GRB 090323 (*left panel*) and GRB 090902B (*right panel*) computed with RMFIT. The 1 to 3 sigma contours are indicated in *blue* around the best position. The location calculated on-board by the FSW is also indicated

locations by the Flight Software on board GBM, automatic locations by ground software, and human-guided locations.

When a burst trigger occurs, on-board software determines a direction to the source using the relative rates in the 12 NaI detectors. This method has the advantage that it can produce locations over a very wide field-of-view, but has the limitation that the accuracy is of degree scale. The NaI rates are compared to a table of calculated relative rates for each of the 1634 directions ( $\sim 5$  deg resolution) in spacecraft coordinates. The location with the best Chi-squared fit is converted into right ascension and declination using spacecraft attitude information and transmitted to the ground as TRIGDAT data (described below). The on-board table is calculated for rates integrated over 50–300 keV, for a specified assumed GRB spectrum. It includes nominal corrections for spacecraft scattering and atmospheric scattering, assuming the spacecraft +Z axis (the LAT axis) is zenith pointing. Normally the spacecraft +Z axis will be offset from the zenith by 35 deg, which introduces a small error in the atmospheric scattering correction. Simulations indicate that this algorithm produces location errors of less than 15 deg for strong bursts (fluence  $> 10$  photons  $\text{cm}^{-2}$ ). Location errors for weaker bursts are dominated by statistical fluctuations in the measured count rates.

Improved locations are automatically computed on the ground in near real-time by the Burst Alert Processor (BAP), and later interactively. This final step is usually performed by the GBM Burst Advocates (BAs) on duty and makes use of the TRIGDAT data. The calculation of refined positions from TRIGDAT data can be performed using the RMFIT software and two examples are shown in Figure

## 2. THE FERMI OBSERVATORY

---

2.13. The improved location is always indicated together with the 1 to 3 sigma contours.

Recently Briggs et al. (2009) presented a Bayesian model comparison method which can be used to analyze the error distributions of the GBM GRB locations. The GBM location accuracy is limited by statistical fluctuations in the number of photons detected by the detectors, both in the source interval and in the intervals used to determine the background, and by systematic errors. Systematic errors include incorrect modeling of the background or of the spectrum of the source, inaccuracies in the conversion of channels to energy, imperfect modeling of the response of the detector, either in direction or energy, and imperfect modeling of scattering of radiation into the detector from the Spacecraft and the Earth's atmosphere. Briggs et al. (2009) tested the accuracy of GBM GRB locations by comparing the GBM locations (both from the FSW and human-guided) to more accurate locations produced by other instruments (e.g. *Swift* BAT, XRT and UVOT instruments, INTEGRAL IBIS, Super-AGILE, LAT and ground-based telescopes). The result of the Bayesian analysis of the sample for the FSW locations is  $\sigma_{\text{sys}} = 3.1^\circ \pm 3.1^\circ$ , while the human-guided location analysis resulted in a  $\sigma_{\text{sys}}$  of  $3.8^\circ \pm 0.5^\circ$ . Currently the Bayesian analysis of the GBM location samples does not favor models more complicated than a single  $\sigma_{\text{sys}}$  value. This is likely due to the small size of the samples – in modeling the BATSE location error distribution it was found that ~50 reference locations are needed per error model parameter (Briggs et al., 1999b). The GBM Team is working on improving the location algorithms with the goal of improving the location accuracy.

### 2.3.2 Spacecraft Reorientations

The *Fermi* Observatory incorporates the capability to autonomously alter the observing plan to slew to and maintain pointing at a GRB for a set period of time, nominally 5 hr, subject to Earth limb constraints. This allows the LAT to observe delayed high-energy emission, as has been previously observed by instruments on the CGRO (Hurley et al., 1994). Either the GBM or the LAT can generate an Autonomous Repoint Request (ARR) to point at a GRB. A request originating from GBM is transmitted to the LAT. The LAT either revises the recommendation or forwards the request to the spacecraft. The LAT software may, for example, provide a better location to the spacecraft, or cancel the request due to operational constraints. The GBM flight software specifies different repoint criteria depending on whether or not the burst is already within the LAT FoV, defined as within

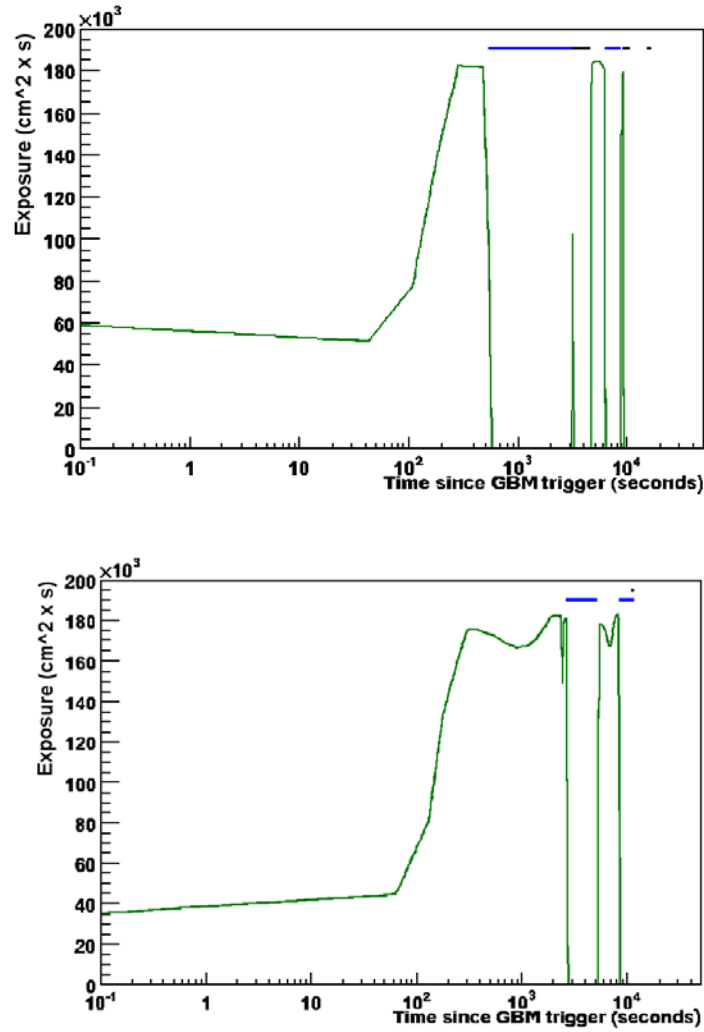


**Figure 2.14:** LAT exposure in  $\text{cm}^2 \cdot \text{s}$  as a function of time for GRB 090323 (*top panel*) and GRB 090328 (*bottom panel*). The binsize is 60 s and the Region of interest (ROI) is of  $15^\circ$ . The time-axis is in logarithmic scale in order to emphasize the low exposure during the the prompt phase. *Blue horizontal lines* indicate periods during which the GRB lies within  $98^\circ$  of Earth limb, while *black horizontal lines* indicate SAA passages (instruments are shut down). The ARR was initiated at  $T_0+46$  s and  $T_0+37$  s for GRB 090323 and GRB 090328, respectively

## 2. THE FERMI OBSERVATORY

---

60° of the +Z axis. An ARR is generated by GBM if the trigger exceeds a specified threshold for peak flux or fluence. These thresholds are reduced if the burst spectrum exceeds a specified hardness ratio.

The GBM flight software includes an algorithm to classify triggers to avoid generating ARRs for non-GRB triggers. The probability that the trigger event is a GRB, as opposed to a solar flare, SGR, particle precipitation event, or known transient source, is calculated using a Bayesian approach that considers the event localization, spectral hardness, and the spacecraft geomagnetic latitude (McIlwain L coordinate). The ARR criteria are adjusted to try to achieve a rate of about twice per month for repointing to a burst detected within the LAT FoV, and approximately twice per year for repointing to a burst not already in the LAT FoV. These criteria will be adjusted as the mission progresses so as to optimize burst observations by the LAT. Two examples of ARR for the very long GRB 090323 and GRB 090328 (see chapter 4) are given in Figure 2.14, which shows the LAT exposure as a function of time. In the first case the LAT follow-up was severely affected by constraints on the Earth avoidance (indicated by *horizontal black lines*) and SAA passages (*blue lines*), thus limiting the observations to two periods, a shorter one from  $T_0$  to  $T_0+500$  s and a longer one around  $T_0+5000$  s. The ARR of GRB 090328 was much more successful: the LAT exposure to the burst is kept at maximum over two very long ( $> 2000$  s) observation periods.

### **Communication between LAT and GBM**

GBM transmits a variety of data on burst triggers to the LAT, which provides the capability to revise event filters to optimize GRB sensitivity, refine the location, or revise a GBM repoint recommendation. Every GBM trigger generates an Immediate Trigger Signal within 5 ms. A series of up to five calculated information packets are then sent, beginning 2 s after the trigger. These packets contain the trigger time, the event localization and categorization, and the timescale and energy band in which the trigger was generated. Finally, a single repoint request message is sent specifying whether or not the event meets the criteria for repointing the spacecraft. The LAT also transmits data to the GBM whenever it produces a burst trigger. The GBM responds to such a signal by reducing the real-time telemetry rate to avoid conflicts with the LAT real-time data. Figure 2.15 summarizes all GBM actions and communication channels discussed so far in a detailed schematic overview of the GBM data flow.

### 2.3.3 TRIGDAT

When a burst trigger occurs in either the LAT or the GBM, a real-time communication channel is opened which the two instruments share. Its function is to transmit information useful for rapid ground based observations. The information so transmitted by GBM is referred to as **TRIGDAT** data. The TRIGDAT data comprise information on background rates, the burst intensity, hardness ratio, and on-board localization and classification. Burst information is updated several times during the event. The bulk of the TRIGDAT data consists of a time history of the burst for all detectors with eight-channel energy resolution and time resolution varying between 64 ms and 8 s. TRIGDAT data are also used by the BAs to produce improved source positions to be distributed via GCN (see also Figure 2.15).

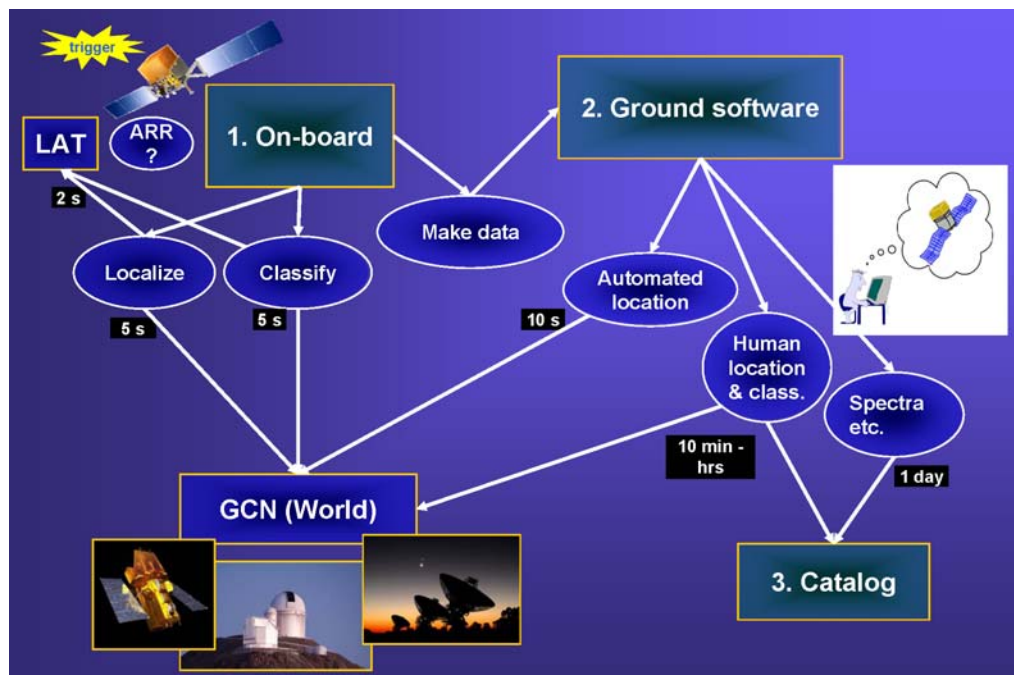


**Figure 2.15:** General scheme of GBM actions taken upon triggering. The first set of actions takes place on-board (1.) and is performed by the FSW. The trigger is first localized and classified, and the significance for spacecraft repointing (ARR) is evaluated and communicated to the LAT. An automated location is quickly transmitted together with other trigger infos to the GCN. TRIGDAT data are then produced and transmitted to the ground (2.) within the first minutes to few hours post trigger and can be analysed by the GBM BAs. Detailed spectral and temporal analysis are performed within hours to days and final results are stored in the official GBM catalog (3.)

### 2.3.4 The RMFIT Analysis Software

RMFIT is a general purpose program for displaying and analyzing FITS (Flexible Image Transport System) spectral data, such as from GRBs and Solar Flares. It can act upon any X-ray or gamma-ray data stored in suitable FITS files. The program has several capabilities:

1. Display of time histories and spectra;
2. Selection of data subsets for display;
3. Creation of a background model and background subtraction;
4. Spectral fitting via forward-folding spectral models.

The data are displayed in multiple windows and much of the data manipulation is done with a mouse. RMFIT is written in IDL and FORTRAN and the distributed version runs on the IDL *Virtual Machine*. An ad-hoc version of RMFIT for GBM and LAT analysis was developed by the GBM Team and is publicly available<sup>2</sup>. For the work presented in the next chapters, RMFIT version 3.2 was used.

RMFIT was specifically developed for burst data analysis by the BATSE team (Mallozzi et al., 2005). It incorporates a fitting algorithm MFIT that employs the forward-folding method (Briggs, 1996), and the goodness of fit is determined either by Chi-squared minimization or through CSTAT statistics, which is equivalent to the XSPEC<sup>3</sup> implementation of the Cash statistic (Cash, 1979). One advantage of MFIT is that it utilizes model variances instead of data variances, which enables more accurate fitting even for low-count data.

---

<sup>2</sup><http://fermi.gsfc.nasa.gov/ssc/data/analysis/>

<sup>3</sup>XSPEC is an X-Ray Spectral Fitting Package (Arnaud, 1996).

# Chapter 3

## GBM Performance<sup>1</sup>

The reconstruction of source locations and the determination of spectral and temporal properties from GBM data requires very detailed knowledge of the full GBM detectors' response. This is mainly derived from computer modeling and Monte Carlo simulations (Kippen, 2004; Hoover et al., 2008), which are supported and verified by experimental calibration measurements. Several calibration campaigns were carried out in the years 2005 to 2008. The calibration of each individual detector (or detector-level calibration) comprises three distinct campaigns: a main campaign with radioactive sources (from 14.4 keV to 4.4 MeV), which was performed in the laboratory of the Max-Planck-Institut für extraterrestrische Physik (MPE, Munich, Germany), and two additional campaigns focusing on the low-energy calibration of the NaI detectors (from 10 to 60 keV) and on the high-energy calibration of the BGO detectors (from 4.4 to 17.6 MeV), respectively. The first one was performed at the synchrotron radiation facility of the Berliner Elektronenspeicherring-Gesellschaft für Synchrotronstrahlung (BESSY, Berlin, Germany), with the support and collaboration of the German Physikalisch-Technische Bundesanstalt (PTB), while the second was carried out at the SLAC National Accelerator Laboratory (Stanford, CA, USA).

Subsequent calibration campaigns of the GBM instrument were performed at system-level, that comprises all flight detectors, the flight Data Processing Unit (DPU) and the Power Supply Box (PSB). These were carried out in the laboratories of the National Space Science and Technology Center (NSSTC) and of the Marshall Space Flight Center (MSFC) at Huntsville (AL, USA) and include mea-

---

<sup>1</sup>The main contents of this chapter are published in Bissaldi et al. (2009a), “*Ground-based calibration and characterization of the Fermi gamma-ray burst monitor detectors*”; *Experimental Astronomy*, 24, 47

### 3. GBM PERFORMANCE

---

surements for the determination of the channel-to-energy relation of the flight DPU and checking of the detectors' performance before and after environmental tests. After the integration of GBM onto the spacecraft, a radioactive source survey was performed in order to verify the spacecraft backscattering in the modeling of the instrument response. These later measurements are summarized in internal NASA reports and will be briefly discussed in the next Chapter.

This chapter focuses on the detector-level calibration campaigns of the GBM instrument, and in particular on the analysis methods and results, which crucially support the development of a consistent GBM instrument response. A comprehensive summary can be also found in Bissaldi et al. (2009a).

## 3.1 Calibration Campaigns

To enable the location of a GRB and to derive its spectrum, a detailed knowledge of the GBM detector response is necessary. The information regarding the detected energy of an infalling gamma-ray photon, which is dependent on the direction from where it entered the detector, is stored into a detector-response matrix (DRM). This must be generated for each detector using computer simulations. The actual detector response at discrete incidence angles and energies has to be measured to verify the validity of the simulated responses. The complete DRM set of the whole instrument system (including LAT and the spacecraft structure) is finally created by simulation of a dense grid of energies and infalling photon directions using the verified simulation tool (Kippen et al., 2007).

The following subsections are dedicated to the descriptions of the three calibration campaigns at detector level. The most complete calibration of all flight and engineering qualification models was performed at the MPE laboratory using a set of calibrated radioactive sources whose type and properties are listed in Table 3.1. Due to the lack of radioactive sources producing lines below 60 keV and in order to study spatial homogeneity properties of NaI detectors, a dedicated calibration campaign was performed at PTB/BESSY. Here, four NaI detectors (FM01, FM02, FM03 and FM04)<sup>2</sup> were exposed to a monochromatic X-ray beam with energy ranging from 10 to 60 keV, and the whole detector's surface was additionally raster-scanned at different energies with a pencil beam perpendicular to the detector's surface. In order to extend the BGO calibration range,

---

<sup>2</sup>Detectors were delivered to MPE for detector level calibration in batches of four, and shortly thereafter shipped to the US for system level calibration. Therefore, as the PTB/BESSY facility was only available for a short time, only one batch of NaIs could be calibrated there.

### 3.1. Calibration Campaigns

**Table 3.1:** Properties of radioactive nuclides used for NaI and BGO calibration campaigns: (1) Half-lives in years (y) or days (d); (2) Decay type producing the gamma-ray ( $\gamma$ ) or X-ray (e.g. K and L) radiation. For nuclides which are part of decay chains, the daughter nuclides producing the corresponding radiation are also given; (3) Line energies in keV; (4) Photon-emission probabilities for the corresponding decays. Values from Schötzig & Schrader (1998)

Nuclide	(1) Half-life	(2) Line origin	(3) Line Energies (keV)	(4) Transition Probability
<sup>22</sup> Na	950.5(4) d	Annih.	511	1.798
		$\gamma$	1274.54	0.9994
<sup>40</sup> K	1.277(8)E9 y	$\gamma$	1460.83	0.1067
<sup>54</sup> Mn	312.15(8) d	$\gamma$	834.84	0.999750(12)
<sup>57</sup> Co	271.83(8) d	$\gamma$	14.41	0.0916(15)
		$\gamma$	122.06	0.8560(17)
		$\gamma$	136.47	0.1068(8)
<sup>60</sup> Co	5.2712(11) y	$\gamma$	1173.23	0.9985(3)
		$\gamma$	1332.49	0.999826(6)
<sup>88</sup> Y	106.630(25) d	$\gamma$	898.04	0.940(3)
		$\gamma$	1836.06	0.9933(3)
<sup>109</sup> Cd	462.1(14) d	Ag-SumK $\alpha$	22.1	0.836(6)
		Ag-SumK $\beta$	25	0.1777(19)
		$\gamma$	88.03	0.03626(20)
<sup>137</sup> Cs	30.13(24) y	Ba-SumK $\alpha$	32.06	0.0553(10)
		Ba-SumK $\beta$	36.6	0.01321(27)
		Ba-137m	661.66	0.8500(20)
<sup>203</sup> Hg	46.604(17) d	$\gamma$	279.2	0.8146(13)
<sup>232</sup> Th	1.405(6)E10 y	<sup>208</sup> Tl ( $\gamma$ )	2614.53	0.3564
<sup>241</sup> Am	432.2(7) y	$\gamma$	59.4	0.359(4)
<sup>241</sup> Am/ <sup>9</sup> Be	432.2 (7) y	$\gamma$	4430	0.00004

### 3. GBM PERFORMANCE

another dedicated calibration campaign was carried out at the SLAC laboratory. Here, the BGO EQM detector<sup>3</sup> was exposed to three gamma-ray lines (up to 17.6 MeV) produced by the interaction of a proton beam of  $\sim 340$  keV, generated with a small Van de Graaff accelerator, with a LiF-target. A checklist showing which detectors were employed at each detector-level calibration campaign is given in Table 3.2 (columns 4 to 6). Note that the detector numbering scheme used for the pre-flight calibration and adopted throughout this work is different to the one used for in-flight analysis, as indicated in columns 2 and 3.

#### 3.1.1 MPE Laboratory Setup and Instrumentation

The measurements performed at MPE resulted in an energy calibration with various radioactive sources and, in addition, a calibration of the angular response of the detectors at different incidence angles of the radiation. The detectors and the radioactive sources were fixed on special holders which were placed on wooden

<sup>3</sup>The BGO flight modules were not available for calibration at the time of measurements, since they had already been shipped for system integration.

**Table 3.2:** List of all calibrated GBM detectors. Columns 2 and 3 indicate the detector numbering schemes adopted during calibration analysis and in-flight, respectively. A checklist showing which detectors were employed at each detector-level calibration campaign is given in columns 4 to 6

		Detector #		Calibration campaign		
		This work	In-flight	MPE (14.4–4430 keV)	PTB/BESSY (10–60 keV)	SLAC (4.4–17.6 MeV)
<b>NaI</b>	EQM	–	–	✓	–	–
	FM01	n0	n0	✓	✓	–
	FM02	n1	n1	✓	✓	–
	FM03	n2	n2	✓	✓	–
	FM04	n3	n3	✓	✓	–
	FM05	n4	n4	✓	–	–
	FM07	n6	n6	✓	–	–
	FM08	n7	n7	✓	–	–
	FM09	n8	n8	✓	–	–
	FM10	n9	n9	✓	–	–
	FM11	na	na	✓	–	–
	FM12	nb	nb	✓	–	–
	FM13	n5	n5	✓	–	–
<b>BGO</b>	EQM	–	–	✓	–	✓
	FM01	b0	b0	✓	–	–
	FM02	b1	b1	✓	–	–

### 3.1.1. MPE Laboratory Setup and Instrumentation



**Figure 3.1:** Detector holders with NaI (*left panel*) and BGO detectors (*right panel*) are positioned in front of the radioactive source (on top of the red holder) on their wooden stands during the calibration at the MPE laboratory

stands above the laboratory floor to reduce scattering from objects close to them (see Fig. 3.1). The radioactive sources were placed almost always at the same distance ( $d$ ) from the detector. The position of the detector's wooden stand with respect to the laboratory was never changed during measurements. Due to the unavailability of the flight DPU and PSB, commercial HV and LV power supplies were used and the data were read out by a Breadboard DPU.

The determination of the angular response of the detectors was achieved in the following way: The center of the NaI detector calibration coordinate system was chosen at the center of the external surface of the Be-window of the detector unit, with the X axis pointing toward the radioactive source, the Y axis pointing toward left, and Z axis pointing up (see Figure 3.4, *left panel*). The detectors were mounted on a specially developed holder in such a way that the front of the Be-window was parallel to the Y/Z plane (if the detector is pointed to the source; i.e.  $0^\circ$  position) and so that detectors could be rotated around two axes in order to achieve all incidence angles of the radiation. The detector rotation axes were the Z-axis (Azimuth) and around the X-axis (roll). For BGO detectors, the mounting was such that the very center of the detector (center of crystal) was coincident with the origin of the coordinate system and the  $0^\circ$  position was defined as the long detector axis coincident with the Y-axis. The BGO detectors were only rotated around the Z-axis, and no roll angles were measured in this case.

### 3. GBM PERFORMANCE

---

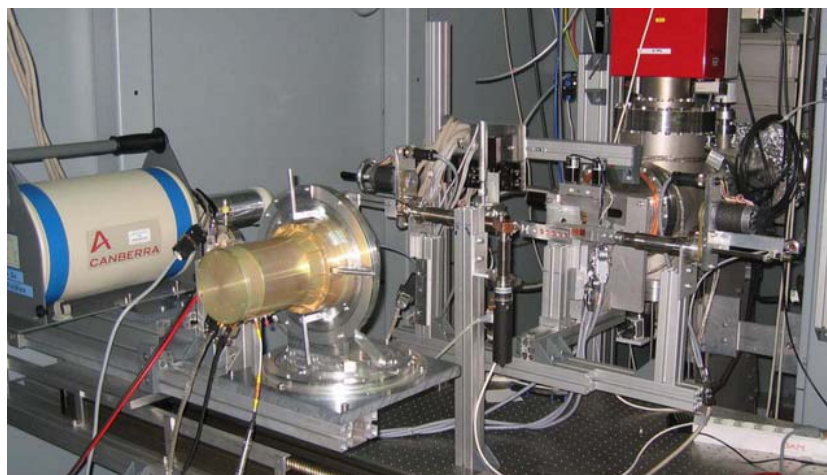


**Figure 3.2:** NaI FM04 detector photographed inside the measurement cave of the BAMline during the low-energy calibration campaign at the electron storage ring BESSY II in Berlin. The HPGe detector is located left of the GBM detector. Both are mounted on the XZ table which was moved by step motors during the scans. The beam exit window of the BAMline is located below the red box visible at the top right corner. The Cu and Al filters holders are placed horizontally between the window and the detectors

#### 3.1.2 NaI Low-Energy Calibration at PTB/BESSY

The calibration of the NaI detectors in the low photon energy range down to 10 keV was performed with monochromatic synchrotron radiation with the support of the PTB. A pencil beam of about  $0.2 \times 0.2 \text{ mm}^2$  was extracted from a wavelength-shifter beamline, the “BAMline” (Rieseemeier et al., 2005), at the electron storage ring BESSY II, which is equipped with a double-multilayer monochromator (DMM) and a double-crystal monochromator (DCM) (DCM; see Görner et al., 2001). In the photon energy range from 10 keV to 30 keV DCM and DMM were operated in series to combine the high resolving power of the DCM with the high spectral purity of the DMM. Above 30 keV, a high spectral purity with higher order contributions below  $10^{-4}$  was already achieved by the DCM alone. The tunability of the photon energy was also used to investigate the detectors in the vicinity of the Iodine K-edge at 33.17 keV.

The absolute number of photons in the pencil beam was independently determined by two different methods: firstly by taking at each photon energy a spectrum with a high-purity germanium detector (HPGe) for which a quantum detection efficiency (QDE) of unity had been determined earlier, and secondly by using silicon photodiodes which in turn had been calibrated against PTB primary detector standards such as a cryogenic radiometer and a free-air ionization cham-

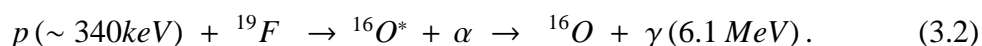
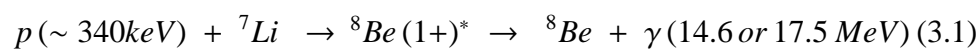
ber (Krumrey et al., 2006). As these photodiodes are operated in the photovoltaic mode, the photon fluxes had to be about four orders of magnitude higher than for the counting detectors. Different pairs of Cu and Al filters were designed for different photon energy ranges so that the transmittance of one filter was in the order of 1 % which can easily be measured. Two identical filters were used in series to achieve the required reduction in flux by four orders of magnitude. A picture of the calibration setup is shown in Figure 3.2.

The effective area of the detectors as a function of the photon energy was determined by scanning the detectors at discrete locations in x– and y–direction over the active area while the pencil beam was fixed in space. During the scan, the intensity was monitored with a photodiode operated in transmission. The effective area is just the product of the average QDE and the active area. In addition, the spatial homogeneity of the QDE was determined by these measurements (see §3.3.3).

The measurements presented in this work were recorded at 18 different energies, namely from 10 to 20 keV in 2 keV steps, from 30 to 37 keV in 1 keV steps and at 32.8, 40, 50 and 60 keV. These accurate measurements allowed to exactly determine the low–energy behavior of the channel–to–energy relation of the NaI detectors (see §3.3.1) and to fine tune the energy range around the Iodine K–edge at 33.17 keV (see §3.3.1). Moreover, three rasterscans of the detector’s surface were performed at 10, 36 and 60 keV in order to study the detectors’ spatial homogeneity (see §3.3.4 for more details).

### 3.1.3 BGO High–Energy Calibration at SLAC

In order to better constrain the channel–to–energy relation and the energy resolution at energies higher than 4.4 MeV, an additional high–energy calibration of the BGO EQM detector was performed at SLAC with a small electrostatic Van de Graaff accelerator (von Kienlin et al., 2007). This produces a proton beam up to ~350 keV and was already used to verify the LAT photon effective area at the low end of the Fermi energy range (20 MeV). When the proton beam produced by the Van de Graaff accelerator strikes a LiF target, which terminates the end of the vacuum pipe (see Figure 3.3, *left panel*), gammas with energies of 6.1 MeV, 14.6 MeV, and 17.5 MeV are produced via the reactions



### 3. GBM PERFORMANCE

---

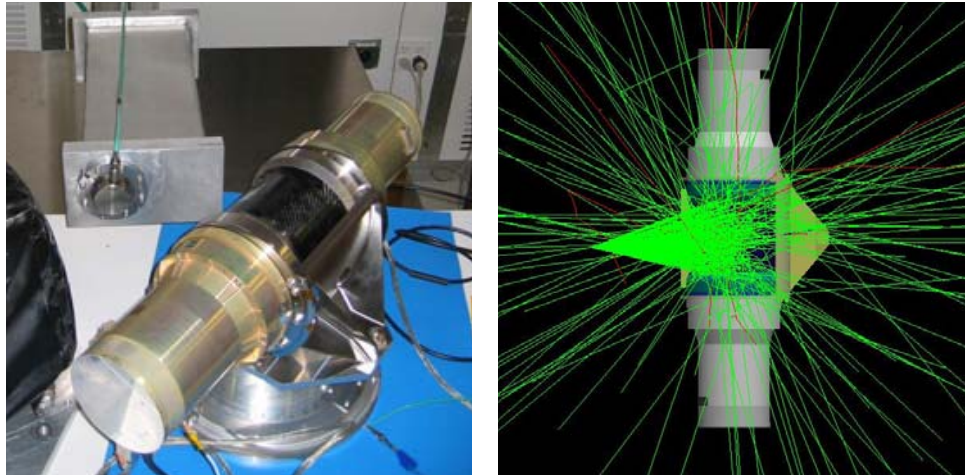


**Figure 3.3:** BGO EQM detector photographed in the SLAC laboratory during the high-energy calibration campaign (*left panel*). The grey box on the left is the end of the proton beam, inside which the LiF target was placed in order to react and produce the desired gamma lines (see Equation 3.1 and 3.2). The *right panel* shows a simulation of the gamma-ray interaction with the detector. Only gamma-rays whose first interaction is within the detector crystal are shown for clarity

The highly excited 17.5 MeV state of  ${}^8\text{Be}$  is created by protons in a resonance capture process at 340 keV on  ${}^7\text{Li}$  (see Equation 3.1). At lower energies, photons are still produced from the Breit-Wigner tail ( $\Gamma = 12$  keV) of the  ${}^8\text{Be}^*$  resonance. The narrow gamma-ray line at 17.5 MeV is produced by the transition to the  ${}^8\text{Be}$  ground state, in which the quantum energy is determined by  $h\nu = Q + 7/8 E_p$ , where  $Q = 17.2$  MeV is the energy available from the mass change and  $E_p = 340$  keV is the proton beam energy. The gamma-ray line observed at 14.6 MeV, which corresponds to transitions to the first excited state of  ${}^8\text{Be}$ , is broadened with respect to the experimental resolution, because of the short lifetime of the state against decay into two alpha-particles. Finally, Equation 3.2 shows that 6.1 MeV gamma-rays are generated when the narrow ( $\Gamma = 3.2$  keV)  ${}^{16}\text{O}$  resonance at 340 keV is hit.

For performing the measurements, the EQM detector was placed as close as possible to the LiF-target at an angle of  $\sim 45^\circ$  with respect to the proton-beam line, in order to guarantee a maximized flux of the generated gamma-rays. Unfortunately, measurements for the determination of the detector's effective area could not be obtained, since the gamma-ray flux was not closely monitored.

### 3.1.4. Simulation of the Laboratory and the Calibration Setup

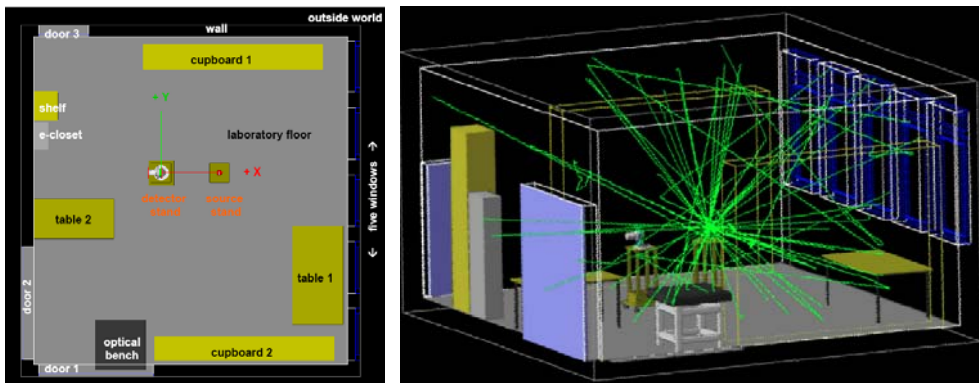


**Figure 3.4:** *Left Panel:* Simulation of the laboratory environment. A top view of the laboratory shows the components of the simulation model of all objects which were present during the calibration campaign. Also shown is the coordinate system adopted (X and Y axis of the right-handed system; +Z axis pointing upward). *Right Panel:* Example of the simulated scattering of the radiation in the laboratory. For clarity, only the first 100 interactions are shown. From Steinle et al. (2007)

### 3.1.4 Simulation of the Laboratory and the Calibration Setup

In order to simulate the recorded spectra of the calibration campaign at MPE to gain confidence in the simulation software used, a very detailed model of the environment in which the calibration took place had to be created. Detailed modeling and simulations of the laboratory were performed by Steinle et al. (2007). This modeling was necessary as all scattered radiation from the surrounding material near and far had to be included to realistically simulate all the radiation reaching the detector<sup>4</sup>. Background measurements with no radioactive sources present were taken to subtract the ever-present natural background radiation in the laboratory. However, the source-induced “background” radiation created by scattered radiation of the non-collimated radioactive sources had to be included in the simulation to enable a detailed comparison with the measured spectra.

The detailed modeling of the calibration setup of the MPE laboratory was performed using the GEANT4-based GRESS<sup>5</sup> simulation software provided by the collaboration team based at the Los Alamos National Laboratory (LANL, USA),

<sup>4</sup>An important argument driving the decision not to use a collimator for measurements with radioactive sources was the fact that the simulation of the laboratory environment with all its scattering represented a necessary and critical test for the simulation software, which later had to include the spacecraft (Wallace et al., 2007).

<sup>5</sup>GEANT4 is a suite of high-energy interaction simulation tools created at CERN (Agostinelli et al., 2003). GRESS is the General Response Simulation System which is developed at LANL. It is based on a modified (extended) version of GEANT4 (Kippen, 2004).

### 3. GBM PERFORMANCE

---

**Table 3.3:** Contribution of simulated laboratory components to the detected photons

Component	NaI			BGO
	22 keV	122 keV	1.275 MeV	4.43 MeV
direct incidence	94.0 %	91.0 %	75.0 %	70.0 %
scattered rad. total	6.0 %	9.0 %	25.0 %	30.0 %
walls	< 0.1 %	0.6 %	12.0 %	13.0 %
source holder	4.6 %	7.5 %	3.0 %	2.0 %
source stand	0.1 %	< 0.1 %	< 0.1 %	< 0.1 %
detector stand	< 0.1 %	< 0.1 %	2.0 %	< 0.1 %
floor	< 0.1 %	0.8 %	8.0 %	15.0 %
other furniture	< 0.1 %	< 0.1 %	< 0.1 %	< 0.1 %
air	1.3 %	< 0.1 %	< 0.1 %	< 0.1 %

who also provided the software model of the detectors (Hoover et al., 2008). The modeling of the whole laboratory included laboratory walls (concrete), windows (aluminum, glass), doors (steel), tables (wood, aluminum), cupboards (wood), a shelf (wood), the electricity distributor closet (steel) the optical bench (aluminum, granite) and the floor (PVC). Moreover, detector and source stands (wood), source holder (PVC, acrylic) and detector holder (aluminum) were modeled in great detail (see Figure 3.4, *left panel*). A summary of the comparison of the measurements and the simulation, with respect to the influence of the various components of the calibration environment is given in Table 3.3 and a sample plot of the scattered radiation is given in Figure 3.4, *right panel*.

Additional simulations of the other calibration campaigns, in particular for the PTB/ BESSY one, are planned. In the case of SLAC measurements, the simulation tools were only used to determine the ratios between full–energy peaks and escape peaks (see Figure 3.3, *right panel*): no further simulation of the calibration setup is foreseen.

## 3.2 Calibration Data Analysis

### 3.2.1 Database and software

The complete calibration database collected at the MPE and SLAC laboratories comprises around 1450 ASCII files, while the PTB/BESSY dataset is about 2350 Hierarchical Data Format (HDF) files. Each dataset was processed with a dedicated software, primarily written by myself for this analysis purpose, based on the IDL programming language (Versions 6.3 and 6.4). A completely new IDL routine library was obtained in the end, which is available at MPE for similar calibration tasks. The detailed analysis procedure is described step by step in the following subsections.

### 3.2.2 Processing of Calibration Runs

#### Background subtraction

During each calibration campaign, all spectra measured by the GBM detectors were recorded together with the information necessary for the analysis, i.e.

- The total number of detected counts;
- The duration of the measurement in milliseconds (ms);
- The type of the recorded counts (“data-type” or “background-type”);
- The number of recording channels ( $n=4096$  for every set of measurements).

Shortly before or after the collection of data runs, additional background measurements were recorded for longer periods. Every run was then normalized to an exposure time of 1 hour, and the background was subsequently subtracted from the data. Data, background (bkg) and background subtracted data (bkgsb) for each channel are reported as count rates (‘counts/hour’). In the case of measurements performed at PTB/BESSY, natural background contribution could be neglected due to the very high beam intensities and to the short measurement times. In some cases, especially at higher energies, where measured spectra can look particularly noisy, data had to be rebinned for a better analysis result.

Figures 3.5 to 3.8 show a series of sample spectra collected with detectors NaI FM04, BGO FM02 and BGO EQM. These particular detectors were chosen arbitrarily to present the whole analysis, since it was checked that all other detectors behave in an identical way (see §3.3.2 and §3.3.3). In Figure 3.5, four calibration runs recorded at PTB/BESSY at different photon energies (10, 33, 34 and 60 keV) highlight the appearance of an important feature of the NaI spectra.

### 3. GBM PERFORMANCE

Below the characteristic Iodine (I) K-shell binding energy of 33.17 keV (or “K-edge” energy), spectra display only the full-energy peak, which moves toward higher channel numbers with increasing photon energy (see *panels a* and *b*). For energies higher than the K-edge energy, a second peak appears to the left of the full-energy peak (see *panels c* and *d*), which is caused by the escape of characteristic X-rays resulting from K-shell transitions (*fluorescence* of Iodine). The energy of this fluorescence escape peak equals the one of the full-energy peak minus the X-ray line energy (Thompson & Vaughan, 2001). The contributions of the different Iodine  $K\alpha$  and  $K\beta$  fluorescence lines can not be resolved by the detector.

NaI spectra from radioactive sources recorded at MPE are shown in Figure 3.6. A detailed description of the full-energy peaks characterizing every source is given in §3.2.2. Beside full-energy and Iodine escape peaks, spectra from high-energy radioactive lines show more features (i.e. see the  $^{137}\text{Cs}$  spectrum in Figure

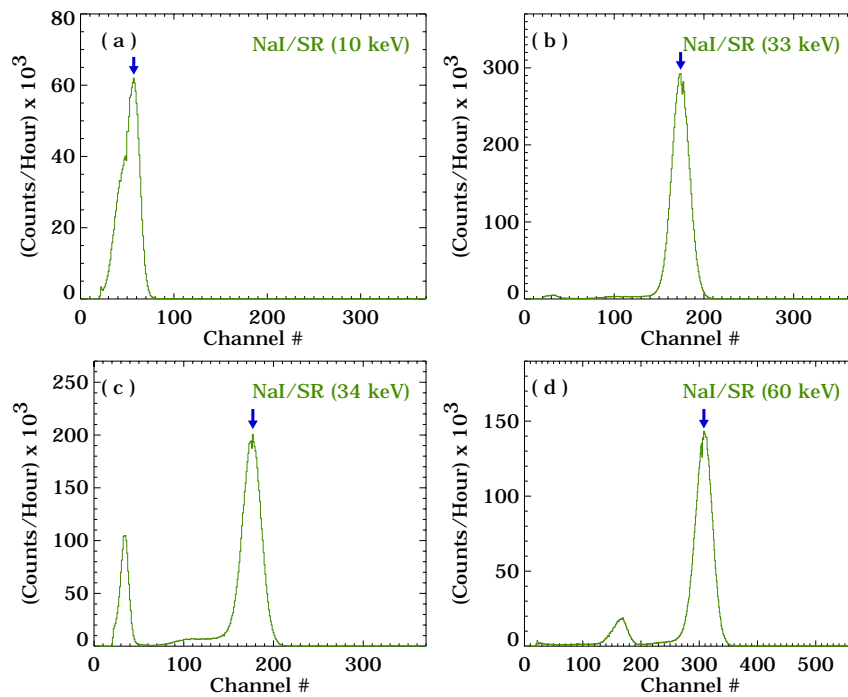


**Figure 3.5:** Spectra measured with monochromatic synchrotron radiation (SR) at PTB/ BESSY with detector NaI FM04. *Blue arrows* indicate the full-energy peak position. Results for four different photon energies are shown: (a) 10 keV, (b) 33 keV, (c) 34 keV, and (d) 60 keV. The two top panels (*a* and *b*) display spectra collected below the Iodine K-edge energy (i.e. < 33.17 keV). Above this energy (*panels c* and *d*), the characteristic Iodine escape peak is clearly visible to the left of the full-energy peak

### 3.2.2. Processing of Calibration Runs

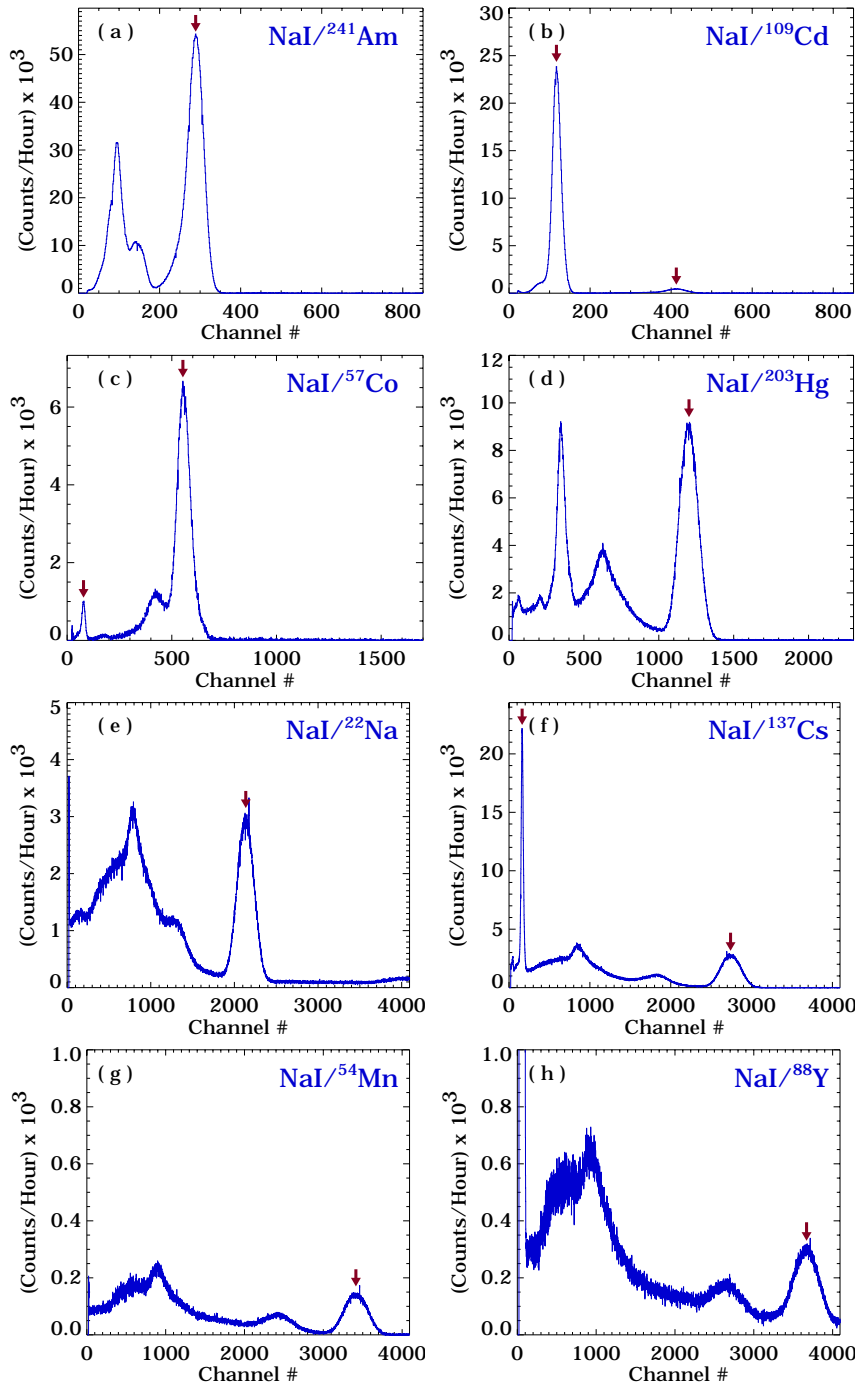


**Figure 3.6:** Normalized background-subtracted spectra measured at MPE with detector NaI FM04 from the following radioactive sources: (a)  $^{241}\text{Am}$ , (b)  $^{109}\text{Cd}$ , (c)  $^{57}\text{Co}$ , (d)  $^{203}\text{Hg}$ , (e)  $^{22}\text{Na}$  (f)  $^{137}\text{Cs}$ , (g)  $^{54}\text{Mn}$ , and (h)  $^{88}\text{Y}$ . Red arrows indicate the full-energy peak(s) position

### 3. GBM PERFORMANCE

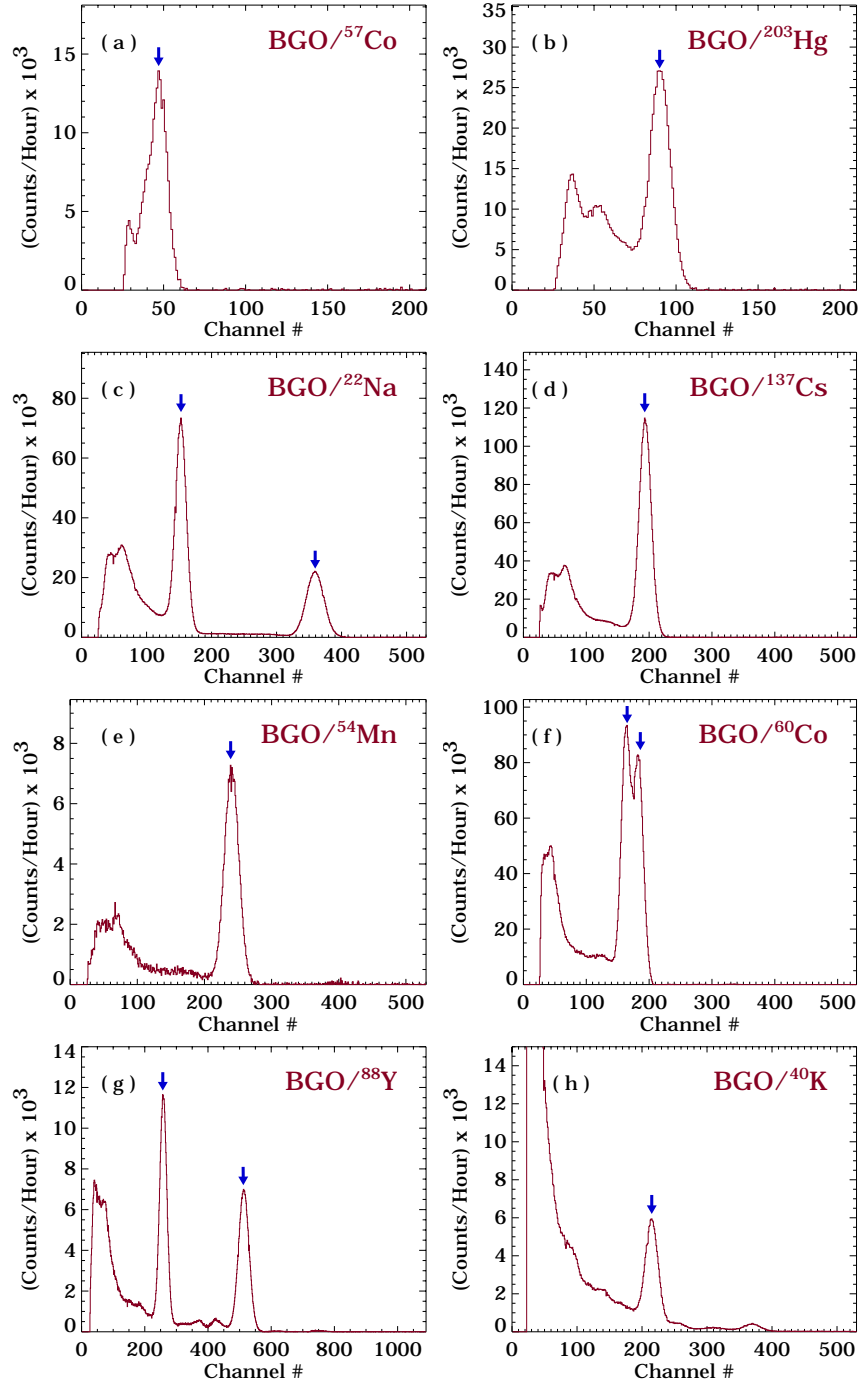


**Figure 3.7:** Normalized background-subtracted spectra measured at MPE with BGO FM02 from the following radioactive sources: (a)  $^{57}\text{Co}$ , (b)  $^{203}\text{Hg}$ , (c)  $^{22}\text{Na}$ , (d)  $^{137}\text{Cs}$ , (e)  $^{54}\text{Mn}$ , (f)  $^{60}\text{Co}$ , (g)  $^{88}\text{Y}$ , and (h)  $^{40}\text{K}$ . *Blue arrows indicate the full-energy peak(s) position*

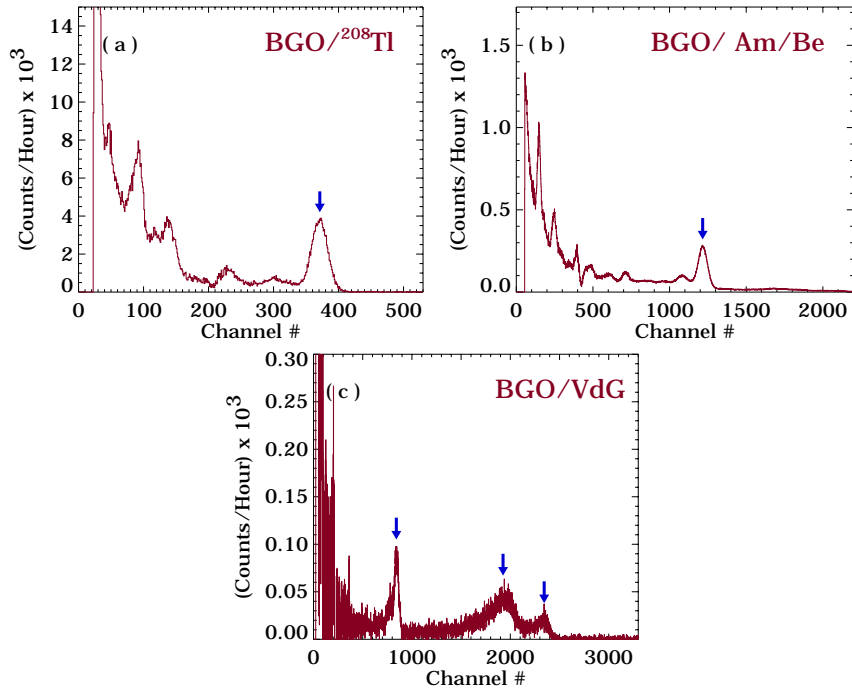


**Figure 3.8:** Normalized background–subtracted spectra measured at MPE with BGO FM02 (*panels a–b*) from the following radioactive sources: (a)  $^{208}\text{Tl}$  and (b) Am/Be. The spectrum in *panel c* was recorded at SLAC with the EQM during one of the the Van de Graaff (VdG) runs. *Blue arrows* indicate the full–energy peak(s) position

3.6, *panel f*), such as the low–energy X radiation (due to internal scattering of gamma–rays very close to the radioactive material) at the very left of the spectrum, the Compton distribution, which is a continuous distribution due to primary gamma–rays undergoing Compton scattering within the crystal, and a backscatter peak at the low–energy end of the Compton distribution.

Similarly, BGO spectra from radioactive sources collected at MPE and SLAC with detector FM02 and BGO EQM are presented in Figures 3.7 and 3.8. The spectrum produced by the Van de Graaff proton beam at SLAC, which was measured with the spare detector BGO EQM, is shown in *panel c* of Figure 3.8.

### 3. GBM PERFORMANCE

---

#### Analysis of the Full–Energy Peak

Radioactive lines emerge from the measured spectra as peaks of various shapes and with multiple underlying contributions. The developed peak fitting procedures were computed adopting two IDL fit packages, namely *mpfit* and *curvefit*. Depending on the specific spectrum, one or more Gaussians in the form

$$G(x) = \frac{A}{w} \cdot \sqrt{\frac{4 \ln 2}{\pi}} e^{-4 \ln 2 \frac{(x - x_c)^2}{w^2}} \quad (3.3)$$

were added in order to fit the data. The three free parameters are

- the peak area **A**;
- the peak center  $x_c$ ; and
- the full width at half maximum **w**

w is related to the standard deviation ( $\sigma$ ) of the distribution through the relation

$$w = 2 \sqrt{2 \ln 2} \cdot \sigma \approx 2.35 \cdot \sigma. \quad (3.4)$$

For the analysis of the measured full–energy peaks, further background components, i.e.

- Linear:  $B_l(x) = a_{Bl} + b_{Bl} x$
- Quadratic:  $B_q(x) = a_{Bq} + b_{Bq} x + c_{Bq} x^2$
- Exponential:  $B_e(x) = a_{Be} \cdot \exp^{-b_{Be} \cdot x}$ ,

as well as Gaussian components had to be modeled in addition to the main Gaussian(s), in order to account for non–photo–peak contributions, such as the overlapping Compton distributions, the backscattered radiation caused by the presence of the uncollimated radioactive source in the laboratory or other unknown background features. In the case of PTB/BESSY spectra, asymmetries appearing at the low–energy tail of the full–energy peak were neglected by choosing a smaller region of interest and fitting only the right side of the peak. As already mentioned, no background was modeled under these spectra.

#### Multiple–Peak Constraints

Since both NaI and BGO detectors are not always able to fully separate two lines lying close to each other and thus resulting in a single broadened peak, particular constraints between line parameters of single peak components were fixed before running the fitting routines. The relation between two line areas ( $A_1$  and  $A_2$ )

**Table 3.4:** Fit constraints adopted for the analysis of some double peaks for NaI and BGO detectors.  $K_{area}$  represents a calculated ratio between the peak areas of the given lines. The error on  $K_{area}$  is of the order of 2%

Nuclide	Detector	Double Line Energy (keV)	$K_{area}$
<sup>109</sup> Cd	NaI	22.1 – 25	4.88
<sup>137</sup> Cs	NaI	32.06 – 36.6	5.33
<sup>57</sup> Co	NaI	122.06 – 136.47	8.14
<sup>60</sup> Co	BGO	1173.23 – 1332.49	0.99
<sup>8</sup> Be	BGO	5619 – 6130	0.20
<sup>8</sup> Be	BGO	14075 – 14586	0.29
<sup>8</sup> Be	BGO	17108 – 17619	0.27

arises from the transition probability  $P$  of the single line energies (see Table 3.1, column 4). A ratio between areas,  $K_{area} = P_1/P_2$ , was obtained by considering those probabilities together with the transmission probability for the detector entrance window and the relative transmission of the photons between source and detector. Finally, the ratios were determined through detailed simulations performed for seven double lines measured with NaI and BGO detectors, and are listed in Table 3.4.

### Systematic Errors

An important consideration when fitting mathematical functions to these data is that the calculated statistical errors of the fit parameters are always within 0.1 % in the case of line areas and FWHM, or even 0.01 % in the case of line centers. Such extreme precisions cause very high chi-square values in subsequent analysis, as in the determination of the channel-to-energy relation, which extends over an entire energy decade in the case of NaI detectors. Moreover, it was noticed that by slightly changing the initial fitting conditions, such as the region of interest around the peak or the type of background, parameter values suffered from substantial changes with respect to a precedent analysis. This effect is particularly strong in the analysis of multiple peaks, where more Gaussians and background functions are added and the number of free parameters increases. In order to account for this effects and to get a more realistic evaluation of the fit parameter errors, we decided to analyse several times one spectrum per source (measured at normal incidence by detectors NaI FM04 and BGO FM02), each time putting different initial fitting conditions.

This procedure was repeated several times (usually ~10–20 times, i.e. until the

### 3. GBM PERFORMANCE

**Table 3.5:** NaI FM04 fitting results for the determination of the systematic errors for  $^{22}\text{Na}$  (at 511 keV) and for  $^{137}\text{Cs}$  (at 32.06 keV). Columns 1 and 2 show 15 measurements of the peak area  $A$  and line width  $w$ , respectively, in the case of  $^{22}\text{Na}$ . 9 measurements of the peak center  $x_c$  in the case of  $^{137}\text{Cs}$  are listed in column 3

$^{22}\text{Na} - 511\text{ keV}$		$^{137}\text{Cs} - 32.06\text{ keV}$
$A$ (Ch. counts/hour)	$w$ (Ch.)	$x_c$ (Ch. #)
$(689.4 \pm 1.1) \cdot 10^3$	$228.0 \pm 0.4$	$161.74 \pm 0.05$
$(689.5 \pm 1.5) \cdot 10^3$	$228.0 \pm 0.5$	$161.73 \pm 0.07$
$(687.8 \pm 2.3) \cdot 10^3$	$228.4 \pm 0.7$	$161.62 \pm 0.09$
$(692.1 \pm 2.1) \cdot 10^3$	$229.0 \pm 0.7$	$161.51 \pm 0.05$
$(695.2 \pm 2.4) \cdot 10^3$	$229.9 \pm 0.8$	$161.50 \pm 0.07$
$(699.6 \pm 1.2) \cdot 10^3$	$231.1 \pm 0.4$	$161.32 \pm 0.11$
$(699.6 \pm 1.7) \cdot 10^3$	$231.1 \pm 0.6$	$161.75 \pm 0.11$
$(701.2 \pm 2.1) \cdot 10^3$	$231.3 \pm 0.7$	$161.76 \pm 0.08$
$(705.0 \pm 1.3) \cdot 10^3$	$232.0 \pm 0.4$	$161.60 \pm 0.09$
$(701.9 \pm 2.9) \cdot 10^3$	$231.9 \pm 0.9$	
$(684.8 \pm 1.0) \cdot 10^3$	$226.5 \pm 0.3$	
$(683.0 \pm 2.2) \cdot 10^3$	$226.8 \pm 0.7$	
$(692.6 \pm 1.1) \cdot 10^3$	$228.3 \pm 0.3$	
$(688.0 \pm 2.0) \cdot 10^3$	$227.7 \pm 0.6$	
$(690.9 \pm 2.3) \cdot 10^3$	$228.6 \pm 0.7$	
$E(A) \pm \sigma_A$ $(692 \pm 7) \cdot 10^3$	$E(w) \pm \sigma_w$ $229.0 \pm 1.9$	$E(x_c) \pm \sigma_{x_c}$ $161.62 \pm 0.13$

systematic contribution was not further increasing and a good chi-square value of the individual fit was produced), thus obtaining a dataset of fit parameters and respective errors. For each error dataset, standard deviations ( $\sigma$ ) were calculated, resulting in values of the order of 1 % for line areas and FWHMs and of 0.1 % for line centers, and were finally added to the fit error, thus obtaining realistic errors.

An example of this procedure is shown in Table 3.5, which summarizes the results from 2 radioactive sources ( $^{22}\text{Na}$  and  $^{137}\text{Cs}$ ). In the case of the 511 keV peak (line 11), the first two columns underline that in fact the systematic error for the area parameter  $A$  and the FWHM parameter  $w$  are bigger than the statistical errors from the fit. Similar considerations regard the 32.06 keV line, whose line center parameter  $x_c$  can strongly vary from fit to fit. Analogous calculations were performed for each peak and for both detectors. The resulting standard deviations are summarized in Tables 3.6 and 3.7.

### 3.2.2. Processing of Calibration Runs

**Table 3.6:** Standard deviations of the three fit parameters of each radioactive line used for the NaI calibration

Tabulated line energy (keV)	$\sigma_A$ (Ch.·Counts/hour)	$\sigma_{x_c}$ (Ch.)	$\sigma_w$ (Ch. #)
14.41	$0.6 \cdot 10^3$	0.15	0.27
22.1	$1.2 \cdot 10^4$	0.017	0.5
25	$2.5 \cdot 10^3$	0.4	1.1
32.06	$2.2 \cdot 10^3$	0.13	0.4
36.6	$0.6 \cdot 10^3$	0.6	0.8
59.4	$1.7 \cdot 10^4$	0.20	0.5
88.03	$0.4 \cdot 10^3$	0.17	1.0
122.06	$2.2 \cdot 10^3$	0.18	0.5
136.47	$2.8 \cdot 10^2$	0.6	1.8
279.2	$2.7 \cdot 10^3$	0.14	0.3
511	$0.7 \cdot 10^4$	0.10	1.9
661.66	$1.7 \cdot 10^3$	0.15	0.7
834.84	$2.6 \cdot 10^2$	1.0	4
898.04	$1.3 \cdot 10^3$	0.8	3

**Table 3.7:** Standard deviations of the three fit parameters of each radioactive line used for the BGO calibration

Tabulated line energy (keV)	$\sigma_A$ (Ch.·Counts/hour)	$\sigma_{x_c}$ (Ch.)	$\sigma_w$ (Ch. #)
124.59	$1.6 \cdot 10^4$	0.4	0.8
279.2	$1.8 \cdot 10^4$	0.16	0.5
511	$2.3 \cdot 10^4$	0.06	0.26
661.66	$5 \cdot 10^4$	0.06	0.3
834.84	$3 \cdot 10^3$	0.06	0.3
898.04	$1.2 \cdot 10^3$	0.018	0.09
1173.23	$7 \cdot 10^4$	0.22	0.5
1274.54	$8 \cdot 10^3$	0.08	0.27
1332.49	$5 \cdot 10^4$	0.27	0.4
1460.83	$3 \cdot 10^3$	0.05	0.4
1836.06	$2.8 \cdot 10^3$	0.06	0.4
2614.63	$2.6 \cdot 10^3$	0.26	0.5
4430	$6 \cdot 10^2$	0.15	1.3
6130	$7 \cdot 10^2$	1.2	1.1
14500	$8 \cdot 10^2$	3	9
17500	$1.2 \cdot 10^3$	9	19

### 3. GBM PERFORMANCE

---

#### Results

The fitting results for 17 lines measured by NaI FM04 are presented graphically in Figures 3.9 and 3.10. In each panel, the fitted line energies are given in the top right corner. Fits to the data are shown in *red*. Gaussian components, describing the full-energy peaks, and background components are shown as *solid blue* and *dotted green curves*, respectively. *Dashed blue curves* represent either background peaks (as in Figure 3.9, *panels b, c, d*) or Iodine escape peaks (as in Figure 3.10, *panels b* and *c*). For energies above 300 keV the Iodine escape peak is no longer fitted as an extra component but is absorbed by the full-energy peak. The tails observed at energies lower than 20 keV (Figure 3.9, *panels a* and *b*) are supposed to be due to scattering from the entrance window materials or to some L-shell escape X-rays.

Results for 16 fitted BGO lines are shown in Figures 3.11 and 3.12. Each full-energy peak was modeled with a single Gaussian (*solid blue curves*) over an exponential background (*dotted green curves*). The line from  $^{57}\text{Co}$  at 124.59 keV (Figure 3.11, *panel a*) lies outside the nominal BGO energy range (150 keV–30 MeV) and shows a strong asymmetric broadening on the left of the full-energy peak, which can be described by an additional Gaussian component (*dashed blue curve*). *Panels c, e* of Figure 3.12 show fitted lines from spectra taken at SLAC with BGO EQM. For some spectra, energies of the first and second pair production escape peaks, which lie  $\sim 511$  keV and  $\sim 1$  MeV below the full-energy peak, respectively, are reported in the top right of each plot. Some of these secondary lines were included in the determination of the BGO channel-to-energy relation (see §3.3.1).

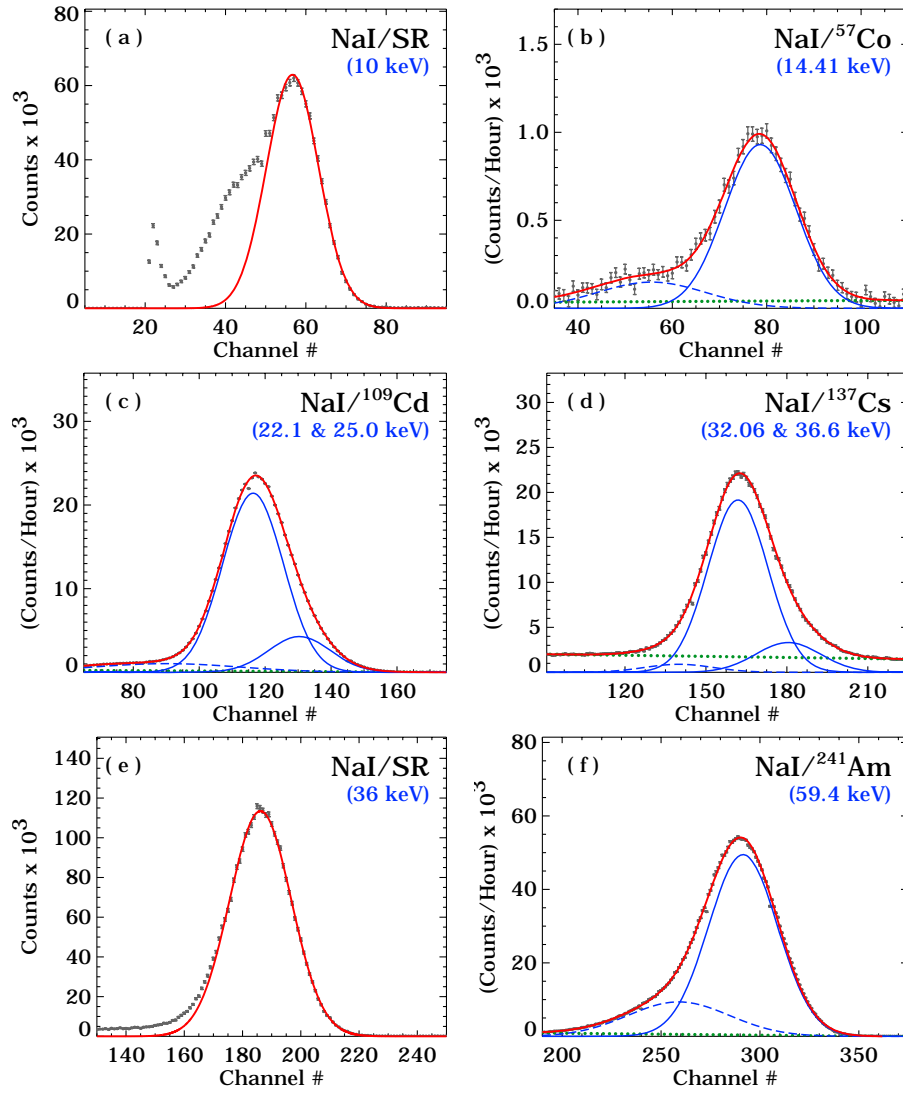


**Figure 3.9:** Full-energy peak analysis of NaI lines. Data points (in *black*) are plotted with statistical errors. Line fits (*solid red curves*) arise from the superposition of different components: (i) one (or more) Gaussian functions describing the full-energy peak(s) (*solid blue curves*); (ii) secondary Gaussian functions modeling the Iodine escape peaks or other unknown background features (*dashed blue curves*); (iii) a constant, linear, quadratic or exponential function accounting for background contributions (*dotted green curves*). For PTB/BESSY line analysis the background contributions could be neglected and only the fit to the full-energy peak was performed starting from 4 to 10 channels before the maximum

### 3. GBM PERFORMANCE

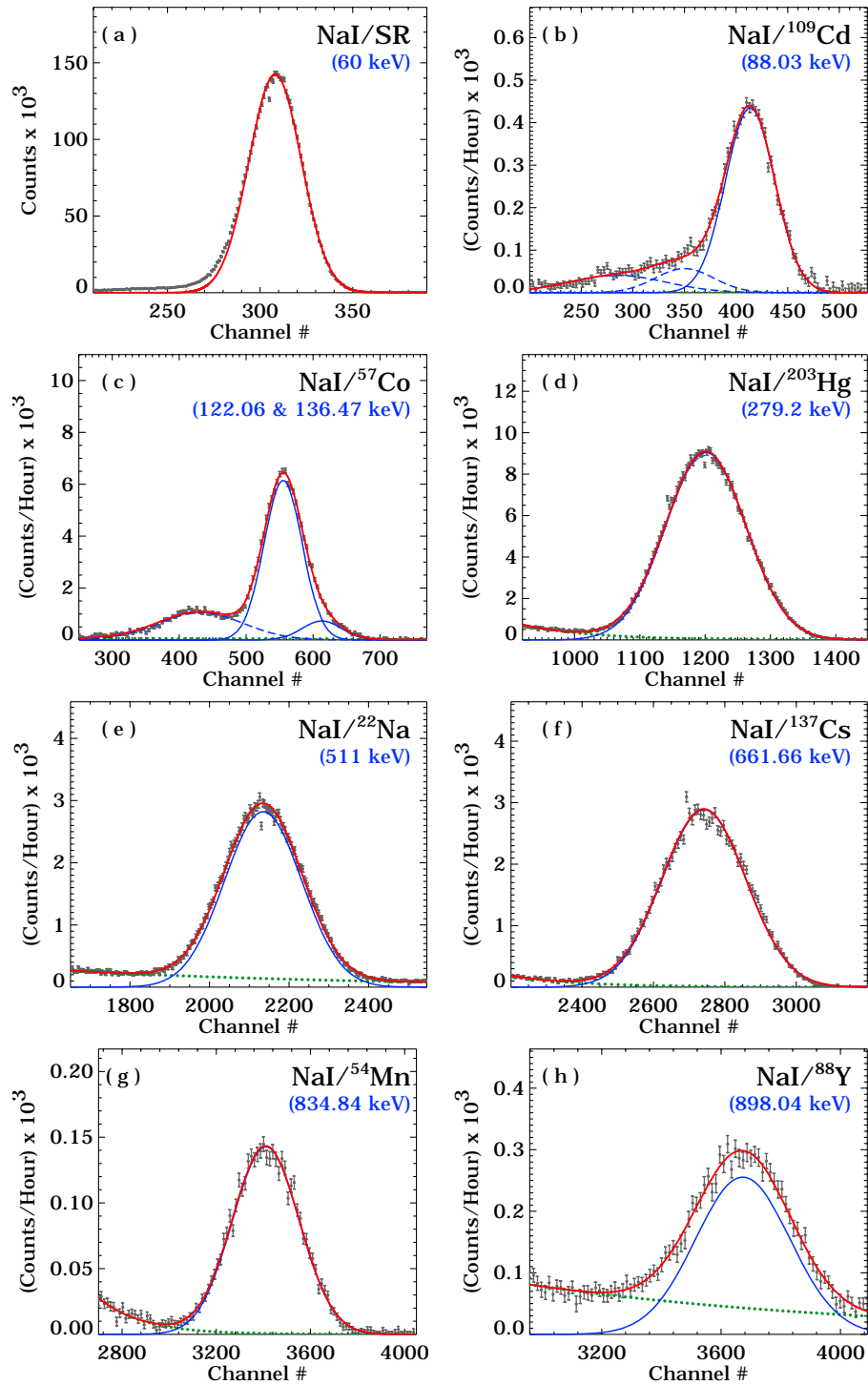


**Figure 3.10:** Full-energy peak analysis of NaI lines. Color code same as in Figure 3.9

### 3.2.2. Processing of Calibration Runs

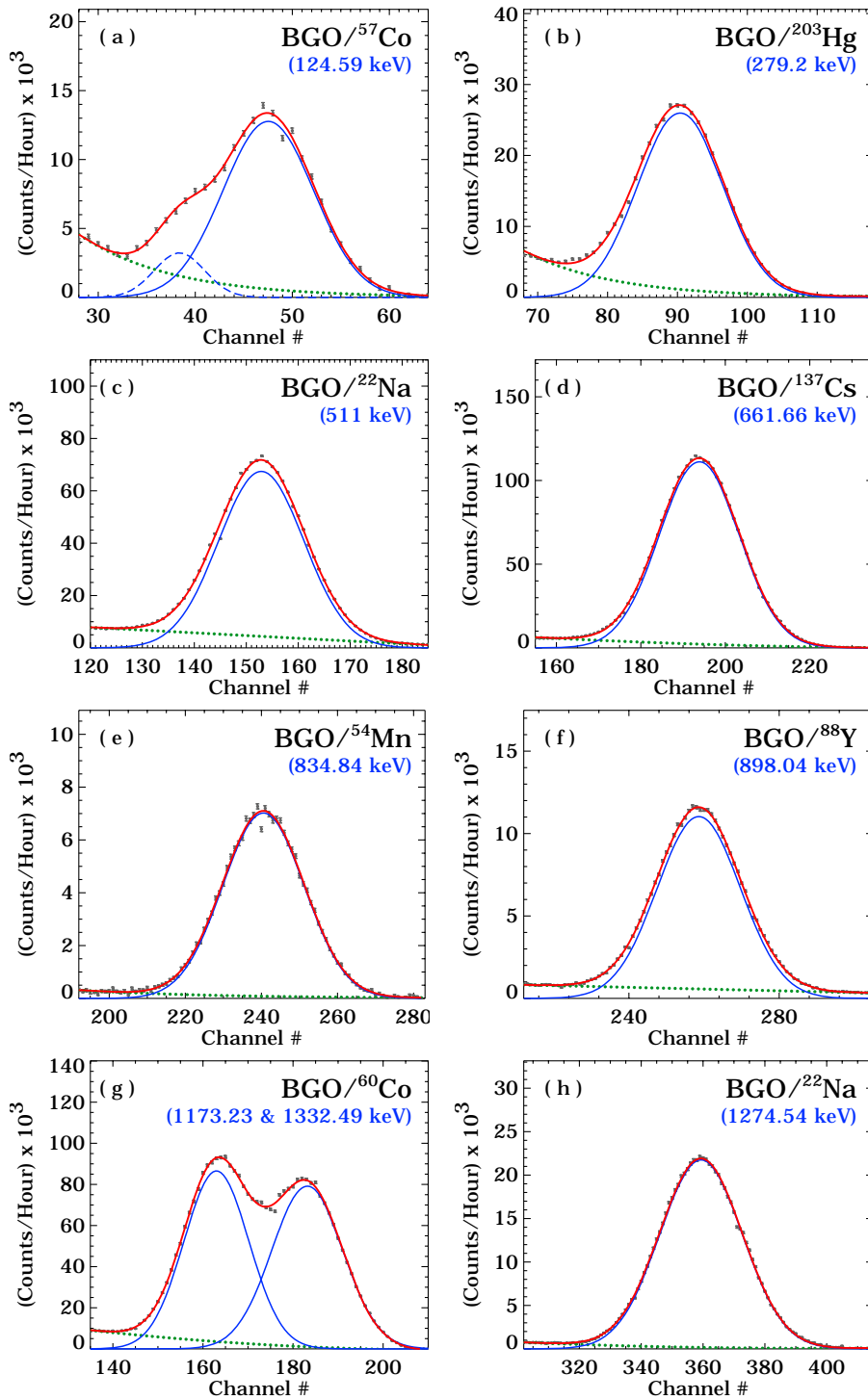
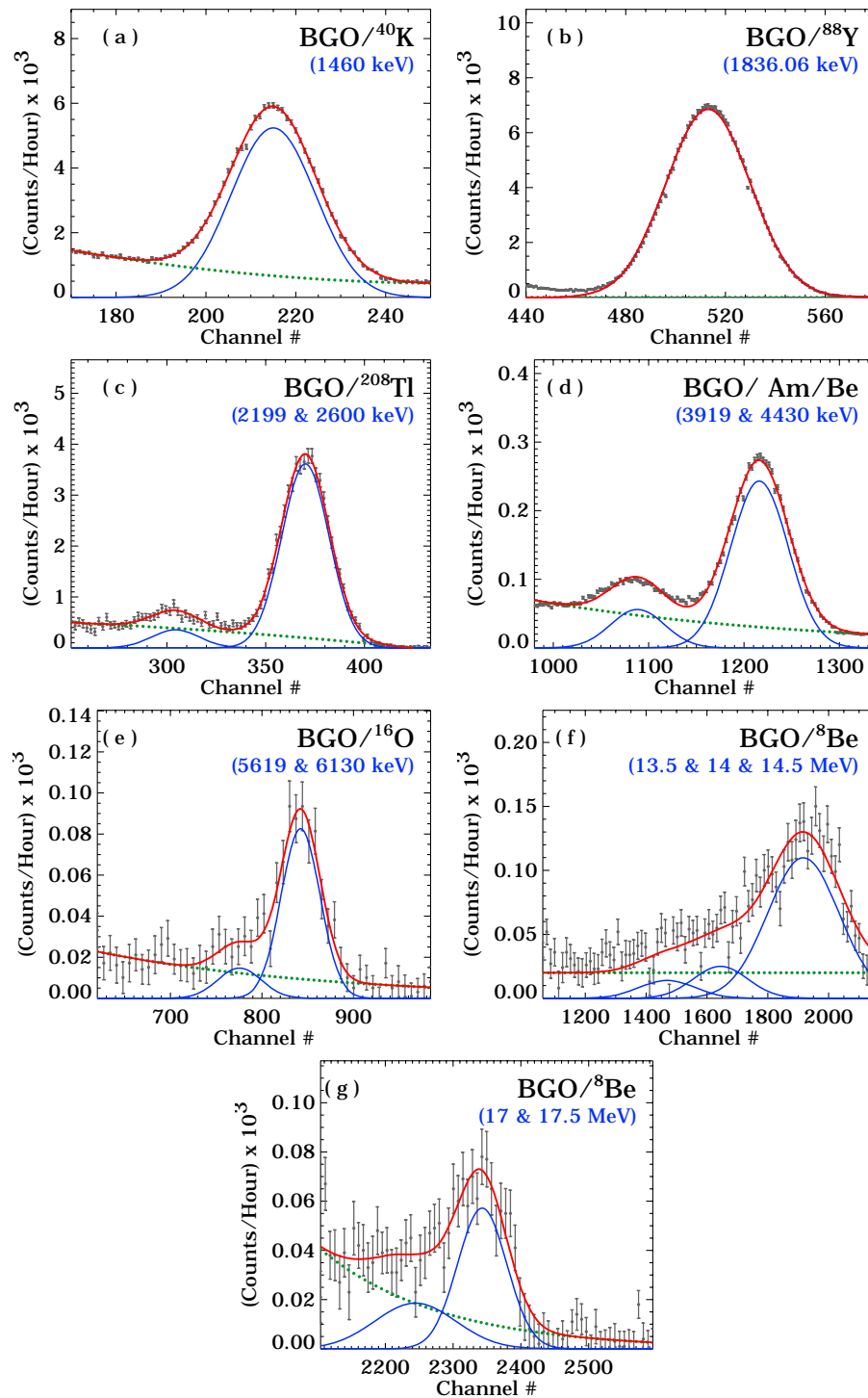


Figure 3.11: Full-energy peak analysis of four BGO lines. Color code same as in Figure 3.9

### 3. GBM PERFORMANCE



**Figure 3.12:** Full-energy peak analysis of six BGO lines. Color code same as in Figure 3.9

### 3.3 Calibration Results

#### 3.3.1 Channel-to-Energy (CE) Relation

##### NaI Nonlinear Response

Several decades of experimental studies of the response of NaI(Tl) to gamma rays have indicated that the scintillation efficiency mildly varies with the deposited energy (Engelkemeir et al., 1989; Iredale, 1961; Prescott & Narayan, 1969; Moszynski et al., 2002). Such nonlinearity must be correctly taken into account when relating the pulse-height scale (i.e. the channel numbers) to gamma-ray energies. Figure 3.13 shows the pulse height per unit energy (normalized to a value of unity at 661.66 keV) versus incident photon energy  $E_\gamma$  as measured by detector NaI FM04. The data points include radioactive source measurements performed at MPE (*triangles*) together with additional low-energy measurements taken at PTB/BESSY between 10 and 60 keV (*squares*). Perfectly linear response would correspond to a horizontal line on this plot. The departure from linearity is most pronounced at low energies, but a small degree of curvature is evident over the whole energy range. The dip that is visible in this plot occurs at a characteristic energy corresponding to the K-shell binding energy in Iodine, i.e. 33.17 keV (previously mentioned in §3.2.2). Photoelectrons ejected by incident gamma-rays just above the K-shell absorption edge have very little kinetic energy, so that the response drops. Just below this energy, however, K-shell ionization is not pos-

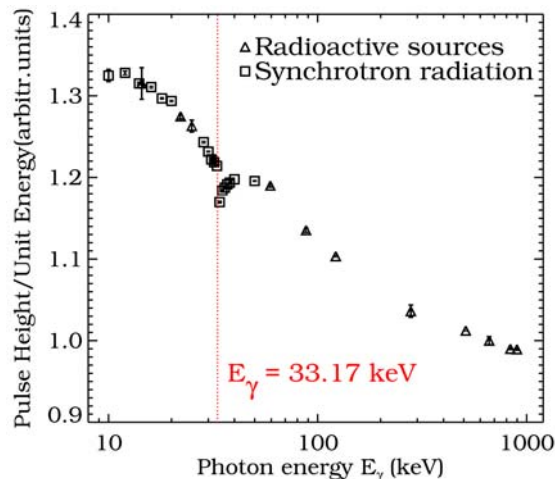


**Figure 3.13:** The differential linearity measured for detector NaI FM04, normalized to unity at 661.66 keV. Perfectly linear response would correspond to a horizontal distribution

### 3. GBM PERFORMANCE

---

sible and L-shell ionization takes place. Since the binding energy is lower, the ejected photoelectrons are more energetic, which causes a rise in the response.

The addition of measurements taken at PTB/BESSY with four NaI detectors (see §3.1.2) for computing the NaI response is particularly necessary in the region around the K-edge energy, since the radioactive sources used at MPE only sample it with four lines, three of which (22.1, 25 and 32.06 keV) belong to double peaks and the first line from  $^{57}\text{Co}$  at 14.41 keV shows asymmetries and broadening (see Figure 3.9, *panel a*). From the collected PTB/BESSY data with detector FM04, line fitting results were obtained for 18 spectra collected at energies from 10 to 20 keV in 2 keV steps, from 29 to 38 keV in 1 keV steps and at 32.8, 40, 50 and 60 keV.

#### **PTB/Bessy Data Sample**

This sample of PTB/BESSY data was analysed with ORIGIN in 2006. Systematic errors have been recently calculated and added to the statistical errors as previously described. In order to compute a valuable NaI CE relation, the energy range was initially split into two regions, one below and one above the K-edge energy. Due to the limited number of datapoints in both regions, PTB/BESSY data were fitted with a quadratic function of the form  $E = a + bx_c + cx_c^2$ , where  $E$  is the line energy in keV and  $x_c$  is the line-center position in channels. Results for the fit parameters are given in Table 3.8. The fitted energies and residuals are given in Table 3.9.

The main difficulty in analysing data taken at PTB/BESSY together with data taken with radioactive sources in the MPE laboratory is the particular re-scaling. In this case one has to deal with data taken with a single detector (FM04) and adopting a particular electronic setup and has to combine them with data taken with all detectors with a (slightly) different electronic setup. Since no precise HV dependence is available for all FM detectors, a scaling factor ( $sf$ ) was determined empirically by:

1. Building a grid of parameter values ( $\alpha$  and  $\beta$ ) for a linear rescaling of the PTB/BESSY raw channels ( $Ch' = \alpha + \beta \cdot Ch$ );
2. Determining the best couple of parameters  $\alpha$  and  $\beta$  which minimizes the Chi-square of the energy-to-channel relation of all data (PTB/BESSY + radioactive sources)

Table 3.10 shows the best parameters calculated for each NaI detector. These values were subsequently used to rescale all PTB/BESSY data.

### 3.3.1. Channel-to-Energy (CE) Relation

**Table 3.8:** Quadratic fit parameters below and above the K-edge for PTB/BESSY data

Energy range	a	b	c	$\chi^2$
10–33 keV	$0.98 \pm 0.40$	$0.144 \pm 0.006$	$(2.32 \pm 0.24) \cdot 10^{-4}$	1.9
34–900 keV	$9.4 \pm 1.3$	$0.111 \pm 0.011$	$(1.74 \pm 0.24) \cdot 10^{-4}$	0.7

**Table 3.9:** CE relation below (*left table*) and above (*right table*) the K-edge for PTB/ BESSY data measured with detector FM04. Fitted energies and residuals in the case of a quadratic fit. Fit parameters are given in the first row of Table 3.8

Tabulated line energy (keV)	Line Center			Tabulated line energy (keV)	Line Center		
	Measured (channels)	Fitted (keV)	Res. (%)		Measured (channels)	Fitted (keV)	Res. (%)
10	$57.5 \pm 2.0$	10.02	-0.19	34	$172.7 \pm 0.9$	33.8	0.7
12	$69.2 \pm 1.2$	12.0	-0.4	35	$179.9 \pm 0.5$	35.00	-0.00
14	$79.9 \pm 0.6$	13.96	0.29	36	$185.6 \pm 0.4$	35.99	0.02
16	$91.0 \pm 0.4$	16.00	0.01	37	$191.41 \pm 0.25$	37.02	-0.05
18	$101.35 \pm 0.29$	17.9	0.3	38	$196.95 \pm 0.24$	38.01	-0.02
20	$112.34 \pm 0.23$	20.1	-0.3	40	$208.0 \pm 0.4$	40.02	-0.04
28.5	$153.8 \pm 0.4$	28.6	-0.4	50	$259.6 \pm 0.4$	49.94	0.12
30	$160.42 \pm 0.13$	30.03	-0.09	60	$307.8 \pm 0.6$	60.07	-0.11
31	$164.50 \pm 0.13$	30.92	0.25				
32	$169.31 \pm 0.14$	31.99	0.04				
33	$173.95 \pm 0.09$	33.03	-0.08				

**Table 3.10:** Scaling factors between PTB/BESSY and MPE data for each NaI detector

FM	$\alpha$	$\beta$	FM	$\alpha$	$\beta$	FM	$\alpha$	$\beta$
01	-4.858	0.987	05	-1.770	0.953	10	-0.992	0.953
02	-1.740	0.974	07	-3.582	0.968	11	0.126	0.951
03	1.878	0.947	08	-0.956	0.965	12	-2.474	0.963
04	-1.474	0.962	09	-1.288	0.946	13	-1.046	0.964

#### Fit Routines

For  $E < 33.17$  keV, data were fitted with a second degree polynomial (parabola), while for  $E > 33.17$  keV the following empirical function was adopted:

$$E(x_c) = a + b \cdot \sqrt{x_c} + c \cdot x_c + d \cdot \ln x_c, \quad (3.5)$$

where  $E$  is the line energy in keV and  $x_c$  is the line-center position in channels. Errors for the tabulated line energies were initially not taken into account. However, line center positions have an error as a result of the peak fitting ( $\Delta x_c$ ). Therefore, we decided first to assign to each energy an error of the same order of magnitude of the corresponding center. Then data were fitted (using these temporary values) with a second degree polynomial, in order to get a preliminary guess

### 3. GBM PERFORMANCE

of the CE relation parameters. These were used to compute  $E_1 = E(x_c - \Delta x_c)$ ,  $E_2 = E(x_c + \Delta x_c)$  and  $E_3 = E(x_c)$ . The energy error is finally given by:

$$\Delta E = \frac{\Delta E_{23} - \Delta E_{31}}{2} = \frac{(E_2 - E_3) + (E_3 - E_1)}{2} = \frac{E_2 - E_1}{2} \quad (3.6)$$

Fitted energies with residuals for all NaI detectors are given in Tables 3.13 to 3.16 in the following pages. All CE relations are also displayed in Figures 3.14 to 3.19. In these plots, radioactive sources data (*triangles*) and PTB/BESSY data (*squares*) are fitted together with a second degree polynomial below 33.17 keV (*red curves*) and with the empirical function above 33.17 keV (*blue curves*). No-

**Table 3.11:** Quadratic fit parameters and Chi-square values calculated for each NaI FM detector below the K-edge

FM	a	b	c	$\chi^2$
01	$1.5 \pm 0.3$	$0.151 \pm 0.006$	$(2.27 \pm 0.21) \cdot 10^{-4}$	1.5
02	$1.2 \pm 0.3$	$0.150 \pm 0.006$	$(2.40 \pm 0.21) \cdot 10^{-4}$	1.3
03	$0.9 \pm 0.4$	$0.147 \pm 0.006$	$(2.74 \pm 0.22) \cdot 10^{-4}$	1.5
04	$1.1 \pm 0.4$	$0.152 \pm 0.006$	$(2.43 \pm 0.21) \cdot 10^{-4}$	1.3
05	$1.1 \pm 0.4$	$0.154 \pm 0.006$	$(2.45 \pm 0.22) \cdot 10^{-4}$	1.4
07	$1.3 \pm 0.3$	$0.154 \pm 0.006$	$(2.33 \pm 0.22) \cdot 10^{-4}$	1.4
08	$1.1 \pm 0.4$	$0.149 \pm 0.006$	$(2.50 \pm 0.22) \cdot 10^{-4}$	1.3
09	$1.1 \pm 0.4$	$0.155 \pm 0.006$	$(2.52 \pm 0.22) \cdot 10^{-4}$	1.3
10	$1.1 \pm 0.4$	$0.152 \pm 0.006$	$(2.55 \pm 0.22) \cdot 10^{-4}$	1.3
11	$1.0 \pm 0.4$	$0.150 \pm 0.006$	$(2.62 \pm 0.22) \cdot 10^{-4}$	1.4
12	$1.1 \pm 0.3$	$0.155 \pm 0.006$	$(2.34 \pm 0.22) \cdot 10^{-4}$	1.4
13	$1.1 \pm 0.4$	$0.151 \pm 0.006$	$(2.45 \pm 0.22) \cdot 10^{-4}$	1.3

**Table 3.12:** Empirical fit parameters and Chi-square values calculated for each NaI FM detector above the K-edge

FM	a	b	c	d	$\chi^2$
01	$49.8 \pm 2.6$	$0.227 \pm 0.13$	$0.2527 \pm 0.0012$	$-12.0 \pm 0.8$	34
02	$76.8 \pm 2.6$	$1.646 \pm 0.13$	$0.2418 \pm 0.0012$	$-20.5 \pm 0.8$	24
03	$46.6 \pm 2.4$	$0.185 \pm 0.12$	$0.2524 \pm 0.0011$	$-11.2 \pm 0.7$	50
04	$61.3 \pm 2.8$	$1.125 \pm 0.14$	$0.2446 \pm 0.0013$	$-16.2 \pm 0.9$	34
05	$52.9 \pm 2.7$	$0.580 \pm 0.14$	$0.2514 \pm 0.0013$	$-13.3 \pm 0.8$	45
07	$60.8 \pm 2.7$	$0.890 \pm 0.15$	$0.2490 \pm 0.0014$	$-15.6 \pm 0.9$	30
08	$38.4 \pm 2.8$	$-0.540 \pm 0.14$	$0.2620 \pm 0.0013$	$-8.1 \pm 0.9$	38
09	$50 \pm 3$	$0.660 \pm 0.17$	$0.2501 \pm 0.0015$	$-12.8 \pm 1.0$	19
10	$55.7 \pm 2.7$	$0.624 \pm 0.14$	$0.2507 \pm 0.0014$	$-14.0 \pm 0.9$	31
11	$49.2 \pm 2.7$	$0.334 \pm 0.14$	$0.2528 \pm 0.0013$	$-12.1 \pm 0.8$	44
12	$56.3 \pm 2.8$	$0.696 \pm 0.15$	$0.2519 \pm 0.0014$	$-14.3 \pm 0.9$	63
13	$73 \pm 3$	$1.378 \pm 0.16$	$0.2443 \pm 0.0014$	$-19.0 \pm 0.9$	24

### 3.3.1. Channel-to-Energy (CE) Relation

ticeably, the analysis of the NaI detectors shows very similar results. In particular, all calculated relations give fit residuals below 1 %, as required. The obtained fit parameters are reported hereafter in Tables 3.11 and 3.12.

**Table 3.13:** CE relation for NaI detectors FM01–FM07 below the K-edge. Fitted energies and residuals in the case of a quadratic fit. The corresponding fit parameters are given in Table 3.11

FM	Tabulated line energy (keV)	Line Center			FM	Tabulated line energy (keV)	Line Center		
		Measured (channels)	Fitted (keV)	Res. (%)			Measured (channels)	Fitted (keV)	Res. (%)
<b>01</b>	10	51.9 ± 2.0	9.97	0.27	<b>02</b>	10	54.3 ± 2.0	10.00	-0.02
	12	63.5 ± 1.2	12.01	-0.11		12	65.7 ± 1.2	12.03	-0.27
	14	74.1 ± 0.6	14.0	0.4		14	76.2 ± 0.6	14.0	0.3
	14.4	78.0 ± 1.5	14.7	-1.8		14.4	78.6 ± 0.8	14.42	-0.04
	16	85.0 ± 0.4	16.00	0.03		16	87.0 ± 0.4	16.00	0.01
	18	95.22 ± 0.29	18.0	0.3		18	97.02 ± 0.29	17.9	0.3
	20	106.07 ± 0.23	20.1	-0.4		20	107.72 ± 0.23	20.1	-0.4
	22.1	116.07 ± 0.20	22.09	0.04		22.1	117.67 ± 0.19	22.10	0.01
	25	129.4 ± 0.6	24.9	0.6		25	131.2 ± 0.5	24.94	0.26
	28.5	147.0 ± 0.4	28.6	-0.4		28.5	148.2 ± 0.4	28.6	-0.4
	30	153.54 ± 0.13	30.03	-0.11		30	154.57 ± 0.13	30.03	-0.10
	31	157.57 ± 0.13	30.93	0.24		31	158.55 ± 0.13	30.92	0.25
	32	162.32 ± 0.14	31.99	0.04		32	163.24 ± 0.14	31.99	0.04
	32.06	163.0 ± 0.5	32.14	-0.24		32.06	163.7 ± 0.5	32.10	-0.12
33	166.90 ± 0.09	33.02	-0.06	33	167.76 ± 0.09	33.02	-0.07		
<b>03</b>	10	56.34 ± 2.0	10.09	-0.9	<b>04</b>	10	53.9 ± 2.0	9.99	0.09
	12	67.40 ± 1.2	12.09	-0.7		12	65.1 ± 1.2	12.03	-0.21
	14	77.6 ± 0.6	13.99	0.10		14	75.5 ± 0.6	14.0	0.4
	14.4	78.8 ± 0.8	14.2	1.4		14.4	78.3 ± 0.8	14.5	-0.5
	16	88.1 ± 0.4	16.01	-0.06		16	86.2 ± 0.4	16.00	0.02
	18	97.84 ± 0.29	17.9	0.3		18	96.07 ± 0.29	17.9	0.3
	20	108.24 ± 0.23	20.06	-0.29		20	106.64 ± 0.23	20.1	-0.4
	22.1	118.03 ± 0.19	22.11	-0.02		22.1	116.35 ± 0.19	22.08	0.10
	25	132.0 ± 0.5	25.1	-0.4		25	130.4 ± 0.5	25.06	-0.22
	28.5	147.5 ± 0.4	28.6	-0.3		28.5	146.6 ± 0.4	28.6	-0.4
	30	153.77 ± 0.13	30.02	-0.07		30	152.92 ± 0.13	30.03	-0.11
	31	157.62 ± 0.13	30.92	0.26		31	156.84 ± 0.13	30.92	0.25
	32	162.18 ± 0.14	31.99	0.04		32	161.47 ± 0.14	31.99	0.04
	32.04	162.40 ± 0.22	32.04	0.06		32.04	161.81 ± 0.22	32.07	-0.02
33	166.58 ± 0.09	33.03	-0.09	33	165.94 ± 0.09	33.02	-0.07		
<b>05</b>	10	53.1 ± 2.0	9.98	0.19	<b>07</b>	10	52.1 ± 2.0	10.0	0.4
	12	64.2 ± 1.2	12.02	-0.15		12	63.4 ± 1.2	12.00	-0.03
	14	74.4 ± 0.6	14.0	0.4		14	73.8 ± 0.6	13.9	0.4
	14.4	77.5 ± 0.8	14.5	-0.9		14.4	77.2 ± 0.9	14.6	-1.2
	16	85.0 ± 0.4	16.00	0.03		16	84.5 ± 0.4	15.99	0.05
	18	94.84 ± 0.29	17.9	0.3		18	94.51 ± 0.29	18.0	0.3
	20	105.31 ± 0.23	20.1	-0.4		20	105.14 ± 0.23	20.1	-0.4
	22.1	114.88 ± 0.19	22.07	0.14		22.1	114.88 ± 0.20	22.08	0.10
	25	128.9 ± 0.5	25.08	-0.32		25	128.4 ± 0.6	24.9	0.3
	28.5	144.9 ± 0.4	28.6	-0.4		28.5	145.3 ± 0.4	28.6	-0.4
	30	151.14 ± 0.13	30.03	-0.11		30	151.67 ± 0.13	30.04	-0.12
	31	155.03 ± 0.13	30.92	0.24		31	155.62 ± 0.13	30.93	0.24
	32	159.62 ± 0.14	31.99	0.04		32	160.28 ± 0.14	31.99	0.04
	32.04	159.94 ± 0.07	32.06	-0.00		32.04	160.8 ± 0.3	32.10	-0.12
33	164.04 ± 0.09	33.02	-0.06	33	164.77 ± 0.09	33.02	-0.06		

### 3. GBM PERFORMANCE

**Table 3.14:** CE relation for NaI detectors FM08–FM13 below the K-edge. Fitted energies and residuals in the case of a quadratic fit. The corresponding fit parameters are given in Table 3.11

FM	Tabulated line energy (keV)	Line Center			FM	Tabulated line energy (keV)	Line Center		
		Measured (channels)	Fitted (keV)	Res. (%)			Measured (channels)	Fitted (keV)	Res. (%)
<b>08</b>	10	54.6 ± 2.0	10.03	-0.25	<b>09</b>	10	53.1 ± 2.0	9.99	0.07
	12	65.8 ± 1.2	12.1	-0.4		12	64.2 ± 1.2	12.03	-0.22
	14	76.2 ± 0.6	13.96	0.26		14	74.3 ± 0.6	14.0	0.4
	14.4	78.5 ± 0.8	14.39	0.14		14.4	77.1 ± 0.8	14.5	-0.6
	16	86.9 ± 0.4	16.00	-0.01		16	84.8 ± 0.4	16.00	0.02
	18	96.85 ± 0.29	17.9	0.3		18	94.55 ± 0.29	17.9	0.3
	20	107.45 ± 0.23	20.1	-0.3		20	104.94 ± 0.23	20.1	-0.4
	22.1	117.27 ± 0.20	22.09	0.07		22.1	114.48 ± 0.19	22.08	0.11
	25	131.5 ± 0.5	25.1	-0.4		25	128.3 ± 0.5	25.06	-0.23
	28.5	147.5 ± 0.4	28.6	-0.4		28.5	144.2 ± 0.4	28.6	-0.4
	30	153.85 ± 0.13	30.03	-0.09		30	150.41 ± 0.13	30.03	-0.11
	31	157.78 ± 0.13	30.92	0.25		31	154.26 ± 0.13	30.92	0.25
	32	162.43 ± 0.14	31.99	0.04		32	158.81 ± 0.14	31.99	0.04
	32.04	162.7 ± 0.4	32.05	0.04		32.04	159.2 ± 0.3	32.07	-0.03
33	166.91 ± 0.09	33.03	-0.08	33	163.20 ± 0.09	33.02	-0.07		
<b>10</b>	10	53.8 ± 2.0	10.02	-0.22	<b>11</b>	10	54.8 ± 2.0	10.0	-0.4
	12	65.0 ± 1.2	12.1	-0.4		12	65.9 ± 1.2	12.1	-0.5
	14	75.2 ± 0.6	13.96	0.26		14	76.1 ± 0.6	13.97	0.21
	14.4	77.5 ± 0.8	14.40	0.09		14.4	78.1 ± 0.8	14.4	0.4
	16	85.8 ± 0.4	16.00	-0.01		16	86.7 ± 0.4	16.00	-0.02
	18	95.60 ± 0.29	17.9	0.3		18	96.47 ± 0.29	17.9	0.3
	20	106.07 ± 0.23	20.1	-0.4		20	106.92 ± 0.23	20.1	-0.3
	22.1	115.74 ± 0.19	22.08	0.08		22.1	116.61 ± 0.19	22.09	0.06
	25	129.8 ± 0.5	25.1	-0.4		25	130.8 ± 0.5	25.1	-0.5
	25.8	145.6 ± 0.4	28.6	-0.4		28.5	146.4 ± 0.4	28.6	-0.3
	30	151.89 ± 0.13	30.03	-0.10		30	152.62 ± 0.13	30.03	-0.09
	31	155.77 ± 0.13	30.92	0.25		31	156.50 ± 0.13	30.92	0.25
	32	160.36 ± 0.14	31.99	0.04		32	161.07 ± 0.14	31.99	0.04
	32.04	160.7 ± 0.4	32.06	0.00		32.04	161.31 ± 0.29	32.04	0.05
33	164.79 ± 0.09	33.03	-0.08	33	165.49 ± 0.09	33.03	-0.08		
<b>12</b>	10	52.9 ± 2.0	10.0	0.5	<b>13</b>	10	54.4 ± 2.0	10.00	0.01
	12	64.2 ± 1.2	12.00	-0.01		12	65.6 ± 1.2	12.03	-0.25
	14	74.5 ± 0.6	13.9	0.4		14	76.0 ± 0.6	14.0	0.3
	14.4	77.9 ± 0.8	14.6	-1.2		14.4	78.6 ± 0.8	14.45	-0.24
	16	85.2 ± 0.4	15.99	0.05		16	86.7 ± 0.4	16.00	0.02
	18	95.11 ± 0.29	18.0	0.3		18	96.62 ± 0.29	17.9	0.3
	20	105.69 ± 0.23	20.1	-0.4		20	107.21 ± 0.23	20.1	-0.4
	22.1	115.33 ± 0.19	22.07	0.14		22.1	116.98 ± 0.19	22.1	0.4
	25	129.1 ± 0.5	25.00	0.02		25	130.8 ± 0.5	25.01	-0.04
	28.5	145.6 ± 0.4	28.6	-0.4		28.5	147.2 ± 0.4	28.6	-0.4
	30	151.98 ± 0.13	30.04	-0.12		30	153.54 ± 0.13	30.03	-0.10
	31	155.90 ± 0.13	30.93	0.24		31	157.46 ± 0.13	30.92	0.25
	32	160.54 ± 0.14	31.99	0.04		32	162.10 ± 0.14	31.99	0.04
	32.04	160.95 ± 0.25	32.08	-0.07		32.04	162.44 ± 0.24	32.07	-0.02
33	165.01 ± 0.09	33.02	-0.06	33	166.58 ± 0.09	33.02	-0.07		

### 3.3.1. Channel-to-Energy (CE) Relation

**Table 3.15:** CE relation for NaI detectors FM01–FM07 above the K-edge. Fitted energies and residuals in the case of an empirical fit. The corresponding fit parameters are given in Table 3.12

FM	Tabulated line energy (keV)	Line Center			FM	Tabulated line energy (keV)	Line Center		
		Measured (channels)	Fitted (keV)	Res. (%)			Measured (channels)	Fitted (keV)	Res. (%)
<b>01</b>	34	167.6 ± 0.9	33.7	0.8	<b>02</b>	34	168.5 ± 0.9	33.9	0.4
	35	172.8 ± 0.5	34.7	0.8		35	173.6 ± 0.5	34.8	0.5
	36	178.4 ± 0.4	35.8	0.6		36	179.1 ± 0.4	35.9	0.4
	37	184.14 ± 0.25	36.91	0.24		37	184.77 ± 0.25	36.93	0.20
	38	189.61 ± 0.24	37.99	0.04		38	190.16 ± 0.24	37.97	0.09
	40	200.5 ± 0.4	40.2	-0.4		40	200.9 ± 0.4	40.08	-0.19
	50	251.4 ± 0.4	50.7	-1.4		50	251.2 ± 0.4	50.4	-0.8
	59.4	292.88 ± 0.23	59.6	-0.4		59.4	295.09 ± 0.26	59.9	-0.9
	60	299.1 ± 0.6	61.0	-1.7		60	298.2 ± 0.6	60.6	-1.0
	88.03	417.6 ± 0.4	87.7	0.4		88.03	418.0 ± 0.4	87.89	0.16
	122.06	563.44 ± 0.23	121.7	0.3		122.06	560.42 ± 0.23	121.6	0.4
	279.2	1213 ± 5	279.11	0.03		279.2	1205 ± 4	279.90	-0.25
	511	2151.3 ± 0.5	511.95	-0.19		511	2133.6 ± 0.5	511.76	-0.15
	661.66	2750 ± 10	661.74	-0.01		661.66	2735 ± 7	662.15	-0.07
	834.84	3419 ± 3	829.5	0.6		834.84	3412 ± 3	831.4	0.4
898.04	3678.0 ± 2.0	894.5	0.4	898.04	3665.2 ± 2.0	894.7	0.4		
<b>03</b>	34	167.27 ± 0.9	33.8	0.5	<b>04</b>	34	166.6 ± 0.9	33.8	0.6
	35	172.2 ± 0.5	34.8	0.6		35	171.7 ± 0.5	34.8	0.7
	36	177.6 ± 0.4	35.8	0.5		36	177.2 ± 0.4	35.8	0.5
	37	183.10 ± 0.25	36.92	0.22		37	182.74 ± 0.25	36.91	0.23
	38	188.35 ± 0.24	37.96	0.11		38	188.07 ± 0.24	37.97	0.07
	40	198.8 ± 0.4	40.06	-0.16		40	198.7 ± 0.4	40.12	-0.29
	50	247.6 ± 0.4	50.2	-0.5		50	248.3 ± 0.4	50.5	-1.0
	59.4	294.12 ± 0.27	60.3	-1.5		59.4	291.92 ± 0.29	60.1	-1.1
	60	293.3 ± 0.6	60.12	-0.20		60	294.8 ± 0.6	60.7	-1.2
	88.03	421.7 ± 0.6	89.1	-1.2		88.03	412.8 ± 0.6	87.6	0.4
	122.06	559.89 ± 0.23	121.4	0.6		122.06	556.25 ± 0.23	121.6	0.4
	279.2	1209 ± 7	278.65	0.20		279.2	1201 ± 6	279.34	-0.05
	511	2150.5 ± 0.5	511.98	-0.19		511	2136.1 ± 0.5	511.74	-0.15
	661.66	2750 ± 6	661.59	0.01		661.66	2740 ± 9	662.22	-0.08
	834.84	3431.0 ± 2.3	832.2	0.3		834.84	3413.3 ± 2.2	830.3	0.6
898.04	3679.4 ± 1.7	894.5	0.4	898.04	3669.6 ± 2.8	894.2	0.4		
<b>05</b>	34	164.7 ± 0.9	33.8	0.7	<b>07</b>	34	165.5 ± 0.9	33.8	0.6
	35	169.7 ± 0.5	34.8	0.7		35	170.6 ± 0.5	34.8	0.7
	36	175.2 ± 0.4	35.8	0.5		36	176.0 ± 0.4	35.8	0.5
	37	180.68 ± 0.25	36.91	0.25		37	181.66 ± 0.25	36.92	0.22
	38	185.96 ± 0.24	37.96	0.09		38	187.02 ± 0.24	37.98	0.06
	40	196.5 ± 0.4	40.10	-0.25		40	197.7 ± 0.4	40.12	-0.29
	50	245.7 ± 0.4	50.5	-0.9		50	247.6 ± 0.4	50.5	-1.1
	59.4	290.44 ± 0.29	60.3	-1.5		59.4	289.72 ± 0.23	59.7	-0.5
	60	291.7 ± 0.6	60.5	-0.9		60	294.3 ± 0.6	60.7	-1.2
	88.03	412.1 ± 0.9	88.09	-0.07		88.03	414.2 ± 0.4	88.10	-0.08
	122.06	552.96 ± 0.23	121.5	0.5		122.06	555.48 ± 0.23	121.6	0.4
	279.2	1195 ± 4	279.04	0.06		279.2	1193 ± 10	278.2	0.4
	511	2125.6 ± 0.5	512.00	-0.20		511	2124.7 ± 0.3	511.42	-0.08
	661.66	2720 ± 5	661.54	0.02		661.66	2716 ± 11	660.15	0.23
	834.84	3387.5 ± 1.7	830.1	0.6		834.84	3389.1 ± 2.4	829.8	0.6
898.04	3648 ± 3	895.70	0.26	898.04	3634 ± 3	891.4	0.7		

### 3. GBM PERFORMANCE

**Table 3.16:** CE relation for NaI detectors FM08–FM13 above the K–edge. Fitted energies and residuals in the case of an empirical fit. The corresponding fit parameters are given in Table 3.12

FM	Tabulated line energy (keV)	Line Center			FM	Tabulated line energy (keV)	Line Center		
		Measured (channels)	Fitted (keV)	Res. (%)			Measured (channels)	Fitted (keV)	Res. (%)
<b>08</b>	34	167.6 ± 0.9	33.8	0.7	<b>09</b>	34	163.9 ± 0.9	33.8	0.7
	35	172.7 ± 0.5	34.7	0.8		35	168.9 ± 0.5	34.8	0.7
	36	178.2 ± 0.4	35.8	0.5		36	174.2 ± 0.4	35.83	0.5
	37	183.75 ± 0.25	36.91	0.23		37	179.71 ± 0.25	36.94	0.16
	38	189.10 ± 0.24	37.97	0.07		38	184.94 ± 0.24	38.01	-0.03
	40	199.8 ± 0.4	40.12	-0.29		40	195.4 ± 0.4	40.2	-0.4
	50	249.5 ± 0.4	50.5	-0.9		50	244.2 ± 0.4	50.6	-1.2
	59.4	293.15 ± 0.23	59.9	-0.8		59.4	—	—	—
	60	296.1 ± 0.6	60.5	-0.8		60	289.8 ± 0.6	60.7	-1.2
	88.03	419.9 ± 0.9	88.3	-0.3		88.03	407.7 ± 0.7	87.94	0.11
	122.06	562.06 ± 0.24	121.5	0.5		122.06	549.75 ± 0.23	121.76	0.24
	279.2	1210 ± 9	279.00	0.07		279.2	1187 ± 4	278.57	0.23
	511	2139.5 ± 0.4	511.76	-0.15		511	2117.8 ± 0.5	511.50	-0.10
	661.66	2726 ± 10	660.11	0.23		661.66	2713 ± 5	661.25	0.06
	834.84	3390.5 ± 2.1	829.3	0.7		834.84	3388.3 ± 2.3	831.3	0.4
898.04	3636 ± 3	892.1	0.7	898.04	3643 ± 4	895.44	0.29		
<b>10</b>	34	165.5 ± 0.9	33.8	0.5	<b>11</b>	34	166.2 ± 0.9	33.8	0.6
	35	170.5 ± 0.5	34.8	0.6		35	171.2 ± 0.5	34.8	0.7
	36	175.9 ± 0.4	35.8	0.5		36	176.6 ± 0.4	35.8	0.5
	37	181.42 ± 0.25	36.92	0.21		37	182.08 ± 0.25	36.91	0.24
	38	186.70 ± 0.24	37.97	0.09		38	187.34 ± 0.24	37.96	0.10
	40	197.2 ± 0.4	40.08	-0.20		40	197.9 ± 0.4	40.09	-0.21
	50	246.4 ± 0.4	50.3	-0.6		50	246.9 ± 0.4	50.4	-0.7
	59.4	290.43 ± 0.23	59.9	-0.9		59.4	292.54 ± 0.27	60.3	-1.5
	60	292.4 ± 0.6	60.3	-0.6		60	292.8 ± 0.6	60.4	-0.6
	88.03	413.8 ± 0.7	87.94	0.10		88.03	413.9 ± 0.5	87.89	0.16
	122.06	556.21 ± 0.23	121.5	0.4		122.06	556.63 ± 0.23	121.5	0.5
	279.2	1198 ± 9	278.52	0.24		279.2	1199 ± 6	278.3	0.3
	511	2130.1 ± 0.3	511.44	-0.09		511	2133.55 ± 0.29	511.37	-0.07
	661.66	2721 ± 7	659.79	0.28		661.66	2724 ± 4	659.6	0.3
	834.84	3393.2 ± 2.2	829.2	0.7		834.84	3398.1 ± 2.0	829.4	0.7
898.04	3644 ± 4	892.5	0.6	898.04	3651 ± 4	893.1	0.6		
<b>12</b>	34	165.7 ± 0.9	33.7	0.8	<b>13</b>	34	167.3 ± 0.9	33.92	0.24
	35	170.8 ± 0.5	34.7	0.8		35	172.3 ± 0.5	34.9	0.4
	36	176.2 ± 0.4	35.8	0.6		36	177.8 ± 0.4	35.9	0.3
	37	181.81 ± 0.25	36.9	0.3		37	183.40 ± 0.25	36.94	0.16
	38	187.15 ± 0.24	37.95	0.13		38	188.73 ± 0.24	37.97	0.08
	40	197.8 ± 0.4	40.11	-0.27		40	199.4 ± 0.4	40.05	-0.13
	50	247.4 ± 0.4	50.6	-1.1		50	249.1 ± 0.4	50.2	-0.5
	59.4	290.62 ± 0.22	60.1	-1.1		59.4	294.61 ± 0.28	60.07	-1.13
	60	293.9 ± 0.6	60.8	-1.3		60	295.6 ± 0.6	60.3	-0.5
	88.03	410.8 ± 0.4	87.6	0.5		88.03	415.5 ± 0.6	87.5	0.6
	122.06	553.11 ± 0.24	121.4	0.5		122.06	560.34 ± 0.23	121.71	0.29
	279.2	1194 ± 5	279.56	-0.13		279.2	1201 ± 6	278.86	0.12
	511	2116.6 ± 0.4	511.63	-0.12		511	2134.6 ± 0.6	511.82	-0.16
	661.66	2707 ± 9	661.10	0.09		661.66	2731 ± 5	661.07	0.09
	834.84	3354.3 ± 2.4	825.1	1.2		834.84	3406.5 ± 2.3	830.3	0.5
898.84	3616 ± 4	891.34	0.75	898.04	3661 ± 4	894.2	0.4		

### 3.3.1. Channel-to-Energy (CE) Relation

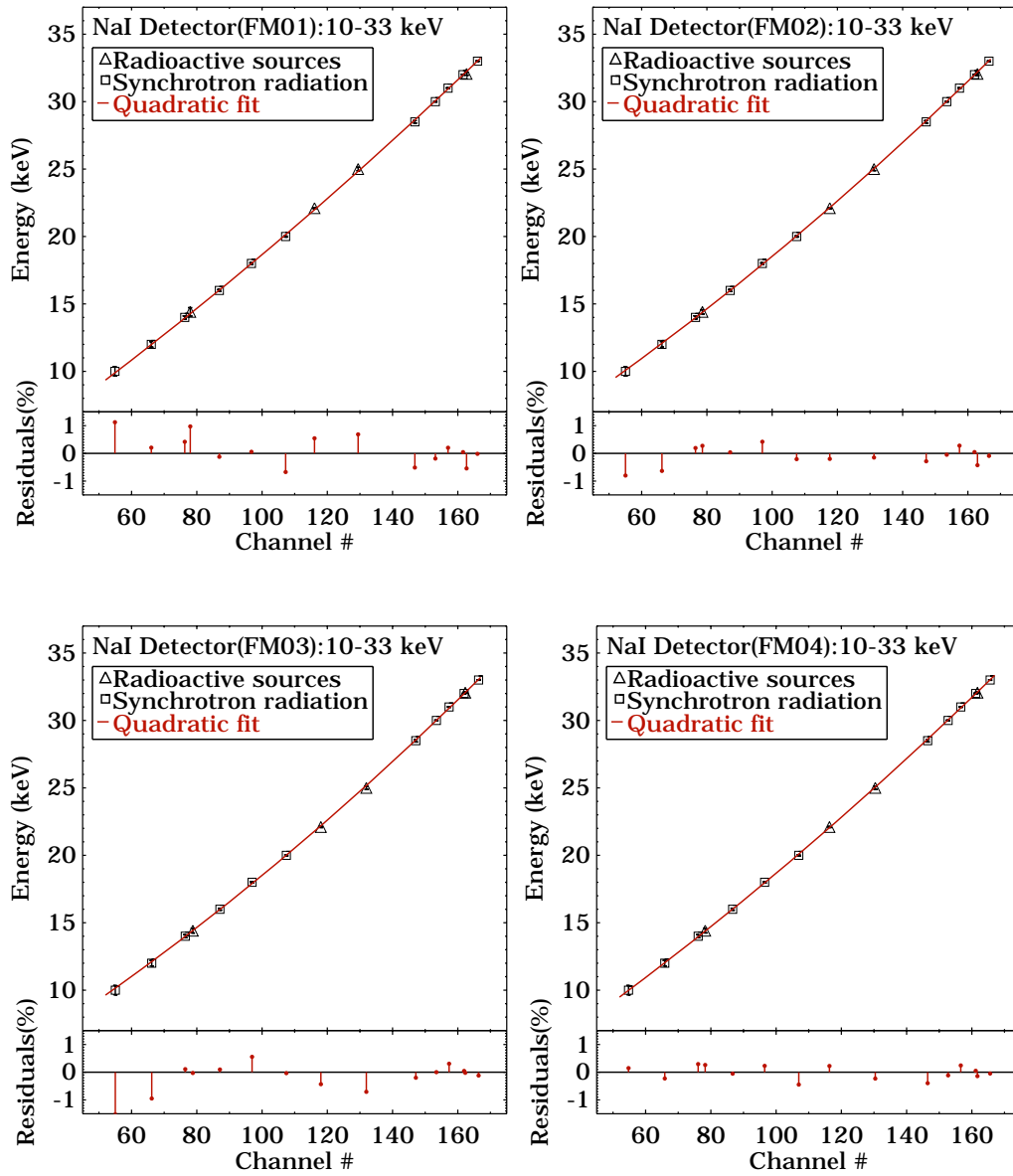


**Figure 3.14:** CE relation calculated below the K-edge energy for the NaI detectors FM01–FM04. MPE data points (*triangles*) and PTB/BESSY data points (*squares*) are fitted together with a second degree polynomial. Residuals to the fits are given in the panel under the plot. Fit parameters are listed in Table 3.11

### 3. GBM PERFORMANCE

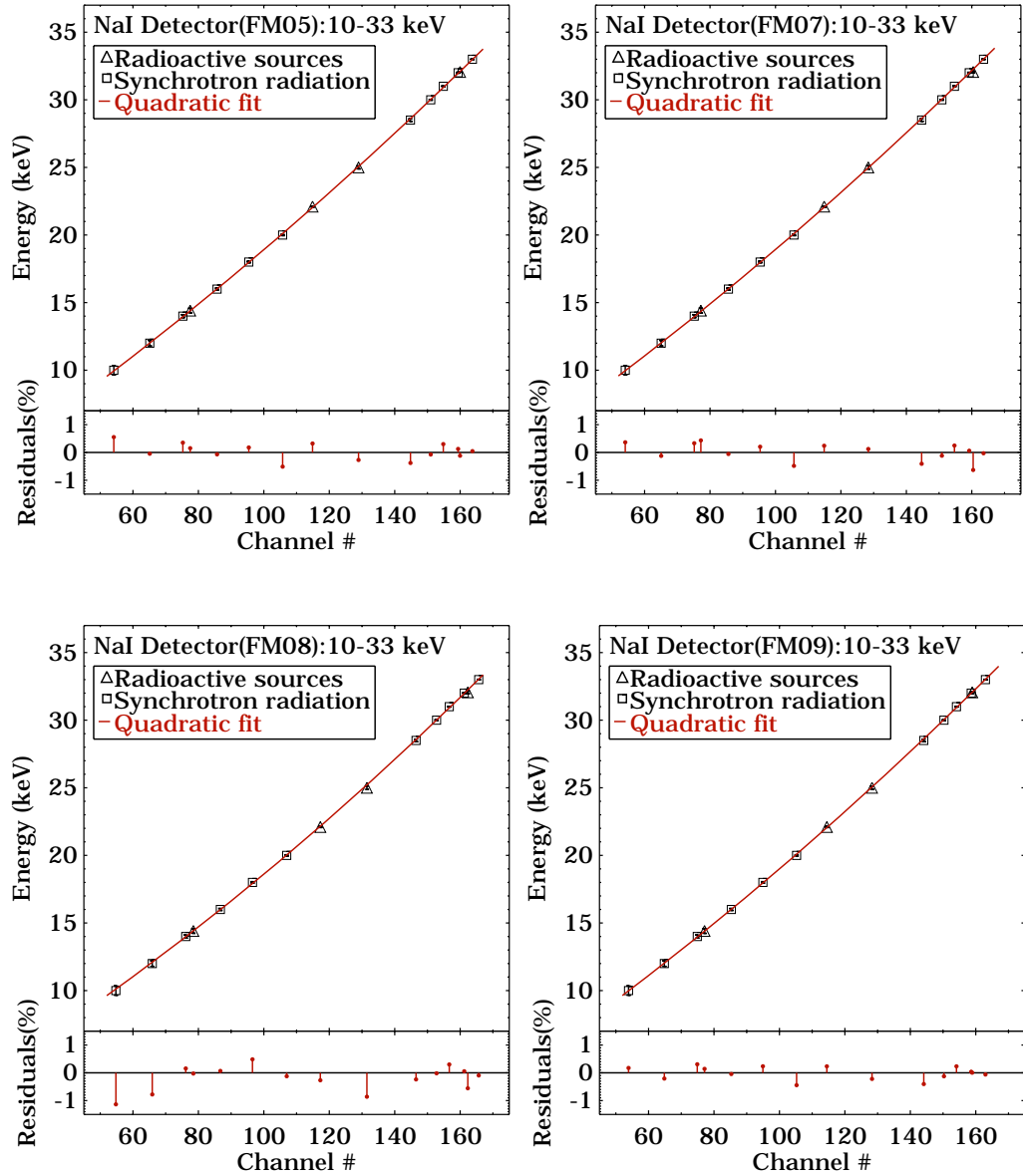


**Figure 3.15:** CE relation calculated below the K-edge energy for the NaI detectors FM05–FM09. Color code same as in Figure 3.14. Fit parameters are listed in Table 3.11

### 3.3.1. Channel-to-Energy (CE) Relation

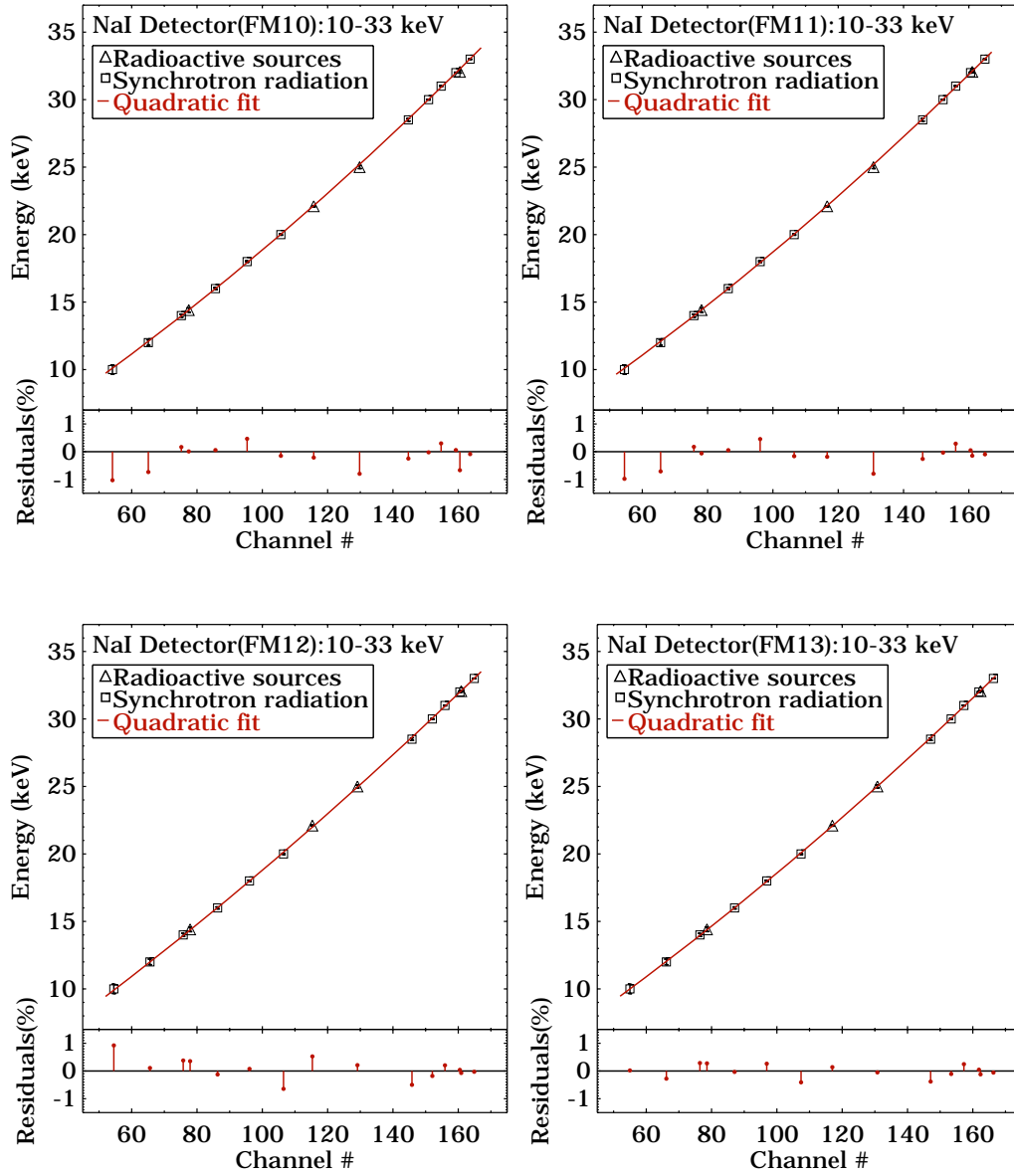


**Figure 3.16:** CE relation calculated below the K-edge energy for the NaI detectors FM10–FM13. Color code same as in Figure 3.14. Fit parameters are listed in Table 3.11

### 3. GBM PERFORMANCE

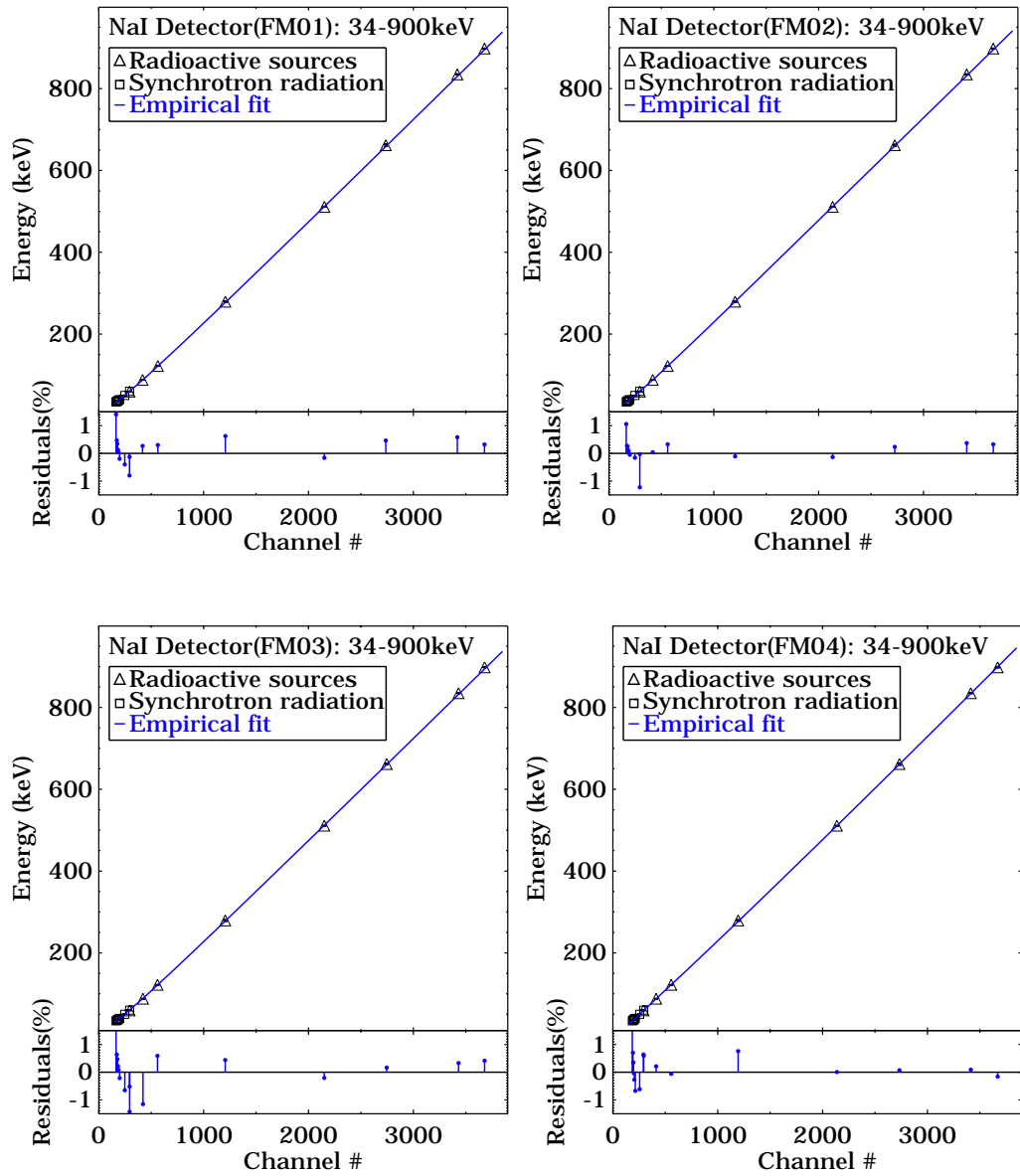


**Figure 3.17:** CE relation calculated above the K-edge energy for the NaI detectors FM01–FM04. MPE data points (*triangles*) and PTB/BESSY data points (*squares*) are fitted together with the empirical function 3.5. Residuals to the fits are given in the panel under the plot. Fit parameters are listed in Table 3.12

### 3.3.1. Channel-to-Energy (CE) Relation

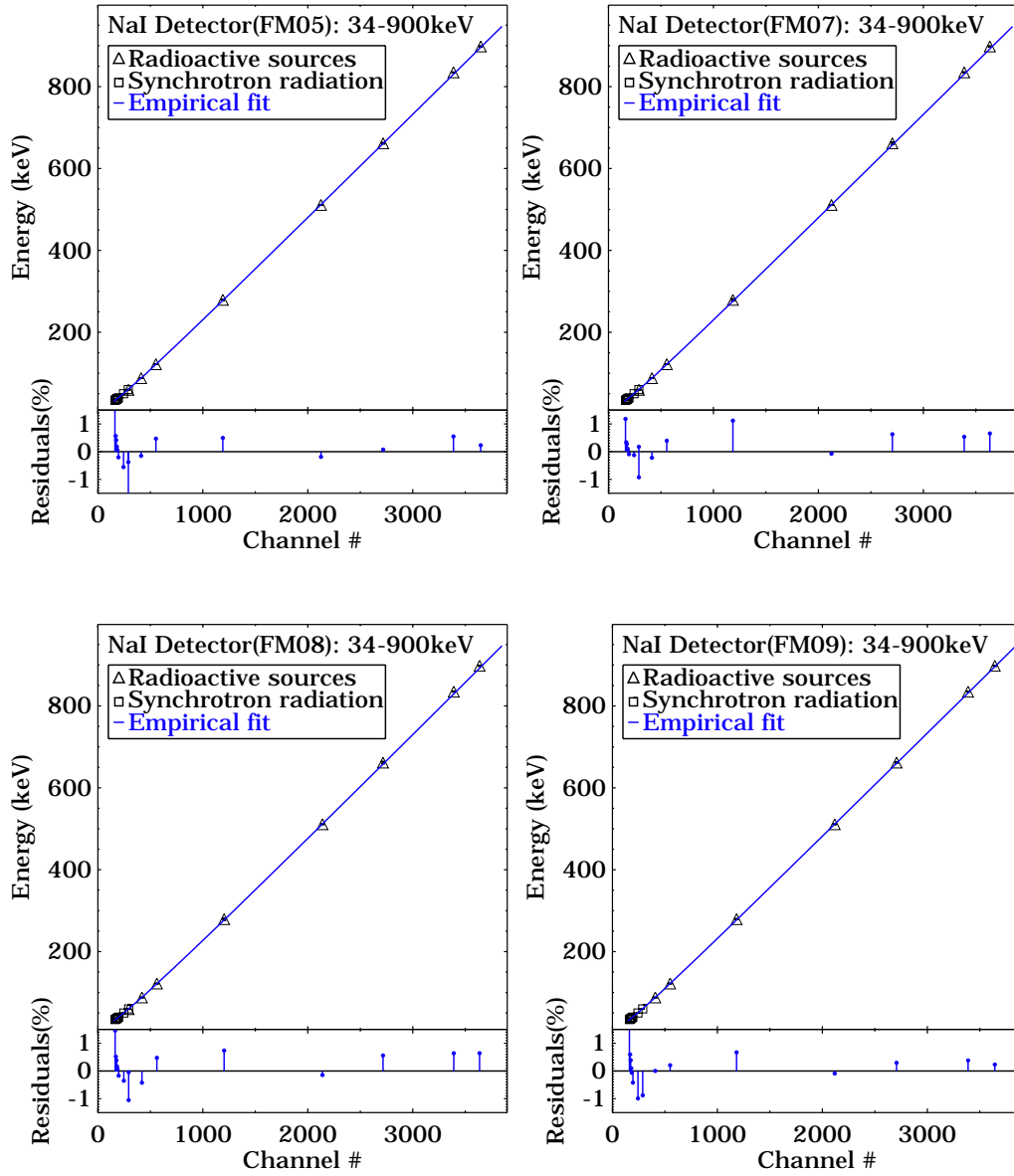


**Figure 3.18:** CE relation calculated above the K-edge energy for the NaI detectors FM05–FM09. Color code same as in Figure 3.17. Fit parameters are listed in Table 3.12

### 3. GBM PERFORMANCE

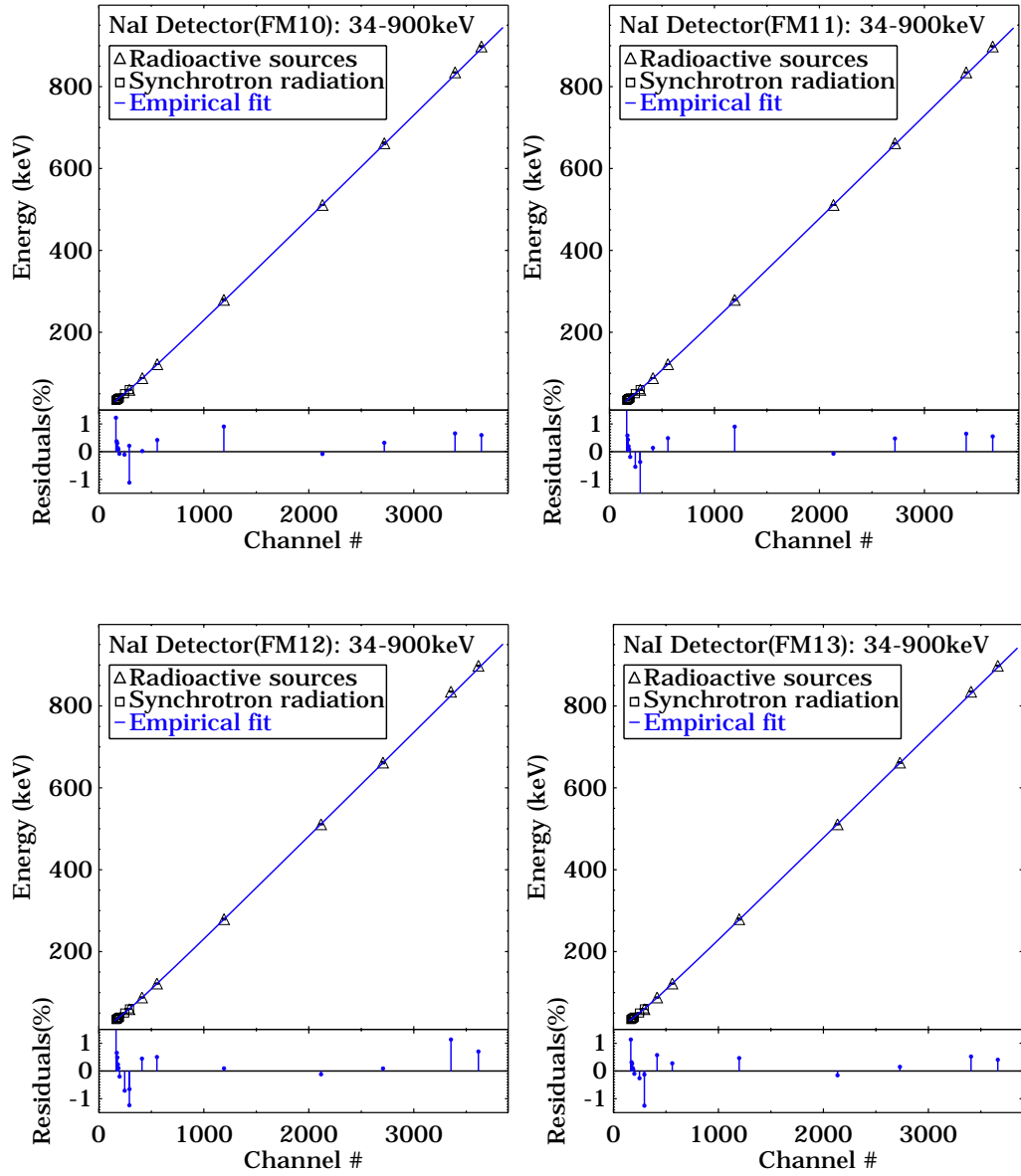


**Figure 3.19:** CE relation calculated above the K-edge energy for the NaI detectors FM10–FM13. Color code same as in Figure 3.17. Fit parameters are listed in Table 3.12

### The Iodine K-edge Region

By taking a closer look to the region around the K-edge energy, the discrepancy between low and high-energy fits becomes clearly visible. Thus, assigning a unique energy to every channel is a more delicate issue. A possible way to solve such an ambiguity is to divide the channels domain into three parts, as shown in Figure 3.20.  $x_e$  and  $x_q$  represent the channels where the empirical and quadratic fit, respectively, assume the value of  $E_K = 33.17$  keV (red and blue diamonds). For all channels in the interval  $x_e < x < x_q$ , a linear relation was calculated in order to assign an average energy to each channel: The green triangles represent the average energies of the two energies calculated with both relations (diamonds and circles). For the analysis of laboratory calibrations, we calculated a K-edge region (region 2) of about five to seven channels for every NaI detector. Results for all 12 NaI FM detectors are shown in Figures 3.21–3.23. On orbit however, due to a much smaller number of channels (128), the flight DPU groups these channels into one “transition” channel (per detector), which is calculated through the LUTs.

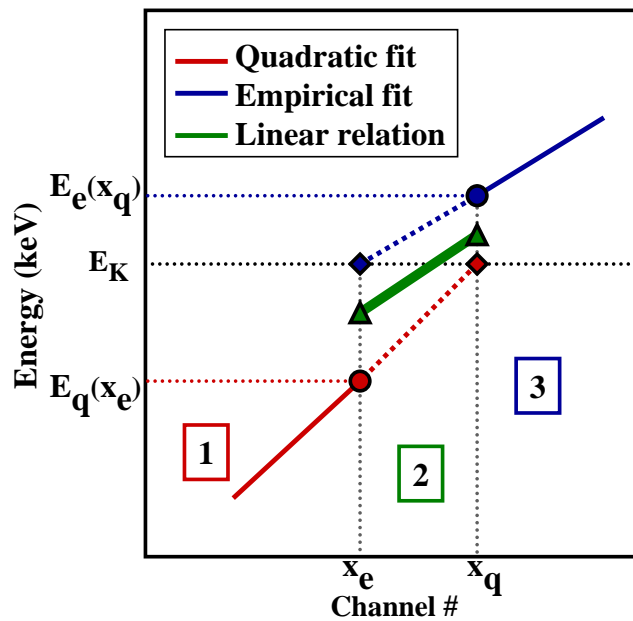


**Figure 3.20:** Schematic representation of the CE relation around the Iodine K-edge energy (see text for details)

### 3. GBM PERFORMANCE

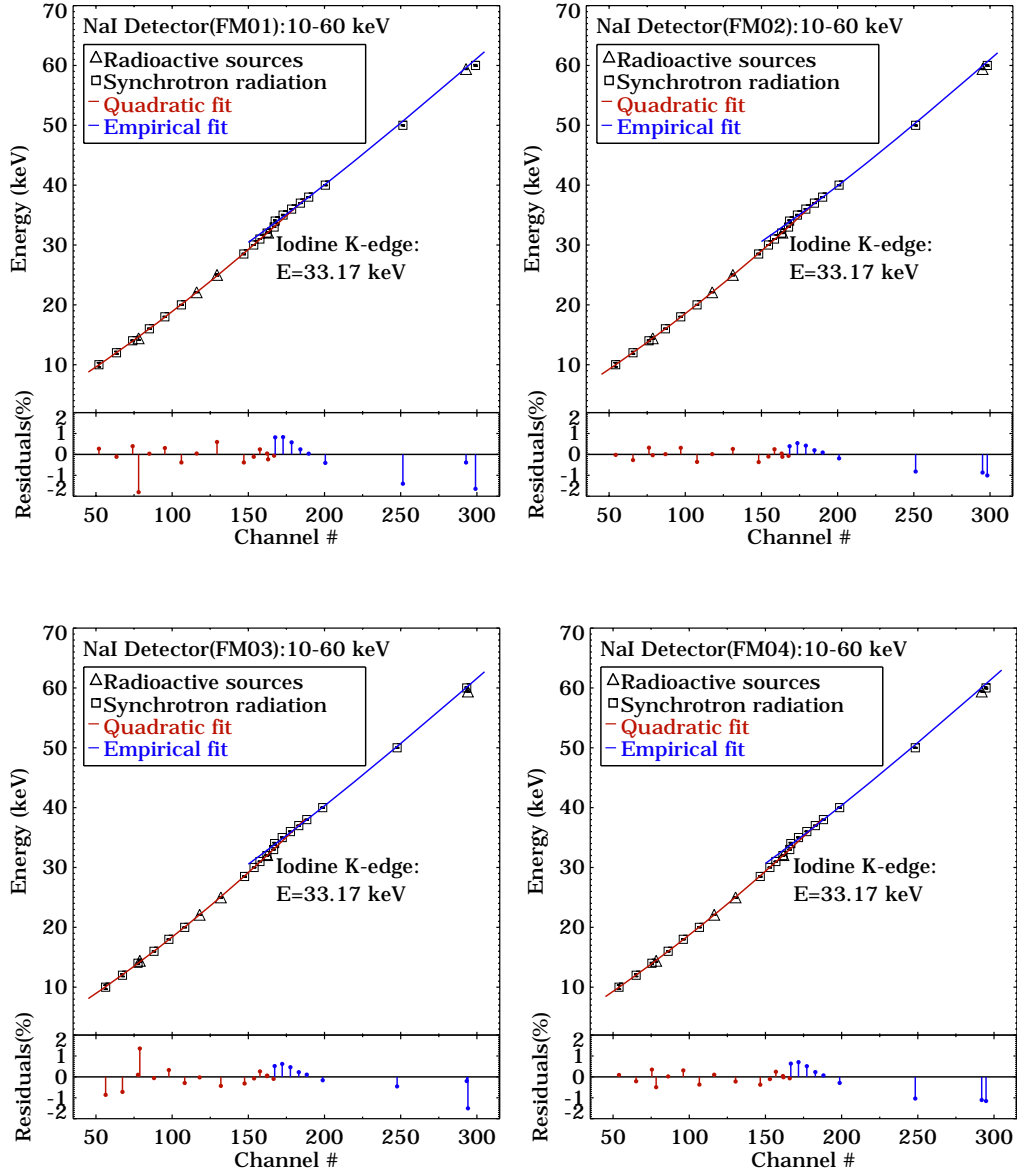


**Figure 3.21:** CE relation around the Iodine K-edge energy for the NaI detectors FM01–FM04. Data points from radioactive source lines (*triangles*) and from synchrotron radiation (*squares*) are fitted together with a quadratic function below the K-edge energy (*red curve*) and with the empirical function above the K-edge energy (*blue curve*). Residuals to the fits are given in the panel under the plot.

### 3.3.1. Channel-to-Energy (CE) Relation

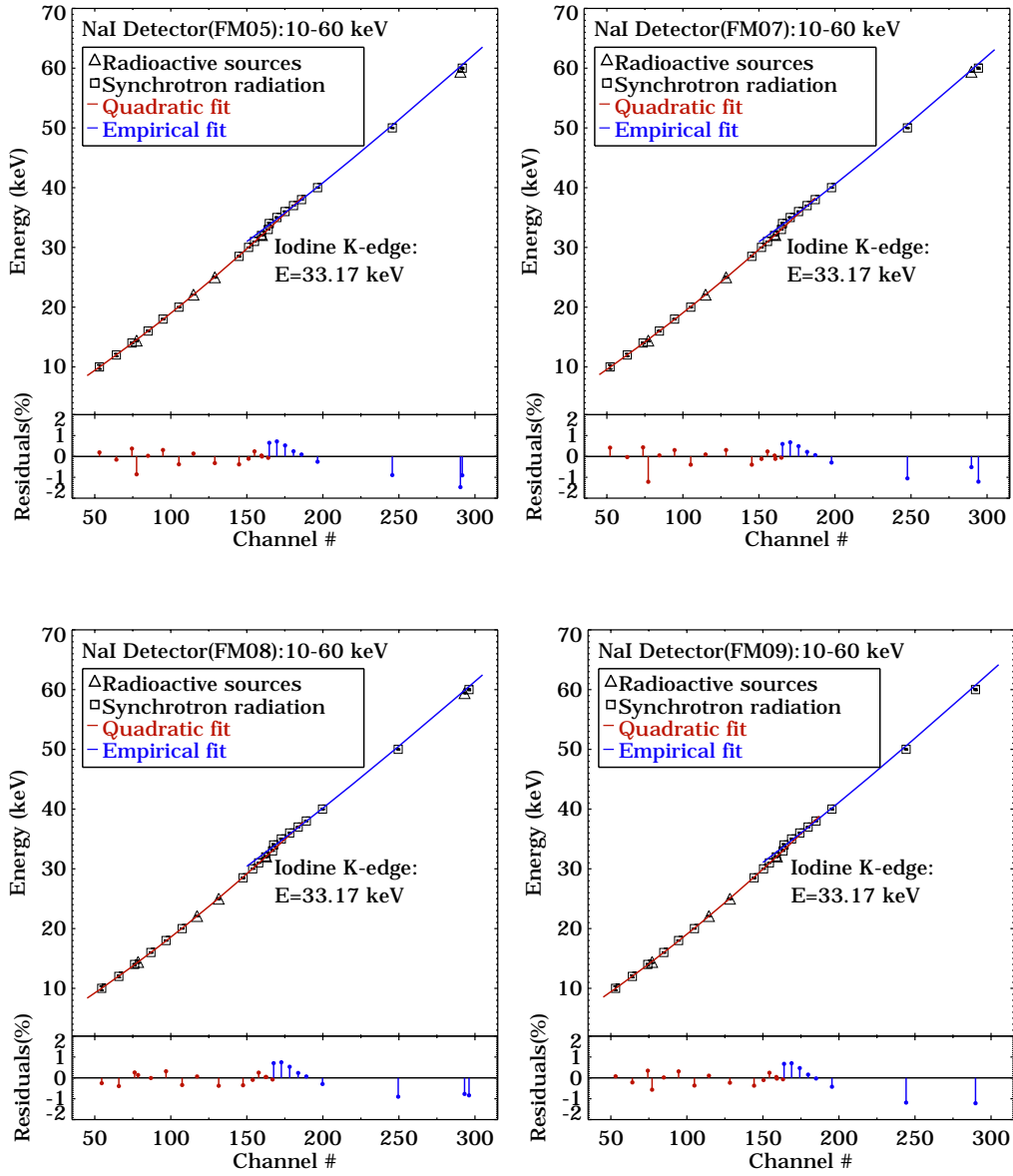


**Figure 3.22:** CE relation around the Iodine K-edge energy for the NaI detectors FM05–FM09. Color code same as in Figure 3.21

### 3. GBM PERFORMANCE

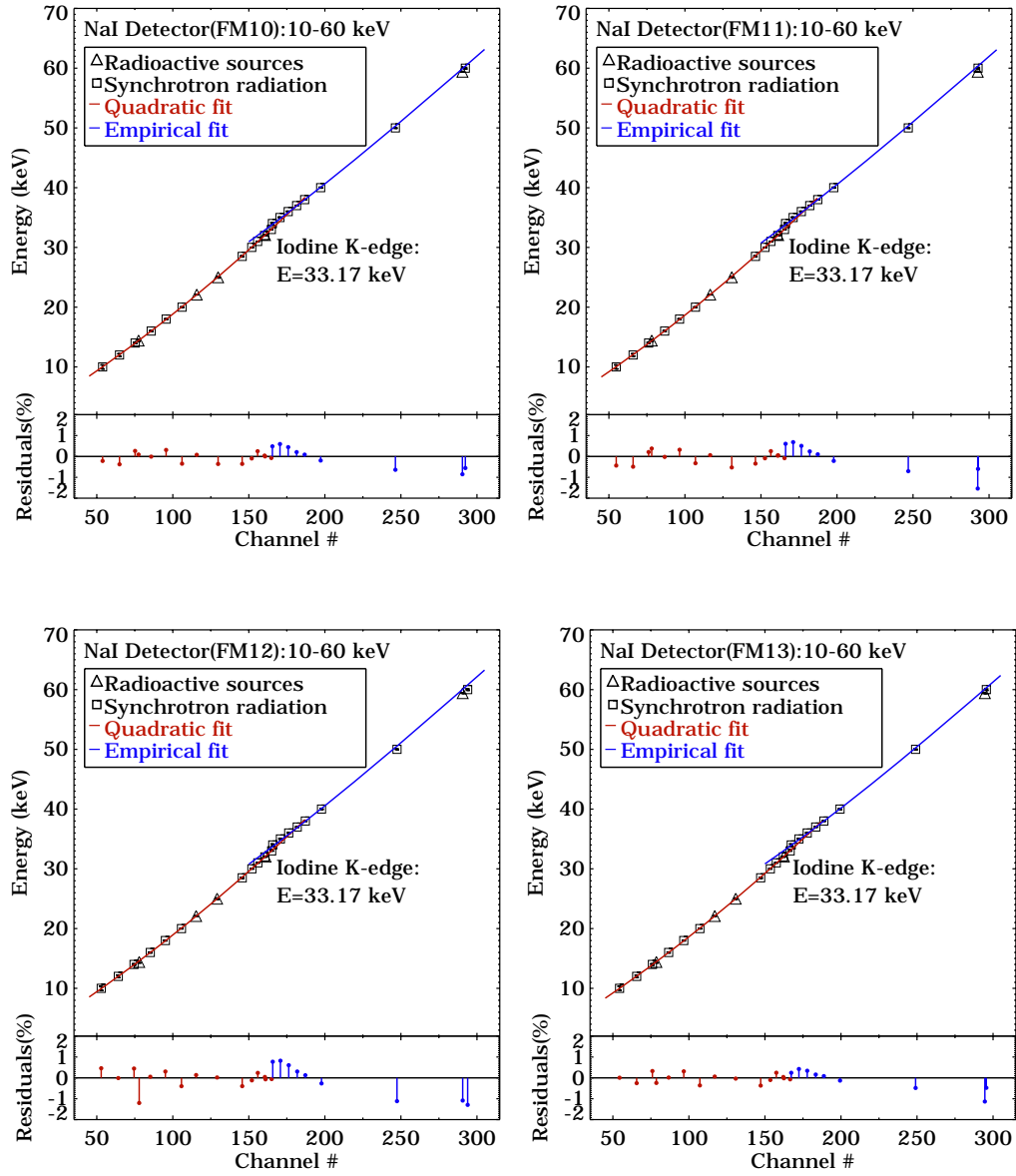


**Figure 3.23:** CE relation around the Iodine K-edge energy for the NaI detectors FM10–FM13. Color code same as in Figure 3.21

#### Simulation Validation

In order to check the accuracy of the obtained CE relation and to validate simulations presented in §3.1.4, radioactive source spectra were compared with simulated data. Figures 3.24 and 3.25 show the 14 previously analysed NaI lines (measured at normal incidence with detector FM12<sup>6</sup>) as a function of energy, that is after applying the CE conversion. Simulated unbroadened and broadened spectra are overplotted as *green* and *red histograms*, respectively. Sample spectra over the full NaI energy range comparing simulation and measurements can be found in (Hoover et al., 2008).

Unbroadened lines represent good guidelines to check the exact position of the full-energy and escape peaks. A good example is the high-energy double peak of <sup>57</sup>Co (Figure 3.24, *panel f*), where simulations confirm the position of both radioactive lines at 122.06 and 136.47 keV, and the presence of the Iodine escape peak around ~90 keV. Still, some discrepancies are evident, e.g. at lower energies. One likely cause of the discrepancies below 60 keV, mostly resulting in a higher number of counts of the simulated data compared to the real data, and which is particularly visible for the <sup>57</sup>Co line at 14.41 keV (Figure 3.24, *panel a*), is the uncertainty about the detailed composition of the radioactive source. Indeed, radioactive isotopes are contained in a small (1 mm) sphere of “salt”. Simulations including this salt sphere were performed and a factor of 3.8 difference in the perceived 14.41 keV line strength was found. The true answer lies somewhere between this and the simulation with no source material, as salt and radioactive isotope are mixed. For the general calibration simulation, a pointsphere of radioactive material not surrounded by salt had been used. Another possible explanation could probably be the leakage of secondary electrons from the surface of the detector leading to a less-absorbed energy. Further discrepancies at higher energies, which are visible in *panels d* and *e* of Figure 3.25, are smaller than 1 %.

#### BGO Response

The determination of a CE relation for the BGO detectors required the additional analysis of the high-energy data taken with the EQM module at SLAC to cover the energy domain between 5 MeV and 20 MeV. In order to combine the radioactive source measurements made with the BGO FMs at MPE and the proton beam induced radiation measurements made with the BGO EQM at SLAC (see §3.1.3),

---

<sup>6</sup>In this case, simulations were not based on measurements performed with detector FM04, because at that time detector FM12 was the first to have a complete set of collected spectra.

### 3. GBM PERFORMANCE

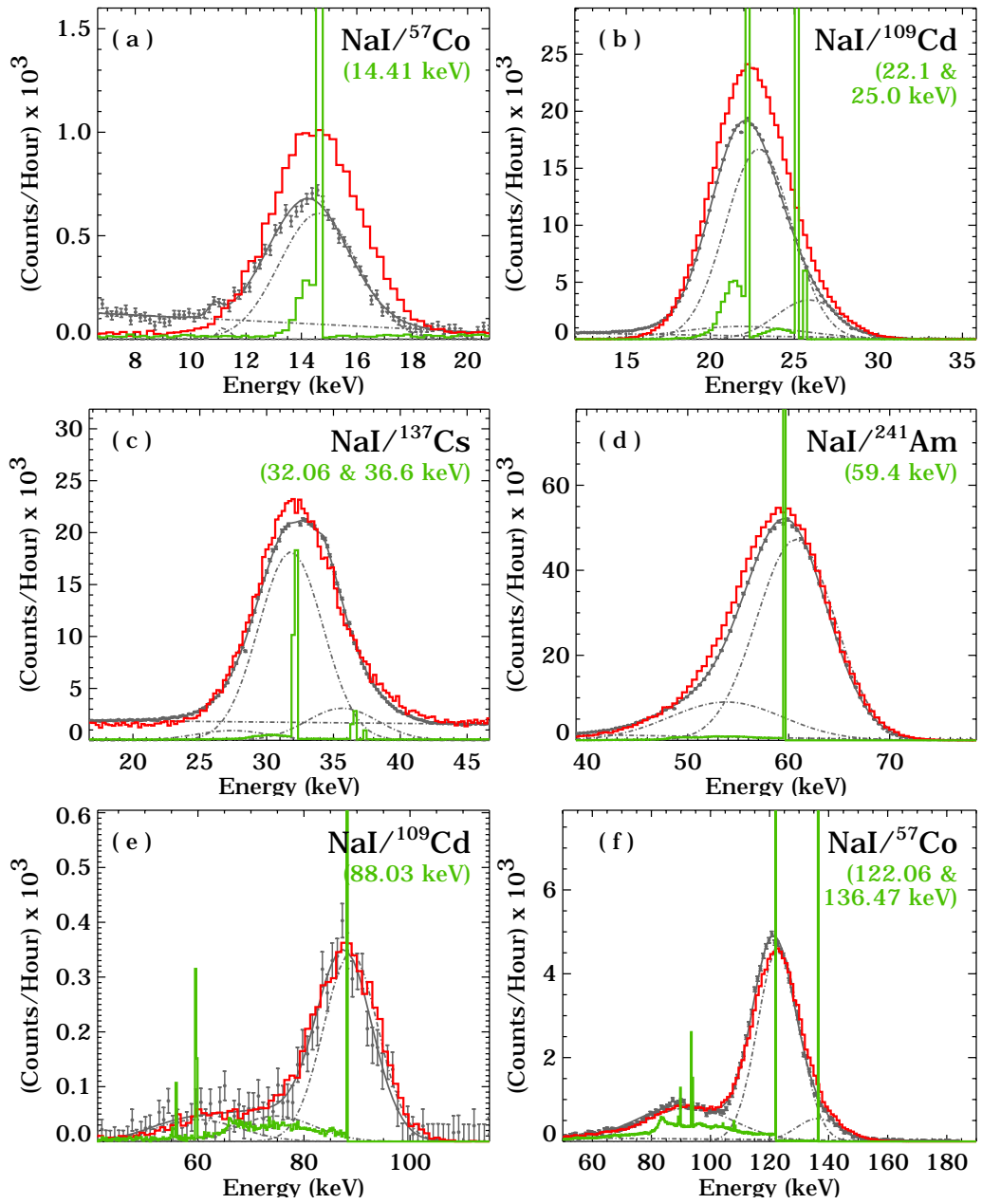


**Figure 3.24:** Comparison between real spectra collected with NaI FM12, after CE conversion, and simulated spectra for six radioactive source lines. Here, line fits and various components, previously described in Figures 3.9 and 3.10, are shown as *solid* and *dashed grey curves*, respectively. Simulated broadened spectra are overplotted in *red*. Unbrodened spectra (*green histograms*) can be considered as guidelines for the exact energy positions of lines and secondary escape peaks (see text). The height of the unbrodened peaks is truncated in most plots to better show the comparison between real and broadened spectra

### 3.3.1. Channel-to-Energy (CE) Relation

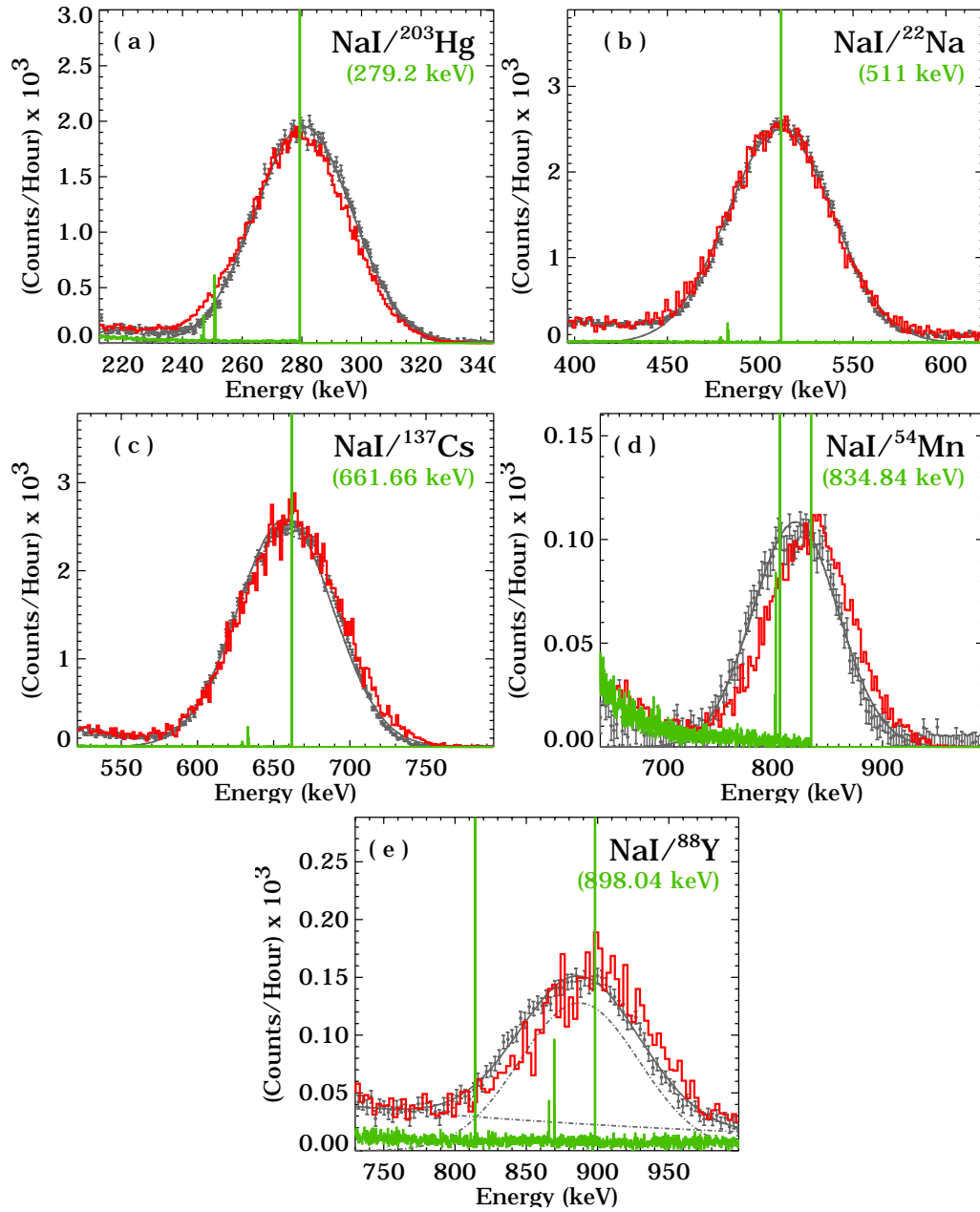


**Figure 3.25:** Comparison between spectra collected with NaI FM12, after CE conversion, and simulated spectra for five radioactive source lines. Color code same as in Figure 3.24

### 3. GBM PERFORMANCE

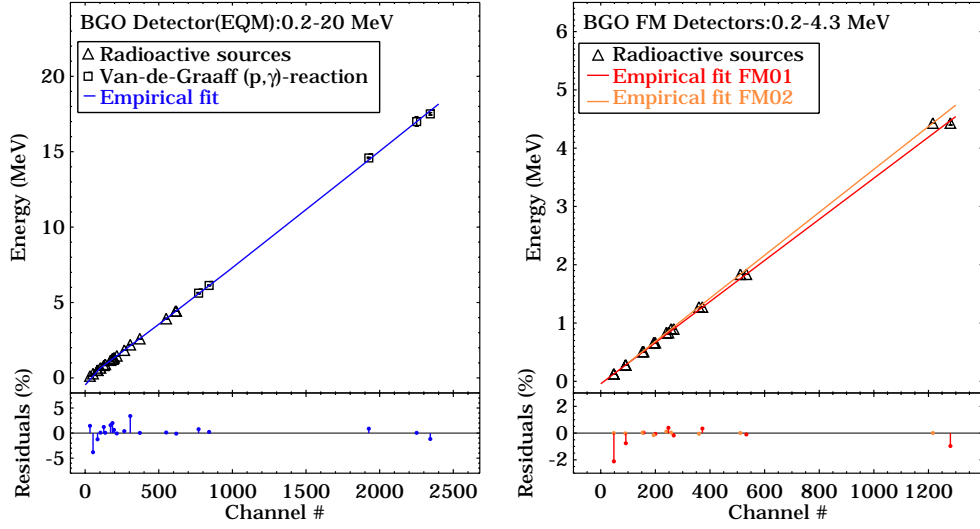


**Figure 3.26:** BGO CE relation and corresponding residuals calculated for EQM detector applying the empirical fit (*blue curve*) of Equation 3.5 over the full energy domain between 0.2 and 20 MeV. Data taken at MPE and at SLAC are marked with *triangles* and *squares*, respectively. Fit parameters for this fit are  $a = -428 \pm 23$ ,  $b = -54 \pm 3$ ,  $c = 8.29 \pm 0.06$  and  $d = 167 \pm 11$ , with a reduced  $\chi^2$  of 7

it was necessary to take into account the different gain settings by application of a scaling factor. The scaling factor was derived by comparing  $^{22}\text{Na}$  and Am/Be measurements (at 511, 1274, and 4430 keV) which were performed at both sites. Due to the very low statistics in the measurements from the high-energy reaction of the Van de Graaff beam on the LiF target (Equation 3.2), first and second electron escape peaks from pair annihilation of the 14.6 MeV line could not be considered in this analysis (see also Figure 3.12, *panel f*). They were mainly used as background reference points in order to help finding the exact position of the 17.5 MeV line. In this way, a dataset of 23 detected lines was available for determining the BGO EQM CE relation.

For the BGO flight modules analysis (FM01 and FM02), a smaller line sam-

**Table 3.17:** Empirical fit parameters of Equation 3.5 and Chi-square values calculated for each BGO detector

BGO	a	b	c	d	$\chi^2$
EQM	$-418 \pm 26$	$-55 \pm 4$	$8.32 \pm 0.07$	$167 \pm 13$	5
FM01	$30 \pm 30$	$10 \pm 3$	$3.35 \pm 0.05$	$-34 \pm 12$	40
FM02	$-10 \pm 5$	$5.2 \pm 0.7$	$3.614 \pm 0.012$	$-19.2 \pm 2.4$	4

### 3.3.2. Energy Resolution

**Table 3.18:** CE relation for BGO detectors EQM (*left table*), FM01 and FM02 (*right tables*). Fitted energies and residuals in the case of an empirical fit. The corresponding fit parameters are given in Table 3.17

BGO	Tabulated line energy (keV)	Line Center			BGO	Tabulated line energy (keV)	Line Center			
		Measured (channels)	Fitted (keV)	Res. (%)			Measured (channels)	Fitted (keV)	Res. (%)	
EQM	124.54	32.8 ± 0.3	122.8	1.4	FM01	124.54	48.1 ± 1.0	127.2	-2.1	
	279.2	53.6 ± 0.6	290	-4		279.2	91.76 ± 0.23	281.3	-0.8	
	511	84.1 ± 0.7	517.4	-1.3		511	156.84 ± 0.07	510.83	0.03	
	661.66	103.9 ± 0.9	661.11	0.08		661.66	199.73 ± 0.07	662.06	-0.06	
	834.84	126.6 ± 1.1	824.7	1.2		834.84	247.78 ± 0.11	831.6	0.4	
	898.04	136.7 ± 1.3	897.45	0.07		898.04	267.09 ± 0.06	899.63	-0.18	
	1173.23	172.5 ± 1.8	1154.7	1.6		1274.54	372.17 ± 0.11	1270.2	0.3	
	1274.54	185.6 ± 2.0	1249.0	2.0		1836.06	533.14 ± 0.11	1837.92	-0.10	
	1332.49	196.0 ± 0.4	1324.0	0.6		4430	1280 ± 10	4472.84	-1.0	
	1460	214.97 ± 0.12	1461.12	-0.08						
	1836.06	265.8 ± 0.8	1829.0	0.4						
	2199	306.3 ± 1.5	2124	3		FM02	124.54	47.68 ± 0.04	124.588	0.002
	2600	371.2 ± 0.3	2599.10	0.04			279.2	90.13 ± 0.19	279.265	-0.023
	3929	550.3 ± 2.6	3924.43	0.12			511	152.87 ± 0.06	510.82	0.03
	4430	618.6 ± 0.4	4434.89	-0.11			661.66	193.90 ± 0.08	662.66	-0.15
	5619	770 ± 5	5575.3	0.8			834.84	240.15 ± 0.12	833.88	0.12
	6130	841.9 ± 1.8	6115.79	0.23			898.04	257.40 ± 0.06	897.73	0.03
	14586	1926 ± 5	14458.0	0.9			1274.54	359.42 ± 0.10	1275.18	-0.05
	17000	2251 ± 40	16992.31	0.05			1836.06	511.19 ± 0.12	1835.920	0.008
17510	2344 ± 11	17716.3	-1.2	4430	1215.9 ± 0.6		4429.814	0.004		

ple between 125 keV and 4.4 MeV was available, still leading to similar results. Differences are due to different gains, caused by the setup constraints, which are described in more detail in §3.3.2. Similarly to the NaI analysis, BGO datasets were fitted with an empirical function (Equation 3.5). Figure 3.26 shows the BGO CE relation for all detectors. Fit parameters are given in Table 3.17, while fitted energies and residuals are listed in Table 3.18. In this case, EQM and FM fit residuals are smaller than 4% and 2%, respectively.

### 3.3.2 Energy Resolution

The energy resolution  $R$  of a detector is conventionally defined as the full width at half maximum ( $w$ ) of the differential pulse height distribution divided by the location of the peak centroid  $H_0$  (Knoll, 1989). This quantity mainly reflects the statistical fluctuations recorded from pulse to pulse. In the case of an approximately linear response, the average pulse amplitude is given by  $H_0 = K N$ , where  $K$  is a proportionality constant, and the limiting resolution of a detector can be calculated as

$$R \equiv \frac{w}{H_0} = \frac{2.35 K \sqrt{N}}{K N} = \frac{2.35}{\sqrt{N}} \quad (3.7)$$

### 3. GBM PERFORMANCE

---

where  $N$  represents the average number of charge carriers (in our case, it represents the number of photoelectrons emitted from the PMT photocathode), and the standard deviation of the peak in the pulse height spectrum is given by  $\sigma = K \sqrt{N}$ .

However, in real detectors the resolution is not only determined by photoelectron statistics, but can be affected by other effects, such as

1. local fluctuations in the scintillation efficiency;
2. nonuniform light collection;
3. variance of the photoelectron collection over the photocathode;
4. contribution from the nonlinearity of the NaI scintillation response;
5. contributions from PMT gain drifts;
6. temperature drift (see e.g. Knoll, 1989).

In order to take all these effects into account, a nonlinear dependence of the energy resolution was assumed:

$$w = \sqrt{a^2 + b^2 E + c^2 E^2} \quad (3.8)$$

This formula is mainly based on traditional physical understanding of scintillation detectors and produces a physically motivated behavior outside the range of measurements. It consists of

1. a constant term,  $a$ , which describes limiting electronic resolution (typically not a noticeable effect in scintillators);
2. a term proportional to the square root of the energy, explaining statistical fluctuations in the numbers of scintillation photons and photo electrons; and
3. a term proportional to the energy, which accounts for the non-ideal “transfer efficiency” of transporting scintillation photons from their creation sites to the PMT photocathode.

For the actual fits the first parameter  $a$  was set to zero, since no significant electronic broadening was observed. Spatial non-uniformity of the energy resolution will be discussed in §3.3.4.

In order to fit the energy resolution, it was necessary to convert the measured widths (in channels) to energies in keV by applying to each detector the corresponding CE relation previously obtained. Fit results for all NaI detectors are listed in Tables 3.19 and 3.20 and are shown in Figures 3.29 and 3.30, while the results for the three BGO detectors (EQM, FM01 and FM02) are displayed in Figure 3.27. In the case of NaI detectors, it was noticed that similar results could also be obtained by excluding those calibration lines which are affected by greater uncertainties of  $w$ , namely the 14.4 keV line from  $^{57}\text{Co}$  and all secondary lines,

i.e. the 25 keV line from  $^{109}\text{Cd}$ , the 36.6 keV from  $^{137}\text{Cs}$  and the 136.6 keV line from  $^{57}\text{Co}$ . As regards the BGO energy resolution, EQM results (see Figure 3.27, *blue triangles*) show poorer energy resolution compared to FM01 (*red squares*) and FM02 (*yellow dots*), which could be explained by minor differences in the detector design (optical coupling). Finally, a common plot of all NaI and BGO flight module detectors is shown in Figure 3.28.

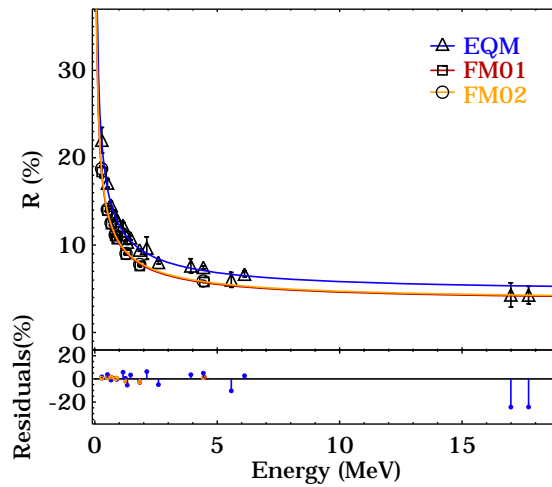


**Figure 3.27:** Energy resolution  $R$  in percentage calculated for all BGO detectors. Residuals showing the relative deviation of  $R$  are given in the panel under the plot. The energy resolution at 1 MeV is about  $10\% \pm 0.5\%$

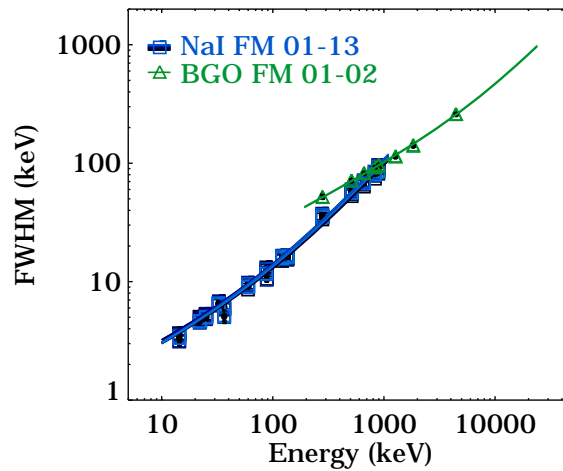


**Figure 3.28:** FWHM (in keV) as a function of Energy for the 12 NaI FM detectors (*blue squares*) and for the two BGO FM detectors (*green triangles*). For both detector types, the standard fit to Equation 3.8 is plotted

### 3. GBM PERFORMANCE

**Table 3.19:** Measured and fitted FWHM values with fit residuals for 14 lines from radioactive sources collected with NaI detectors FM01–FM07

FM	Tabulated line energy (keV)	Line FWHM			Res. (%)	FM	Tabulated line energy (keV)	Line FWHM			Res. (%)
		Measured (channels)	Fitted (keV)	(%)				Measured (channels)	Fitted (keV)	(%)	
<b>01</b>	14.4	19.3 ± 2.3	3.6	27	-9	<b>02</b>	14.4	19.3 ± 1.4	3.6	26	-4
	22.1	24.1 ± 0.6	4.9	22	-1.0		22.1	22.8 ± 0.6	4.7	22	-2.1
	25	24.4 ± 1.4	5.1	21	-4		25	23.8 ± 1.4	5.1	21	-2.2
	32.06	27.3 ± 0.6	6.3	19	1.7		32.06	26.1 ± 0.6	6.3	19	4
	36.6	30.3 ± 2.1	6.2	19	-8.8		36.6	28.4 ± 2.0	5.8	18	-11
	59.4	43.7 ± 0.5	9.5	15	1.3		59.4	40.9 ± 0.6	9.0	15	-1.2
	88.03	54.4 ± 1.4	12	14	0.4		88.03	51.0 ± 1.5	12	14	-1.0
	122.06	66.9 ± 0.6	16	13	-1.3		122.06	64.1 ± 0.5	15	13	0.0
	136.6	68.5 ± 2.3	17	13	-7		136.6	65.3 ± 2.2	17	12	-6
	279.2	145 ± 4	32	12	10		279.2	140 ± 3	31	11	12
	511	230.1 ± 2.8	55	11	4		511	219.3 ± 2.7	53	10	3
	661.66	275 ± 5	70	11	-1.7		661.66	264 ± 5	67	10	-1.5
	834.84	328 ± 7	87	10	-6		834.84	315 ± 7	83	10	-6
	898.04	368 ± 7	94	10	-1.4		898.04	343 ± 7	89	10	-4
<b>03</b>	14.4	17.7 ± 1.5	3.4	25	-7	<b>04</b>	14.4	18.8 ± 1.3	3.6	26	-4
	22.1	21.9 ± 0.5	4.6	21	-0.2		22.1	21.7 ± 0.5	4.5	22	-5
	25	22.7 ± 1.3	5.0	20	-1.0		25	22.5 ± 1.3	4.9	20	-6
	32.06	24.9 ± 0.5	6.1	18	5		32.06	25.9 ± 0.5	6.2	19	4
	36.6	27.8 ± 1.5	5.9	17	-8		36.6	28.6 ± 1.7	6.1	18	-7
	59.4	39.3 ± 0.6	8.6	15	-2.7		59.4	41.2 ± 0.6	9.2	15	-0.4
	88.03	45.6 ± 1.5	12	13	-12		88.03	56.4 ± 1.6	12	14	8
	122.06	62.6 ± 0.5	15	12	-0.5		122.06	65.5 ± 0.5	16	13	-0.1
	136.6	63.7 ± 2.2	16	12	-7		136.6	66.9 ± 2.2	17	13	-6
	279.2	135.7 ± 1.9	30	11	11		279.2	144 ± 6	32	11	11
	511	212.5 ± 2.6	51	10	3		511	228.4 ± 2.6	55	11	3
	661.66	256 ± 5	65	10	-1.5		661.66	275 ± 9	70	11	-2.5
	834.84	299 ± 6	81	10	-8		834.84	331 ± 6	87	11	-6
	898.04	330 ± 6	87	10	-5		898.04	368 ± 10	94	10	-2.2
<b>05</b>	14.4	16.2 ± 1.5	3.1	25	-18	<b>07</b>	14.4	18.6 ± 1.5	3.6	27	-10
	22.1	21.7 ± 0.5	4.6	21	-2.9		22.1	23.4 ± 0.6	4.9	22	-2.0
	25	22.5 ± 1.3	4.9	20	-4		25	24.3 ± 1.4	5.2	21	-2.8
	32.06	25.9 ± 0.6	6.3	19	5		32.06	26.1 ± 0.5	6.3	19	0.2
	36.6	28.1 ± 1.7	5.9	18	-9		36.6	27.7 ± 2.0	5.9	19	-15
	59.4	40.8 ± 0.6	9.1	15	-0.7		59.4	44.0 ± 0.5	9.7	16	2.7
	88.03	49.4 ± 2.1	12	14	-5		88.03	55.1 ± 1.3	13	14	2.3
	122.06	65.4 ± 0.5	16	13	0.5		122.06	66.3 ± 0.5	16	13	-1.2
	136.6	64.6 ± 2.3	17	13	-9		136.6	66.3 ± 2.3	18	13	-10
	279.2	143 ± 6	31	11	12		279.2	145 ± 6	32	12	11
	511	227.6 ± 2.6	55	11	4		511	229.2 ± 2.3	56	11	2.9
	661.66	274 ± 8	70	11	-1.3		661.66	279 ± 9	71	11	-0.8
	834.84	328 ± 5	87	10	-5		834.84	332 ± 6	88	11	-5
	898.04	364 ± 10	93	10	-1.6		898.04	361 ± 10	94	11	-4

### 3.3.2. Energy Resolution

**Table 3.20:** Measured and fitted FWHM values with fit residuals for 14 lines from radioactive sources collected with NaI detectors FM08–FM13

FM	Tabulated line energy (keV)	Line FWHM			
		Measured (channels)	Fitted (keV)	(%)	Res. (%)
<b>08</b>	14.4	19.0 ± 1.8	3.6	27	-9
	22.1	23.0 ± 0.5	4.8	23	-5
	25	24.3 ± 1.3	5.2	22	-4
	32.06	27.7 ± 0.6	6.6	20	4
	36.6	29.3 ± 1.6	6.1	19	-12
	59.4	45.2 ± 0.5	10	16	1.8
	88.03	51.3 ± 2.0	13	15	-10
	122.06	69.8 ± 0.6	17	14	-0.3
	136.6	70.0 ± 2.4	18	13	-8
	279.2	151 ± 8	33	12	11
	511	240.1 ± 2.5	58	11	4
	661.66	285 ± 8	73	11	-1.5
	834.84	335 ± 5	92	11	-7
	898.04	382 ± 11	98	11	-0.5
<b>10</b>	14.4	18.3 ± 1.4	3.5	26	-5
	22.1	21.8 ± 0.5	4.6	21	-3
	25	23.1 ± 1.3	5.0	20	-1.8
	32.06	25.6 ± 0.6	6.3	19	4
	36.6	27.8 ± 1.7	5.9	18	-10
	59.4	42.2 ± 0.5	9.3	15	1.5
	88.03	44.5 ± 1.8	12	14	-18
	122.06	65.6 ± 0.6	16	13	-0.5
	136.6	68.0 ± 2.3	17	13	-5.1
	279.2	143 ± 12	32	11	11
	511	230.0 ± 2.3	56	11	4
	661.66	277 ± 8	71	11	-1.4
	834.84	327 ± 6	88	11	-7
	898.04	376 ± 12	94	11	0.5
<b>12</b>	14.4	18.0 ± 1.5	3.4	26	-9
	22.1	22.1 ± 0.5	4.6	22	-4
	25	22.6 ± 1.4	4.9	21	-7
	32.06	26.2 ± 0.6	6.3	19	2.5
	36.6	29.3 ± 2.0	6.2	18	-6
	59.4	43.3 ± 0.5	9.7	16	2.5
	88.03	49.1 ± 1.3	13	14	-9
	122.06	67.6 ± 0.6	16	13	0.2
	136.6	68.2 ± 2.3	18	13	-7
	279.2	147 ± 5	33	12	9
	511	235.9 ± 2.4	58	11	2.5
	661.66	283 ± 9	74	11	-3
	834.84	341 ± 6	92	11	-6
	898.04	377 ± 12	99	11	-3
<b>09</b>	14.4	16.3 ± 1.5	3.2	25	-14
	22.1	21.0 ± 0.5	4.5	21	-5
	25	21.7 ± 1.3	4.8	20	-6
	32.06	25.6 ± 0.5	6.3	18	6
	36.6	29.4 ± 1.7	6.4	18	-0.8
	59.4	–	–	–	–
	88.03	50.6 ± 1.7	12	14	-2.4
	122.06	65.4 ± 0.6	16	13	-0.1
	136.6	63.4 ± 2.3	17	13	-12
	279.2	144 ± 7	32	12	10
	511	231.0 ± 2.6	56	11	3
	661.66	278 ± 7	72	11	-2.3
	834.84	339 ± 6	89	11	-5
	898.04	388 ± 12	96	11	1.9
<b>11</b>	14.4	18.2 ± 1.4	3.5	26	-7
	22.1	21.7 ± 0.5	4.6	22	-4
	25	23.0 ± 1.3	5.0	21	-2.9
	32.06	25.5 ± 0.5	6.2	19	4
	36.6	26.6 ± 1.5	5.7	18	-15
	59.4	41.5 ± 0.5	9.2	15	0.1
	88.03	54.8 ± 1.5	12	14	5
	122.06	64.7 ± 0.5	16	13	-0.7
	136.6	65.7 ± 2.3	17	12	-8
	279.2	142 ± 5	31	11	12
	511	223.0 ± 2.2	54	11	4
	661.66	271 ± 7	68	10	-0.6
	834.84	319 ± 5	85	10	-6
	898.04	341 ± 11	91	10	-6
<b>13</b>	14.4	17.6 ± 1.4	3.3	26	-11
	22.1	21.9 ± 0.5	4.6	21	-4
	25	23.1 ± 1.4	5.0	20	-3
	32.06	25.5 ± 0.5	6.2	19	4
	36.6	27.9 ± 1.5	5.8	18	-12
	59.4	41.1 ± 0.6	9.0	15	-1.2
	88.03	50.3 ± 1.6	12	14	-3
	122.06	65.7 ± 0.6	16	13	0.9
	136.6	66.7 ± 2.3	17	13	-6
	279.2	141 ± 5	31	11	11
	511	226.2 ± 2.8	55	11	4
	661.66	272 ± 8	69	10	-1.9
	834.84	325 ± 6	86	10	-6
	898.04	344 ± 12	93	10	-7

### 3. GBM PERFORMANCE

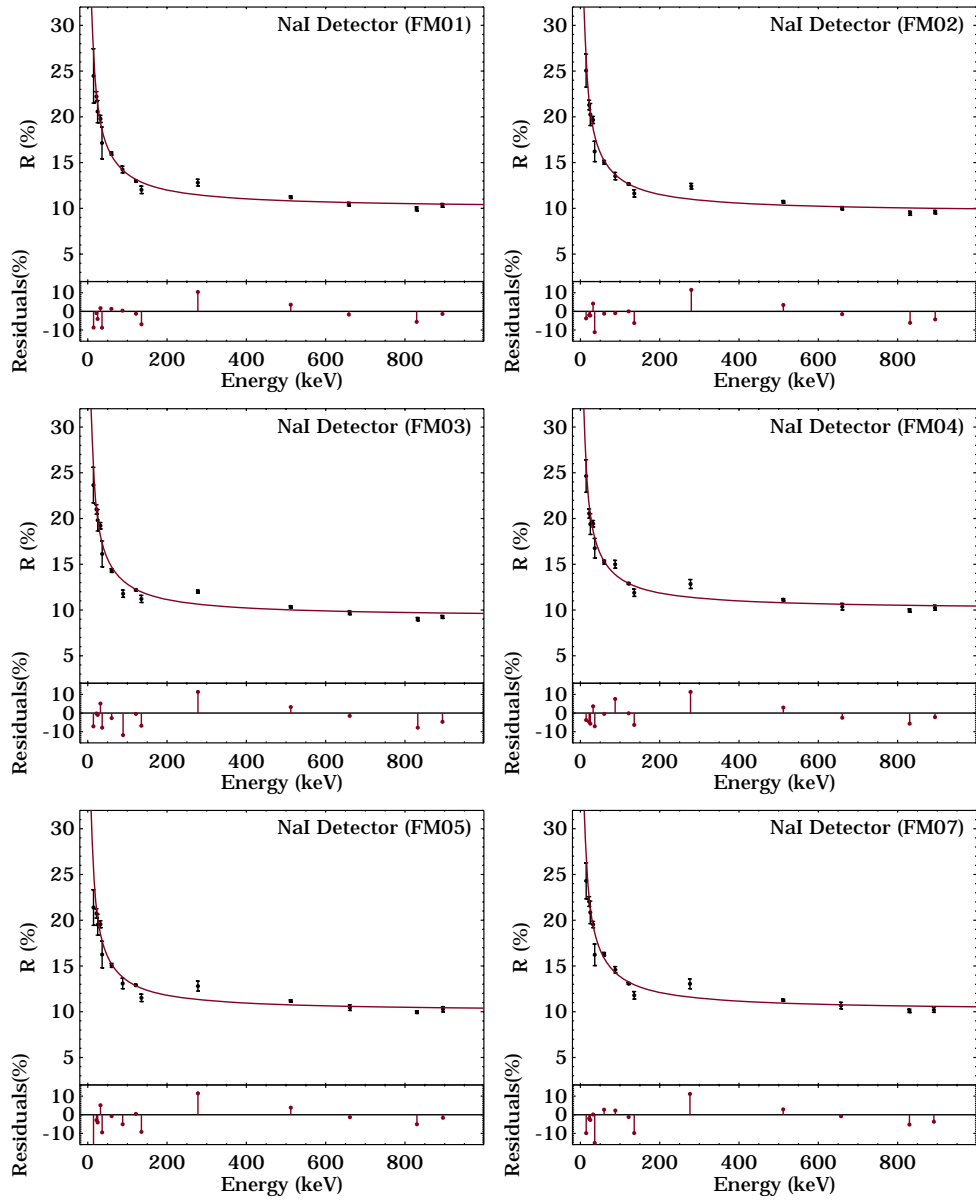


**Figure 3.29:** Energy resolution  $R$  in percentage calculated for NaI detectors FM01–FM07. Residuals are given in the panel under the plot

### 3.3.2. Energy Resolution

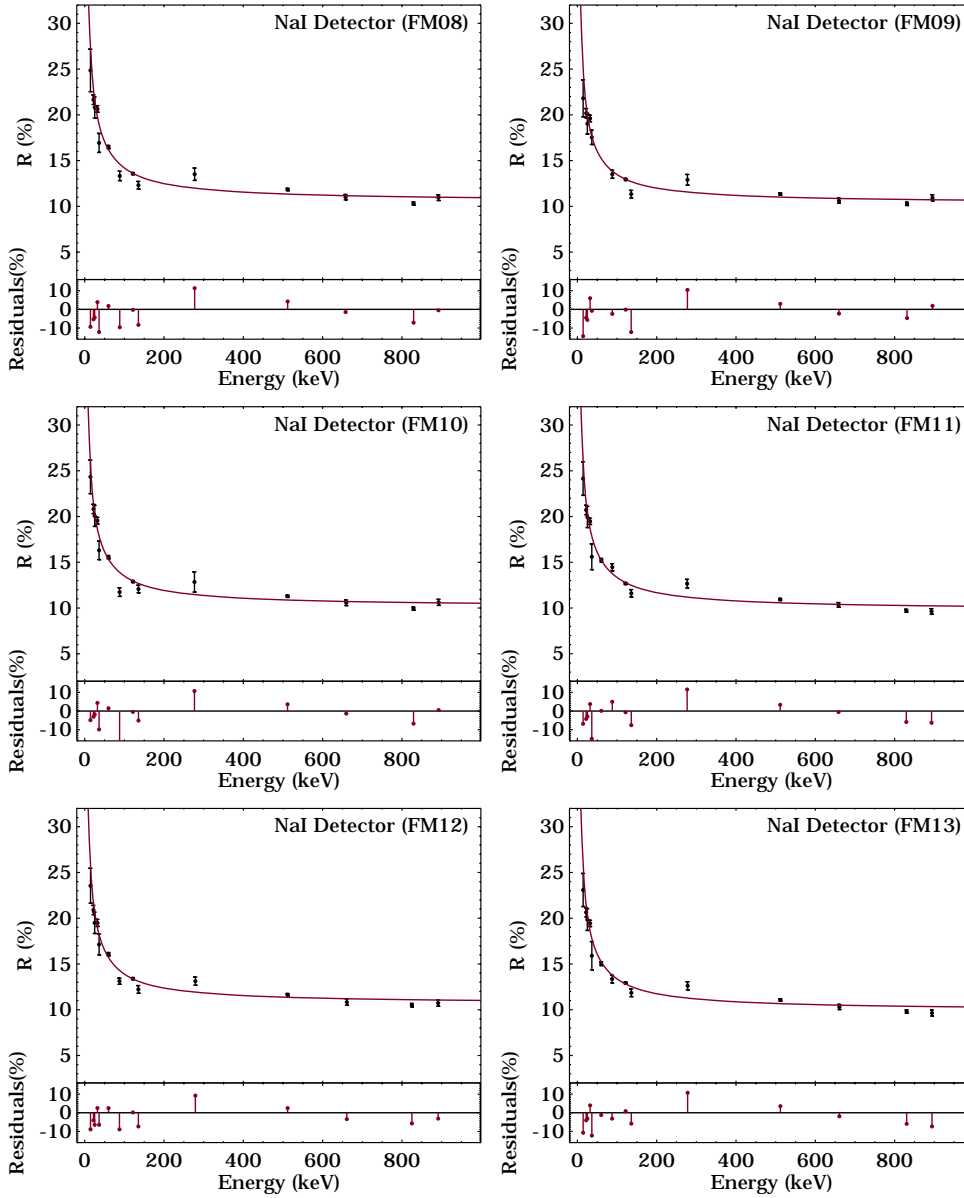


**Figure 3.30:** Energy resolution  $R$  in percentage calculated for NaI detectors FM08–FM13. Residuals are given in the panel under the plot

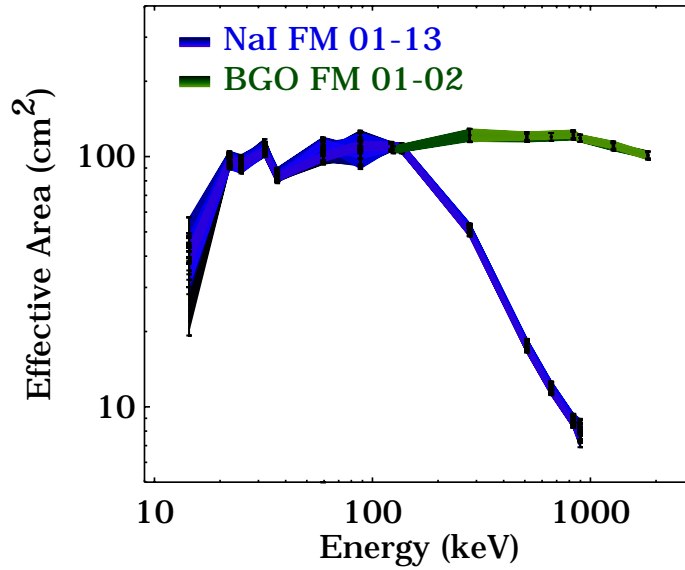


**Figure 3.31:** On-axis effective area of each of the 12 NaI FM detectors and of the two BGO FM detectors

### 3.3.3 Full-Energy Peak Effective Area and Angular Response

The full-energy peak effective area in  $\text{cm}^2$  for both NaI and BGO detectors was computed as:

$$A_{Eff} = \frac{A}{a_c \cdot P_T} \cdot 4\pi d_s^2, \quad (3.9)$$

where  $A$  is the line area (count/s),  $a_c$  is the current source activity (1/s),  $P_T$  is the line transition probability, and  $d_s$  the distance between source and detector (cm). No additional factor to account for flux attenuation between the source and the detector was needed, since its effect above 20 keV is less than 1%. The different line-transition probabilities for each radioactive nuclide which were applied for this analysis can be found in Table 3.1 (column 4). The reference activities were provided in a calibration certificate by the supplier of the radioactive sources<sup>7</sup>. The radioactive source activities at the day of measurement were calculated by taking into account the time elapsed since the calibration reference day. The relative measurement uncertainty of the given activities for all sources is 3 %, with the exception of the Mercury source ( $^{203}\text{Hg}$ ) and the Cadmium source ( $^{109}\text{Cd}$ ), which have an uncertainty of 4 %.

<sup>7</sup>Calibrated radioactive sources were delivered by AEA Technology QSA GmbH (Braunschweig, Germany) together with a calibration certificate from the Deutscher Kalibrierdienst (DKD, Calibration laboratory for measurements of radioactivity, Germany)

### 3.3.3. Full-Energy Peak Effective Area and Angular Response

Results for the on-axis effective area as a function of the energy for all NaI and BGO FM detectors are shown in Figure 3.31. The initial drop below 20 keV is due to a Silicone rubber layer placed between the NaI crystal and the entrance window, which absorbs the X-rays. At energies higher than 300 keV, the NaI detectors become more transparent to radiation and a decrease in the response is observed. The BGO on-axis effective area is constant over the energy range 150 keV–2 MeV, with a mean value of  $120 \pm 6 \text{ cm}^2$ . Unfortunately, the effective area at 4.4 MeV could not be determined, since the activity of the Am/Be source was not known. SLAC measurements could not be used for this purpose either. At 33.17 keV, the effect of the Iodine K-edge is clearly visible as a drop. This energy region was extensively investigated during the PTB/BESSY calibration campaign and is further described in §3.3.4.

For several radioactive sources, off-axis measurements of the NaI and BGO response have been performed. These are extremely important for the interpretation of scattered photon flux both from the spacecraft and from the atmosphere. Figures 3.32 and 3.33 show results for the NaI and the BGO effective area as a function of the irradiation angle over the full  $360^\circ$ . The *top panel* of Figure 3.32 presents NaI FM04 measurements from

- the 32.89 keV line<sup>8</sup> from  $^{137}\text{Cs}$  (*top green curve*);
- the 279.2 keV line from  $^{203}\text{Hg}$  (*middle red curve*);
- the 661.66 keV line from  $^{137}\text{Cs}$  (*bottom yellow curve*).

It's worth noting that all curves, especially the middle one, trace the detector's structure (crystal, housing, and PMT). Furthermore, the bottom curve (661.66 keV) varies very little with the inclination angle because of the high penetration capability of gamma-rays at those energies.

In the case of BGO EQM, measurements performed with  $^{88}\text{Y}$  at 898.04 keV and 1836.06 keV are shown in the *bottom panel* of Figure 3.32 and highlight the two drops in the response due to the presence of the PMTs on both sides of the crystal. Although the BGO detectors are symmetrical, an asymmetry in the curves is caused by the Titanium bracket on one side of the crystal housing, which is necessary for mounting the detectors onto the spacecraft (Figure 3.1, *right panel*). Figure 3.34 shows 42 spectra collected with the BGO EQM with the  $^{88}\text{Y}$  radioactive source placed at different angles around the detector. The photo-peak positions of the 898.04 and 1836.06 keV lines are stable during the whole rotation, while the effective area (and  $w$ ) decrease(s) or increase(s) as presented in

---

<sup>8</sup>In this case, the double line was fitted with a single Gaussian, since the response dramatically drops above  $90^\circ$  and the fit algorithm is not capable of identifying two separate components.

### 3. GBM PERFORMANCE

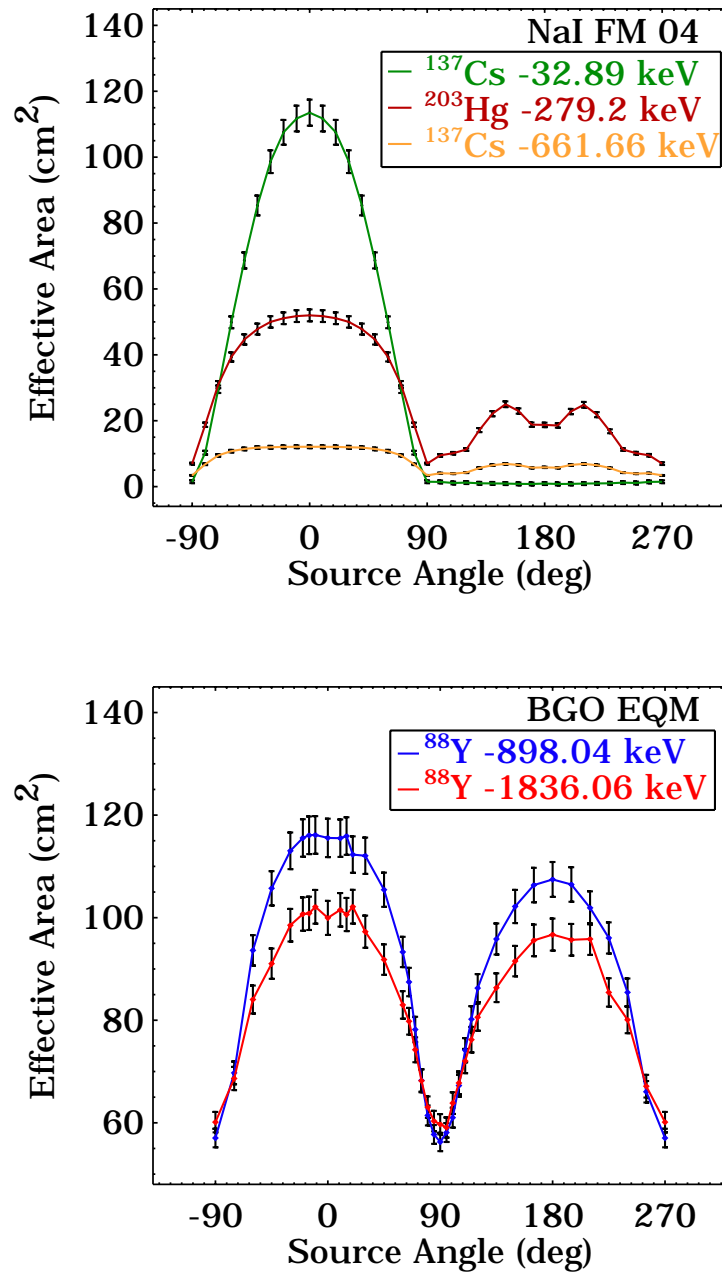


**Figure 3.32:** Off-axis effective area as a function of the irradiation angle (from  $-90^\circ$  to  $270^\circ$ ) for NaI FM04 (left panel) and BGO EQM (right panel). Data are connected with straight lines (no fitting is performed). Different colors represent different line-energies. In the case of NaI, results for three radioactive lines are shown, namely: 32.06 keV from <sup>137</sup>Cs (top green curve), 279.2 keV from <sup>203</sup>Hg (middle red curve), and 661.66 keV from <sup>137</sup>Cs (bottom yellow curve). For BGO, two lines from <sup>88</sup>Y are shown: 898.04 keV (blue curve) and 1836.06 keV (red curve)

### 3.3.3. Full-Energy Peak Effective Area and Angular Response

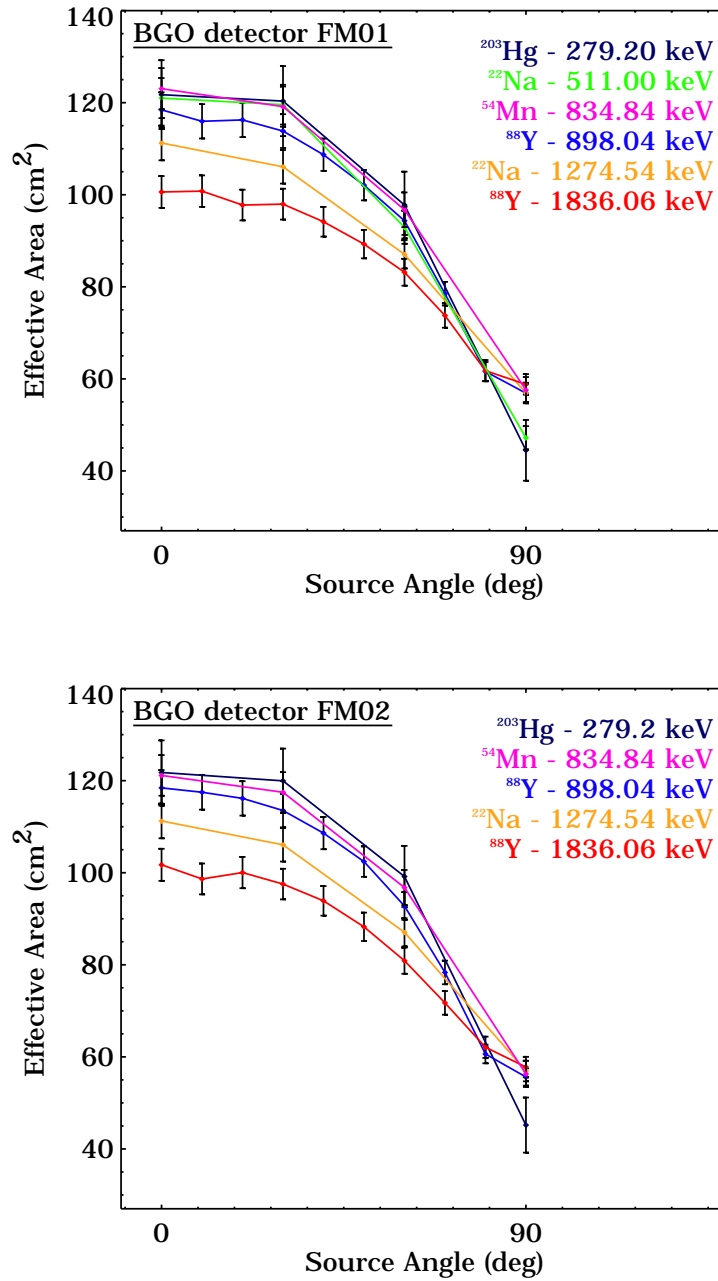


**Figure 3.33:** Off-axis effective area as a function of the irradiation angle (from 0° to 90°) for BGO FM01 (top panel) and FM02 (bottom panel). Data are connected with straight lines (no fitting is performed). Different colors represent different line-energies

### 3. GBM PERFORMANCE

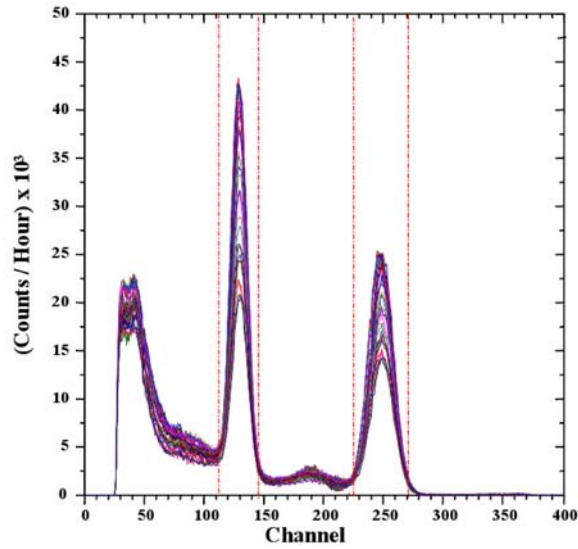


**Figure 3.34:** Normalized background-subtracted spectra measured at MPE with BGO EQM from the  $^{88}\text{Y}$  radioactive source placed at different angles around the detector

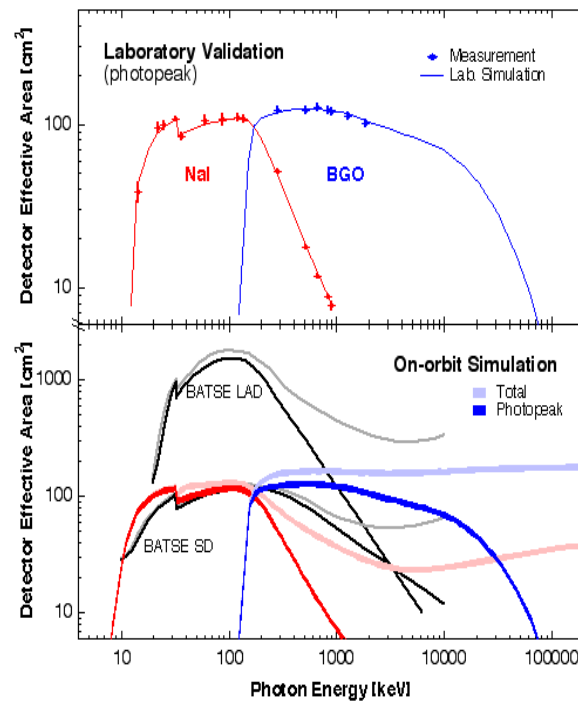


**Figure 3.35:** Energy dependence of the effective area at normal incidence, for both detector types. The lower panel includes the simulated effects of the spacecraft for a representative detector and a comparison with the BATSE LAD and SD detectors

the *bottom panel* of Figure 3.32. Off-axis measurements from several radioactive sources collected with both flight module detectors FM01 and FM02 are shown in Figure 3.33. For several sources, only 4 measurements were taken at 0°, 30°, 60° and 90°. In the case of <sup>88</sup>Y, the sampling is performed every 10°. Measurements below 1 MeV are comparable within the error. The effective area drops, i.e. the BGO crystals become transparent as the source energy increases.

Figure 3.35 shows the dependence of the effective area on energy for both detector types in comparison with the simulated response. Agreement between laboratory measurements and simulations (*upper panel*) is better than ±5%, averaged over all detectors<sup>9</sup>. This is the estimated systematic uncertainty in the simulated response incorporated into the shaded curves of the on-orbit simulations of the *lower panel*. The on-orbit simulations include the effects of spacecraft blockage and scattering. In some cases the total effective area above a few hundred keV is significantly increased due to photons that scatter from the spacecraft into the detector. Results from BATSE LAD and SD detectors are also shown. Despite the smaller effective area in the 20 keV–2 MeV energy range, the GBM instrument shows better performances at both lower (<20 keV) and higher (>10 MeV) energies.

### 3.3.4 QDE and Spatial Uniformity of NaI Detectors

As already mentioned in §3.1.2, the Quantum Detection Efficiency for detector NaI FM04 could be determined through detailed measurements performed at PTB/BESSY at energies between 10 and 60 keV by measuring:

1. The full-energy peak area of the NaI FM04 spectrum at a certain energy;
2. The full-energy peak area of the HPGe detector spectrum<sup>10</sup> (for which  $\text{QDE}_{\text{HPGe}} = 1$ ) at the same energy.

By accounting for the different beam fluxes and duration of measurements, the relation between the two line areas leads to the QDE determination:

$$\text{QDE}_{\text{FM04}} = \frac{f_{\text{MPE}}}{f_{\text{HPGe}}} \cdot \text{QDE}_{\text{HPGe}} . \quad (3.10)$$

In this case  $f$  is given by:

$$f = \frac{A}{\delta t \cdot I} , \quad (3.11)$$

<sup>9</sup>See Hoover et al. (2008) for more details regarding the comparisons of the effective area for NaI and BGO with simulations.

<sup>10</sup>This does not include the small Ge escape peak appearing above 11 keV

### 3. GBM PERFORMANCE

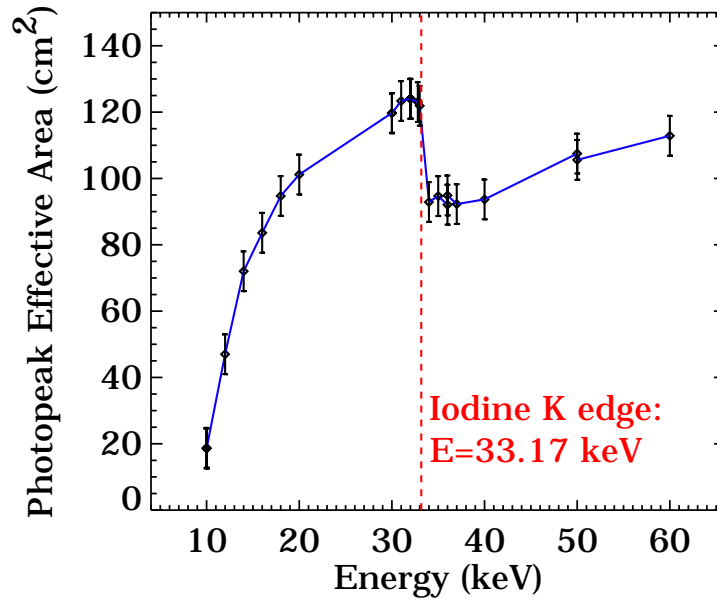


**Figure 3.36:** NaI FM04 effective area calculated from QDE determination of PTB/BESSY data collected between 10 and 60 keV. A relative uncertainty of 5% has been estimated

where  $A$  is the fitted line area,  $\delta t$  is the measurement's lifetime (usually 15 or 300 s for single or rasterscan measurements, respectively) and  $I$  the beam current in nA.

The QDE was determined at all energies by analyzing one spectrum taken in the center of the detector's surface. The effective area can then be calculated by multiplying the QDE with the detector's active area ( $126.7 \text{ cm}^2$ ). Results for 19 lines measured between 10 and 60 keV are shown in Figure 3.36. This Figure can be considered as a zoom at low energies of the NaI effective area in Figure 3.31.

The detector's spatial homogeneity was investigated at PTB/BESSY by means of rasterscans of detector NaI FM04 at three distinct energies, namely 10, 36 and 60 keV. During each rasterscan, 729 runs per detector were recorded with a spacing of 5 mm, 27 in  $x$ -direction and 27 in the  $y$ -direction<sup>11</sup>. For each spectrum, the full-energy peak was analysed as previously described in §3.2.2. Results for the fitted line center (in channel #) and line resolution (in %) are shown in the *top*, *middle* and *bottom* panels of Figure 3.37 for the 10, 36 and 60 keV rasterscans, respectively. From the line center spatial dependence (*right column*) one can notice that some border effects appear toward the edge of the NaI crystal, shifting

<sup>11</sup>In the case of the 36 keV rasterscan, only 328 runs were recorded with a coarser spacing of 10 mm, causing a  $27 \times 14$  coverage over the  $x$ - $y$  plane.

### 3.3.4. QDE and Spatial Uniformity of NaI Detectors

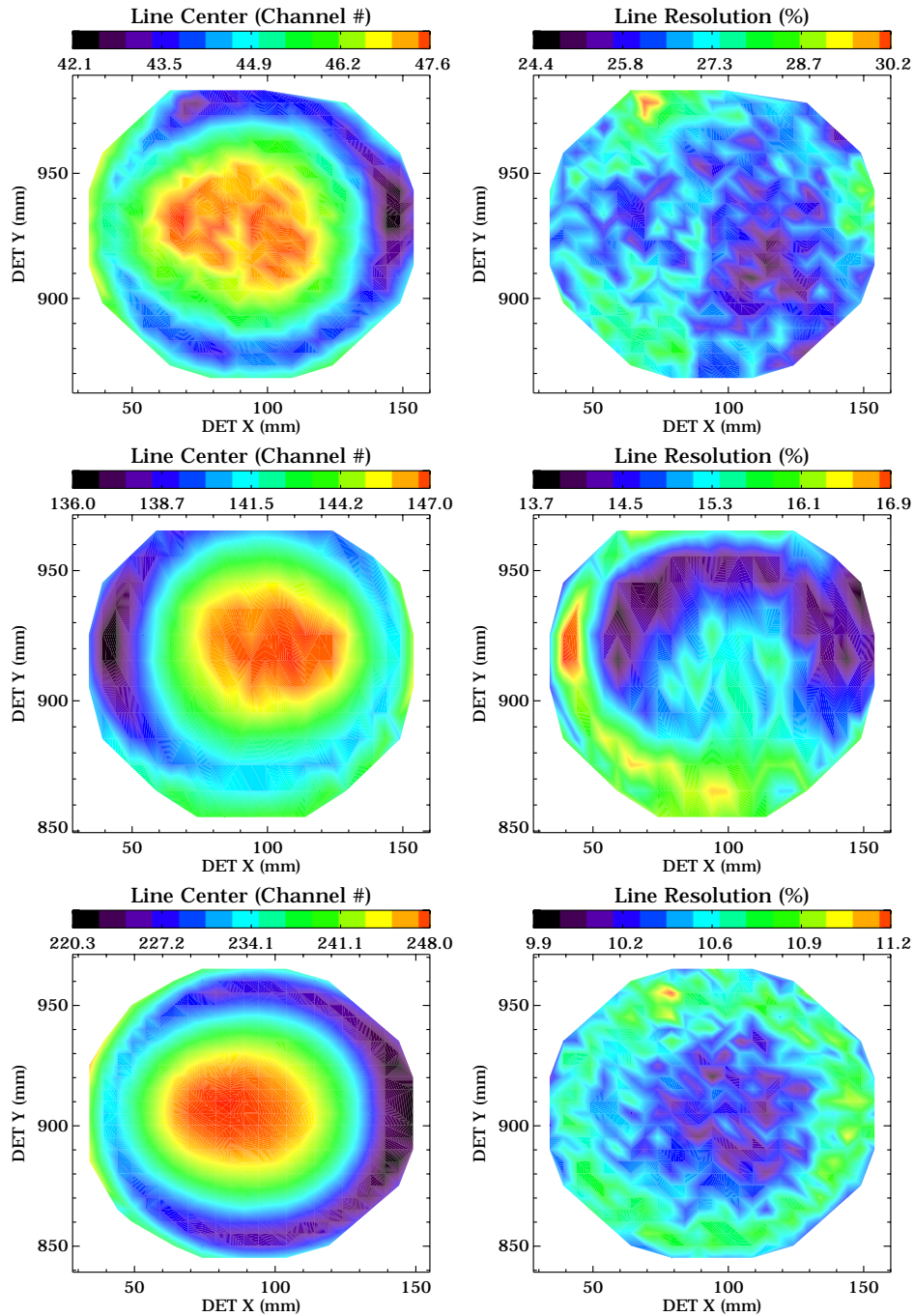


**Figure 3.37:** Contour plots showing results for the PTB/BESSY raster scan at 10 (*top*), 36 (*middle*), and 60 keV (*bottom panel*) of detector NaI FM04. Plots on the *right* show the fit results for the full-energy peak line center as a function of the beam position (in mm). The spatial dependence of the fitted line resolution at different energies is shown in the plots on the *left*

### 3. GBM PERFORMANCE

---

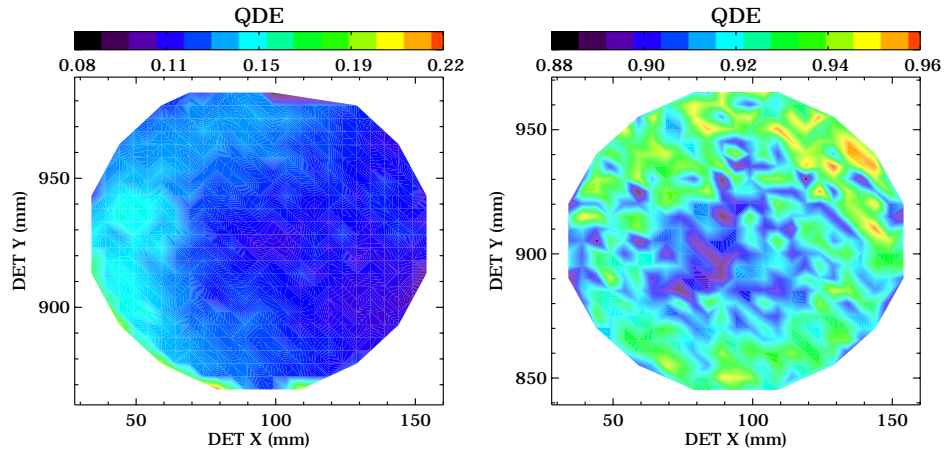


**Figure 3.38:** Spatial dependence of the QDE for the rasterscans performed at 10 (*left panel*) and 60 keV (*right panel*). The QDE at 10 keV shows evidence of asymmetry: this could possibly be explained by non-uniformity of the absorbing material in front of the detector

the full-energy peak to lower channel numbers i.e. energies. This effect is of the order of 12 % at 10 and 60 keV and of 7 % at 36 keV. The line resolution is homogeneous over the whole detector's area, with a mean value of 27%, 15% and 10% at 10, 36 and 60 keV, respectively. While the first two resolutions are comparable to the results obtained with radioactive sources at 14.4 and 36.6 keV, the 60 keV rasterscan gives an improved resolution when compared to the result of 15% obtained with the  $^{241}\text{Am}$  source at 59.4 keV (see Figure 3.9, *panel f*).

The spatial dependence of the QDE is shown in Figure 3.38 for the 10 and 60 keV rasterscans. Unfortunately, the QDE for the 36 keV rasterscan could not be determined because of a problem which occurred during the readout of the beam current. The QDE at 10 keV shows evidence of asymmetry: this could possibly be explained by non-uniformity of the absorbing material in front of the detector, e. g. the silicone layer at the entrance window. As already seen in Figure 2.9 (§2.2.1), a small change in the absorber's thickness can lead to big effects in the transmission. This behavior should be further studied in details by simulations.

### 3.3.5 NaI Detectors High–Voltage dependence

During the first calibration campaign at the MPE laboratories in 2005, several measurements of the gain dependence of the NaI FM detectors from the High Voltage (HV) were taken. The HV applied to each detector is given in Table 3.21. Here, the values recommended by Jena Optronik<sup>12</sup> (JO) are listed in column 2, while the values usually applied during the calibration campaigns are listed in column 3.

**Table 3.21:** Nominal (JO) and adopted (lab) HV values for each NaI FM detector

NaI Detector	U (JO, V)	U (lab, V)
FM01	914	914
FM02	927	923
FM03	900	895
FM04	878	874.5
FM05	881	872
FM07	934	929
FM08	900	895
FM09	932	917.5
FM10	929	918.5
FM11	937	925.5
FM12	925	912
FM13	924	912

Measurements for the gain dependence were performed for the NaI detectors FM01–FM08 and FM13 with the <sup>137</sup>Cs radioactive source. Spectra were recorded for different HV values (from 800 to 930 V) and the photo–peak centers for the 32.06 keV and the 661.66 keV lines were fitted following the procedure previously described in §3.2.2. The dependence of the photo–peak centers from the HV values was investigated applying a power–law fit of the form:

$$x_c = a \cdot U^b . \quad (3.12)$$

Table 3.22 shows the results for the fit parameters  $a$  and  $b$  for each NaI detector, together with the reduced Chi–squared values. Results for both radioactive lines as measured by NaI detector FM04 are also given in Figure 3.39.

<sup>12</sup>The detectors were developed by Jena–Optronik, Germany

### 3. GBM PERFORMANCE

**Table 3.22:** Parameters for the power-law fit given in Equation 3.12 for the gain vs. HV for the NaI detectors FM01–08 and FM13

FM	32.02 keV		661.66 keV	
	a	b	a	b
01	$(3.6 \pm 2.0) \cdot 10^{-17}$	$6.30 \pm 0.08$	$(4.36 \pm 0.05) \cdot 10^{-17}$	$6.688 \pm 0.002$
02	$(6.4 \pm 1.2) \cdot 10^{-17}$	$6.21 \pm 0.03$	$(5.20 \pm 0.06) \cdot 10^{-17}$	$6.651 \pm 0.002$
03	$(1.3 \pm 0.2) \cdot 10^{-17}$	$6.47 \pm 0.02$	$(4.61 \pm 0.06) \cdot 10^{-17}$	$6.700 \pm 0.002$
04	$(1.3 \pm 0.2) \cdot 10^{-17}$	$6.49 \pm 0.02$	$(1.41 \pm 0.02) \cdot 10^{-17}$	$6.898 \pm 0.002$
05	$(7.3 \pm 1.0) \cdot 10^{-18}$	$6.58 \pm 0.02$	$(1.87 \pm 0.02) \cdot 10^{-17}$	$6.856 \pm 0.002$
07	$(4.5 \pm 0.8) \cdot 10^{-17}$	$6.25 \pm 0.02$	$(7.39 \pm 0.09) \cdot 10^{-17}$	$6.594 \pm 0.002$
08	$(3.8 \pm 1.8) \cdot 10^{-17}$	$6.31 \pm 0.07$	$(5.94 \pm 0.07) \cdot 10^{-17}$	$6.662 \pm 0.002$
13	$(3.8 \pm 0.7) \cdot 10^{-17}$	$6.30 \pm 0.03$	$(5.11 \pm 0.06) \cdot 10^{-17}$	$6.664 \pm 0.002$

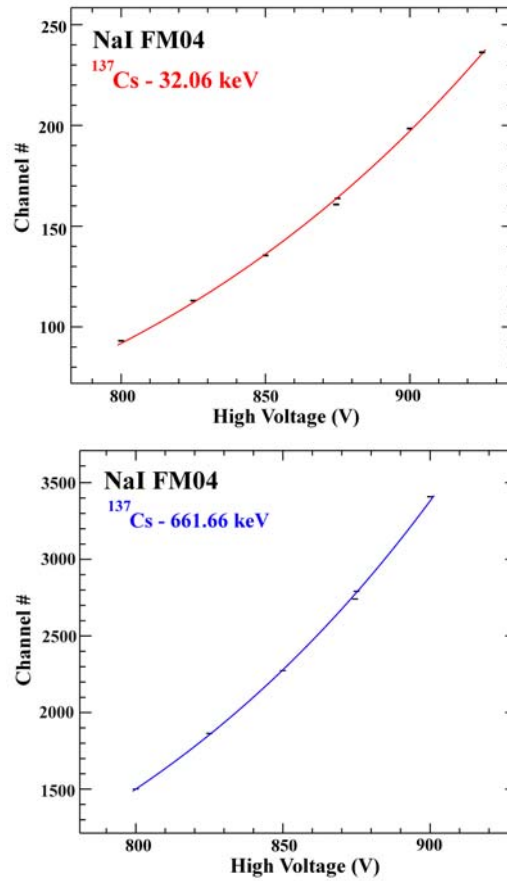


**Figure 3.39:** Example of gain vs. HV at two different energies for the NaI detector FM04

### 3.3.6 NaI EQM Thermal Test

Shortly after launch, a dedicated calibration campaign was performed at the MPE laboratories in order to qualify the detector performance at high temperatures (up to 60° C). Such temperatures were never applied during ground calibration tests (also at spacecraft level). The NaI EQM spare detector was placed in a thermal chamber and irradiated with a  $^{137}\text{Cs}$  radioactive source through a lateral aperture (about 2 cm in diameter). The temperature was then varied over a period of four months (May through August 2009) and kept at about 60° C for a month and a half (see Table 3.23). Figure 3.40 shows a sample of 37 raw spectra collected during the thermal test period.

The photo-peak centers and FWHMs for the 661.66 keV lines were fitted following the procedure previously described in §3.2.2. The temporal dependence of both quantities is shown in Figure 3.41. The top panel shows the change in temperature during the calibration period (*red curve*). The photo-peak center (*middle panel*) decreases abruptly as the temperature is raised from room temperature to 58.6° C after 8 days from the beginning of the data taking. One possible explanation could be a depletion effect: the bonding between the scintillator crystal and the PMT decreases at the crystal's edges. In this way, a smaller number of pho-

**Table 3.23:** Date, time and temperature values measured during the thermal test campaign

YYMMDD	Time	T (°C)	YYMMDD	Time	T (°C)
090513	14:16	25.8	090617	11:08	58.6
090514	14:14	25.9	090619	9:40	58.4
090515	15:27	25.8	090622	8:28	58.6
090518	10:40	25.9	090624	8:44	58.5
090519	17:52	28.0	090626	10:34	58.5
090520	9:25	39.5	090629	14:12	58.5
090522	10:41	58.7	090701	9:35	58.5
090526	9:21	58.6	090702	9:24	54.0
090527	10:54	58.6	090706	8:14	53.4
090528	13:21	58.6	090709	8:47	53.8
090529	11:14	58.6	090710	10:54	49.0
090602	9:42	58.6	090713	8:37	44.2
090603	16:05	58.6	090715	14:01	39.5
090604	14:27	58.6	090716	17:41	34.8
090605	12:21	58.6	090717	9:31	30.2
090608	11:55	58.6	090720	11:22	25.9
090609	13:01	58.6	090723	14:30	25.9
090610	14:35	58.6	090727	9:35	25.8
090615	8:30	58.6			

### 3. GBM PERFORMANCE

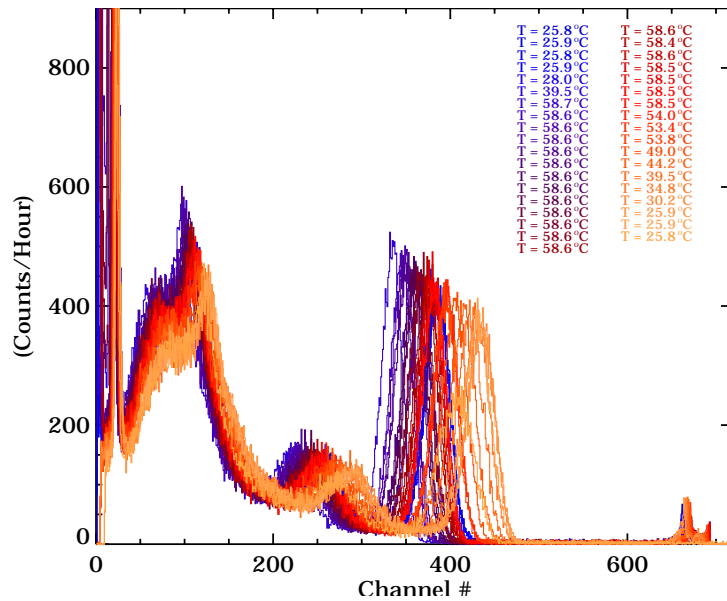


**Figure 3.40:** Collection of 38 spectra (not background–subtracted) recorded during the thermal test at the MPE laboratories with the NaI spare detector (EQM) irradiated by a  $^{137}\text{Cs}$  radioactive source. The exact day, time and temperature values for each recorded spectrum are given in Table 3.23

tons can reach the detector and a broadening of the photo–peak is evident. Thus the line resolution (in %, *bottom panel*) remains nearly constant. During the following 40 days the temperature remains stable and the depletion effect slowly disappears: the photo–peak center readjusts to the initial value (“relaxation” effect). By comparing the values obtained at the beginning and at the end of the calibration campaign, one can conclude that the light yield did not suffer too much from degradation. On the contrary there is evidence of a mild improvement: during the last cooling period (from  $\sim 50$  to  $\sim 80$  days after test start) the line center moves to a slightly higher value than the initial one.

### 3.4 Detector Calibration at System Level

The final (post–integration) calibration prior to launch was carried out in late March 2008 during the last Comprehensive Performance tests (CPTs) at the AstroTech facility, near the Kennedy Space Center (Florida, USA). Individual radioactive sources were placed at a distance of 50 cm in front of each cluster of 3 detectors and data were accumulated for 15 min. The eight calibration sources comprise  $^{57}\text{Co}$ ,  $^{109}\text{Cd}$ ,  $^{137}\text{Cs}$ ,  $^{133}\text{Ba}$  (line at 80.998 keV used for NaI calibration),

### 3.4. Detector Calibration at System Level

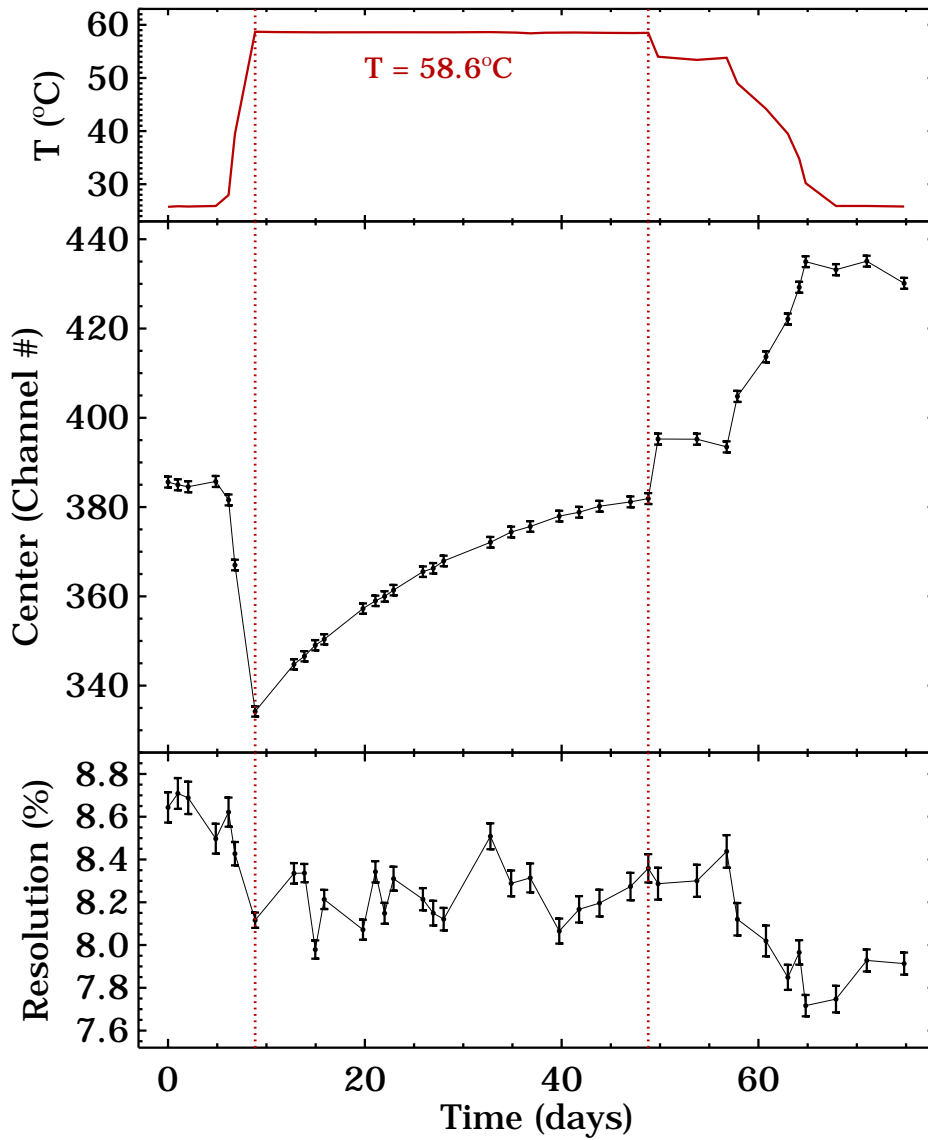


**Figure 3.41:** Temporal evolution of the fitted photo-peak center (*middle panel*) and resolution (*bottom panel*). Dotted vertical lines delimit the period during which the temperature was kept stable at  $58.6^\circ\text{C}$

### 3. GBM PERFORMANCE

$^{54}\text{Mn}$ ,  $^{233}\text{Th}$  (line at 934.1 keV, used for BGO calibration)  $^{22}\text{Na}$ , and  $^{40}\text{K}$  (see Table 3.1 for more details). The main analysis of the calibration data was carried out between 2008 and 2009 and represents the official input for the current GBM DRM determination. Hereafter, a brief overview of the main characteristics and differences with respect to detector–level calibration results is presented.

#### 3.4.1 Channel–to–Energy Conversion

Due to the paucity of gamma–ray lines below the K–edge energy (33.17 keV, see §3.3.1 ) PTB/BESSY measurements were included for the low–energy fit. These measurements (10–60 keV) were made when the FM04 PMT was operating at a high voltage value of 874.5 V, while the nominal HV for this detector is 870 V. Hence the channel numbers of the line centroids ( $ch_B$ ) of all the PTB/BESSY measurements had to be reduced by applying a linear rescaling of the form:

$$ch'_B = \alpha + \beta \cdot ch_B . \quad (3.13)$$

Moreover, the prototype DPU was used during measurements performed at the MPE laboratories. By comparing the line centroids of the same lines made at MPE and during CPTs, it is found that the flight DPU has a slightly higher gain and the ratio of gains is also a function of energy. Hence while comparing the

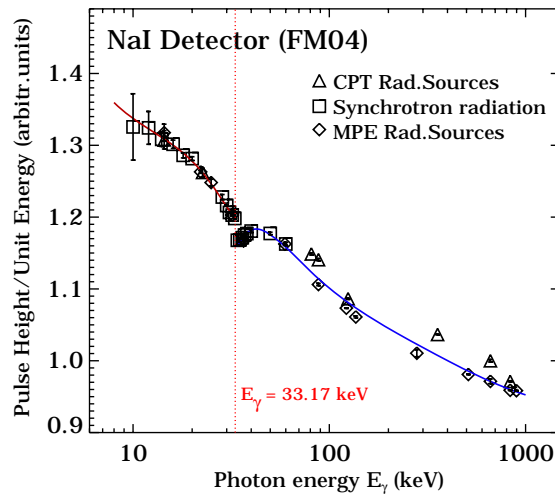


**Figure 3.42:** CE relation calculated below (*red line*) and above (*blue line*) the K–edge energy for the NaI detector FM04 using cubic spline functions. The fit comprises CPT (*triangles*), PTB/BESSY (*squares*) and MPE (*diamonds*) measurements

MPE measurements with the CPT ones, a correction of the line centroids had to be applied. A second linear rescaling of the form of Equation 3.13 was applied to the MPE channel numbers. All measurements below and above the K–edge energy were finally fitted applying cubic spline functions<sup>13</sup> with 4 and 6 nodes, respectively. The energies at the required channel numbers were computed using spline interpolation routines. Results in terms of pulse height per unit energy are shown in Figure 3.42 for the NaI detector FM04. Some discrepancies are still visible at high energies for the CPT measurements (*triangles*), which do not agree with the MPE–BESSY smooth fit (*blue line*). This deviation from linearity could be due to different fitting algorithms between the two data samples and is smaller than what is required by the instrument specifications (GBM Proposal, 1999). More details regarding the most recent GBM calibration results can be found in GBM internal documents.

## 3.5 On–Orbit Performance and Operations

A comprehensive series of calibrations and performance tests were made on the GBM, both at the detector level, as extensively discussed in the previous Chapter, and at the system level in different configurations and locations. Calibration at the system level was performed (i) first at the National Space Science and Technology Center (NSSTC, Alabama, USA) using a non–flight cable harness on a bench with all flight detectors, the flight DPU and the flight HVPS; and (2) following integration of GBM on the spacecraft. These comprise tests performed at the Naval Research Laboratory (NRL, Washington DC, USA) and at General Dynamics (Phoenix, USA). All calibrations provide valuable input data for on–orbit data analysis, for use in the DRMs that were developed, and to indicate long–term trends in the performance of the detectors or possible degradation following environmental tests.

Validation of the GBM energy calibration was performed before launch (see §3.3.1), but also during flight. The flight electronics have been verified to be highly linear, so it becomes important to map out the non–linear light output of the NaI detectors, especially at the low–energy end. In orbit, there are a number of lines at known energies in the background spectra that may be used both to validate the calibration as well as to serve as features to lock in the automatic gain

---

<sup>13</sup>The spline is a special function defined piecewise by polynomials, which are joined together at fixed points called knots or nodes (see e.g. Schoenberg, 1946).

### 3. GBM PERFORMANCE

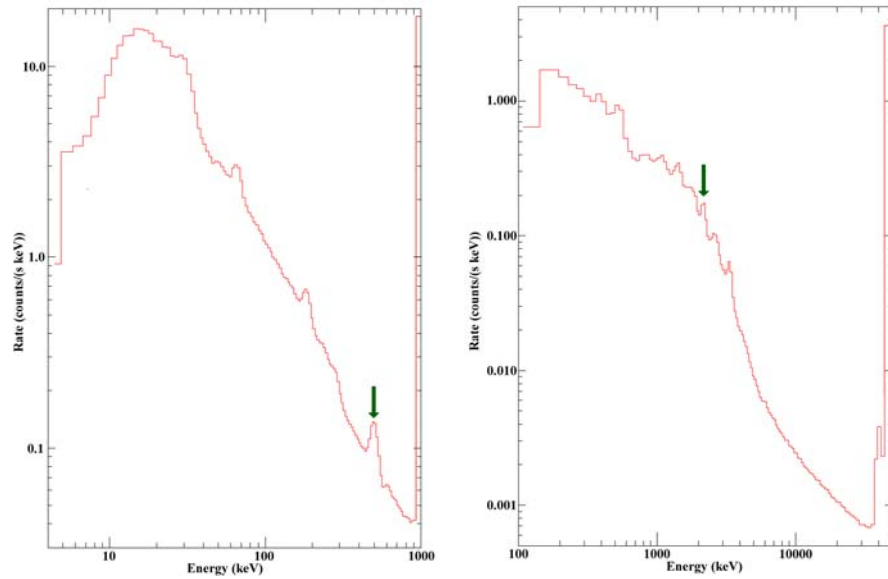


**Figure 3.43:** Background spectrum for a NaI (*on the left*) and BGO (*on the right*) detectors (2.4 hour accumulation). The 511 keV line used for the NaI AGC and the 2.2 MeV line used for the BGO AGC are marked with *green vertical arrows*. At low energies the NaI and BGO electronics noise are cut at about 5 and 110 keV, respectively. The highest NaI energy bin and the highest few BGO energy bins are overflow channels. From Meegan et al. (2009)

control (AGC) function of the GBM FSW. Figures 3.43 and 3.44 show 2.4 hr. and a whole orbit of accumulations of background spectra from a NaI and a BGO detector, respectively. The background continua above  $\sim 150$  keV in both types of detectors are dominated by secondary cosmic-ray-produced photons. This background source has as a major component of the Earth gamma-ray albedo, and to a lesser extent, secondary gamma rays generated in local materials of the detectors and the spacecraft. This component of the background is modulated by the geomagnetic latitude, as the spacecraft traverses its orbit (see Figure 3.44). Below  $\sim 150$  keV, the uncollimated GBM detectors have a significant counting rate from the diffuse X-ray background. This contribution is, of course, dependent upon the sky viewing fraction of the detectors that is not blocked by the Earth or spacecraft. In the NaI detectors, materials in front of the detector windows begin to limit the response significantly in the energy region 8 keV to  $\sim 20$  keV (see Figure 2.9 of §2.2.1) resulting in the low-energy drop seen in Figure 3.43, *left panel*. The highest few channels of the spectra from both types of detectors are the “overflow channels”. These channels contain counts due to energy deposits in the scintillators that are above the maximum set for the detector,  $\sim 1$  MeV for

### 3.5. On–Orbit Performance and Operations

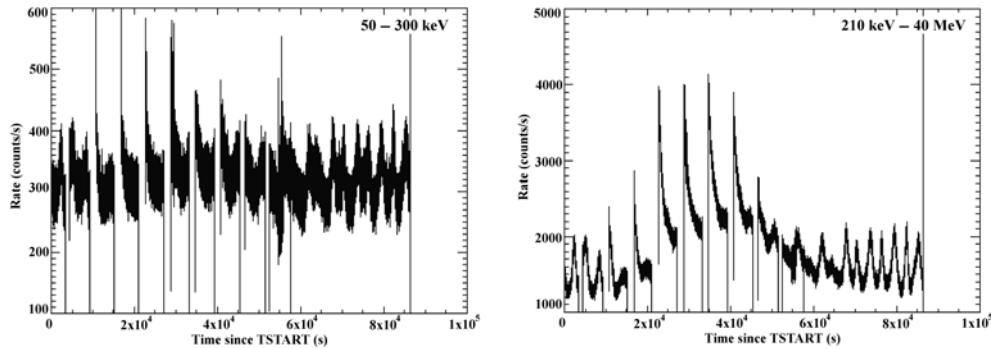


**Figure 3.44:** NaI (*left*) and BGO (*right*) detector background rates over a whole orbit in the NaI (50–300 keV) energy range, and over the full BGO energy range, respectively. From Meegan et al. (2009)

the NaI detectors and  $\sim 45$  MeV for the BGO detectors. The gradual upturn of the background in the BGO detectors above  $\sim 10$  MeV is due to the logarithmically increasing width of the energy channels, increasing faster than the spectral decrease of the gamma–ray background continuum.

For the NaI detectors, the 511 keV annihilation line is used for AGC, which is nearly always visible (see Figure 3.43, *left panel*). As another valuable reference point, each spectrum exhibits a shoulder below the 33 keV Iodine K–edge feature. Two other prominent lines are observed from two excited energy levels of  $^{127}\text{I}$ , which are at 57.6 keV and 202.9 keV. These features are believed to be due to fast neutron excitation, followed by nuclear de–excitation of this isotope. The BGO background spectrum is rich and varying, with spectral features due to activation from the hard radiation that the observatory passes through in the South Atlantic Anomaly (SAA), as well as persistent atmospheric features. The strong line at 2.2 MeV is due to neutron capture in the large amount of hydrogen contained in the hydrazine tanks of the spacecraft. This line is used for the AGC system of the BGO detectors. A line at 1.46 MeV is due to  $^{40}\text{K}$ , primarily from the potassium contained in the glass in the PMTs of the BGO detectors. Nitrogen and oxygen nuclear excitation lines also appear but are not well–separated from the continuum. Other line features are mainly due to unresolved and/or unidentified activation and excitation lines in the BGO crystal by protons and neutrons in the ambient environment. In the temporal plots (Figure 3.44), times of zero rate are due to turning off the PMTs during SAA passes. These plots show the effect of activation by the SAA, particularly in the BGO detectors, as well as high rates near the SAA boundaries. The high voltage is adjusted when the fitted spectral line has

### 3. GBM PERFORMANCE

---

moved from the desired position by more than 1.4% in the NaIs and by more than 1.0% in the NaIs. The gains of the NaI detectors are typically adjusted two or more times per day, showing a daily period. The gains of the BGO detectors, which have much higher thermal inertia, are adjusted much less frequently.

## Chapter 4

# First Year of GBM Scientific Results

The *Fermi* GBM is performing on orbit as expected. The total trigger count from the time triggering was enabled in June 2008 through December 2009 is 655. This does not include commanded triggers during the checkout phase and during the testing of the 2kbps downlink. Nearly 90% of the triggers are scientifically interesting. About 380 of these triggers were classified as GRBs, which leads to a GRB trigger rate of  $\sim 260$  bursts/year. Moreover, GBM triggered 168 times on SGR outbursts, and 30 times on TGF signals. A small number of weak solar flares was also detected in November 2008 and in October and December 2009. Several other triggers include particle precipitation events, accidentals caused by statistical fluctuations in the background, Cygnus X-1 fluctuations, and events with uncertain classifications.

As of December 2009, GBM detected 14 bursts in common with the LAT. These amazing detections mainly fulfill the primary science goal of GBM, which is the joint analysis of spectra and time histories of GRBs observed by both *Fermi* instruments. For every trigger, GBM provides near-real time on-board burst locations to permit repointing of the spacecraft and to obtain LAT observations of delayed emission from bursts, as previously discussed in chapter 2. In the case of common GBM-LAT detections, the autonomous repointing was successfully issued six out of 14 times, usually resulting in five hours of pointed observations of the burst position following the GBM trigger. Moreover, on-board GBM and LAT refined locations are rapidly disseminated to the community, often permitting extensive multiwavelength follow-up by *Swift* or other space-based observatories, and by numerous ground-based telescopes, thus allowing redshift determinations.

This chapter focuses on the main GBM scientific results collected during the first year of operation and to whose achievement I largely contributed. It is struc-

## 4. FIRST YEAR OF GBM SCIENTIFIC RESULTS

---

tured as follows: First of all, §4.1 presents an example of the GBM-only analysis of two long GRBs detected in March 2009, GRB 090323 and GRB 090328. These bursts had a large X-ray, optical and radio follow-up, and were also detected by the LAT. An overview of some other joint GBM-LAT detected GRBs is then given in §4.2, followed by a more detailed description of the spectral analysis and theoretical results for the very energetic GRB 090902B (§4.3). Finally, the first burst observed shortly after *Fermi*'s launch by GBM and *Swift*, namely GRB 080810, is presented in §4.4.

### 4.1 GRB 090323 and GRB 090328<sup>1</sup>

In the following sections, I report the observations and analysis of gamma-ray emission from two GRBs detected within a week of each other in late March 2009, namely GRB 090323 and GRB 090328. These results are also summarized in Bissaldi (2010a) and Bissaldi (2010b).

Both GRBs have several interesting features. They were initially within the LAT field of view at an angle of  $60^\circ$  and  $67^\circ$ , respectively. Luckily, they were bright enough to trigger an autonomous repointing of the spacecraft, thus allowing observations by the LAT for five hours (subject to Earth avoidance, see chapter 2, Figure 2.14). The ARRr were initiated at  $T_0+46$  s and  $T_0+37$  s for GRB 090323 and GRB 090328, respectively. Moreover, both GRBs were detected by the LAT Automated Science Processing (ASP) by using 6 hours of data. The improved locations obtained by the LAT instruments made it possible to extensively follow-up the bursts. GRB 090323 was followed-up in the X-ray and in the optical by *Swift* (Kennea et al., 2009a) and by many ground-based telescopes (e.g., Updike et al., 2009). The spectroscopic redshift of  $z = 3.6$  was determined by Chornok et al. (2009) using Gemini-South (GMOS). In the case of GRB 090328, the bright afterglow was discovered by *Swift* in both the X-ray (Kennea et al., 2009b) and optical bands (Oates, 2009), while the spectroscopic redshift of  $z = 0.736$  was determined by Cenko et al. (2009). These two events represent the first LAT GRBs to be detected in the radio. They were both observed by the Very Large Array (VLA) at a frequency of 8.46 GHz (Harrison et al., 2009; Frail et al., 2009). Moreover, GRB 090323 was detected by the Westerbork Synthesis Radio Telescope (WRST) at a frequency of 4.9 GHz (van der Horst et al., 2009b). Furthermore,

---

<sup>1</sup>The main contents of this section are published in Bissaldi (2010a), “*GRB 090323 and GRB 090328: two long high-energy GRBs detected with Fermi*”; *Venice 2009 GRB Conference Proceedings in press*

there is strong evidence of emission detected in the LAT up to late times. These results will be extensively discussed in an upcoming paper (Abdo et al., 2010b), for which I'm responsible as "contact author". Here, I will mainly focus on the GBM-only analysis of these GRBs, including temporal and spectral properties, both time-integrated and time-resolved.

### 4.1.1 Observations of GRB 090323

On March 23, 2009, at 00:02:42 UT, the GBM triggered on and localized GRB 090323 (trigger 259459364). The burst triggered in the 50–300 keV energy range on 2048 ms integration time and had a trigger significance of  $5\sigma$ . Significant emission was observed in all NaI detectors on the same spacecraft side (n6–nb). Moreover, BGO detector b1 detected the burst up to  $\sim 3$  MeV. Due to the repointing maneuver, the detectors' angles with respect to the burst location had to be carefully examined over the whole burst duration. This is a crucial step before computing the correct detector response matrices (DRMs) for each individual detector over a particular burst interval.

The detectors' orientation with respect to the burst was calculated from  $T_0$  out to  $T_0+400$  s for NaI detectors n6 through nb and is shown schematically in six panels in Figure 4.1. Detector n9 shows the smallest and most stable angle with respect to the burst over the whole duration: it is comprised between  $27^\circ$  and  $35^\circ$ . All other NaI detectors significantly suffer from the repointing manoeuvre from  $\sim T_0+60$  s onward. Therefore, detector nb can only be used over the first part of the burst, while detectors n6 and n7 get the smallest angles only towards the end of it. The raw GRB light curve as seen by detector n9 without any background subtraction is shown in Figure 4.2. The strong effect of the spacecraft slew after the ARR was initiated is noticeable in the changing behavior of the observed background, which is nearly flat before the trigger and is strongly decreasing at later times.

The background-subtracted GRB light curve is shown in Figure 4.3 and is characterized by (i.) a first group of peaks showing a lot of substructure between  $T_0$  and  $T_0+70$  s; (ii.) a plateau with very little emission from  $T_0+70$  s to  $\sim T_0+110$  s; and (iii) three late well-defined and equally-spaced peaks, each about 10 s long. By combining the orientation changes with the peculiarities of the GRB profile, the burst was divided in seven intervals (*a* to *g*) for the spectral analysis, which are shown in Figure 4.3 as grey-shaded areas. The burst's  $T_{90}$  and  $T_{50}$  values were computed analysing CTIME data for detectors n9 and nb. They

#### 4. FIRST YEAR OF GBM SCIENTIFIC RESULTS

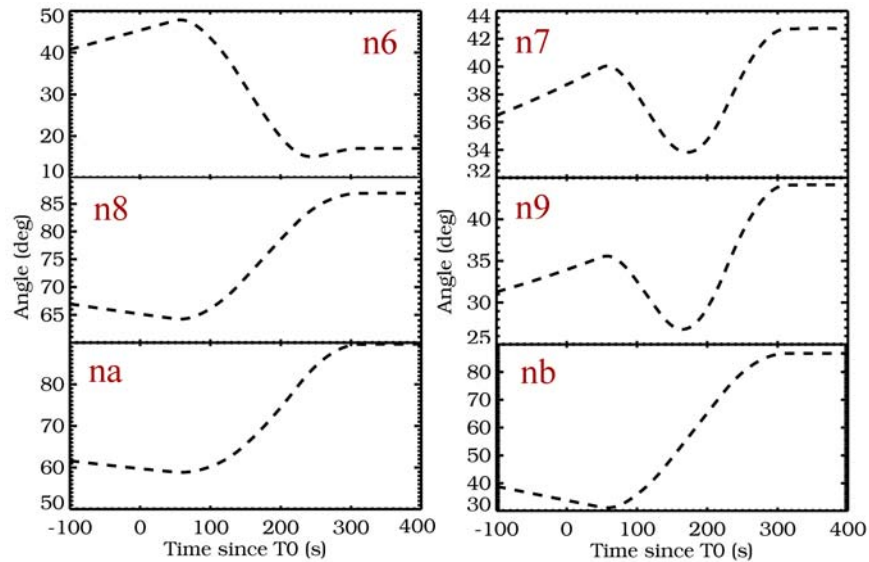


**Figure 4.1:** Temporal evolution of the angular distance (in degrees) between source and NaI detectors n6–nb for GRB 090323. The detectors which are used for the spectral analysis are n6, n7, n9 and nb

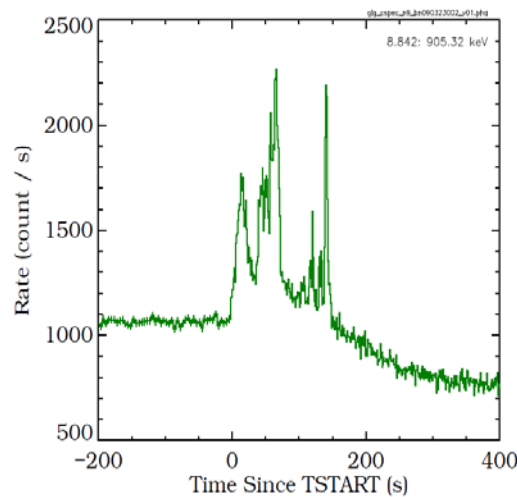


**Figure 4.2:** Light curve of GRB 090323 as seen by the NaI detector n9. No background subtraction is performed in order to show the effect of the ARR on the detector’s orientation with respect to the source

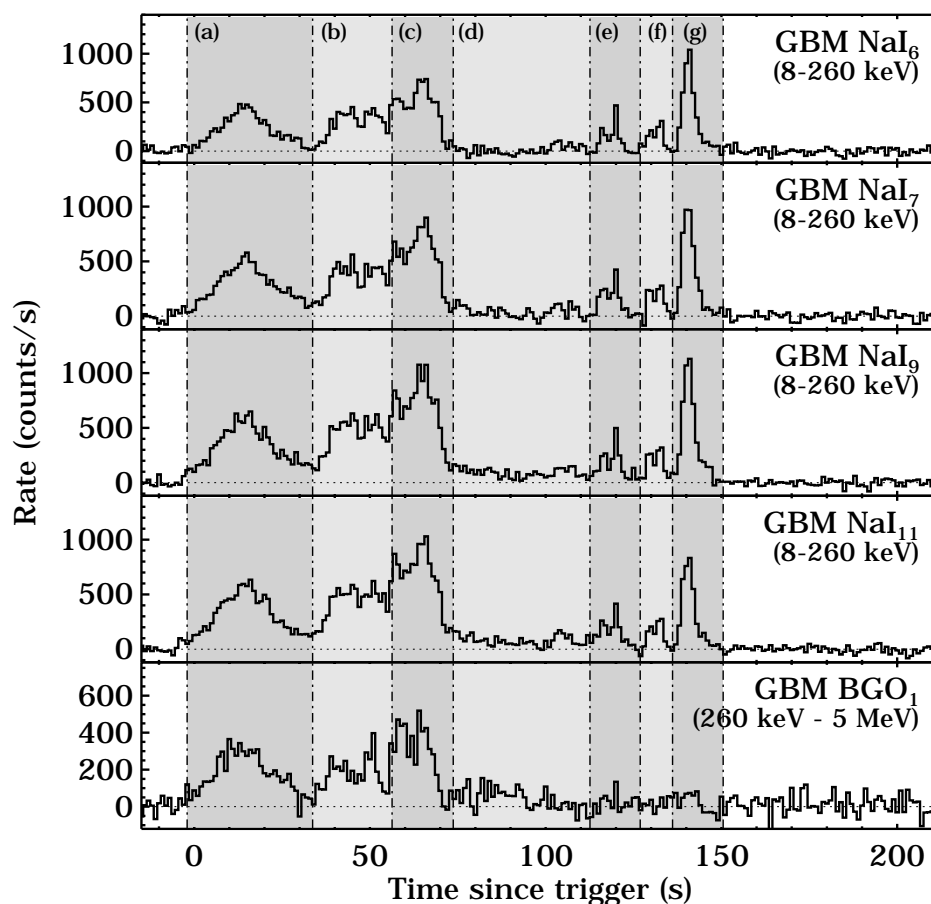


**Figure 4.3:** Light curves for GRB 090323 observed with the GBM, from lowest to highest energies. All panels represent the background-subtracted light curves for four NaI and one BGO detector. NaI detectors n6, n7, n9 and nb are shown in the 8–260 keV energy band (top four panels), while the bottom panel shows the corresponding plot for BGO detector b1, between 260 keV and 5 MeV. In all cases, the binwidth is 1s. Vertical dash-dotted lines denote the seven time intervals (*a* to *g*) chosen for the time-resolved spectral analysis

were found to be  $T_{90} = 133.1 \pm 1.4$  s and  $T_{50} = 42 \pm 4$  s, respectively, where the error bars reflect the  $1\sigma$  statistical uncertainties.

## 4.1.2 Observations of GRB 090328

Five days after the detection of GRB 090323, i.e. on March 28, 2009, at 09:36:47 UT, the GBM triggered on and localized GRB 090328 (trigger 259925808). The burst triggered over the same integration time and in the same energy range as

#### 4. FIRST YEAR OF GBM SCIENTIFIC RESULTS

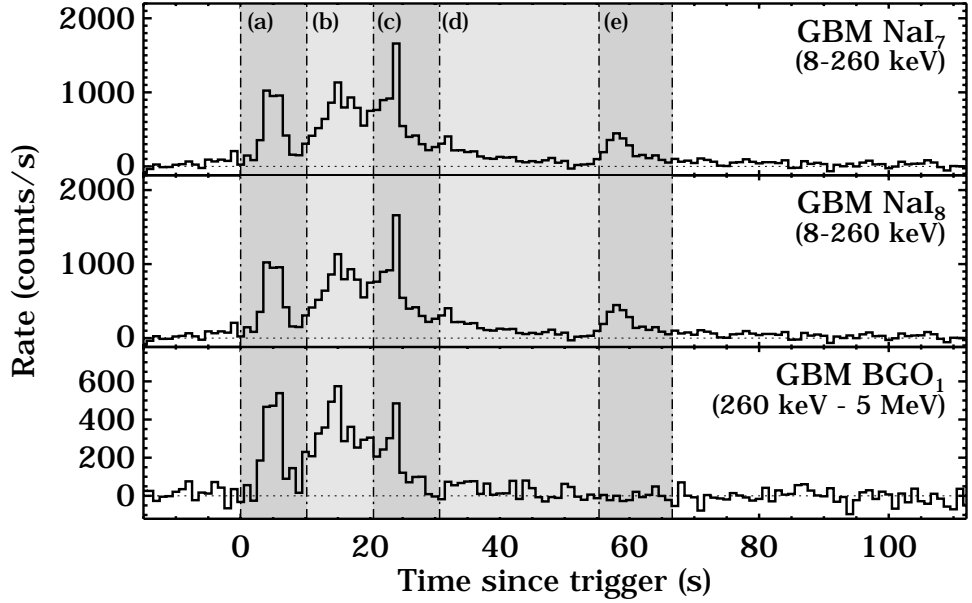


**Figure 4.4:** Light curves for GRB 090328 observed with the GBM, from lowest to highest energies. All panels represent the background-subtracted light curves for two NaI and one BGO detector. NaI detectors n7 and n8 are shown in the 8–260 keV energy band (top two panels), while the bottom panel shows the corresponding plot for BGO detector b1, between 260 keV and 5 MeV. In all cases, the binwidth is 1s. Vertical dash-dotted lines denote the five time intervals (*a* to *e*) chosen for the time-resolved spectral analysis

GRB 09323, namely 2048 ms and 50–300 keV. The trigger significance was  $5.1\sigma$ . Significant emission was observed in nine NaI detectors, including all detectors on one side of spacecraft (n6–nb) plus n3 and n4. The burst was detected by BGO detector b1 up to  $\sim 2$  MeV. Also in this case, an ARR was issued from GBM to LAT, so that the detectors’ angles with respect to the burst location had to be carefully examined over the whole burst duration. Detectors n7 and n8 are relatively stable in orientation during the burst’s main emission (angles between  $26^\circ$  and  $22^\circ$ , and between  $28^\circ$  and  $30^\circ$ , respectively) and therefore represent the best choice for the spectral analysis.

Light curves for GRB 090328 are shown in Figure 4.4. The burst profile is very similar to the one of GRB 090323, the difference being the total duration of the detected emission. While GRB 090323 extended over 150 s, GRB 090328 has much shorter duration with  $T_{90} = 57 \pm 3$  s and  $T_{50} = 15.4 \pm 1.0$  s. For the spectral analysis, the burst was divided in five intervals (*a* to *e*).

Columns 2 and 3 of Table 4.1 summarize the interval time selection and the

corresponding NaI detector pairs chosen for spectral analysis of each burst. Response matrices were calculated in the middle of each interval.

### 4.1.3 Time–Resolved Spectral Analysis

Spectral analysis was performed using the GBM data only. This analysis includes data from the NaI detectors n6, n7, n9 and nb and the BGO detector b1 in the case of GRB 090323, and from the NaI detectors n7 and n8, and the BGO detector b1 in the case of GRB 090328. The NaI data are fit from 8 keV to 1 MeV and the BGO data from 250 keV to 40 MeV using the TTE data type. Since TTE files only include data from  $\sim T_0 - 30$  s to  $\sim T_0 + 300$  s, the background evaluation for each time interval had to be computed using the CSPEC data type. The fits were performed with the spectral analysis software package RMFIT (version 3.2), which has the capability of reading and importing backgrounds from CSPEC data type into the TTE data types.

Due to the length and the slewing constraints, a time–integrated spectral fit of GRB 090323 can not be performed using all NaI detectors, but only with n9 (which kept the source at a small angle for the whole duration of the emission) and b1. For the time–resolved spectral analysis, the best NaI detector pair was fitted together with BGO detector b1 with various spectral models, such as (i) the simple power–law (*PL*) function; (ii) a power–law function with an exponential high–energy cutoff (*Comptonized*), where the cutoff energy is parameterized as  $E_{\text{peak}}$ ; and (iii) a typical GRB *Band* function. The time–integrated spectrum of GRB 090323 is best modeled by a Band function with an  $E_{\text{peak}}$  of about 600 keV. In the case of GRB 090328, the time–integrated spectrum is best modeled by a power–law with exponential high–energy cutoff with an  $E_{\text{peak}}$  of about 750 keV.

Results for GRB 090323 and GRB 090328 for the time–resolved spectral analysis of both events are given in Table 4.1. Spectral evolution throughout the bursts is apparent from the changing  $E_{\text{peak}}$  values. In the case of GRB 090323, the highest  $E_{\text{peak}}$  is measured during the first emission episode (interval *a*), which is best fitted by a Band model. The counts spectra is shown in Figure 4.5, *top panel*. The value of the low–energy spectral index  $\alpha$  remains fairly stable throughout the whole burst, while the high–energy spectral index  $\beta$  is constrained only in the first (*a*) and last (*g*) intervals. The plateau phase of the burst (*interval e*) is best fit by a simple power–law with an index of  $\sim 1.6$ .

In the case of GRB 090328, the time–integrated spectrum is best modeled by a power–law with exponential high–energy cutoff.  $E_{\text{peak}}$  is higher than the one of

#### 4. FIRST YEAR OF GBM SCIENTIFIC RESULTS

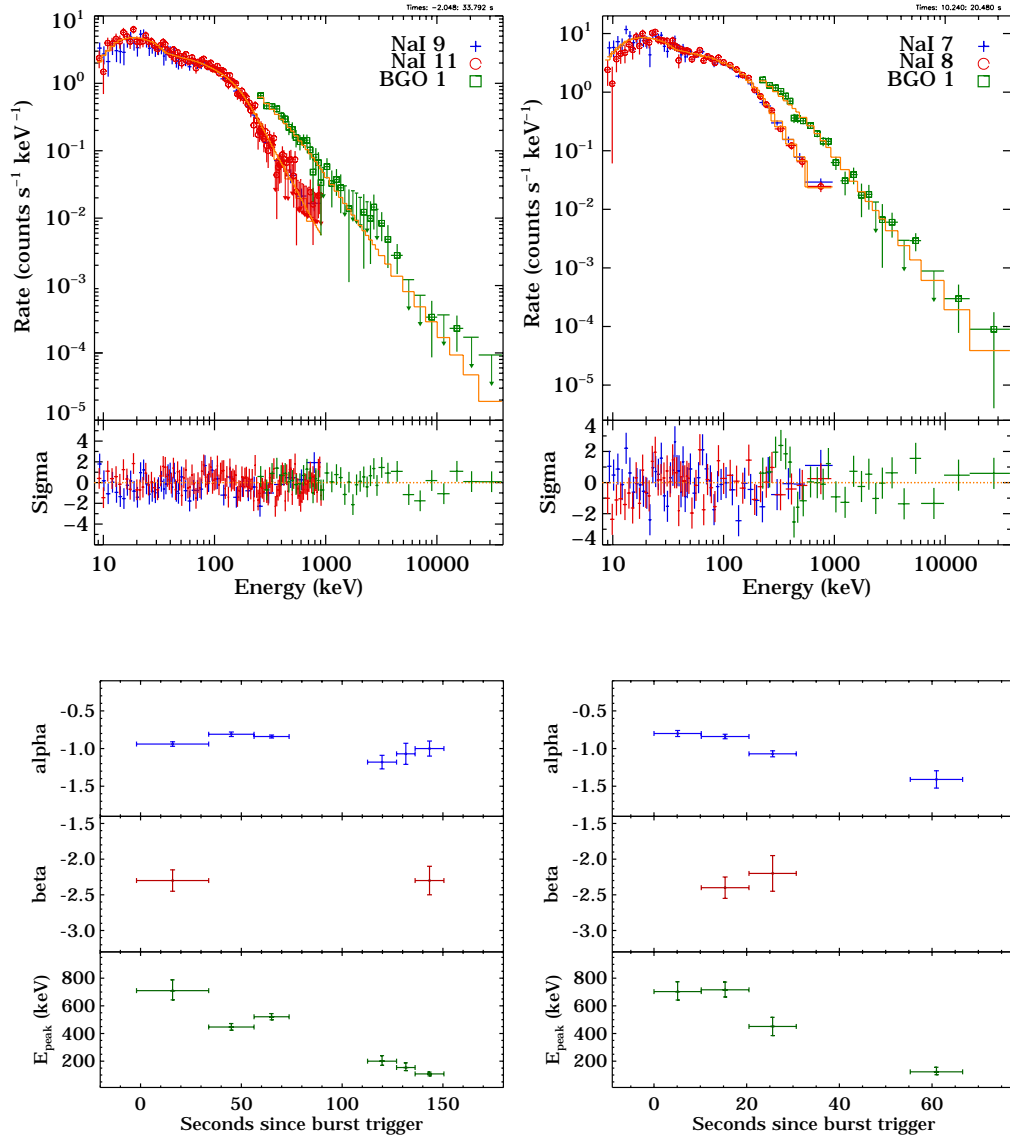


**Figure 4.5:** Top panels: Band fit of GBM data for interval *a* of GRB 090323 (left) and componentized fit to GBM data for interval *a* of GRB 090328 (right). Bottom panels: Temporal evolution of the spectral parameters  $\alpha$ ,  $\beta$  and  $E_{\text{peak}}$  for GRB 090323 (left) and GRB 090328 (right)

Table 4.1: Spectral fit parameters for GRB 090323 and GRB 090328

Interval	Det.	Time range (s)	Model	$E_{\text{peak}}^a$ (keV)	$\alpha^b$	$\beta^c$	$\gamma^d$	CSTAI/DOF	Energy fluence ( $\text{erg cm}^{-2}$ , 8 keV–1 MeV)
<b>GRB 090323</b>									
...	n9,b1	-2.0–150.5	<i>Band</i>	591 <sup>(+36)</sup> <sub>(-33)</sub>	-1.05 ( $\pm 0.02$ )	-2.7 <sup>(+0.2)</sup> <sub>(-0.4)</sub>	...	888/237	(1.22 $\pm$ 0.02) $\times 10^{-4}$
<b>a.</b>	n9,nb,b1	-2.0–33.8	<i>Band</i>	710 <sup>(+78)</sup> <sub>(-67)</sub>	-0.94 ( $\pm 0.03$ )	-2.3 <sup>(+0.1)</sup> <sub>(-0.2)</sub>	...	474/356	(3.48 $\pm$ 0.06) $\times 10^{-5}$
<b>b.</b>	n9,nb,b1	33.8–56.3	<i>Comp</i>	447 <sup>(+25)</sup> <sub>(-23)</sub>	-0.81 ( $\pm 0.03$ )	...	...	517/357	(2.72 $\pm$ 0.04) $\times 10^{-5}$
<b>c.</b>	n9,nb,b1	56.3–73.7	<i>Comp</i>	521 <sup>(+23)</sup> <sub>(-22)</sub>	-0.84 ( $\pm 0.02$ )	...	...	475/357	(3.47 $\pm$ 0.04) $\times 10^{-5}$
<b>d.</b>	n9,nb,b1	73.7–112.6	<i>PL</i>	...	...	...	-1.57 ( $\pm 0.02$ )	663/359	(1.06 $\pm$ 0.02) $\times 10^{-5}$
<b>e.</b>	n7,n9,b1	112.6–127.0	<i>Comp</i>	200 <sup>(+40)</sup> <sub>(-30)</sub>	-1.18 ( $\pm 0.09$ )	...	...	437/358	(3.76 $\pm$ 0.22) $\times 10^{-6}$
<b>f.</b>	n7,n9,b1	127.0–136.2	<i>Comp</i>	154 <sup>(+34)</sup> <sub>(-22)</sub>	-1.07 <sup>(+0.14)</sup> <sub>(-0.13)</sub>	...	...	371/358	(2.34 $\pm$ 0.14) $\times 10^{-7}$
<b>g.</b>	n6,n9,b1	136.2–150.5	<i>Band</i>	108 <sup>(+13)</sup> <sub>(-14)</sub>	-1.00 <sup>(+0.11)</sup> <sub>(-0.09)</sub>	-2.3 ( $\pm 0.2$ )	...	450/358	(5.99 $\pm$ 0.22) $\times 10^{-6}$
<b>GRB 090328</b>									
...	n7,n8,b1	0.0–66.6	<i>Comp</i>	744 <sup>(+50)</sup> <sub>(-47)</sub>	-1.07 ( $\pm 0.02$ )	...	...	644/360	(5.09 $\pm$ 0.04) $\times 10^{-5}$
<b>a.</b>	n7,n8,b1	0.0–10.2	<i>Comp</i>	703 <sup>(+71)</sup> <sub>(-61)</sub>	-0.80 ( $\pm 0.04$ )	...	...	388/361	(1.20 $\pm$ 0.02) $\times 10^{-5}$
<b>b.</b>	n7,n8,b1	10.2–20.5	<i>Band</i>	716 <sup>(+56)</sup> <sub>(-52)</sub>	-0.84 ( $\pm 0.03$ )	-2.4 <sup>(+0.1)</sup> <sub>(-0.2)</sub>	...	430/360	(2.01 $\pm$ 0.03) $\times 10^{-5}$
<b>c.</b>	n7,n8,b1	20.5–30.7	<i>Band</i>	451 ( $\pm 66$ )	-1.07 <sup>(+0.05)</sup> <sub>(-0.04)</sub>	-2.2 <sup>(+0.3)</sup> <sub>(-0.3)</sub>	...	436/360	(1.22 $\pm$ 0.02) $\times 10^{-5}$
<b>d.</b>	n7,n8,b1	30.7–55.3	<i>PL</i>	...	...	...	-1.52 ( $\pm 0.03$ )	480/362	(4.12 $\pm$ 0.15) $\times 10^{-6}$
<b>e.</b>	n7,n8,b1	55.3–66.6	<i>Comp</i>	123 <sup>(+33)</sup> <sub>(-21)</sub>	-1.41 <sup>(+0.12)</sup> <sub>(-0.11)</sub>	...	...	354/361	(1.87 $\pm$ 0.12) $\times 10^{-6}$

<sup>a</sup>Fitted  $E_{\text{peak}}$  for the *Band* or *Comptonized (Comp)* models;<sup>b</sup>Low-energy spectral index  $\alpha$  for the *Band* or *Comptonized* models;<sup>c</sup>High-energy spectral index  $\beta$  for the *Band* model;<sup>d</sup>Spectral index  $\gamma$  for the *PL* model.The time range values are relative to the trigger time  $T_0$ .

## 4. FIRST YEAR OF GBM SCIENTIFIC RESULTS

---

GRB 090323 and has a value of about 750 keV. The spectral evolution is similar, too, with a decreasing  $E_{\text{peak}}$  and a Band model that can be well constrained only in the second and third intervals ( $b$  and  $c$ ). The highest  $E_{\text{peak}}$  is measured during the second emission episode (interval  $b$ ) and its counts spectrum is shown in the bottom panel of Figure 4.5. Again, the plateau phase of the burst (interval  $d$ ) is best fit by a simple power-law. In this case, the index is  $\sim 1.5$ .

The energy fluences in the 8–1000 keV range were computed for both GRBs for the time-integrated and time-resolved spectra and are listed in the last column of Table 4.1. The 128 ms peak photon flux over the same energy range is  $15.6 \pm 1.2 \text{ ph s}^{-1} \text{ cm}^{-2}$  in the case of GRB 090323 and  $23.6 \pm 0.9 \text{ ph s}^{-1} \text{ cm}^{-2}$  in the case of GRB 090328. Knowing the GRB redshifts and assuming a standard cosmology model with  $H_0 = 70 \text{ km/s/Mpc}$ ,  $\Omega_M = 0.3$ ,  $\Omega_\Lambda = 0.7$ , we calculated the isotropic energy releases in the cosmological rest-frame, resulting in values of  $E_{\text{iso}} \cong 4 \times 10^{54} \text{ erg}$  and  $E_{\text{iso}} \cong 1 \times 10^{53} \text{ erg}$ , respectively. The rest-frame peak energies are  $\sim 2.4 \text{ MeV}$  and  $\sim 1.3 \text{ MeV}$ , respectively.

### 4.2 Joint GBM–LAT Observations

With the combination of its two instruments, *Fermi* can simultaneously observe GRBs with an unprecedented effective area above 100 MeV. Thanks to *Fermi*, the number of GRBs ever detected at high energies has rapidly increased during the first few months of the mission, providing more statistics and, for the first time, enough events at high energy for performing a detailed temporal–spectral analysis. As of December 1<sup>st</sup> 2009, 13 GRBs have been detected by the LAT at energies above 100 MeV. They are listed in Table 4.2 together with their main properties, such as duration (column 2), number (column 3) and highest energy of the measured LAT events (column 8), type of emission (columns 5–7) and redshift information (column 9). References to all GCNs published by the GBM and LAT collaborations are given in column 10.

In the current section, I briefly present an overview of the four most interesting GBM–LAT bursts recently published by the *Fermi* Collaboration, namely (i) GRB 080825C (Abdo et al., 2009a), (ii) GRB 080916C (Abdo et al., 2009b), (iii) GRB 081024B (Abdo et al., 2010a), and (iv) GRB 090510 (Abdo et al., 2009d). A separate section is finally devoted to the detailed description and analysis of the energetic GRB 090902B (§4.3).

**Table 4.2:** Properties of joint GBM–LAT detected bursts

GRB (1)	Duration (2)	# Events >100 MeV (3)	ARR (4)	Delayed Onset (5)	Long-lived Emission (6)	Extra Component (7)	Highest Energy (GeV) (8)	Redshift (9)	GBM/LAT GCN # (10)
080825C	long	~10	no	?	yes	no	0.57	–	8141 <sup>a</sup> , 8183 <sup>b</sup> , 8184 <sup>c</sup>
080916C	long	>100	no	yes	yes	?	13.2	4.35 <sup>l</sup>	8245 <sup>d</sup> , 8246 <sup>e</sup> , 8278 <sup>f</sup>
081024B	short	~10	no	yes	yes	?	3.1	–	8407 <sup>g</sup> , 8408 <sup>h</sup>
081215	long	–	–	–	–	–	–	–	8678 <sup>i</sup> , 8684 <sup>j</sup>
090217	long	~10	no	no	no	no	0.87	–	8902 <sup>k</sup> , 8903 <sup>l</sup>
090323	long	~20	yes	?	yes	?	?	3.57 <sup>2</sup>	9035 <sup>m</sup> , 9021 <sup>n</sup>
090328	long	~20	yes	?	yes	?	?	0.736 <sup>3</sup>	9044 <sup>o</sup> , 9057 <sup>p</sup> , 9077 <sup>q</sup>
090510	short	>150	yes	yes	yes	yes	31.3	0.903 <sup>4</sup>	9334 <sup>r</sup> , 9336 <sup>s</sup> , 9350 <sup>t</sup>
090626	long	~20	no	?	yes	?	?	–	9579 <sup>u</sup> , 9584 <sup>v</sup>
090902B	long	>200	yes	yes	yes	yes	33.4	1.822 <sup>5</sup>	9866 <sup>w</sup> , 9867 <sup>x</sup> , 9872 <sup>y</sup>
090926A	long	>150	yes	yes	yes	yes	19.6	2.106 <sup>6</sup>	9933 <sup>z</sup> , 9934 <sup>aa</sup> , 9974 <sup>ab</sup>
091003A	long	~20	yes	?	?	?	1.2	0.897 <sup>7</sup>	9983 <sup>ac</sup> , 9985 <sup>ad</sup>
091031	long	~20	no	?	?	?	2.2	–	10115 <sup>ae</sup> , 10163 <sup>af</sup>

<sup>a</sup>van der Horst & Connaughton (2008); <sup>b</sup>Bouvier et al. (2008); <sup>c</sup>van der Horst et al. (2008); <sup>d</sup>Goldstein & van der Horst (2008); <sup>e</sup>Tajima et al. (2008); <sup>f</sup>van der Horst & Goldstein (2008); <sup>g</sup>Omodei (2008); <sup>h</sup>Connaughton & Briggs (2008); <sup>i</sup>Preece (2008); <sup>j</sup>McEnery et al. (2008); <sup>k</sup>von Kienlin (2009a); <sup>l</sup>Ohno et al. (2009a); <sup>m</sup>van der Horst et al. (2009a); <sup>n</sup>Ohno et al. (2009b); <sup>o</sup>McEnery et al. (2009a); <sup>p</sup>Rau et al. (2009a); <sup>q</sup>Cutini et al. (2009); <sup>r</sup>Ohno et al. (2009c); <sup>s</sup>Guiriec et al. (2009); <sup>t</sup>Omodei et al. (2009); <sup>u</sup>von Kienlin (2009b); <sup>v</sup>Piron et al. (2009); <sup>w</sup>Bissaldi & Connaughton (2009); <sup>x</sup>de Palma et al. (2009a); <sup>y</sup>de Palma et al. (2009b); <sup>z</sup>Bissaldi (2009); <sup>aa</sup>Uehara et al. (2009); <sup>ab</sup>Bissaldi et al. (2009b); <sup>ac</sup>Rau (2009); <sup>ad</sup>McEnery et al. (2009b); <sup>ae</sup>McBreen & Chaplin (2009); <sup>af</sup>de Palma et al. (2009c);

<sup>1</sup>Greiner et al. (2009b); <sup>2</sup>Chornok et al. (2009); <sup>3</sup>Cenko et al. (2009); <sup>4</sup>Rau et al. (2009b); <sup>5</sup>Cucchiara et al. (2009a); <sup>6</sup>Malesani et al. (2009); <sup>7</sup>Cucchiara et al. (2009b).

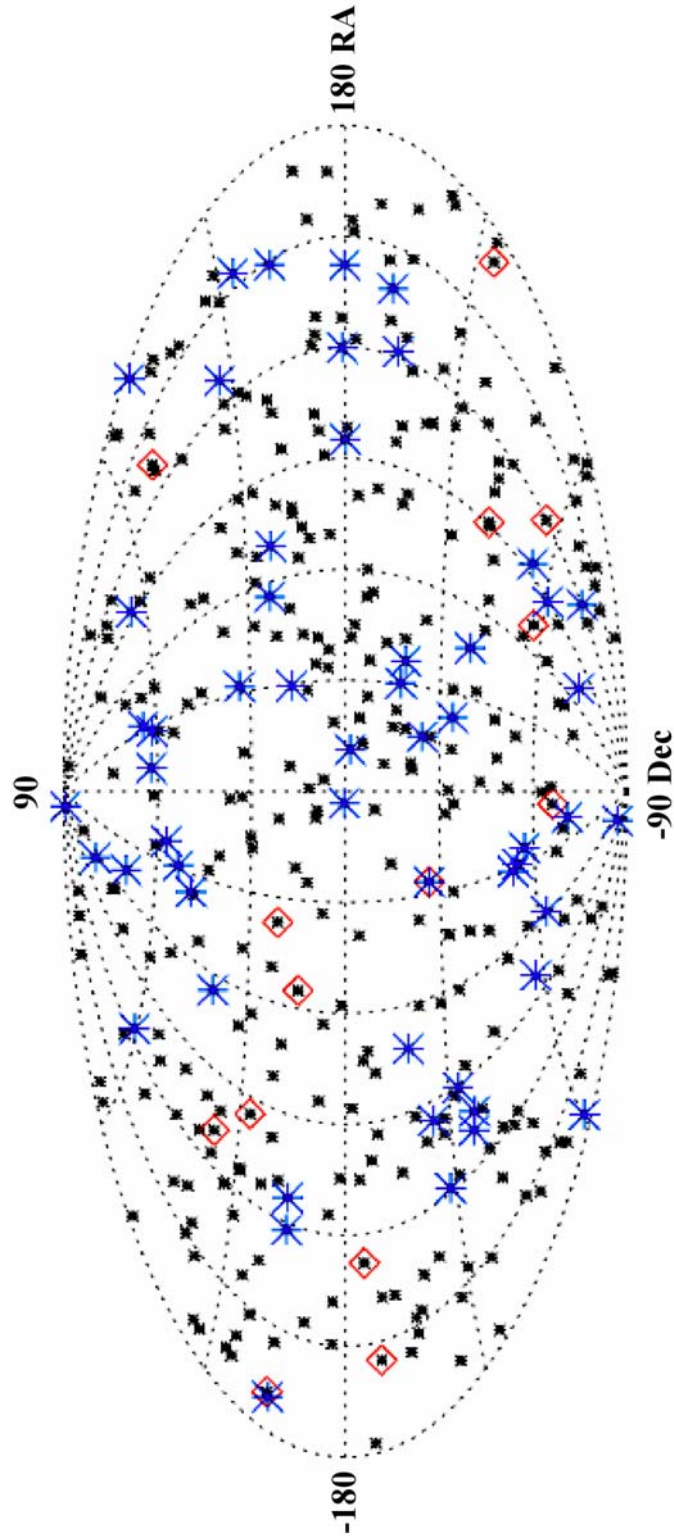


**Figure 4.6:** Sky map in galactic coordinates of 375 GRBs detected by *Fermi*-GBM (*black stars*) as of January 22, 2010. Bursts jointly observed by the LAT and by *Swift* are marked as *red diamonds* (14 events) and *blue stars* (54 events), respectively

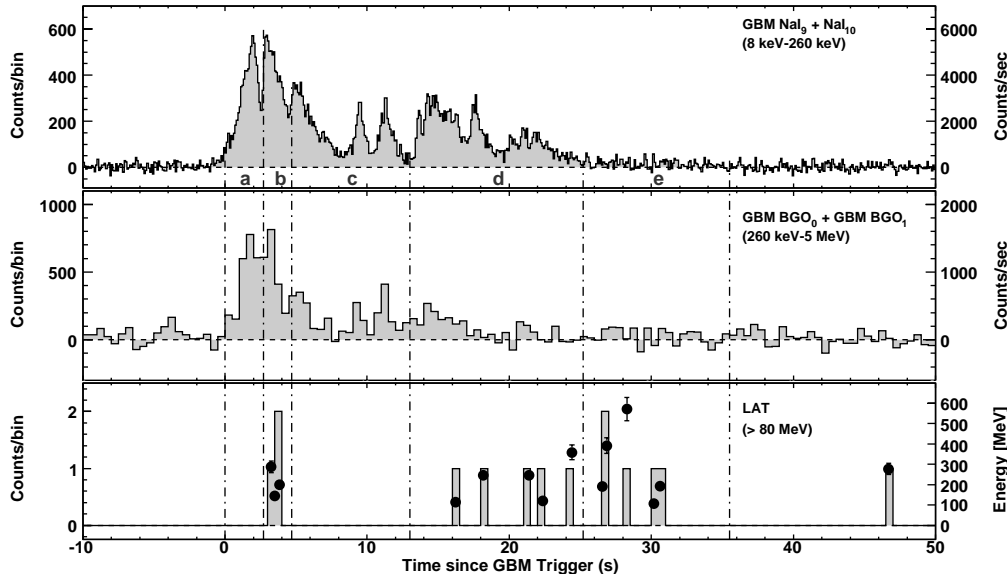


**Figure 4.7:** Light curves of GRB 080825C observed by the GBM and LAT instruments. The *top panel* shows the sum of the counts, in the 8–260 keV energy band, of two NaI detectors (n9 and na, background–subtracted). The second is the corresponding plot for both BGO detectors b0 and b1, between 260 keV and 5 MeV. The per–second counting rate is reported on the right for convenience. The LAT light curve in the bottom panel has been generated using events above 80 MeV. Black dots, along with their error bars (systematic uncertainty in the LAT energy measurement) represent the  $1\sigma$  energy range (right y–axis) for each LAT event. The vertical dash–dotted lines indicate the time bins used in the time–resolved spectral analysis. From Abdo et al. (2009a)

## GRB 080825C

The burst of the 25th August 2008, was the first GRB firmly detected by the LAT, with 13 events above 80 MeV. The GBM flight software triggered at 14:13:48 UT on the signal from GRB 080825C (trigger 241366429), localizing it at  $\sim 60^\circ$  from the LAT boresight at the time of the trigger, which puts it at the edge of the LAT FoV where the effective area is a factor of  $\sim 3$  less than on–axis. The top two panels of Figure 4.7 show the background–subtracted light curves of the two brightest NaI detectors (n9 and na) and of the two BGO detectors. The GRB exhibits a multiple–peak structure with the two brightest peaks seen right after onset. The  $T_{90}$  and  $T_{50}$  durations of the event were estimated to be (8–1000 keV)  $\sim 27$  s and  $\sim 13$  s, respectively.

The LAT “transient” selected events (see chapter 2, §2.1.4) above 100 MeV, detected close to the GBM position around the trigger time are shown in the bot-

#### 4. FIRST YEAR OF GBM SCIENTIFIC RESULTS

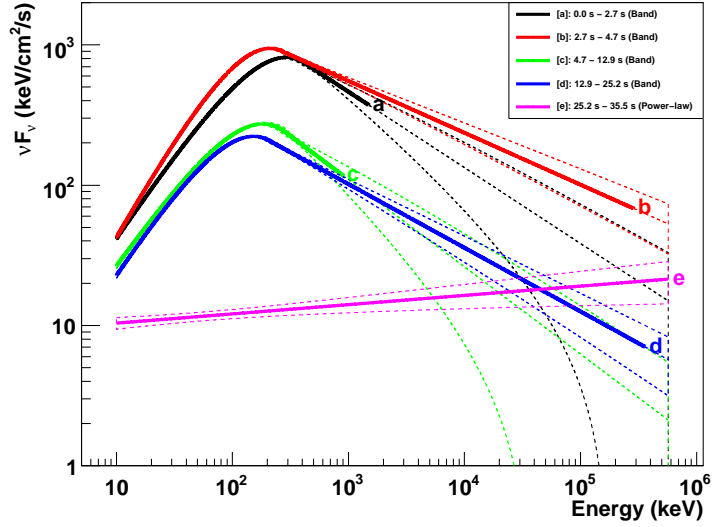


**Figure 4.8:** Time-resolved spectral analysis results for GRB080825C. Best-fit spectra for time bins *a* to *e* are shown in *thick solid lines* that reach up to the largest detected photon energy in each time bin, while the corresponding (same color) *thin dashed lines* represent the  $1\sigma$  confidence contours for each fit. From Abdo et al. (2009a)

tom panel of Figure 4.7. The LAT data shows a count rate increase that is spatially and temporally correlated with the GBM emission (for a statistical significance of more than  $6\sigma$ ). From the LAT light curve, the emission above 100 MeV is apparently delayed by few seconds (2.7 seconds, *interval a*) but this delay is not statistically significant due to the lack of events. As measured in the GBM, the first peak is spectrally softer than subsequent peaks, and the LAT does not see any counts above 100 MeV during this time. The pulse in the GBM light curve at *interval b* is accompanied by LAT emission, while the three pulses during *interval c* are not. In *interval d* both LAT and GBM emission are present, while *interval e*, in which the LAT records the highest energy event for this burst ( $572 \pm 58$  MeV), does not show evident GBM emission. A search for a possible afterglow emission was performed up to 13 ks after the trigger time but no significant emission was found.

Detailed spectroscopy of the combined GBM and LAT data was performed and is shown in Figure 4.8 in the standard  $\nu F\nu$  representation. The time-integrated spectrum and the time bins *a* to *d* are best fit to a significant degree by the Band function with the high-energy spectral index consistent with  $-2.5$ . They display the typical hard-to-soft evolution of  $E_{\text{peak}}$  (Norris et al., 1986), starting at almost

300 keV and decreasing to  $\sim 150$  keV. Except for the second interval, the values of  $\alpha$  and  $\beta$  are constant within their uncertainties. For *interval e* (no evident GBM emission) the spectrum is adequately described by a single power-law with a photon index of  $\sim -1.9$ . This is significantly harder than the values of  $\beta$  in all of the earlier time bins. This fact, combined with the detection of the highest energy events, suggest that the late-time broad high-energy peak arises from a separate spectral component to that responsible for the low-energy emission. This is consistent with an origin from a distinct physical region, in particular from external shocks (reverse of forward, see chapter 1, §1.2.2 and §secFireb), rather than by internal dissipation within the GRB outflow.

### GRB 080916C

Another very interesting burst is the energetic and long-duration GRB 080916C (Abdo et al., 2009b). Detected at 00:12:45 UT on September 16, 2008, the GRB produced large signals in 9 of the 12 NaI detectors and in one of the two BGO detectors. At the time of the trigger, the GRB was located  $\sim 48^\circ$  from the LAT boresight and on-ground analysis revealed a bright source consistent with the GRB location. The LAT refined localization enabled rapid follow-up by *Swift* and by ground-based telescopes, and a redshift of  $z = 4.35 \pm 0.15$  could be determined (Greiner et al., 2009b). The light curve of GRB 080916C is shown in Figure 4.9. The total number of LAT counts after background subtraction in the first 100 s after the trigger was  $> 3000$ . After applying standard selection cuts Atwood et al. (2009) for transient sources with energies greater than 100 MeV and directions compatible with the burst location, 145 events remained (panel 4), and 14 events had energies  $> 1$  GeV. The light curve was divided into five time intervals (*a to e*). At low energy, two bright peaks are observed in *interval a* and *interval b*. In the LAT detector the first peak is not significant, showing that the  $>100$  MeV emission is delayed with respect to the GBM emission. The delayed onset of the GRB 080916C LAT pulse, which coincides with the rise of the second peak in the GBM light curve, indicates that the two peaks may originate in spatially distinct regions, as was the case of GRB 080825C previously described. The highest energy photon of 13.2 GeV was observed during *interval d*.

The spectral evolution of GRB 080916C during the prompt emission is always consistent with a Band function, for which the spectral parameters evolve with time, characterizing observed temporal behaviour (Figure 4.10). After the first interval there is no significant evolution in either  $\alpha$  or  $\beta$ . In contrast,  $E_{\text{peak}}$  evolves

#### 4. FIRST YEAR OF GBM SCIENTIFIC RESULTS

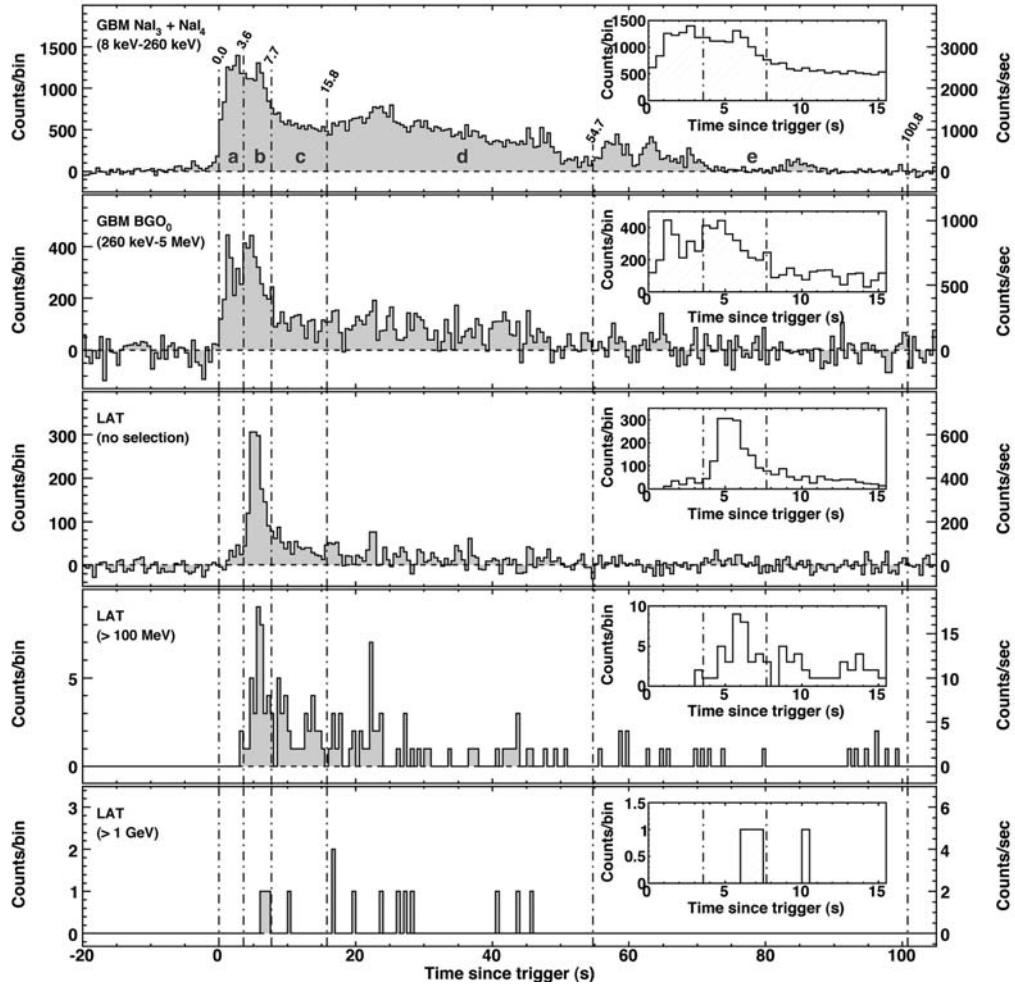


**Figure 4.9:** Light curves of GRB 080916C observed by the GBM and LAT instruments. The *top panel* shows the sum of the counts, in the 8–260 keV energy band, of two NaI detectors (n3 and n4, background–subtracted). The second is the corresponding plot for BGO detector 0, between 260 keV and 5 MeV. The LAT light curves in the bottom three panels have been generated using all events, events above 100 MeV and above 1 GeV, respectively. The vertical dash–dotted lines indicate the time bins used in the time–resolved spectral analysis. The inset panels give views of the first 15 s from the trigger time. In all cases, the bin width is 0.5 s; the per–second counting rate is reported on the right for convenience. From Abdo et al. (2009b)

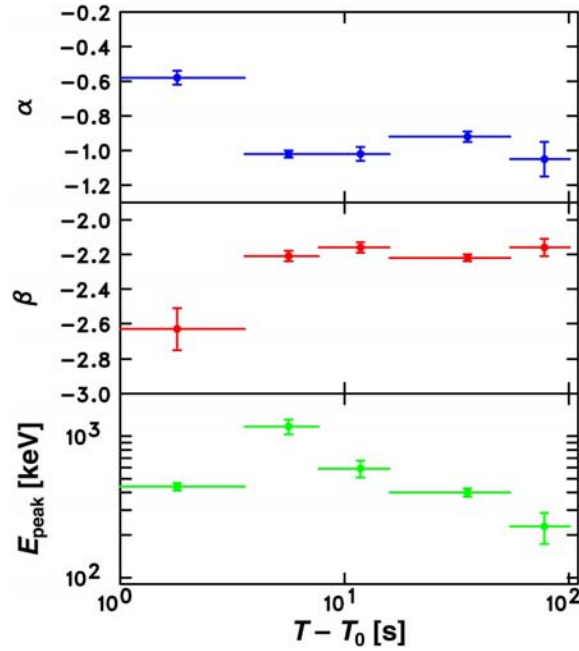


**Figure 4.10:** GRB 080916C fit parameters for the Band function,  $\alpha$ ,  $\beta$  and  $E_{\text{peak}}$  as a function of time. From Abdo et al. (2009b)

from the first time bin to reach its highest value in the second time bin, then softened through the remainder of the GRB. The fact that the event energy spectra up to  $\sim 100$  s are consistent with a single model suggests that a single emission mechanism dominates. A non-thermal synchrotron emission is the favored emission mechanism at keV to MeV energies, however, it should be accompanied by a synchrotron self-Compton (SSC) spectral component produced from electrons that Compton upscatter their synchrotron photons to gamma-ray energies potentially in the LAT energy band. The apparent absence of an SSC component indicates that the magnetic energy density is much higher than the electron energy density or that the SSC  $\nu F_\nu$  spectrum peaks at  $\gg 10$  GeV and thus cannot be detected.

Moreover, a long-lived emission in the LAT was found, lasting several hundreds of seconds longer than seen with GBM. It is intriguing that this emission in the LAT band exhibits different temporal behaviors from those in the GBM band. In particular, this measurement indicates a temporal break in the GBM band in contrary to the continuous decay in the LAT band. The LAT high-energy tail may indicate cascades induced by ultra-relativistic ions accelerated in GRBs (Dermer & Atoyan, 2006), or angle-dependent scattering effects (Wang et al., 2006).

#### 4. FIRST YEAR OF GBM SCIENTIFIC RESULTS

---

The redshift information combined with LAT and GBM measurements provides several kinematic constraints on this GRB. Between 10 keV and 10 GeV in the observer’s frame, the fluence is  $f = 2.4 \times 10^{-4}$  erg cm<sup>-2</sup> which gives an apparent isotropic energy release of  $E_{\text{iso}} \approx 8.8 \times 10^{54}$  erg. This is  $\sim 4.9$  times the Solar rest energy, and therefore strongly suggests that the GRB outflow powering this emission occupied only a small fraction ( $\lesssim 10^{-2}$ ) of the total solid angle, and was collimated into a narrow jet. Given the intensity of observed photons, a large bulk Lorentz factor  $\Gamma$  is required to avoid the attenuation of high-energy photons in a compact emission region expected from rapid variability (Krolik & Pier, 1991). Using the Band function as the target radiation field and setting to unity the optical depth  $\tau_{\gamma\gamma}$  to gamma-ray pair production attenuation of the highest-energy observed photon,  $\Gamma_{\text{min}} \approx 608 \pm 15$  and  $887 \pm 21$  are obtained in *interval d* and *interval b*, respectively.

#### **GRB 081024B**

GRB 081024B was the first short GRB with observed emission above GeV energies. It triggered the GBM FSW at 21:22:41 UT on October 24, 2008 (trigger 246576161), and the LAT detected an increased count rate associated with it. Selecting LAT “transient” events with energy above 100 MeV, the significance for the detection of this burst is above  $6\sigma$ . The multi detector light curve is shown in Figure 4.11 and was divided in three intervals (*a* to *c*). The third panel shows the LAT signal without any selection. The quality of these events is not good enough to use them in the spectral analysis, but the properties of the ensemble can be assessed quantitatively. The last panel shows the light curve of the “transient” selected events with well defined direction and energy ( $>100$  MeV). The highest energy events are a 3.1 GeV and a  $1.7 \pm 0.1$  GeV photon. For GRB 081024B, the  $T_{50}$  ( $T_{90}$ ) is 0.33 s (0.66 s) in the NaI detectors, 0.15 s (0.27 s) in the BGO, while it is significantly longer for the LAT, corresponding to 0.9 s (2.1 s) for the full statistic light curve and 1.5 s (2.6 s) selecting only the events above 100 MeV. Moreover, GRB 081024B was searched for spectral lags, however no energy-dependent delay between any of the data types was found.

A time-resolved spectral analysis was performed in all intervals. In *interval a* the best fit to the GBM data is obtained with a power-law with exponential cutoff. The LAT upper limit on the photon flux in the 100 MeV–10 GeV energy range is consistent with the extrapolated flux from the COMPT function fitted to the GBM data. *Interval b* is best represented by a Band function, while *interval c* is

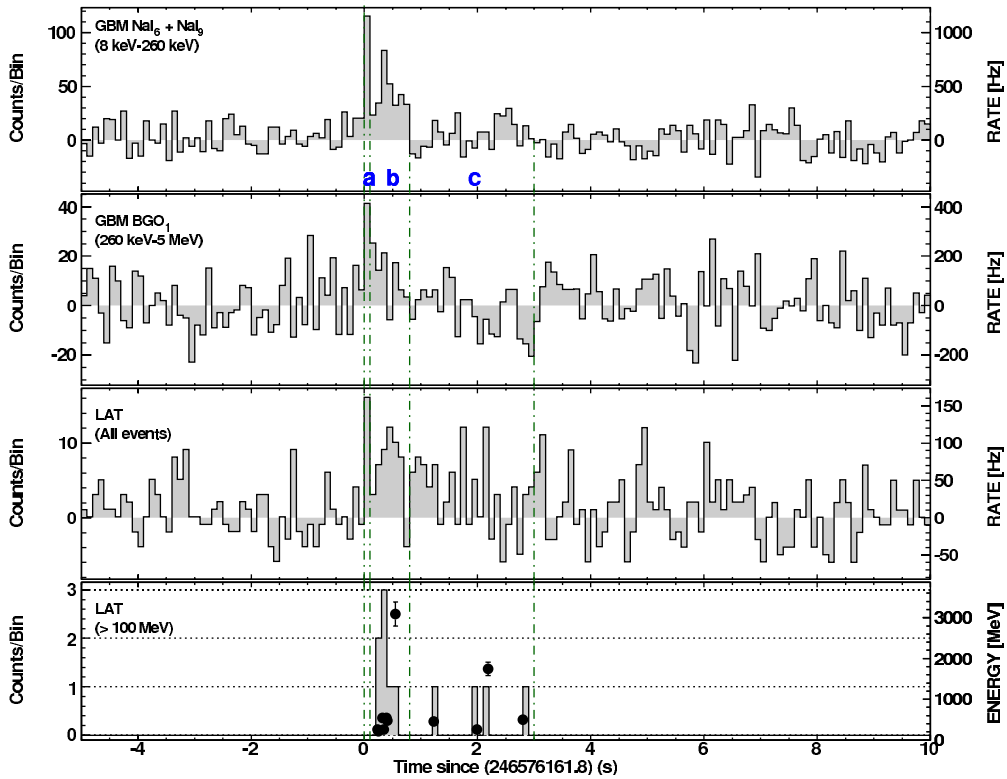


**Figure 4.11:** Multi-instrument light curve for GRB 081024B. The top panel shows the sum of the background subtracted signal from two NaI detectors. The second panel is one BGO detector. The third panel shows all the events recorded by the LAT, without any selection on the quality of the events (background subtracted). The fourth panel shows the selected “transient” events above 100 MeV. The energy of events is reported at the right axis of the plot. The vertical dash-dotted lines indicate the time bins used in the time-resolved spectral analysis. From Abdo et al. (2010a)

best represented by a simple power-law. Unlike GRB 930131 (Kouveliotou et al., 1994), the 3 GeV photon is well correlated with the second low-energy pulse. While the majority of long GRB spectra are well fitted by the conventional Band function, previous spectral analyses of short GRBs have mostly used the cutoff power-law function. The exponential cut-off implies that the bulk motion of short GRBs is not necessarily ultra-relativistic, owing to the compactness problem for high-energy photons above  $m_e c^2$  (Mészáros, 2002). This difference between long and short GRBs may be due to poor counting statistics at high energies in short GRBs, stressing the need for a larger sample with sufficient high-energy photons in the MeV–GeV bands. As was already discussed for GRB 080825C and GRB 080916C, a delayed onset of a GeV pulse was observed in GRB 081024B,

## 4. FIRST YEAR OF GBM SCIENTIFIC RESULTS

---

too. The long-lasting tail of GeV emission is also a common feature of these GRBs.

### GRB 090510

GRB 090510 is an extremely bright short burst, detected on board by the LAT and by the GBM (trigger 263607781) on May 10, 2009, at 00:22:59.97 UT (Abdo et al., 2009d). More than 50 events above 100 MeV were detected in the first second after the GBM trigger (more than 10 events were detected above 1 GeV in the same interval). Ground-based optical spectroscopy data provided a redshift measurement of  $z = 0.903 \pm 0.003$  (Rau et al., 2009b). The GRB light curve is shown in Figure 4.12 and consists of several pulses. After the first dim short spike near trigger-time, the flux returns to background level; the main GBM emission starts at 0.53 s and lasts  $<0.5$  s. The main LAT emission above 100 MeV starts at  $\sim 0.63$  s and lasts  $\sim 1$  s with a decaying tail that extends to  $\sim 200$  s. A single 31-GeV photon was detected at 0.829 s, which coincides in time with the last of the seven GBM pulses.

Detailed spectroscopy was performed of the combined GBM and LAT data. The time-integrated spectrum is best fit to a significant degree by a Band function with an additional power-law component, with an extremely high  $E_{\text{peak}}$  of  $\sim 4$  MeV,  $\alpha \sim -0.6$ ,  $\beta \sim -3$ , and a PL Index  $\gamma \sim -1.6$ . The fluence for this burst in the 10 keV–30 GeV energy range is  $(5.02 \pm 0.26) \times 10^{-5} \text{ erg cm}^{-2}$ , and the isotropic energy is  $E_{\text{iso}} = (1.08 \pm 0.06) \times 10^{53} \text{ erg}$ . About 37% of the fluence is due to the presence of the extra component, and the EBL (see chapter 2, §2.1.4) affects the total fluence for  $< 1\%$ . Four individual time intervals (*a* to *d*) are best fitted as follows (see also Figure 4.13):

- *interval a*: Band function with steep beta (fixed at -5.0) and no evidence of extra component;
- *interval b*: Band plus power-law component;
- *interval c*: Band plus power-law component, where beta was fixed to the value from the previous bin and the extra component can be fit with a similar index.
- *interval d*: LAT only data are best fit by a power-law with a steeper index of  $\sim -1.9$ . The extrapolation of the fit at low energy is inconsistent with GBM upper limits. This could be due to a spectral break.

The LAT detector recorded also a long high-energy tail, lasting for about a minute, during which more than 150 events above 100 MeV ( $>20$  above 1 GeV) were

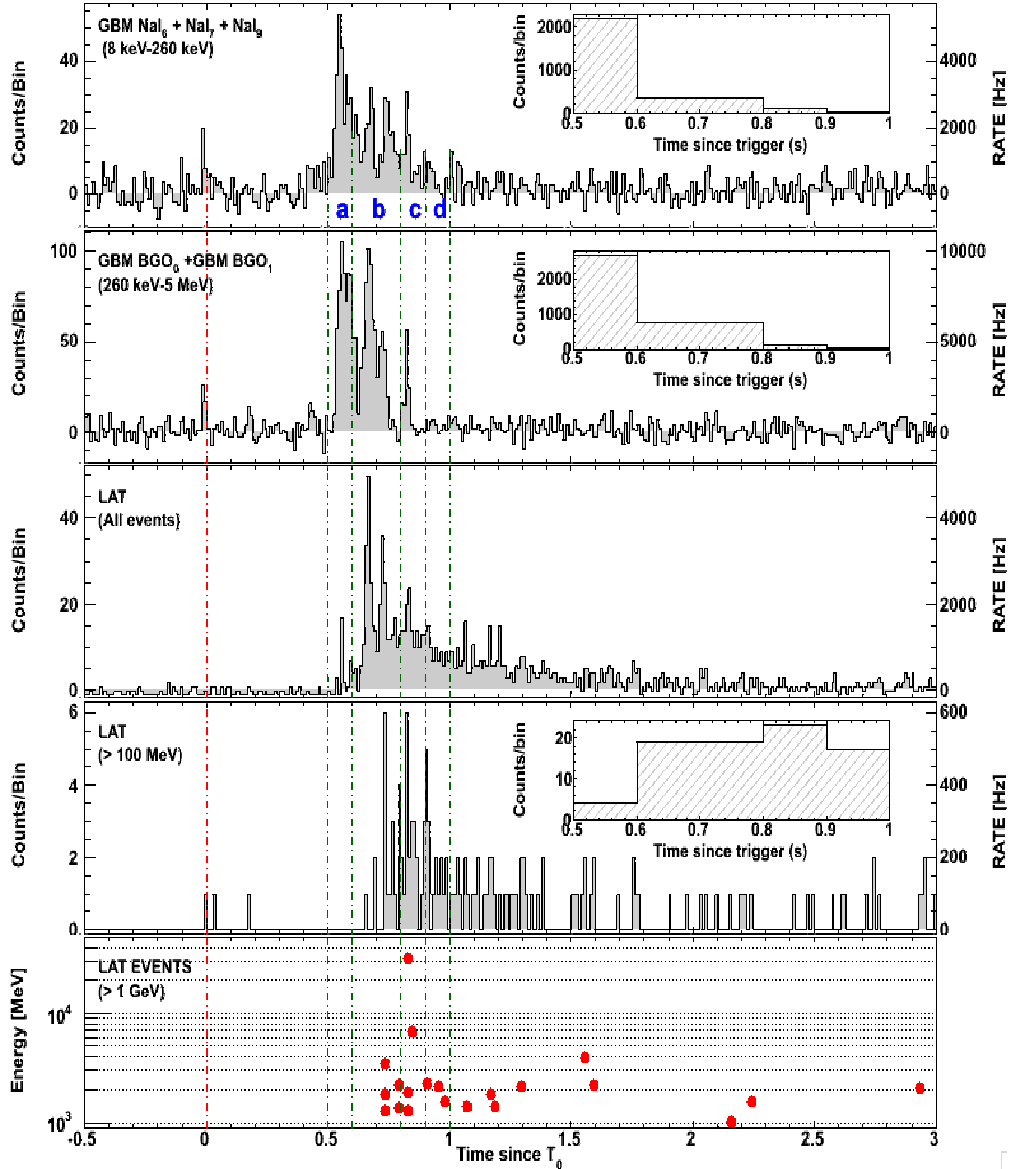


**Figure 4.12:** Multi-instrument light curve for GRB 090510. The top panel shows the sum of the background subtracted signal from two NaI detectors. The second panel is one BGO detector. The third panel shows all the events recorded by the LAT, without any selection on the quality of the events (background subtracted). The fourth panel shows the selected “transient” events above 100 MeV. The energy of events  $>1$  GeV is reported in the bottom panel. In all light curves, the time-bin width is 10 ms. The vertical dash-dotted lines indicate the time bins used in the time-resolved spectral analysis. The per-second count rate is displayed on the right for convenience. From Abdo et al. (2009d)

#### 4. FIRST YEAR OF GBM SCIENTIFIC RESULTS

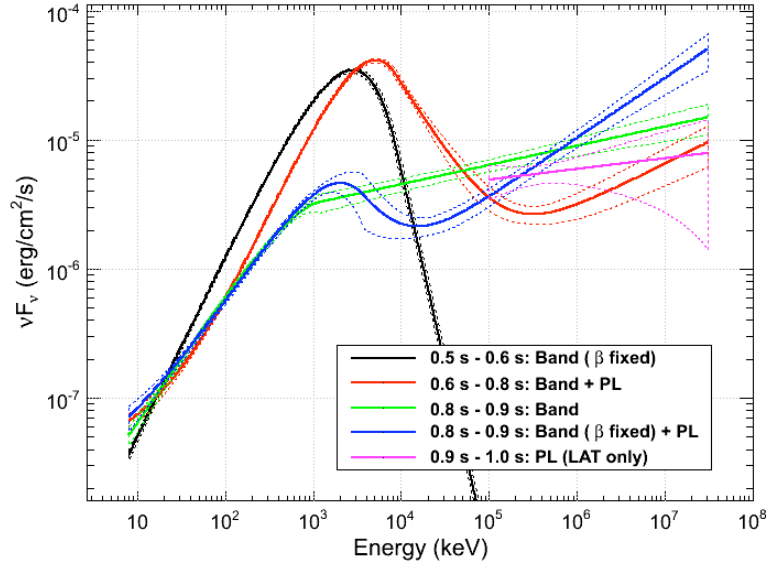


**Figure 4.13:** Time-resolved spectral analysis results for GRB 090510. Best-fit spectra for time bins *a* to *d* are shown in *thick solid lines* that reach up to the largest detected photon energy in each time bin, while the corresponding (same color) *thin dashed* lines represent the  $1\sigma$  confidence contours for each fit. *Interval c* is fitted with two different models for better comparison, namely a simple Band function (*green line*), and a Band function where beta was fixed to the value from the previous bin plus the extra component (*blue line*). From Abdo et al. (2009d)

detected. All these events are positionally consistent with the position of the GRB.

The known distance of GRB 090510 and the detection of  $>1$  GeV photons less than a second from its onset allow to constrain the possible variation of the speed of light with photon energy (known as photon dispersion: one form of the Lorentz Invariance Violation, LIV). While special relativity assumes that there is no fundamental length-scale associated with such invariance, there is a fundamental scale (the Planck scale,  $l_{\text{Planck}} \approx 1.62 \times 10^{-33}$  cm or  $E_{\text{Planck}} = M_{\text{Planck}} c^2 \approx 1.22 \times 10^{19}$  GeV), at which quantum effects are expected to strongly affect the nature of space-time. For this burst, no evidence for the violation of Lorentz invariance is found, and a lower limit of  $1.2 E_{\text{Planck}}$  is found on the scale of a linear energy dependence, subject to reasonable assumptions about the emission. These results disfavor quantum-gravity theories in which the quantum nature of space-time on a very small scale linearly alters the speed of light.

## 4.3 GRB 090902B<sup>2</sup>

This section gives a detailed report on the observation of the bright, long gamma-ray burst GRB 090902B detected by the GBM and LAT instruments. More information can be found in (Abdo et al., 2009e), a joint GBM–LAT paper for which I was “contact author”. GRB 090902B represents one of the brightest GRBs to have been observed by the LAT, which detected several hundred photons during the prompt phase. With a redshift of  $z = 1.822$ , this burst is among the most luminous detected so far by *Fermi*. Time-resolved spectral analysis reveals a significant power-law component in the LAT data that is distinct from the usual Band model emission that is seen in the sub-MeV energy range, similarly to what is seen in GRB 090510. Moreover, this power-law component appears to extrapolate from the GeV range to the lowest energies and is more intense than the Band component both below  $\sim 50$  keV and above 100 MeV. The LAT detected a photon with the highest energy (33.4 GeV) so far measured from a GRB. This event arrived 82 seconds after the GBM trigger and  $\sim 50$  seconds after the prompt-phase emission had ended in the GBM band. These results imply new constraints on models of GRB emission and on EBL models (see §4.3.3).

### 4.3.1 Observations and Light Curves

On September 2<sup>nd</sup>, 2009, at 11:05:08.31 UT, the GBM FSW triggered on and localized the bright burst GRB 090202B (trigger 273582310). The burst was within the LAT field of view initially at an angle of  $51^\circ$  from the boresight. This event was sufficiently bright in the GBM that an ARR was made, and the spacecraft began slewing within 10 seconds towards the burst. This burst was detected up to  $\sim 5$  MeV by GBM, and emission was significantly detected by the LAT, with 39 photons above 1 GeV. The highest energy photon had  $E = 33.4_{-3.5}^{+2.7}$  GeV and arrived 82 seconds after the GBM trigger; and the initial analyses detected photons as late as 300 seconds after the trigger.

The burst was followed-up in the X-ray and optical by *Swift* (Kennea & Stratta, 2009; Swenson & Stratta, 2009) and the afterglow redshift of  $z = 1.822$  was measured by Cucchiara et al. (2009a) using the GMOS spectrograph mounted on the Gemini–North telescope.

---

<sup>2</sup>The main contents of this section are published in Abdo et al. (2009e), “*Fermi Observations of GRB 090902B: A distinct spectral component in the prompt and delayed emission*”; *The Astrophysical Journal*, 706, 138 (Contact authors: E. Bissaldi, J. Chiang, F. De Palma and S. McBreen)

#### 4. FIRST YEAR OF GBM SCIENTIFIC RESULTS

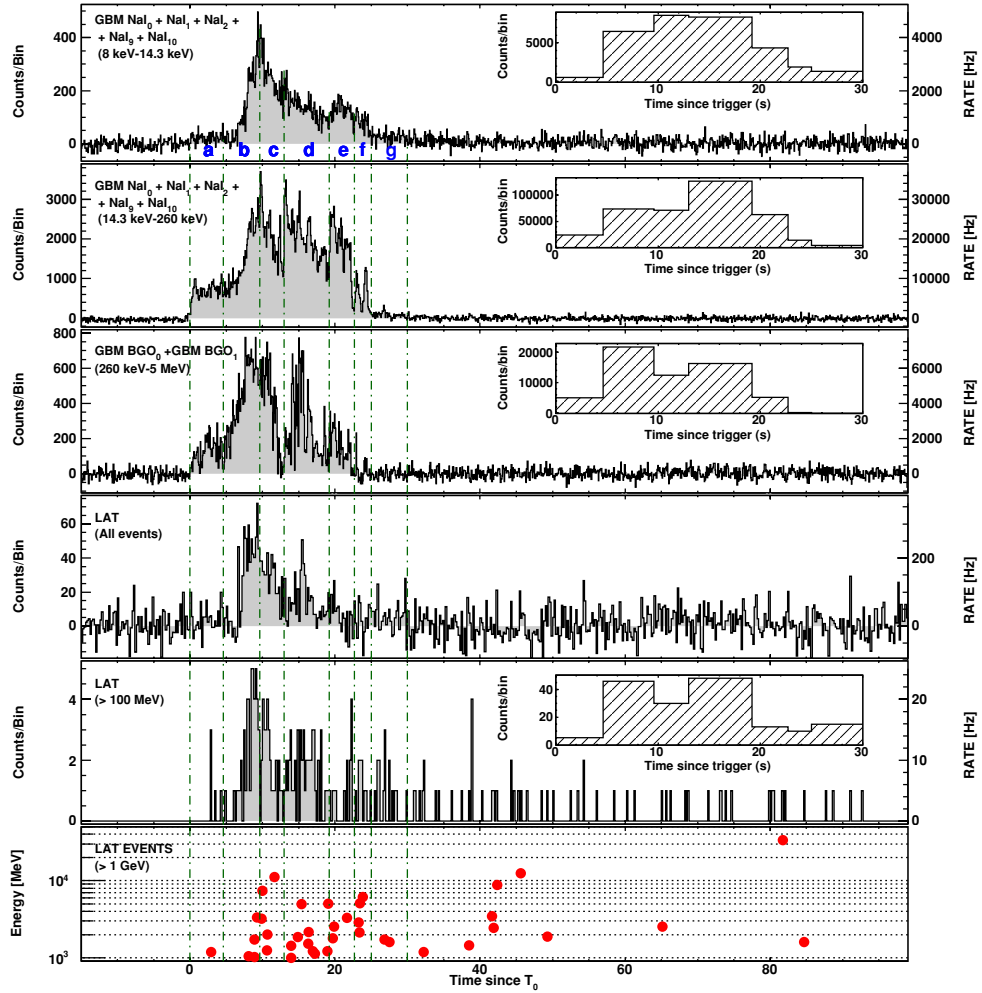


**Figure 4.14:** GBM and LAT light curves of GRB 090902B. The data from the GBM NaI detectors were divided into soft (8–14.3 keV) and hard (14.3–260 keV) bands in order to reveal any obvious similarities between the light curve at the lowest energies and that of the LAT data. The fourth panel shows all LAT events that pass the on-board gamma filter, while the fifth and sixth panels show data for the “transient” class event selection for energies > 100 MeV and > 1 GeV, respectively. The vertical lines indicate the boundaries of the intervals used for the time-resolved spectral analysis. The insets show the counts for the corresponding dataset binned using these intervals in order to illustrate the relative numbers of counts considered in each spectral fit. From Abdo et al. (2009e)

The GBM and LAT light curves are shown in several energy bands in Figure 4.14. The top three panels show data from the most brightly illuminated NaI and BGO detectors of the GBM, and the bottom three panels show the LAT data with various event selections. In the bottom panel, the measured photon energies are plotted as a function of time. From the GBM light curves, it can be seen that at energies  $\lesssim 1$  MeV the prompt phase ends approximately 25 seconds after  $T_0$ . Detailed analysis of the GBM data for energies 50–300 keV yields a formal T90 duration of 21.9 seconds starting at  $T_0 + 2.2$  s. By contrast, the LAT emission  $> 100$  MeV clearly continues well after this time range.

On time scales longer than the prompt phase, the LAT detects emission from GRB 090902B as late as 1 ks after the GBM trigger. The spectrum of this emission is consistent with a power-law with photon index  $\gamma = -2.1 \pm 0.1$ , and its flux ( $> 100$  MeV) declines as  $t^{-1.5 \pm 0.1}$  over the interval ( $T_0 + 25, T_0 + 1000$  s). The LAT observations are interrupted by entry of the Earth’s limb into the FOV, but analysis of data after  $T_0 + 3600$  s, when the source location is again unocculted, shows that any later emission lies below the LAT sensitivity (Figure 4.15). The  $1\sigma$  upper limit obtained for data after  $T_0 + 3600$  is consistent with an extrapolation of the  $t^{-1.5}$  decay. Similar late-time emission for energies  $> 100$  MeV that extends well beyond the prompt phase has been seen for five earlier bursts by *Fermi*: GRB 080916C, GRB 090323, GRB 090328, GRB 090510, independently seen by AGILE (Giuliani et al., 2010) and by *Fermi*, and GRB 090626.

### 4.3.2 Time-resolved Spectral Analysis

Spectral analysis was performed using the data from both the GBM and the LAT. This analysis includes data from the NaI detectors n0, n1, n2, n9 and na, both BGO detectors b0 and b1, and LAT “transient” class data, with front- and back-converting events considered separately. The NaI data are fit from 8 keV to 1 MeV and the BGO from 250 keV to 40 MeV using TTE data. The LAT data are fit from 100 MeV to 200 GeV. An effective-area correction of 0.9 has been fit to the BGO data to match the model normalizations given by the NaI data; this correction is consistent with the uncertainties in the GBM detector responses. The fits were performed with the spectral analysis software package RMFIT (version 3.1). For further details on the data extraction and spectral analysis procedures see Abdo et al. (2009b) and Abdo et al. (2009d).

The time-integrated spectrum of GRB 090902B is best modeled by a Band function (Band et al., 1993) and a power-law component (see Table 4.3). The

#### 4. FIRST YEAR OF GBM SCIENTIFIC RESULTS

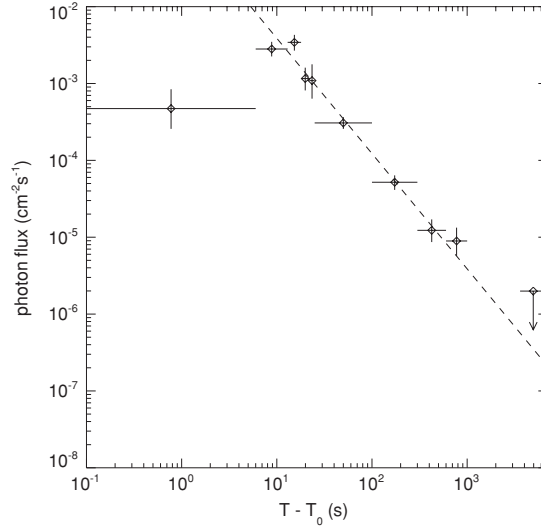


**Figure 4.15:** Light curve of GRB 090902B for energies 0.1–300 GeV from unbinned likelihood fits to the LAT data. After the prompt phase, extended or afterglow emission consistent with a temporal profile  $\propto t^{-1.5}$  (dashed line) lasts until  $\sim T_0 + 1000$  s. The upper limit at times  $> T_0 + 3600$  s was derived from the data collected after the source emerged from occultation by the Earth

power-law component significantly improves the fit between 8 keV and 200 GeV both in the time-integrated spectrum and in the individual time intervals where there are sufficient statistics. It is also required when considering only the GBM data (8 keV–40 MeV) for the time-integrated spectrum, as its inclusion causes an improvement of  $\approx 2000$  in the CSTAT statistics over the Band function alone. When data below  $\sim 50$  keV are excluded, a power-law component can be neglected in the GBM-only fits. This power-law component contributes a significant part of the emission both at low ( $< 50$  keV) and high ( $> 100$  MeV) energies. Figure 4.16 shows the counts and unfolded  $\nu F_\nu$  spectra for a Band function with a power-law component fit to the data for *interval b* (when the low energy excess is most significant) using the parameters given in Table 4.3.

Spectral evolution is apparent in the Band-function component from the changing  $E_{\text{peak}}$  values throughout the burst, while  $\beta$  remains soft until *interval e* when it hardens significantly.  $\beta$  is similarly hard in *interval f*, after which the Band function component is no longer detected. The hardening of  $\beta$  is accompanied by an apparent hardening of the power-law index  $\gamma$ , which until *interval e* does not exhibit much variation. However, this is not definitive since the flux is too low to constrain  $\gamma$  in *interval e* and *interval f* separately. A spectral fit of the sum of

### 4.3.2. Time-resolved Spectral Analysis

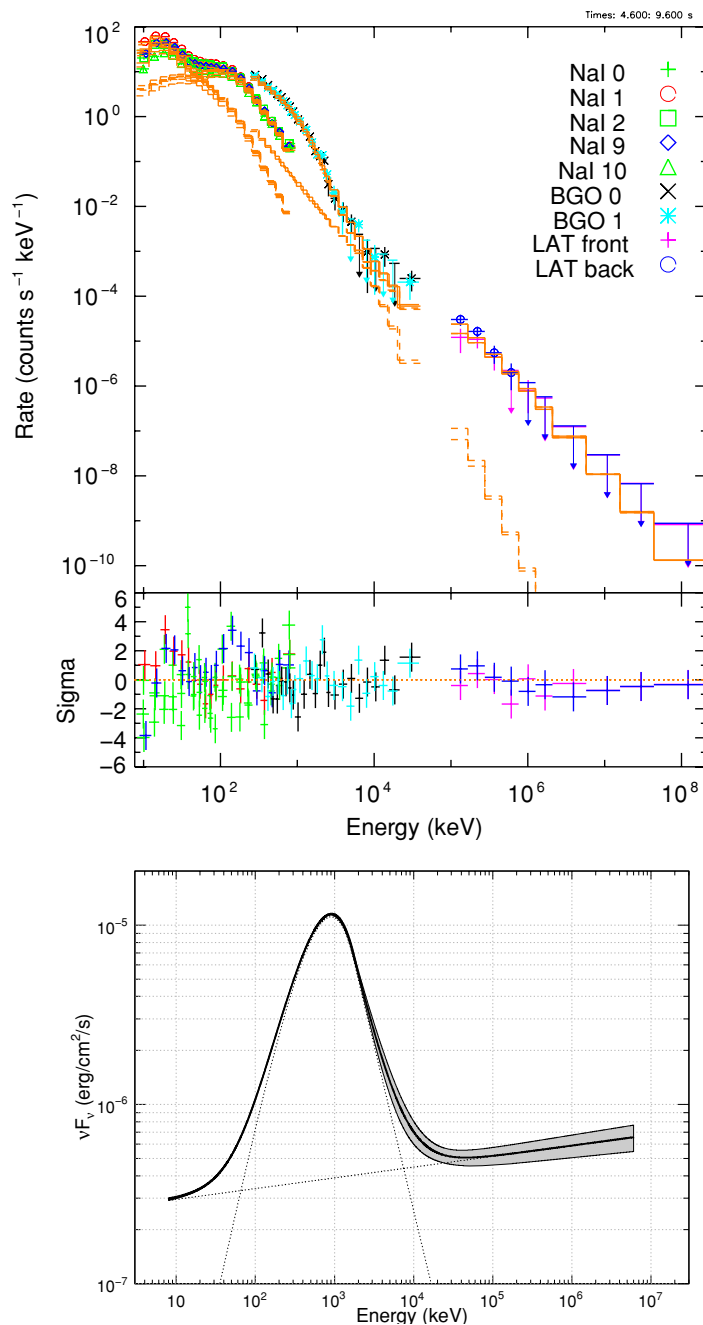


**Figure 4.16:** Joint fit of GBM and LAT data to *interval b*, ( $T_0 + 4.6, T_0 + 9.6$  s). Top: Counts spectrum; separate model components are plotted, Band (dashed), power-law (solid). Bottom: Unfolded  $\nu F_\nu$  spectrum. The extension of the  $> 100$  MeV power-law component to the lowest energies ( $< 50$  keV) is shown

## 4. FIRST YEAR OF GBM SCIENTIFIC RESULTS

---

these two intervals confirms the presence of both a harder  $\beta$  and a harder  $\gamma$ , with a clear statistical preference for the inclusion of the power-law component. An equally good fit is obtained in the combined  $e + f$  interval if this power-law has an exponential cut-off at high energies, with the preferred cut-off energy lying above 2 GeV. Finally, one can note that in *interval b*, a marginally better fit is achieved using a model with the additional power-law component having an exponential cut-off at high energies. The improvement is at the  $\sim 3\sigma$  level and indicates weak evidence for a cutoff in the second component, placing a lower limit on the cutoff energy in this interval of about 1 GeV.

### 4.3.3 Discussion and Interpretation

The *Fermi* data for GRB 090902B show for the first time clear evidence of excess emission both at low energies ( $\lesssim 50$  keV) and at high energies ( $>100$  MeV), while the Band function alone fits data at intermediate energies adequately. These excesses are well-fit by a single power-law component suggesting a common origin. This power-law component accounts for  $\approx 24\%$  of the total fluence in the 10 keV–10 GeV range, and its photon index is hard, with a value  $\sim -1.9$  throughout most of the prompt phase. Such a hard component producing the observed excess at low energies is difficult to explain in the context of leptonic models by the usual synchrotron self-Compton (SSC) mechanisms.

In the simplest versions of these models, the peak of the SSC emission is expected to have a much higher energy than the synchrotron peak at MeV energies, and the SSC component has a soft tail that is well below the synchrotron flux at lower energies and so would not produce excess emission below  $\sim 50$  keV. Hadronic models, either in the form of proton synchrotron radiation (Razzaque et al., 2009) or photohadronic interactions (Asano et al., 2009), can produce a hard component with a similar low energy excess via direct and cascade radiation (e.g., synchrotron emission by secondary pairs at low energies). However, the total energy release in hadronic models would exceed the observed gamma-ray energy of  $E_{\text{iso}} = 3.63 \times 10^{54}$  erg significantly and may pose a challenge for the total energy budget. Collimation into a narrow jet may alleviate the energy requirements, since the actual energy release from GRB 090902B can be smaller by a jet beaming factor  $> 1/\Gamma_0^2$  from the apparent isotropic value, where  $\Gamma_0$  is the bulk Lorentz factor of the fireball.

From the observation of a  $11.16_{-0.58}^{+1.48}$  GeV photon in *interval c*, the highest energy during the prompt phase and thus the most constraining, a minimum value

Table 4.3: Spectral fit parameters for GRB 090902B

Interval	Time range (s)	$E_{\text{peak}}^a$ (keV)	$\alpha^b$	$\beta^c$	$\gamma^d$	CSTAT DOF	$\Delta\text{CSTAT}$	Energy fluence ( $\text{erg cm}^{-2}$ , 8 keV–1 MeV)
...	0.0–30.0	726 ( $\pm 8$ )	-0.61 ( $\pm 0.01$ )	-3.8 ( $^{+0.2}_{-0.3}$ )	-1.93 ( $^{+0.01}_{-0.01}$ )	2562/963	2005	(4.59 $\pm$ 0.05) $\times 10^{-4}$
<b>a.</b>	0.0–4.6	526 ( $\pm 12$ )	-0.09 ( $\pm 0.04$ )	-3.7 ( $^{+0.3}_{-0.8}$ )	-1.87 ( $^{+0.04}_{-0.05}$ )	901/963	43	(3.72 $\pm$ 0.13) $\times 10^{-5}$
<b>b.</b>	4.6–9.6	908 ( $^{+15}_{-14}$ )	0.07 ( $\pm 0.03$ )	-3.9 ( $^{+0.2}_{-0.8}$ )	-1.94 ( $\pm 0.02$ )	1250/963	3165	(1.44 $\pm$ 0.03) $\times 10^{-4}$
<b>c.</b>	9.6–13.0	821 ( $\pm 16$ )	-0.26 ( $\pm 0.03$ )	-5.0 ( $^{+0.8}_{-0.8}$ )	-1.98 ( $\pm 0.02$ )	1310/963	2109	(9.42 $\pm$ 0.24) $\times 10^{-5}$
<b>d.</b>	13.0–19.2	529 ( $\pm 9$ )	-0.65 ( $\pm 0.02$ )	-3.2 ( $^{+0.1}_{-0.2}$ )	-1.86 ( $\pm 0.02$ )	1418/963	199	(1.29 $\pm$ 0.03) $\times 10^{-4}$
<b>e.</b>	19.2–22.7	317 ( $\pm 8$ )	-0.78 ( $\pm 0.02$ )	-2.4 ( $\pm 0.1$ )	...	1117/965	...	(4.8 $\pm$ 0.2) $\times 10^{-5}$
<b>f.</b>	22.7–25.0	236 ( $^{+25}_{-33}$ )	-1.30 ( $^{+0.04}_{-0.03}$ )	-2.2 ( $\pm 0.1$ )	...	1077/965	...	(1.0 $\pm$ 0.1) $\times 10^{-5}$
<b>e.+f.</b>	19.2–25.0	327 ( $\pm 8$ )	-0.91 ( $\pm 0.02$ )	-2.6 ( $\pm 0.1$ )	-1.59 ( $\pm 0.20$ )	1219/963	16	(6.1 $\pm$ 0.4) $\times 10^{-5}$
<b>g.</b>	25.0–30.0	...	...	...	-1.93 ( $^{+0.25}_{-0.26}$ )	1209/967	...	(6.8 $\pm$ 0.8) $\times 10^{-6}$

<sup>a</sup>Fitted  $E_{\text{peak}}$  for the *Band* or *Comptonized (Comp)* models;

<sup>b</sup>Low-energy spectral index  $\alpha$  for the *Band* or *Comptonized* models;

<sup>c</sup>High-energy spectral index  $\beta$  for the *Band* model;

<sup>d</sup>Spectral index  $\gamma$  for the *PL* model.

The time range values are relative to the trigger time  $T_0$ .

#### 4. FIRST YEAR OF GBM SCIENTIFIC RESULTS

---

of the bulk Lorentz factor  $\Gamma_{\min} \approx 1000$  can be derived using the flux variability time scale of  $t_v \approx 53$  ms found in the BGO data. This limit follows from the constraint that the opacity for  $e^\pm$  pair production with target photons fitted by the Band+PL model in *interval c* is less than unity for the 11.16 GeV photon (see, e.g., Fenimore et al., 1993a; Baring & Harding, 1997; Lithwick & Sari, 2001). This high  $\Gamma_{\min}$  value is of the same order as the values derived for GRB 080916C (Abdo et al., 2009a) and GRB 090510 (Abdo et al., 2010a), both of which have been detected at  $> 10$  GeV with the LAT.

The delayed onset of the  $\gtrsim 100$  MeV emission from the GBM trigger has been modeled for GRB 080916C as arising from proton synchrotron radiation in the prompt phase (Razzaque et al., 2009) and for GRB 090510 as arising from electron synchrotron radiation in the early afterglow phase (Kumar & Barniol Duran, 2009; Ghirlanda et al., 2009). In order to produce the peak of the LAT emission at  $\sim T_0 + 9$  s in the early afterglow scenario for GRB 090902B from deceleration of the GRB fireball, a value of  $\Gamma_0 \approx 1000$  is required. This is similar to  $\Gamma_{\min}$  calculated above, but the observed large amplitude variability on short time scales ( $\approx 90$  ms) in the LAT data, which is usually attributed to prompt emission, argues against such models. Also, the appearance of the power-law component extending down to  $\approx 8$  keV within only a few seconds of the GRB trigger disfavors an afterglow interpretation. The proton synchrotron model, on the other hand, requires a rather large total energy budget, as mentioned previously.

Yet another interpretation of the observed excess in the high and low energies may be provided by two non-thermal power-law components along with a thermal component from the jet photosphere (Mészáros & Rees, 2000; Ryde, 2004). The thermal component, broadened by temperature variations, then accounts for the  $\gtrsim 100$  keV–few MeV emission with  $\Gamma_0 \approx 930$  (Pe’er et al., 2007), although fits of such a model to our data do not improve over the Band+PL model. Furthermore, it is difficult for the photospheric model to explain the delayed onset of the  $\gtrsim 100$  MeV emission.

The detection of the 33.4 GeV photon, 82 seconds after the GRB trigger and well after the soft gamma-ray emission subsided, may help to constrain the origin of the late-time decay of the power-law component, which goes as  $t^{-1.5}$ . A synchrotron origin of the 33.4 GeV photon would be difficult since it would require significant energy gain by electrons over a gyroradius and a bulk Lorentz factor  $> 1500$ . In the case of diffusive shock-acceleration, the energy losses in the upstream region of the shock may dominate (see, e.g., Li & Waxman, 2006) and prevent acceleration of electrons to an energy high enough to radiate a 33.4 GeV

photon. An interpretation by afterglow SSC emission is still possible, however.

The constraints on the quantum gravity mass scale from GRB 090902B using the time-of-flight test (Amelino-Camelia et al., 1998) are much weaker than those from GRB 090510 (Abdo et al., 2009d) due to the larger interval, 82 seconds, between  $T_0$  and the arrival time of the 33.4 GeV photon. However, the moderately high redshift ( $z = 1.822$ ) of GRB 090902B allows us to use this photon to probe and constrain EBL models (see e.g. Gilmore et al., 2009; Finke et al., 2009). The 33.4 GeV photon would not be absorbed by the EBL in any models except for the “fast evolution” and the “baseline” models by Stecker et al. (2006), which give optical depths of  $\tau_{\gamma\gamma} = 7.7$  and 5.8, respectively. Spectral fits of the LAT data with and without the predicted EBL absorption from Stecker’s models were performed, assuming a simple power-law as the intrinsic emission model. Based on Monte-Carlo simulations, Stecker’s fast evolution and baseline models are disfavored at a  $> 3\sigma$  level.

## 4.4 GBM and BAT Observations of GRB 080810<sup>3</sup>

Common scientific interest between *Fermi* and *Swift* provides strong motivation for using GBM and BAT data to conduct a cross-calibration via correlative observations of GRBs, resulting in joint spectral fits, thus enabling the analysis of multi-wavelength spectral and temporal evolution.

GRB 080810 was one of the first bursts to trigger both *Swift* and GBM. It also represents the first burst for which a GCN Circular was issued by the GBM team. The GRB was subsequently monitored over the X-ray and UV/optical bands by *Swift*, in the optical by several ground-based telescopes and was detected in the radio by the VLA. The redshift was found to be  $3.355 \pm 0.005$  (Prochaska et al., 2008).

Well-sampled bursts such as GRB 080810 enable us to investigate more thoroughly the myriad of models which exist for GRBs, with the ultimate goal of a complete and consistent description of GRB emission from early to late times. This section mainly focuses on the observations and results covering the X-ray and gamma-ray burst emission from 080810. Moreover, the spectral fits discussed hereafter represent the first GBM-BAT joint fits to be published in Page,

---

<sup>3</sup>The main contents of this section are published in Page, Willingale, Bissaldi, et al. (2009), *Multiwavelength observations of the energetic GRB 080810: detailed mapping of the broad-band spectral evolution*; *Monthly Notices of the Royal Astronomical Society*, 400, 134

Willingale, Bissaldi, et al. (2009). In that paper, we also present detailed modeling of the multi-wavelength broadband spectral evolution and discuss the redshift determination using a thermal interpretation to provide an alternative spectral fit.

### 4.4.1 Observations and Analyses

*Swift* and *Fermi* both triggered on GRB 080810 at 13:10:12 UT on 2008 August 10, with the *Swift*-XRT and UVOT detecting the afterglow as soon as they were on target. The best *Swift* position is that determined from the UVOT refined analysis (Holland & Page, 2008): R.A. =  $23^{\text{h}}47^{\text{m}}10.48^{\text{s}}$ , decl. =  $+00^{\circ}19'11.3''$  (J2000; estimated uncertainty of  $0.6''$ ), consistent with the ROTSE-III (Robotic Optical Transient Search Experiment; Rykoff, 2008) and NOT (de Ugarte Postigo et al., 2008) localisations.

#### Gamma-rays

GRB 080810 was clearly detected by the BAT (Sakamoto et al., 2008a) over all energy bands (see Figure 4.17), although the emission above about 100 keV is weaker than at the lower energies. The  $T_{90}$  (15–150 keV) is  $108 \pm 5$  s (estimated error including systematics); the fluence over this time is  $4.2 \times 10^{-6}$  erg  $\text{cm}^{-2}$ . The slow rise of the emission, over which there are multiple, overlapping peaks, started about 20 s (observer's frame) before the trigger. Konus-Wind also detected GRB 080810, but observed the burst in waiting mode (Sakamoto et al., 2008b), meaning only 3-channel spectra were available, covering 20 keV–1 MeV.

GBM triggered on the burst as well (Meegan et al., 2008), identifying the same pulses as did the BAT (Figure 4.17). Unfortunately the burst was outside the field of view of the LAT. The NaI detectors provide similar  $T_{90}$  estimates to that measured by the BAT, while the higher energy BGO durations are shorter; values are given in Table 4.4. This is a consequence of the hard-to-soft evolution (see, e.g., Table 4.5), combined with the different sensitivities of the instruments.

Time-sliced spectra from both the BAT and the NaI and BGO detectors, covering 0–10, 10–20, 20–27, 40–53 and 100–106 s after the trigger, were fitted with single and cut-off power-laws and the results are given in Table 4.5. The useful energy ranges for the BAT, NaI and BGO spectral fitting are 15–150, 8–1000 and 0.2–40 MeV, respectively. The spectra and models were extensively tested in both XSPEC (Arnaud, 1996) and RMFIT; these methods provided consistent results and so the numbers given here are those from XSPEC. Because BAT spectra are created already background-subtracted and have non-Poissonian errors,

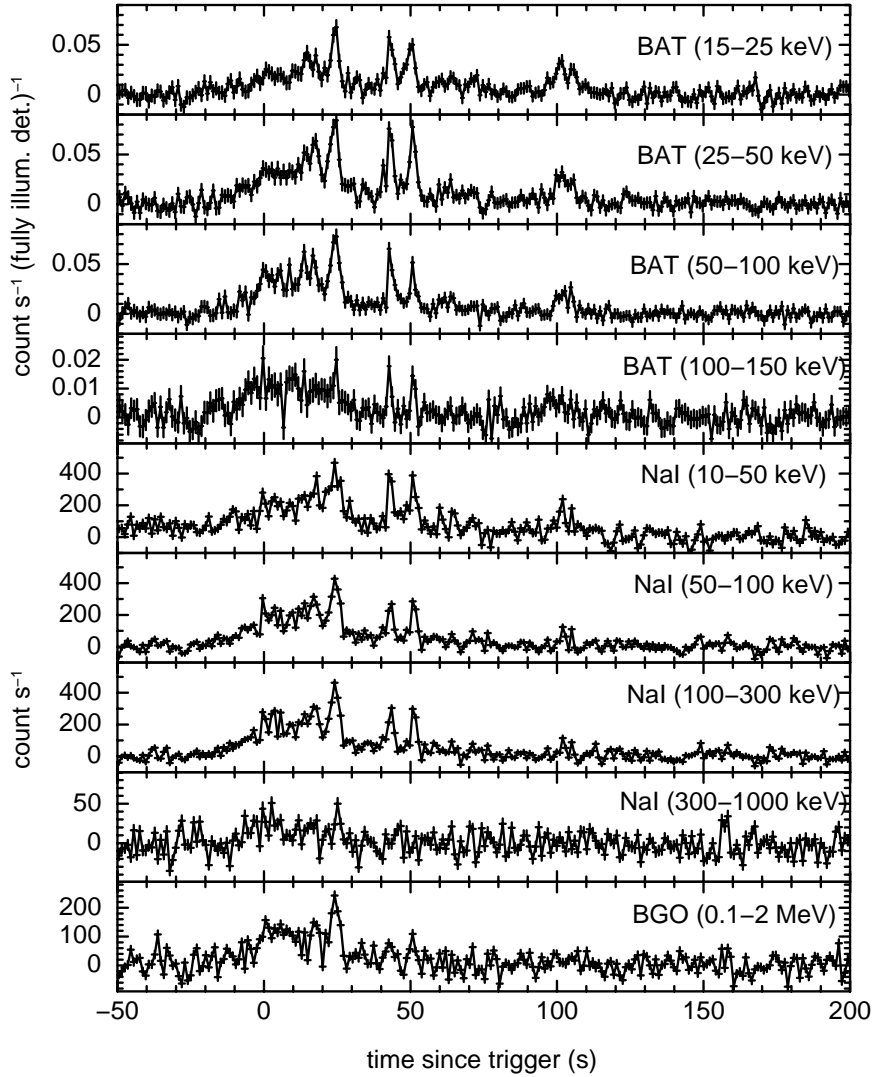


**Figure 4.17:** The BAT (*top four panels*) and GBM (*bottom five panels*) light curves of GRB 080810, over their standard energy bands. Note that the ordinate scale for the 100–150 keV BAT curve (*fourth panel*) and the 300–1000 keV NaI curve (*eighth panel*) are different from the lower-energy bands, because the emission was much weaker. The BGO light curve is shown down to 100 keV, but spectral analysis is performed only for data  $>200$  keV. The *Swift* light curves are in units of  $\text{count s}^{-1}$  (fully illuminated detector) $^{-1}$ , while the GBM curves are  $\text{count s}^{-1}$

#### 4. FIRST YEAR OF GBM SCIENTIFIC RESULTS

**Table 4.4:** GRB 080810  $T_{90}$  measurements over a range of energy bands. The longer duration at lower energies shows that the emission softened over time

Instrument	Band (keV)	$T_{90}$ (s)
<b>Average</b>		
<i>Swift</i> -BAT	15–150	$108 \pm 4$
<i>Fermi</i> -NaI	10–1000	$113 \pm 2$
<i>Fermi</i> -BGO	200–20 000	$73 \pm 7$
<b>Energy-sliced</b>		
<i>Swift</i> -BAT	15–100	$105 \pm 4$
<i>Swift</i> -BAT	100–150	$55 \pm 9$
<i>Fermi</i> -NaI	10–50	$107 \pm 1$
<i>Fermi</i> -NaI	50–100	$81 \pm 1$
<i>Fermi</i> -NaI	100–300	$73 \pm 1$

Cash/Castor statistics cannot be used<sup>4</sup>; hence all results were obtained using  $\chi^2$  statistics.

Using the F-test, the Band function is not a statistical improvement over the simpler cut-off power-law, with the high-energy index  $\beta$  unconstrained in each case. For the fits presented here, the normalisations of the GBM detectors were tied together at a value of 1.23 relative to the normalisation of the BAT, which was itself fixed at unity. This constant of normalisation for the GBM was determined by simultaneously fitting all five intervals of data, but allowing the other fit parameters to vary between the intervals.

Sakamoto et al. (2009) found a correlation between the photon index from a simple power-law fit to a BAT GRB spectrum and  $E_{\text{peak}}$ , thus allowing an estimate of the peak energy from the limited BAT energy bandpass. The correlation for a source  $15^\circ$  off-axis (GRB 080810 was approximately  $20^\circ$  off-axis),  $\log(E_{\text{peak}}) = 3.184 - 0.793 \gamma$  (where the index  $1.3 \leq \gamma \leq 2.3$ ), was used to produce the estimated  $E_{\text{peak}}$  values given in Table 4.5 (marked as ‘est.’); BAT slewed during the interval 12–64 s after the trigger, so  $E_{\text{peak}}$  was estimated for the last (100–106 s) spectrum using the on-axis approximation. The spectrum extracted for 0–10 s after the trigger has too hard a photon index to allow the use of this approximation, while 10–20 s is just consistent with the range. The  $1\sigma$  spread of the relation has been included in the error estimation. These estimated peak energies are consistent with those found from jointly fitting the BAT and GBM data, although the error bars on the measurements are very large.

The numbers show that the peak energy moves to lower values over time; this

<sup>4</sup>see <http://heasarc.gsfc.nasa.gov/docs/xanadu/xspec/manual/XSappendixCash.html>

#### 4.4.1. Observations and Analyses

**Table 4.5:** Power-law (PL), cut-off power-law (CutPL) and quasithermal (PL+Therm) fits to the GRB 080810 time-sliced spectra from GBM and BAT; the NaI n7, n8, nb and BGO b1 detectors were fitted simultaneously each time. The  $E_{\text{peak}}$  values for the BAT single power-law fits are estimated from the relation given by Sakamoto et al. (2009)

Time (s since trigger)	Detectors	Model	$\alpha$	$E_{\text{peak}}$ (keV)	BB kT (keV)	$\chi^2/\text{dof}$
0–10	BAT	PL	$0.92 \pm 0.13$	—	—	66/56
0–10	GBM	PL	$1.48 \pm 0.04$	—	—	582/488
0–10	GBM	CutPL	$1.06^{+0.13}_{-0.17}$	$807^{+1113}_{-470}$	—	509/485
0–10	GBM+BAT	PL	$1.43 \pm 0.03$	—	—	694/544
0–10	GBM+BAT	CutPL	$0.95^{+0.12}_{-0.13}$	$602^{+537}_{-252}$	—	580/543
0–10	GBM+BAT	PL+Therm	$1.63 \pm 0.11$	—	$62 \pm 9$	597/542
10–20	BAT	PL	$1.24 \pm 0.10$	$159^{+738}_{-92}$ (est.)	—	30/56
10–20	GBM	PL	$1.56 \pm 0.04$	—	—	568/486
10–20	GBM	CutPL	$1.07^{+0.15}_{-0.18}$	$346^{+378}_{-160}$	—	505/485
10–20	GBM+BAT	PL	$1.53 \pm 0.03$	—	—	622/544
10–20	GBM+BAT	CutPL	$1.09^{+0.11}_{-0.12}$	$353^{+275}_{-139}$	—	536/543
10–20	GBM+BAT	PL+Therm	$1.69^{+0.10}_{-0.09}$	—	$46^{+8}_{-8}$	553/542
20–27	BAT	PL	$1.23 \pm 0.11$	$162^{+757}_{-99}$ (est.)	—	39/56
20–27	GBM	PL	$1.53 \pm 0.04$	—	—	538/486
20–27	GBM	CutPL	$1.11^{+0.13}_{-0.14}$	$434^{+425}_{-190}$	—	476/485
20–27	GBM+BAT	PL	$1.50 \pm 0.03$	—	—	596/544
20–27	GBM+BAT	CutPL	$1.12^{+0.10}_{-0.11}$	$452^{+356}_{-176}$	—	516/543
20–27	GBM+BAT	PL+Therm	$1.64^{+0.09}_{-0.08}$	—	$53^{+11}_{-9}$	538/542
40–53	BAT	PL	$1.60 \pm 0.10$	$82^{+160}_{-32}$ (est.)	—	60/56
40–53	GBM	PL	$1.69 \pm 0.06$	—	—	620/486
40–53	GBM	CutPL	$1.27^{+0.23}_{-0.24}$	$188^{+464}_{-114}$	—	602/485
40–53	GBM+BAT	PL	$1.67 \pm 0.05$	—	—	682/544
40–53	GBM+BAT	CutPL	$1.41^{+0.13}_{-0.16}$	$230^{+538}_{-175}$	—	664/543
40–53	GBM+BAT	PL+Therm	$1.78^{+0.15}_{-0.11}$	—	$28^{+15}_{-9}$	668/542
100–106	BAT	PL	$1.71 \pm 0.19$	$69^{+97}_{-52}$ (est.)	—	55/56
100–106	GBM	PL	$2.14^{+0.28}_{-0.23}$	—	—	600/486
100–106	GBM	CutPL	$0.99^{+0.83}_{-1.47}$	$49^{+472}_{-49}$	—	593/485
100–106	GBM+BAT+XRT	PL	$1.46 \pm 0.02$	—	—	904/585
100–106	GBM+BAT+XRT	CutPL	$1.05^{+0.07}_{-0.08}$	$39^{+12}_{-9}$	—	725/584
100–106	GBM+BAT+XRT	PL+Therm	$1.46 \pm 0.03$	—	$2.6^{+0.4}_{-0.7}$	797/583

is demonstrated graphically in Figure 4.18. The single power-law fits also show that  $\alpha$  increased (softened) until at least 53 s. The spectrum from 100–106 s covers a flare in the XRT emission, which explains the harder (flatter) photon index.

Extracting simultaneous BAT and GBM spectra over  $T_0-4 - T_0+26$  s (i.e., the brightest interval; Figure 4.19, *bottom panel*), a cut-off power-law model is significantly better than a single power-law, with  $\alpha = 1.05^{+0.07}_{-0.08}$  and  $E_{\text{peak}} = 569^{+290}_{-181}$  keV, corresponding to an isotropic energy release of  $E_{\text{iso}} \sim 3 \times 10^{53}$  erg (1 keV–10 MeV in the rest frame)

Figure 4.19 plots the XRT, BAT and NaI spectra between 100–106 s. There is only a tenuous detection in the BGO at this time, so that its spectrum has not

#### 4. FIRST YEAR OF GBM SCIENTIFIC RESULTS

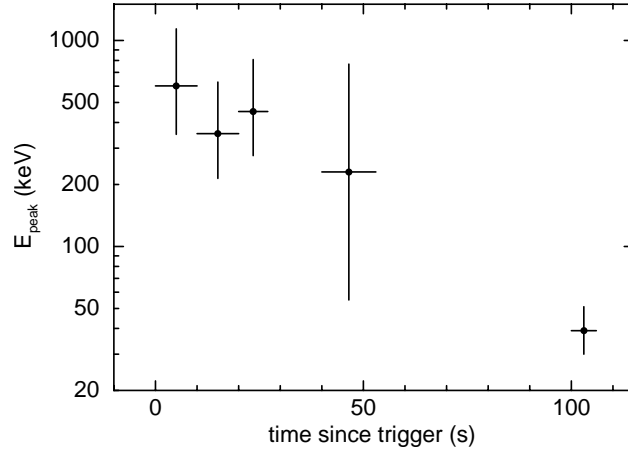


**Figure 4.18:** GRB 080810  $E_{\text{peak}}$  evolution, measured from joint *Fermi–Swift* fits. Note that  $E_{\text{peak}}$  moves from higher to lower energies with time

been included in the plot for clarity; it was, however, used in the fit to help in constraining  $E_{\text{peak}}$ . Note that in both plots the BAT data appear lower on the ordinate axis simply because of the way the normalisations are defined.

#### Inter-Calibration

The inter-calibration of the BAT and GBM is a work in progress and pre-launch simulations and detection estimates were discussed by Stamatikos et al. (2008); further results will be presented in Stamatikos et al. (in prep). As mentioned in the previous section, the normalizations of the GBM detectors were all tied together for the current paper, finding a mean value of  $1.23 \pm 0.06$  compared to a BAT value of unity. Allowing the normalisations to vary between the GBM detectors, while again simultaneously fitting all the datasets with a cut-off power-law, produced the following relative constants: NaI n7 =  $1.24^{+0.09}_{-0.08}$ , n8 =  $1.18 \pm 0.08$ , nb =  $1.32^{+0.10}_{-0.09}$  and BGO b1 =  $1.88^{+0.31}_{-0.27}$ , where, as before, the BAT constant was fixed to unity. Thus, the GBM detectors agree quite well, with a typical discrepancy of  $\lesssim 20\%$ .

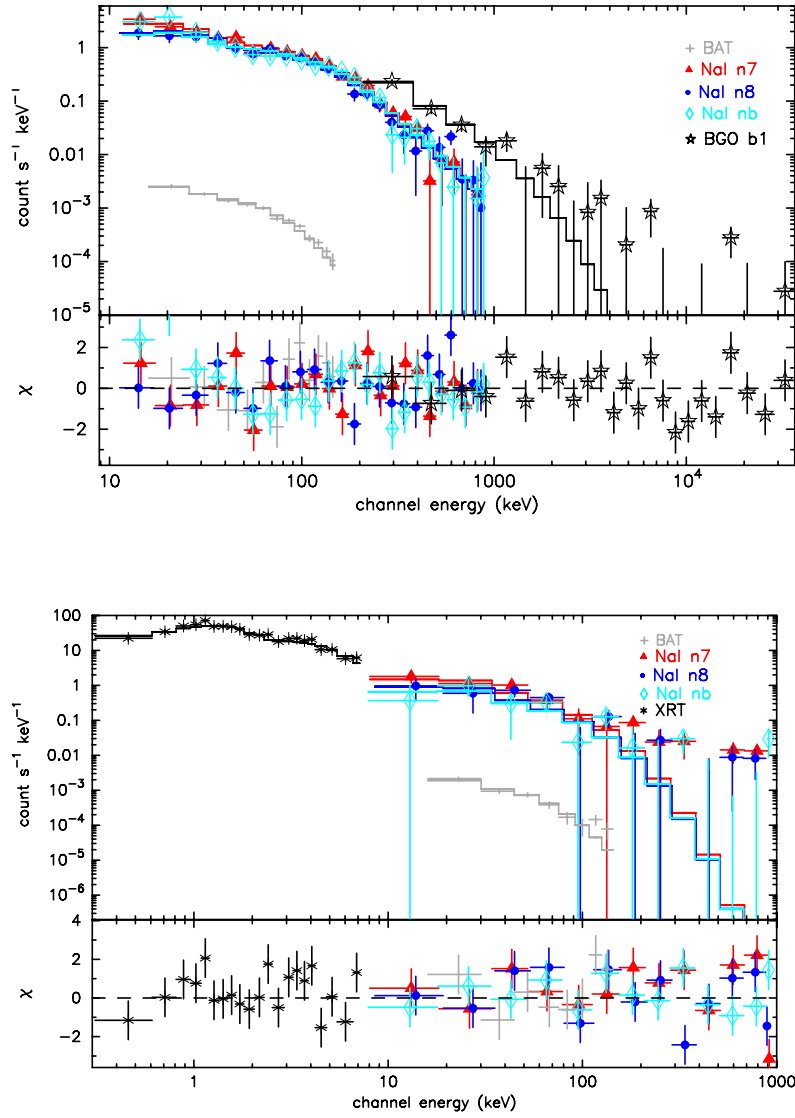


**Figure 4.19:** *Top panel:* GBM and BAT spectra of GRB 080810 from  $T_0-4$  to  $T_0+26$  s. The residuals are plotted in terms of sigma, with error bars of  $1\sigma$ . *Bottom Panel:* GBM, BAT and XRT spectra from  $T_0+100$  to  $T_0+106$  s. The residuals are plotted in terms of sigma, with error bars of  $1\sigma$

#### 4. FIRST YEAR OF GBM SCIENTIFIC RESULTS

---

# Chapter 5

## BGO–Bright GRBs

Some of the most exciting results of the pre-*Fermi* gamma-ray burst science came from EGRET at MeV–GeV energies, as previously discussed in Chapter 1. With *Fermi*, it is now possible to search for different spectral signatures from GRBs (as for GRB 090510 and GRB 090902B already discussed in §4.2 and §4.3) up to several GeVs, over an unprecedentedly broad energy range, and observations carried out so far look extremely promising. Unfortunately, the number of GRBs detected by LAT above 100 MeV still represents a minority with respect to the total number of GRBs observed by GBM (~4%).

GRB spectra in the MeV–GeV range are usually well-described by a single power-law with an index in the approximate range of -1 to -3. This range is in agreement with the distributions of the high-energy power-law indices observed with the BATSE LADs in the ~30 keV–2 MeV energy range (Kaneko et al., 2006). However, due to the power-law nature of GRB spectra, photon counts above ~1 MeV are usually very low, and this, combined with the fact that the field-of-view of the LAT detector is limited, results in much fewer GRBs observed in the multi-MeV band than in keV-band observations.

Detailed calculations of LAT upper limits are currently performed by the LAT team, and are mainly based on the brightest bursts detected by GBM inside the LAT FoV. The determination of a consistent sample for upper limit calculations can be established by selecting those bursts which have a strong signal in the GBM BGO detectors (0.2–40 MeV). This Chapter focuses on the selection methodology and spectral analysis of a sample of BGO–bright bursts detected by GBM during its first year. Selections are based on the peak count rate measured by the most illuminated BGO detector and cross-checked with the measured energy fluence and peak photon flux values to assure good statistics. Furthermore, the sample

includes several short GRBs. Different photon models were used to fit each time–integrated spectrum. Using these results, correlations among spectral parameters are finally discussed.

### 5.1 Selection Methodology

Since the complete spectral catalog of the first year GBM bursts is still in preparation, a different approach was chosen in order to select the GRB sample. This is mainly based on count–rate excess above background measured by the BGO detectors during the burst emission episode ( $T_{90}$ ). GBM data types and data energy ranges vary for each burst and for each detector. The following subsections discuss the methodology employed for the burst selection, the data type selection, and time and energy interval selections.

#### 5.1.1 Event Selection

The primary selection was made based on the analysis of the GBM TRIGDAT telemetry packets, which are automatically produced during a trigger and contain all trigger information such as locations, classifications and accumulated rates (see §2.3.3). The BGO maximum (“Max”) rates observed over a short period after trigger time ( $<4$  s) are produced from the accumulations made for the trigger algorithms and are evaluated as statistical significance (SNR) versus the background. This is simply counts per 1.024 s, for each channel and each detector, and is calculated as the mean of past data. Typically, the background interval will range from about -36 s to -4 s with respect to the trigger time, thus excluding the most recent few seconds of data and avoiding in most cases the contamination by pre–trigger data from the burst. Those bursts showing an increase of more than 80 counts/s over background in at least one BGO detector were selected. The resulting total number of GRBs included in this spectral analysis is 56 (“All”), which represents a  $\sim 20\%$  of all bursts detected during the first year of operation. These bursts are listed in Table 5.1, along with the trigger information, data types, NaI and BGO detector numbers, time intervals, and angle to the LAT boresight. This latter value represents the initial angle from the source calculated at trigger time and can vary or rather decrease over the burst duration especially when an ARR was positively performed by the *Fermi* spacecraft. GRB names reported in italics refer to bursts which were not reported in any GCN circular.

**Table 5.1:** Basic properties of 56 bright GRBs

<b>GRB Name</b>	<b>GBM Trig. #</b>	<b>Trig. Time (MET)</b>	<b>NaI Det. #</b>	<b>BGO Det. #</b>	<b>LAT Angle (deg)</b>	<b>Data Type</b>	<b>Time Interval</b> Start (s) Stop (s)	
080723B	080723.557	238512142	4	0	107	CSPEC	0.004	60.161
080723E	080723.985	238549063	2,5	0	113	CSPEC	0.004	48.897
080725B	080725.541	238683564	6,7	1	50	TTE	-0.064	0.384
080802	080802.386	239361311	4,5	0	125	TTE	-0.256	0.640
080807	080807.993	239845833	0,1,2	0	74	CSPEC	-1.376	21.152
080816B	080816.989	240623035	7,11	1	70	TTE	-0.128	1.024
080817A	080817.161	240637931	2,5	0	80	CSPEC	0.004	25.600
080825C	080825.593	241366429	9,10	1	60	CSPEC	0.004	25.216
080905A	080905.499	242308736	6,7	1	28	TTE	-0.064	0.960
080906B	080906.212	242370312	0,1,3	0	32	CSPEC	-1.408	5.760
080916C	080916.009	243216766	3,4	0	52	CSPEC	0.004	50.689
080925	080925.775	244060556	6,7	1	38	CSPEC	0.004	30.976
081006	081006.604	244996175	0,3	0	16	TTE	-0.384	1.792
081009	081009.690	245262818	8,11	1	96	CSPEC	-2.688	30.080
081012B	081012.045	245466323	9,10	1	66	TTE	-0.128	0.768
081024B	081024.891	246576161	6,9	1	16	TTE	-0.128	0.512
081101B	081101.532	247236325	2,5	0	116	CSPEC	0.003	8.704
081105B	081105.614	247589032	1,2	0	87	TTE	-0.064	0.128
081110	081110.601	248019944	7,8	1	67	TTE	0.000	15.104
081121	081121.858	248992528	10,11	1	140	CSPEC	0.003	21.504
081122	081122.520	249049693	0,1	0	21 (ARR)	TTE	-0.384	17.536
081125	081125.496	249306820	10,11	1	126	CSPEC	0.003	9.344
081126	081126.899	249428050	0,1	0	18	CSPEC	-3.968	40.065
081129	081129.161	249623525	10,11	1	118	CSPEC	0.003	19.584
081207	081207.680	250359527	9,10	1	56	CSPEC	0.003	100.354
081209	081209.981	250558317	8,11	1	107	TTE	-0.128	0.256
081215A	081215.784	251059717	9,10	1	89	CSPEC	0.004	7.424
081216	081216.531	251124240	8,11	1	99	TTE	-0.128	1.024
081224	081224.887	251846276	6,9	1	17 (AAR)	CSPEC	0.002	12.448
081226B	081226.509	251986391	6,7	1	22	TTE	-0.064	0.256
081231	081231.140	252386462	6,9	1	21	CSPEC	-4.096	27.648
090102	090102.122	252557732	10,11	1	87	CSPEC	0.003	18.688
090131	090131.090	255060563	9	1	40	CSPEC	0.003	42.241
090217	090217.206	256539404	6,9	1	34	CSPEC	0.003	34.944
090219	090219.074	256700780	5	0	137	TTE	-0.064	0.576
090227	090227.310	257412359	0,3	0	20	CSPEC	0.003	21.376
090227B	090227.772	257452263	1,2	0	72 (ARR)	TTE	-0.016	0.200
090228	090228.204	257489602	0,1	0	16	TTE	-0.008	0.152
090305B	090305.052	257908477	0,3	0	40	TTE	-0.128	1.024
090308B	090308.734	258226586	3,7	0,1	50	TTE	-0.128	1.408
090323	090323.002	259459364	9	1	53 (ARR)	CSPEC	0.003	71.681
090328	090328.401	259925808	7,8	1	63 (ARR)	CSPEC	0.003	30.720

## 5. BGO–BRIGHT GRBS

**Table 5.1:** (continued)

GRB Name	GBM Trig. #	Trig. Time (MET)	NaI Det. #	BGO Det. #	LAT Angle (deg)	Data Type	Time Interval Start (s) Stop (s)	
090328B	090328.713	259952826	9,10	1	74 (ARR)	TTE	-0.064	0.128
090424	090424.592	262275130	7,8	1	71	CSPEC	0.002	19.712
090425	090425.377	262343012	4	0	105	CSPEC	44.225	84.161
090429D	090429.753	262721039	0,1	0	33	TTE	-0.256	0.512
090510	090510.016	263607781	6,7	1	13 (ARR)	TTE	0.512	0.960
090528B	090528.516	265206153	7,8	1	65	CSPEC	0.003	60.417
090529B	090529.564	265296722	3,4	0	69 (ARR)	CSPEC	0.002	11.072
090531B	090531.775	265487758	6,9	1	26	TTE	-0.128	0.832
090617	090617.208	266907600	0,1,3	0	45	TTE	-0.032	0.192
090618	090618.353	267006508	4	0	130	CSPEC	59.905	104.960
090620	090620.400	267183385	6,7	1	60	CSPEC	0.003	14.592
090621B	090621.922	267314847	2,5	0	108	TTE	-0.128	0.256
090623	090623.107	267417259	7,11	1	73	CSPEC	-1.920	40.064
090626	090626.189	267683530	0	0	15	CSPEC	-0.256	60.161

### 5.1.2 Detector Selection

As previously discussed in Chapter 2, two or more NaI detectors must have a statistically–significant rate increase above the background rate in order to trigger the GBM FSW. Requiring two detectors to be above their thresholds increases the threshold against statistical fluctuations, and suppresses triggering due to non–astrophysical effects that appear in only one detector, such as phosphorescence spikes. Before performing any spectral analysis, the detector geometry must be carefully taken into account. Detectors which see the burst at an angle  $>40^\circ$ , or which suffer from blockages (by the solar panels, by the LAT or by the spacecraft itself) were excluded. Sometimes this results in a single NaI detector to be chosen for the spectral analysis, which is then fitted together with the mostly illuminated BGO detector. The best detector combination for each burst is given in columns 4 (NaIs) and 5 (BGO) of Table 5.1.

### 5.1.3 Data Type Selection

The GBM data types were discussed in detail in §2.2.4 and summarized in Table 2.4. All three data types, CSPEC, CTIME and TTE, are used in this work. CTIME and CSPEC data are considered in burst–mode (64 ms and 1.024 s temporal resolution). In case of very short bursts, TTE data are rebinned finer than the nominal

resolution (128 ms). The BGO peak count–rate analysis and the determination of the burst durations ( $T_{100}$ ) are based on CTIME files, which have the finest temporal resolution with modest energy resolution consisting of 8 energy channels. CSPEC and TTE data provide an energy resolution consisting of 128 energy channels and were selected for the spectral analysis. The coarse time–resolution CSPEC data are used here as background data for the TTE,  $\sim 500$  s before the trigger and after the TTE accumulation is finished. TTE data are collected up to 300 s post–trigger, and in all cases discussed hereafter cover the whole burst duration. For each GRB, the data type used is listed in column 7 of Table 5.1.

### 5.1.4 Time and Energy Interval Selections

Since no time–resolved spectral analysis was planned for this work, data were usually not binned in time. Only some of the short bursts, e.g. GRB 090227B or GRB 090510, were binned finer than the nominal resolution of 128 ms. The background model is determined by fitting a low–order ( $\leq 4$ ) polynomial function to spectra to cover time intervals before and after each burst, for at least a few hundred seconds. The burst start time is usually the trigger time. Columns 8 and 9 of Table 5.1 list the time intervals used for each burst. The chosen sample of 56 GRBs includes 15 bursts with a duration  $T_{90} < 2$  s (8–1000 keV, *short GRBs*), and 41 bursts with a duration  $T_{90} > 2$  s (8–1000 keV, *long GRBs*). The three longest bursts with durations greater than 100 s are GRB 090323, GRB 096018 and GRB 081207. Table 5.2 gives the durations calculated for all 56 bursts by using both NaI and BGO CTIME data, which are also shown in Figure 5.2. In the case of BGO durations, a rough estimate of the total duration in terms of “ $T_{100}$ ” was performed with RMFIT by considering all but the last (overflow) BGO energy channels, i.e. over the energy range  $\sim 150$  keV– $\sim 38$  MeV. A scatter plot of BGO versus NaI durations is also shown in Figure 5.1. The *dashed red line* indicates perfect proportionality. Most of the bursts tend to be shorter at higher energies than at lower energies.

As mentioned in §2.2.1 and §2.2.2, the usable energy range for the NaI detectors is  $\sim 8$  keV–1 MeV and for the BGO detectors it is  $\sim 250$  keV–40 MeV. The lowest 4 or 5 channels of CSPEC and TTE and 1 channel of CTIME data are usually excluded. Likewise, the highest few channels of CSPEC and TTE data and normally the very highest channel of CTIME data represent overflow channels and are also not usable.

## 5. BGO–BRIGHT GRBS

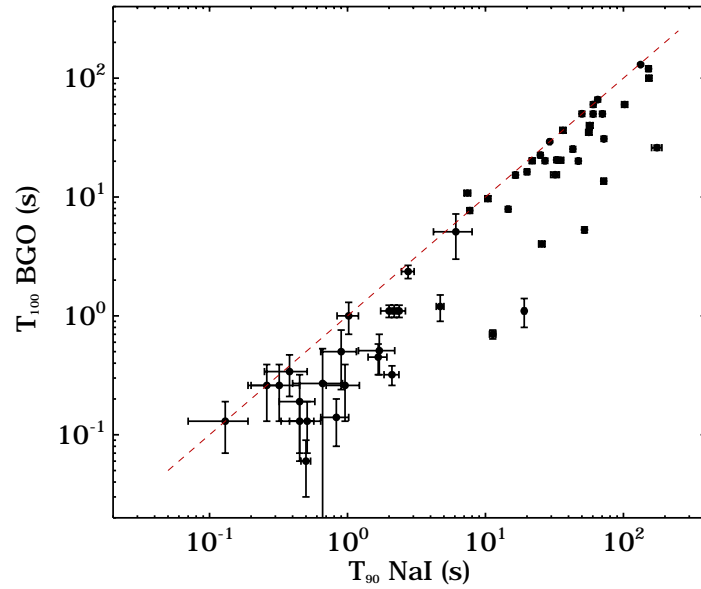


**Figure 5.1:** GBM BGO vs. NaI durations for 56 BGO–bright bursts

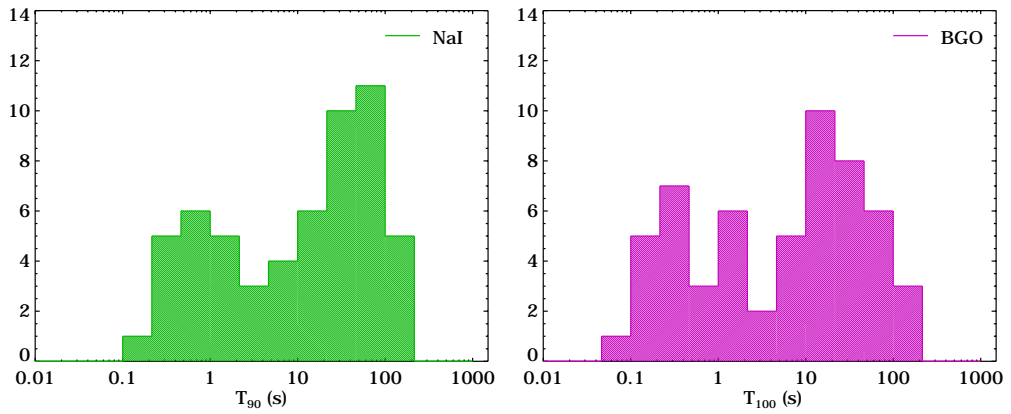


**Figure 5.2:** GBM NaI (*left panel*) and BGO (*right panel*) duration distributions for 56 BGO–bright bursts. The bimodal distribution looks similar to the one presented in Figure 1.4 of chapter 1

### 5.1.4. Time and Energy Interval Selections

**Table 5.2:** Burst durations calculated with NaI and BGO CTIME data ( $T_{90}$  and  $T_{100}$ , respectively) for 56 BGO–bright bursts

<b>GBM Trig. #</b>	<b>NaI <math>T_{90}</math> 8–1000 keV</b>	<b>BGO <math>T_{100}</math> 0.2–40 MeV</b>	<b>GBM Trig. #</b>	<b>NaI <math>T_{90}</math> 8–1000 keV</b>	<b>BGO <math>T_{100}</math> 0.2–40 MeV</b>
080723.557	$60.4 \pm 1.5$	$60 \pm 3$	081224.887	$35.0 \pm 1.8$	$20.4 \pm 1.0$
080723.985	$50.0 \pm 0.8$	$50.2 \pm 2.5$	081226.509	$0.38 \pm 0.13$	$0.34 \pm 0.13$
080725.541	$1.7 \pm 0.5$	$0.51 \pm 0.19$	081231.140	$29.2 \pm 0.6$	$29.2 \pm 0.6$
080802.386	$0.50 \pm 0.04$	$0.06 \pm 0.03$	090102.122	$43.0 \pm 0.9$	$25.3 \pm 1.3$
080807.993	$19.1 \pm 0.5$	$1.1 \pm 0.3$	090131.090	$36.4 \pm 1.8$	$36.4 \pm 1.9$
080816.989	$4.7 \pm 0.3$	$1.2 \pm 0.3$	090217.206	$32.8 \pm 0.6$	$20.5 \pm 1.0$
080817.161	$60.3 \pm 0.5$	$50.0 \pm 2.5$	090219.074	$0.51 \pm 0.13$	$0.13 \pm 0.06$
080825.593	$27.0 \pm 0.5$	$20.2 \pm 1.0$	090227.310	$47.1 \pm 0.5$	$20.1 \pm 1.0$
080905.499	$1.02 \pm 0.18$	$1.0 \pm 0.3$	090227.772	$1.67 \pm 0.26$	$0.45 \pm 0.13$
080906.212	$2.75 \pm 0.29$	$2.36 \pm 0.3$	090228.204	$0.83 \pm 0.19$	$0.14 \pm 0.06$
080916.009	$65.1 \pm 0.7$	$66 \pm 3$	090305.052	$2.37 \pm 0.26$	$1.1 \pm 0.13$
080925.775	$21.8 \pm 0.9$	$20.2 \pm 1.0$	090308.734	$2.18 \pm 0.13$	$1.1 \pm 0.13$
081006.604	$6.1 \pm 1.9$	$5.1 \pm 2.1$	090323.002	$133.1 \pm 1.4$	$130 \pm 3$
081009.690	$175 \pm 15$	$26 \pm 1.3$	090328.401	$57 \pm 3$	$40.0 \pm 2.0$
081012.045	$0.90 \pm 0.26$	$0.5 \pm 0.26$	090328.713	$0.32 \pm 0.13$	$0.26 \pm 0.13$
081024.891	$0.66 \pm 0.26$	$0.27 \pm 0.26$	090424.592	$52.2 \pm 1.0$	$5.3 \pm 0.3$
081101.532	$7.4 \pm 0.4$	$10.8 \pm 0.5$	090425.377	$72 \pm 3$	$13.6 \pm 0.7$
081105.614	$0.26 \pm 0.13$	$0.26 \pm 0.13$	090429.753	$11.3 \pm 0.6$	$0.70 \pm 0.06$
081110.601	$20.0 \pm 0.6$	$16.3 \pm 0.8$	090510.016	$2.1 \pm 0.26$	$0.32 \pm 0.06$
081121.858	$25.0 \pm 0.5$	$22.5 \pm 1.1$	090528.516	$102 \pm 5$	$60 \pm 3$
081122.520	$25.6 \pm 1.3$	$4.03 \pm 0.20$	090529.564	$10.4 \pm 0.5$	$9.7 \pm 0.5$
081125.496	$14.6 \pm 0.3$	$7.9 \pm 0.4$	090531.775	$2.0 \pm 0.26$	$1.1 \pm 0.13$
081126.899	$56.1 \pm 2.8$	$35.0 \pm 1.7$	090617.208	$0.45 \pm 0.12$	$0.13 \pm 0.06$
081129.161	$32.0 \pm 2.3$	$15.4 \pm 0.8$	090618.353	$152 \pm 5$	$120 \pm 6$
081207.680	$153 \pm 7$	$100 \pm 5$	090620.400	$16.5 \pm 0.26$	$15.3 \pm 0.8$
081209.981	$0.45 \pm 0.13$	$0.19 \pm 0.13$	090621.922	$0.13 \pm 0.06$	$0.13 \pm 0.06$
081215.784	$7.7 \pm 0.3$	$7.7 \pm 0.4$	090623.107	$72.2 \pm 0.6$	$30.9 \pm 1.5$
081216.531	$0.96 \pm 0.26$	$0.26 \pm 0.13$	090626.189	$70.4 \pm 0.6$	$50.1 \pm 2.5$

## 5.2 Analysis of the BGO Peak Count Rate

The following analysis is based on the careful examination of BGO CTIME light curves. As previously mentioned, CTIME data have a 64 ms temporal resolution during burst–mode and spectral resolution of 8 energy channels. An example of the CTIME energy–channel boundaries for the very bright GRB 090227B is shown in Table 5.3. Channel edges are controlled using the specific Lookup Tables (LUTs), which map the 4096 raw channels into the 8 energy channels (see §2.2.4). Exact channel boundaries can vary from detector to detector (BGO 0 or 1) and from burst to burst. The burst duration measured with BGO detectors was determined by excluding only the overflow channel (ch. 7, from  $\sim 38$  to  $\sim 50$  MeV) and including the first channel (ch. 0, from  $\sim 120$  to  $\sim 450$  keV). In this way the region between  $\sim 200$  and  $\sim 450$  keV, in which GRBs emit most of their energy, is fully covered.

The BGO CTIME background was computed including pre– and post–trigger time intervals, usually from  $-300$  s to  $+300$  s in case of long bursts and from  $-50$  s to  $+50$  s for short bursts. The background–subtracted light curve was then examined for the maximum or “peak” count rate on the 64 ms–timescale over each individual CTIME energy channel.

The initial sample of 56 bursts was subdivided following the peak analysis results according to the detection significance in the different energy channels. GRBs detected with more than  $3\sigma$  significance in ch. 1 (see Table 5.3) constitute the *MAIN* sample. 50 bursts satisfy this selection criterion. These are further subdivided in other two categories: the *BEST* sample, which includes bursts detected with more than  $3\sigma$  in ch. 2, and the *GOLD* sample, which includes bursts detected with more than  $3\sigma$  in ch. 3. 26 and 11 bursts belong to the *BEST* and

**Table 5.3:** BGO CTIME energy channels for GRB 090227B

Channel #	Energy Interval	
	Start (keV)	Stop (keV)
0	113.25	451.60
1	451.60	973.33
2	973.33	2119.65
3	2119.65	4591.62
4	4591.62	9757.00
5	9757.00	21463.0
6	21463.0	37989.0
7	37989.0	50000.0

*GOLD* samples, respectively. All GRBs jointly detected by LAT and GBM during the first year of operation are included in the *MAIN* sample except for the short GRB 081024B (ID # 54), which has a very low detection significance in the BGO detectors.

Light curves of the four brightest bursts belonging to the *GOLD* sample are shown in Figures 5.3 and 5.4. Three out of these four bursts are short GRBs. Plots on the *left* display the GRB light curves observed by the GBM detectors over 5 energy ranges. The *top panel* shows the 8–200 keV band, covered by the mostly illuminated NaI detector(s). The other four panels show the BGO light curve in different energy ranges, covering the first four CTIME energy channels. The bin width changes from 8 ms in case of short bursts to 128 ms for long ones. On the *right*, the BGO light curve in the 2–5 MeV energy range (*red histogram*) is plotted on top of the NaI light curve in the 8–200 keV energy range (*black histogram*). This highlights possible differences in the arrival times of the high–energy photons with respect to the low–energy ones (spectral lag effect). A brief descriptions of these four brightest events is given hereafter.

1. The brightest events among the whole GBM burst sample (as of December 2009) are GRB 090227B and GRB 090228, both having a  $T_{90} < 1$  s (Figure 5.3). These bursts didn't show any excess in the LAT counts (applying standard analysis methods), but are currently further investigated for possible detection by the LAT (Connaughton et al., 2010);
2. The long burst GRB 081215A (Figure 5.4, *top* plots), another event which was marginally detected by the LAT. Indeed, this burst was at an angle of  $86^\circ$  to the LAT boresight, which means that neither directional nor energy information could be obtained with the standard analysis procedures. Using a non–standard data selection, over 100 counts above background were detected within a 0.5 s interval in coincidence with the main GBM peak. The significance of this excess was greater than  $8\sigma$ . A preliminary study of the LAT instrument performance at such a large inclination suggested that these events are likely to be low–energy gamma–rays, with energies less than 200 MeV (McEnery et al., 2008);
3. The fourth brightest burst is the very energetic short GRB 090510 (Figure 5.4, *bottom* plots) jointly detected by GBM and LAT, whose properties are extensively described in §4.2.

## 5. BGO–BRIGHT GRBS

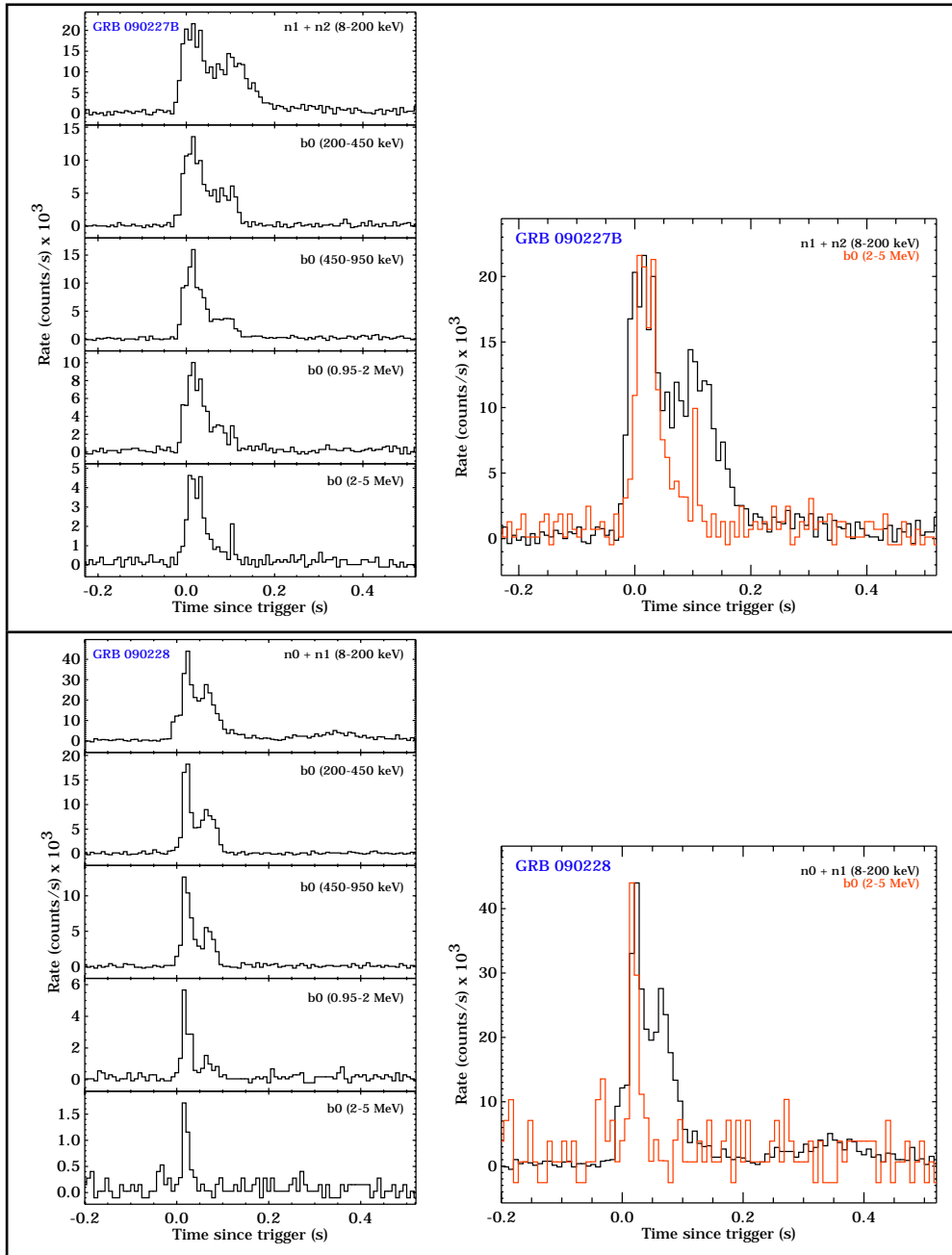


**Figure 5.3:** Background-subtracted light curves of GRB 090227B (*top*) and GRB 090228 (*bottom*) observed by the GBM detectors. Plots on the *left* show the sum of the counts in different energy bands as seen by the mostly illuminated NaI (*top histogram*, in the 8–200 keV energy range) and the BGO detectors (remaining *four histograms*, covering the first four CTIME energy channels). On the *right*, the BGO light curve in the 2–5 MeV energy range (*red histogram*) is plotted on top of the NaI light curve in the 8–200 keV energy range (*black histogram*). In all cases, the bin width is 8 ms

## 5.2. Analysis of the BGO Peak Count Rate

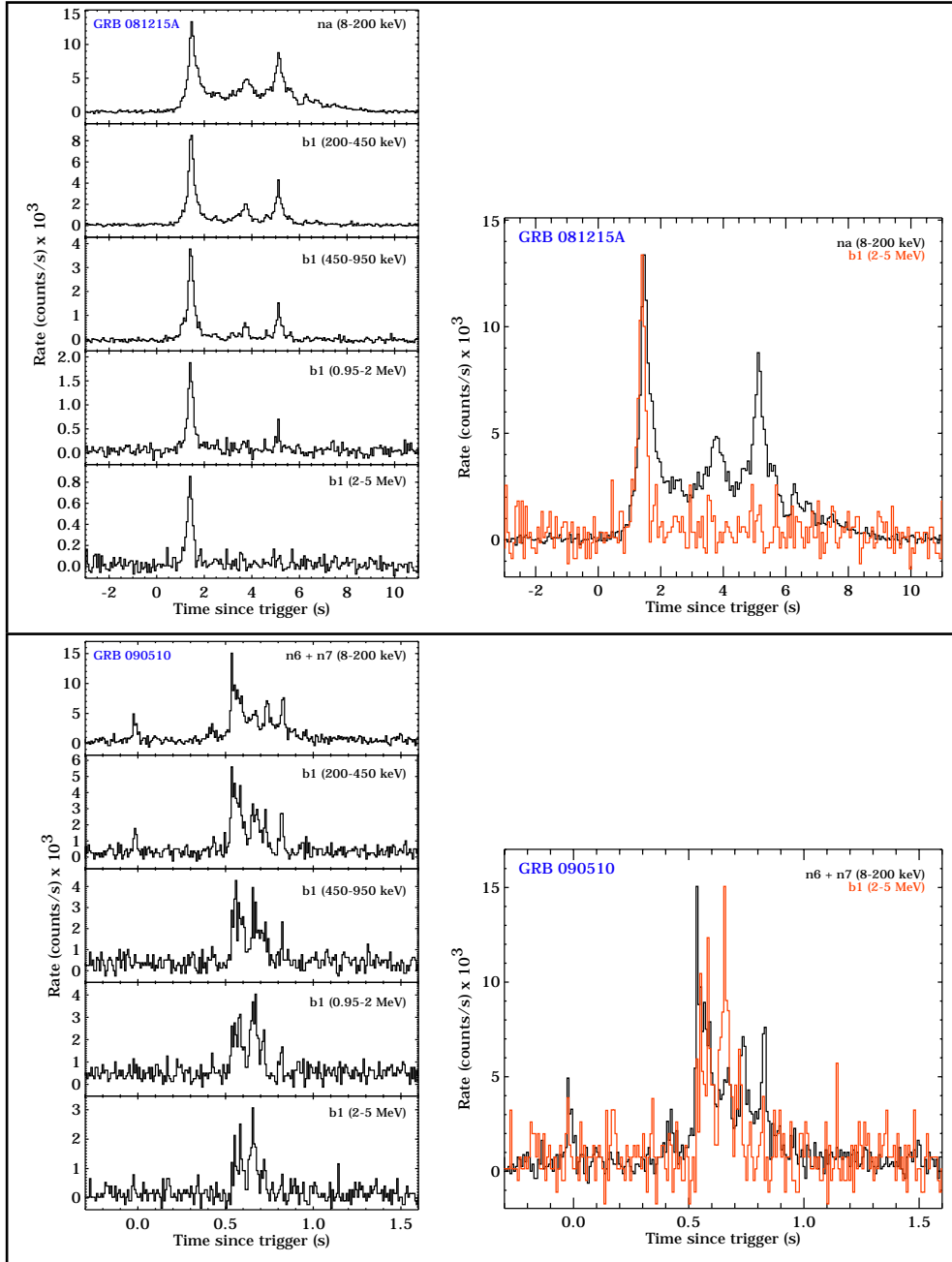


**Figure 5.4:** Background-subtracted light curves of GRB 081215 (*top*) and GRB 090510 (*bottom*) observed by the GBM detectors. The bin width is 128 ms for GRB 081215 and 8 ms for GRB 090510. Color code as in Figure 5.3

## 5. BGO–BRIGHT GRBS

**Table 5.4:** Results for the background–subtracted 64 ms–peak count rates (columns 3–7) and accumulated peak count rates (columns 8 and 9) measured in different energy bands for 56 BGO–bright GRBs. The bursts are sorted according to the peak count rate measured in ch. 1 (column 5) and an unique ID is associated accordingly (column 1)

ID	GBM Trig. #	Peak Count Rate					Accumulated Count Rate	
		ch0-ch6	ch0	ch1	ch2	ch3	ch1	ch2
1	090227.772	2193 ± 50	942 ± 32	605 ± 25	449 ± 23	163 ± 14	798 ± 34	543 ± 31
2	090228.204	1552 ± 42	1012 ± 33	395 ± 21	121 ± 13	20 ± 6	434 ± 23	126 ± 15
3	081215.784	1267 ± 37	717 ± 27	366 ± 20	130 ± 13	48 ± 8	3768 ± 93	967 ± 81
4	090510.016	646 ± 31	260 ± 18	190 ± 16	134 ± 15	56 ± 10	509 ± 32	375 ± 30
5	081216.531	358 ± 23	167 ± 15	106 ± 12	76 ± 11	–	252 ± 21	139 ± 19
6	090424.592	476 ± 27	403 ± 21	88 ± 12	–	–	1185 ± 83	–
7	080807.993	142 ± 21	61 ± 11	64 ± 12	–	–	238 ± 40	–
8	090618.353	239 ± 22	167 ± 15	62 ± 11	24 ± 9	–	6114 ± 342	1439 ± 378
9	081224.887	173 ± 21	125 ± 13	54 ± 11	25 ± 10	15 ± 7	2409 ± 165	–
10	090328.713	183 ± 23	102 ± 14	53 ± 12	–	–	201 ± 33	–
11	081209.981	144 ± 15	85 ± 10	47 ± 8	23 ± 7	–	189 ± 18	57 ± 15
12	090102.122	162 ± 18	99 ± 12	43 ± 9	–	–	1871 ± 142	–
13	090623.107	99 ± 22	52 ± 11	43 ± 12	–	–	1422 ± 239	–
14	090626.189	259 ± 23	203 ± 16	43 ± 10	24 ± 10	–	2305 ± 232	–
15	080825.593	151 ± 25	103 ± 14	42 ± 13	–	–	1230 ± 212	–
16	090328.401	130 ± 17	76 ± 11	39 ± 9	–	–	3400 ± 177	–
17	081012.045	96 ± 18	47 ± 11	38 ± 9	–	–	120 ± 24	–
18	090217.206	111 ± 17	71 ± 11	38 ± 9	17 ± 8	11 ± 5	2212 ± 128	430 ± 128
19	081110.601	125 ± 17	90 ± 12	38 ± 8	14 ± 7	9 ± 5	683 ± 107	–
20	090323.002	92 ± 20	63 ± 11	37 ± 11	–	–	7520 ± 491	–
21	080916.009	105 ± 23	44 ± 11	36 ± 12	34 ± 12	20 ± 9	4095 ± 361	2179 ± 372
22	081125.496	120 ± 24	90 ± 13	33 ± 13	–	–	567 ± 133	–
23	080906.212	64 ± 19	45 ± 10	30 ± 9	24 ± 8	–	125 ± 57	–
24	080816.989	93 ± 16	41 ± 9	28 ± 8	24 ± 8	–	315 ± 36	221 ± 36
25	080723.557	120 ± 17	93 ± 13	28 ± 8	–	–	901 ± 210	–
26	080817.161	71 ± 15	39 ± 8	28 ± 8	23 ± 8	–	2502 ± 175	–
27	081129.161	85 ± 17	64 ± 11	27 ± 9	24 ± 8	–	571 ± 116	–
28	090531.775	85 ± 18	40 ± 10	27 ± 9	25 ± 10	–	172 ± 36	–
29	081231.140	64 ± 16	46 ± 10	27 ± 8	–	–	621 ± 181	–
30	090305.052	104 ± 16	62 ± 10	27 ± 7	–	–	156 ± 27	70 ± 28
31	090528.516	76 ± 21	42 ± 11	26 ± 11	25 ± 11	21 ± 9	1621 ± 314	–
32	081009.690	51 ± 20	29 ± 10	26 ± 11	–	–	695 ± 205	463 ± 214
33	090620.400	97 ± 18	79 ± 11	25 ± 9	–	–	551 ± 121	–
34	081226.509	67 ± 22	75 ± 14	25 ± 11	–	–	48 ± 14	–
35	090227.310	60 ± 20	30 ± 10	25 ± 11	22 ± 10	–	663 ± 178	–
36	081121.858	74 ± 17	44 ± 10	24 ± 9	–	–	879 ± 150	–
37	081101.532	63 ± 16	35 ± 9	24 ± 8	16 ± 8	–	887 ± 95	–
38	090308.734	89 ± 16	61 ± 11	24 ± 8	16 ± 7	11 ± 5	159 ± 29	–
39	090131.090	78 ± 20	73 ± 12	23 ± 10	–	–	–	–
40	080725.541	101 ± 21	62 ± 14	22 ± 10	19 ± 10	–	37 ± 10	–
41	081006.604	41 ± 16	23 ± 8	22 ± 9	–	–	236 ± 111	–
42	080925.775	84 ± 19	54 ± 10	22 ± 10	19 ± 9	15 ± 7	647 ± 160	–
43	081207.680	57 ± 17	37 ± 10	22 ± 9	25 ± 9	–	4214 ± 315	–
44	080723.985	60 ± 14	39 ± 9	20 ± 7	–	–	753 ± 168	–
45	080905.499	52 ± 18	28 ± 10	20 ± 9	–	–	130 ± 38	–
46	081122.520	75 ± 18	50 ± 10	19 ± 9	24 ± 10	–	189 ± 68	–
47	080802.386	77 ± 13	49 ± 9	14 ± 6	–	–	18 ± 8	–

## 5.2. Analysis of the BGO Peak Count Rate

**Table 5.4:** (continued)

ID	GBM Trig. #	Peak Count Rate					Accumulated Count Rate	
		ch0-ch6	ch0	ch1	ch2	ch3	ch1	ch2
48	090219.074	37 ± 12	21 ± 7	13 ± 6	–	–	19 ± 11	–
49	081126.899	38 ± 14	21 ± 8	13 ± 7	22 ± 8	–	351 ± 152	–
50	090429.753	69 ± 15	48 ± 10	13 ± 7	–	–	70 ± 22	–
51	081024.891	29 ± 15	17 ± 8	–	–	–	52 ± 21	–
52	090621.922	51 ± 22	35 ± 13	–	–	–	–	–
53	090529.564	87 ± 22	77 ± 13	–	–	–	–	–
54	081105.614	14 ± 14	11 ± 7	–	–	–	–	–
55	090617.208	59 ± 22	20 ± 10	–	–	–	–	–
56	090425.377	41 ± 17	22 ± 9	–	–	–	–	–

Results for the background–subtracted 64 ms–peak count rate measured in different BGO energy bands are given in Table 5.4, columns 3 through 7. The bursts are sorted according to the peak count rate measured in ch. 1 (column 5) and a unique ID is associated accordingly (column 1). The corresponding distribution of the peak count rate in the different energy bands is shown schematically in four histograms in Figure 5.5. The *blue histogram* includes “All” bursts passing the initial event selection; the *green histogram* includes bursts belonging to the *MAIN* sample, while the *red* and *yellow* histograms show the distribution of bursts belonging to the *BEST* and *GOLD sample*, respectively. Another representation of the BGO peak count rate as a function of the GRB ID is given in the *left panel* of Figure 5.6. As was already mentioned, bursts are sorted according to the peak count rate measured in ch. 1 (*green histogram*). It is worth noting that many bursts belonging to the *MAIN* sample (*green* distributions) are not detected at higher energies, i.e. above 1 MeV. Even when the emission in ch. 0 is relatively high, some bursts show a very steep spectrum with a strong drop–off around 1 MeV, and an even stronger drop–off above 2 MeV. This behavior can be further investigated through the following spectral analysis (see §5.3).

A parallel approach was followed to evaluate not only the 64 ms–peak count rate, but also the accumulated counts detected over the whole GRB duration. This was done by binning all the counts detected over the BGO–burst duration into a single temporal interval, and then measuring the count rate in the energy channels 1 and 2. All bursts belonging to the *MAIN* sample are clearly detected at a  $3\sigma$  level in ch. 1. Results for the background–subtracted accumulated count rates in channels 1 and 2 are given in columns 8 and 9 of Table 5.4 and are schematically shown in the *right panel* of Figure 5.6.

## 5. BGO–BRIGHT GRBS

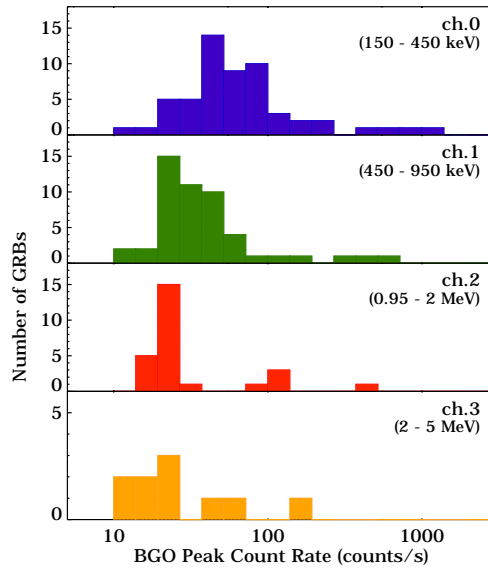


**Figure 5.5:** Distribution of the measured BGO peak count rate in four CTIME energy channels (ch. 0–3) for 56 BGO–bright GRBs. The two *top panels* include 50 bursts belonging to the *MAIN* sample (*blue and green histograms*), while the *bottom panels* include 26 (*BEST* sample, *red histogram*) and 11 (*GOLD* sample, *yellow histogram*) bursts, respectively

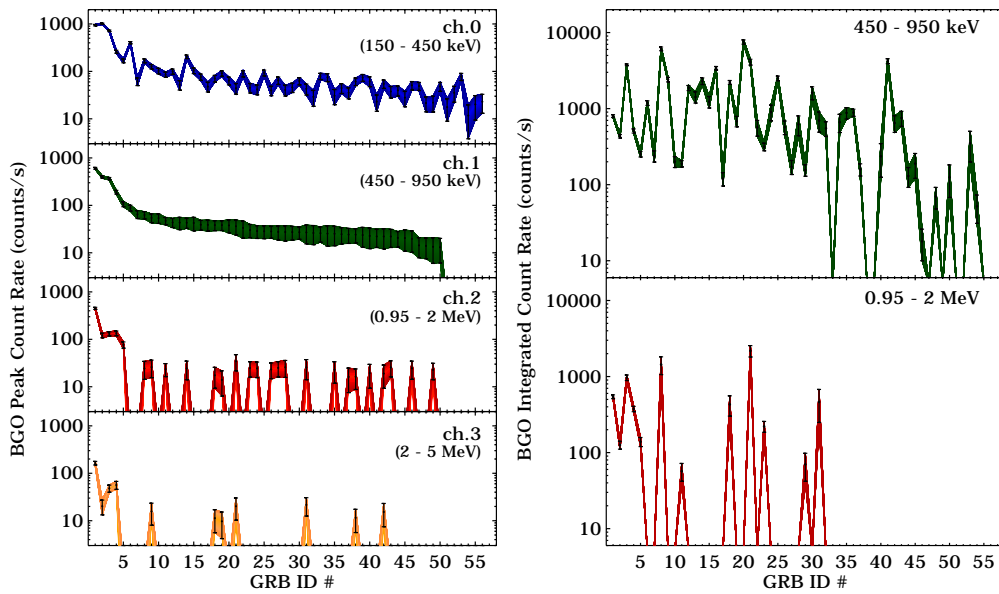


**Figure 5.6:** *Left:* BGO peak count rate measured in four CTIME energy channels (ch. 0–3) for 56 BGO–bright GRBs. Bursts are sorted according to the peak count rate measured in ch. 1 (column 5 of Table 5.4). The burst IDs are listed in column 1. *Right:* Accumulated count rate measured in channel 1 (*top panel*) and 2 (*bottom panel*) for 56 BGO–bright GRBs

### 5.2.1 LAT Detections

An interesting aspect of the BGO peak count–rate analysis emerges by considering only those bursts which are located either inside or at the edge of the LAT FoV. (i. e.  $< 65^\circ$  or between  $65^\circ$  and  $90^\circ$  from the LAT boresight). Figure 5.7 shows the BGO peak count rate measured in channel 1 for 15 and 11 bursts belonging to the *MAIN* sample which respectively fulfill these conditions. The GBM trigger IDs and numbers for both subsamples are listed in top right corner of each plot and also in Table 5.5. *Green circles, orange stars* and *red squares* represent firm, marginal or missing LAT detections, respectively. The *blue dotted line* marks a “detection limit” which I arbitrarily placed at 30 and 100 counts per second in the measured peak count rate. For those bursts with lower rates in channel 1 no detection has been yet reported from the LAT. The only exception is GRB 081224: no clear detection was found at the time of trigger in 2008, but the burst is currently under further investigation. Recently, Pelassa et al. (2010) presented a new technique to recover the signal from GRBs prompt emission between  $\sim 30$  MeV and 100 MeV, which differs from the standard LAT analysis (the so–called “LAT Low–Energy” technique, or LLE). This technique will hopefully confirm the LAT marginal detections and reveal undiscovered emission from the brightest BGO bursts presented in this work.

**Table 5.5:** GRBs belonging to the *MAIN* sample which are located inside (*left table*) or at the edge (*right table*) of the LAT FoV. Bursts are sorted according to channel 1 and a new ID # is associated accordingly

Inside LAT FoV		Edge of LAT FoV	
ID #	GBM Trig. #	ID #	GBM Trig. #
1	090228.204	1	090227.772
2	090510.016	2	081215.784
3	081224.887	3	090424.592
4	090626.189	4	080807.993
5	080825.593	5	090328.713
6	090328.401	6	090102.122
7	090217.206	7	090623.107
8	090323.002	8	081012.045
9	080916.009	9	081110.601
10	081231.140	10	080816.989
11	090305.052	11	080817.161
12	090531.775		
13	090620.400		
14	090308.734		
15	081207.680		

## 5. BGO–BRIGHT GRBS

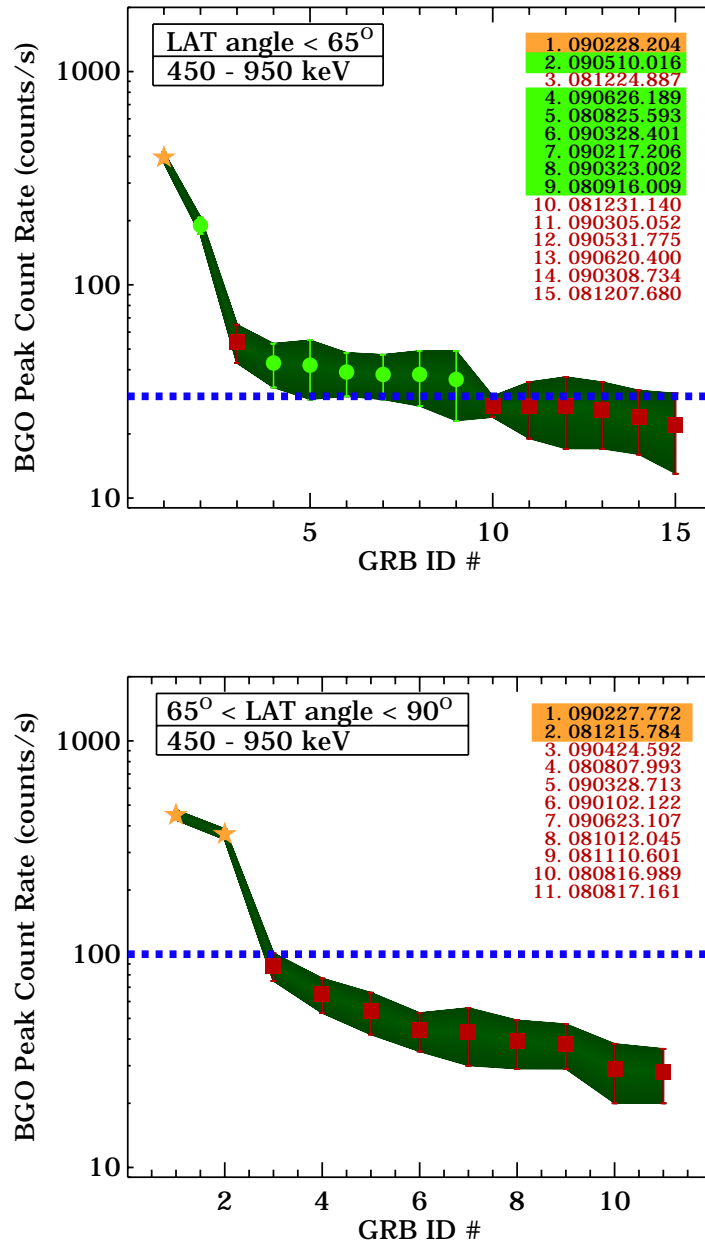


**Figure 5.7:** BGO peak count rate measured in channel 1 for those bursts inside (*left panel*) and at the edge (*right panel*) of the LAT FoV. *Green circles*, *orange stars* and *red squares* represent firm, marginal or missing LAT detections, respectively. The *blue dotted line* marks the “detection limit” placed at 30 and 100 counts/s

The analysis of the BGO peak count rate measured in channel 1 ( $\sim 450$ – $\sim 950$  keV) clearly represents a good candidate for a discriminator of potential LAT detections. In the near future, it would be very interesting to implement the code into the standard GBM analysis tools (RMFIT). Given the burst location relative to the LAT FoV the code could re–draw and update the BGO peak count rate plot in an automatic and possibly very rapid way, thus allowing a prompt alert of LAT BAs on duty.

## 5.2.2 BGO Effective–Area Correction

Beside considering the angle to the LAT boresight, another way is to consider the angle between the source and the BGO detectors. As can be seen in the spacecraft model shown in the *right panel* of Figure 2.10, each BGO detector is mounted parallel to the  $y$ -axis (in spacecraft coordinates). Given the azimuth  $\phi$  and zenith angle  $\theta$  (which indeed corresponds to the LAT boresight angle) for each burst in the sample, the angle with respect to  $y$  is given by the following equation:

$$\beta_y = \arccos(\sin \theta \sin \phi) \quad (5.1)$$

In §3.3.3, the off-axis response of the BGO detectors was studied for both flight module detectors at various angles between  $0^\circ$  and  $90^\circ$ . Assuming that the response is best at  $0^\circ$  (on–axis), a scaling factor can be calculated for each direction and then used to correct the peak count rates. Figure 5.8 shows the correction factors for detector FM01 and FM02 (b0 and b1, respectively). Three energies were considered, roughly corresponding to the CTIME energy channels discussed in

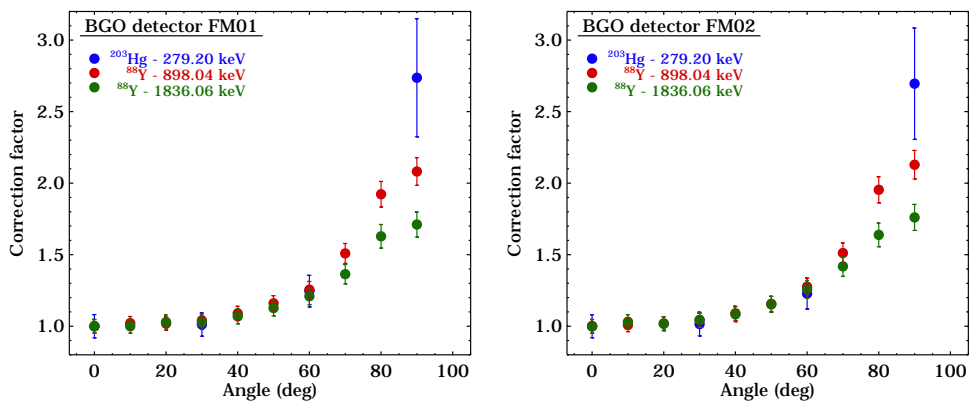


**Figure 5.8:** Effective area correction at different energies

this chapter. Measurements from  $^{203}\text{Hg}$  at 279.20 keV nicely cover the 150–450 keV energy range (channel 0). In this case, measurements were carried out only at 4 different angles ( $0^\circ$ ,  $30^\circ$ ,  $60^\circ$  and  $90^\circ$ ). Thus it is necessary to interpolate between those values in order to cover the whole range between  $0^\circ$  and  $90^\circ$  with a  $10^\circ$  precision. For channel 1 and 2, the best choice consists in measurements collected with the  $^{88}\text{Y}$  radioactive source at 898.04 keV and 1836.06 keV, respectively. The correction factors are relatively small around 1 out to  $\sim 40^\circ$  and rapidly increase towards  $90^\circ$ . At higher energies, the correction factor is not so high as at lower energies. This mainly reflects the strong absorption of low–energy photons by the BGO PMTs.

After having applied the effective–area correction to all peak count rate values previously derived, a hardness ratio (HR) was calculated by dividing the count rates in channel 1 by the count rates in channel 0. Unfortunately, a hardness ratio between channels 2 and 0 could not be calculated, since there aren't enough bursts seen in channel 2 (i.e. in the *BEST* sample). Figure 5.9 shows the intensity of a burst in both channels (channel 0 + channel 1) plotted versus HR for both BGO detectors (*top and bottom panels*, respectively). Different shades of blue indicate different BGO incident angles ( $\beta_y$ , see the color bar at the *top right corner*). In this case,  $\beta_y = 90^\circ$  (data points marked in *light blue*) corresponds to the on–axis geometry, namely where optimal detection occurs and no effective area correction is needed. Bursts detected by the LAT are marked as *dark red crosses*. The angle–corrected intensity measured with the BGO detectors yet appears to be the best discriminator for LAT detections. A limit of 100 counts/s in both channels 0 and 1 can be placed for both BGO detectors. Bursts with higher intensity but with a BGO angle  $< 30^\circ$ , which roughly corresponds to bursts outside the LAT FoV, are not detected by the LAT. The HR calculated through the peak count rate analysis can not be used as a good indicator for possible LAT detections.

## 5.3 Spectral Analysis

### 5.3.1 Photon Models

For all 56 bursts listed in Table 5.1, time–integrated spectra were fitted by a set of photon models that are commonly used to fit GRB spectra. Each of the photon models used provides a different number of free parameters, i.e. different degrees of freedom for each fit. All fits were performed with RMFIT (version 3.2, see §2.3.4). In some cases an effective area correction had to be fit to the BGO data

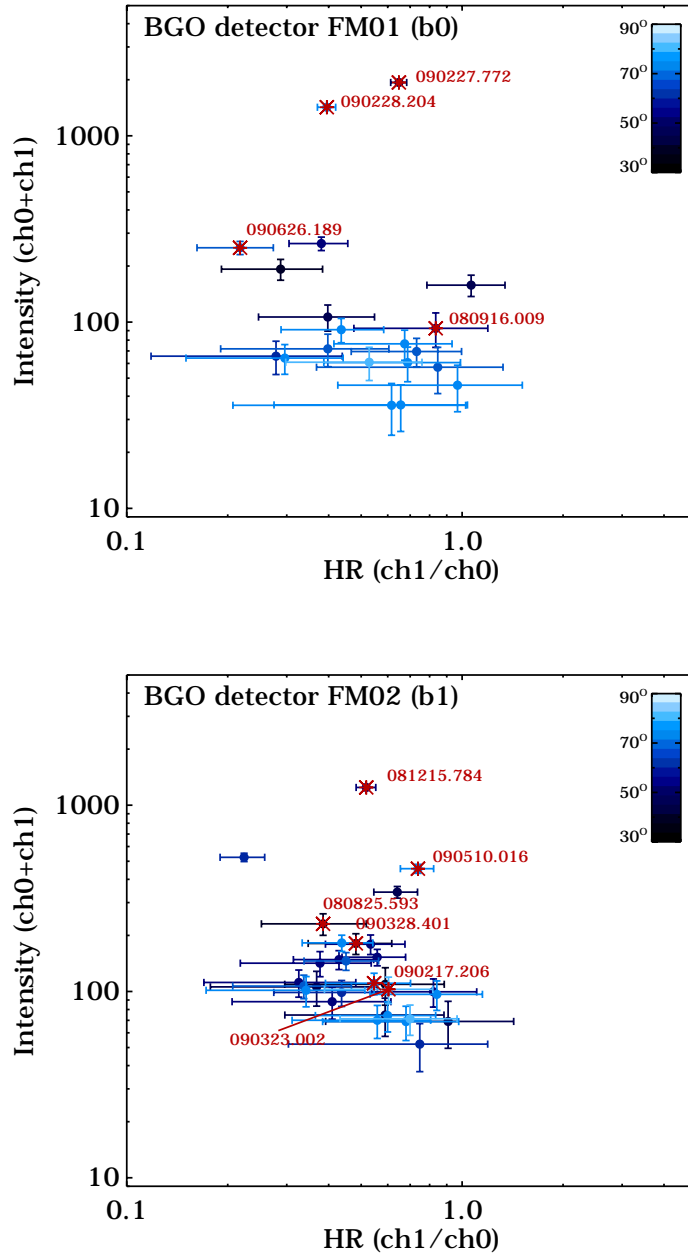


**Figure 5.9:** Intensity vs. hardness ratio (HR) calculated in counts space for all bursts seen by BGO detector b0 (*top panel*) and b1 (*bottom panel*). The BGO angle dependence is indicated in the color bar at the *top right corner*. Optimal detection occurs at 90° (direction perpendicular to the BGO crystal). Bursts fully or marginally detected by the LAT are marked with *dark red crosses*

## 5. BGO–BRIGHT GRBS

---

(as previously shown in the case of GRB 090902B, §4.3) to match the model normalizations given by the NaI data; this correction is usually consistent with the uncertainties in the GBM detector responses.

As briefly discussed in §1.2.1, GRB spectra are usually well represented by a broken power-law in the BATSE energy band. Due to GBM’s broader energy coverage extending smoothly from 8 keV to 40 MeV, the chance for the break energy lying outside this energy range is minimal. Furthermore, soft or dim spectra are excluded by the initial selection on the BGO count rate previously described. Therefore the simple power-law model is excluded from the following analysis. The two models used are briefly reviewed hereafter.

### The Band Model

The empirical GRB model was already discussed in §1.2.1 and adopted for all GBM–LAT GRB analysis presented in chapter 4. It is given by

$$f_{Band}(E) = \begin{cases} A \left( \frac{E}{100 \text{ keV}} \right)^\alpha \exp\left(-\frac{E(2+\alpha)}{E_{\text{peak}}}\right) & \text{if } E < E_c \\ A \left( \frac{(\alpha-\beta)E_{\text{peak}}}{100 \text{ keV}(2+\alpha)} \right)^{\alpha-\beta} \exp(\beta - \alpha) \left( \frac{E}{100 \text{ keV}} \right)^\beta & \text{if } E > E_c \end{cases}, \quad (5.2)$$

where

$$E_c = (\alpha - \beta) \frac{E_{\text{peak}}}{2 + \alpha} \equiv (\alpha - \beta)E_0$$

and  $E_0$  is the  $e$ -folding energy of the fit. The model consists of 4 parameters: the amplitude  $A$  in photons  $\text{s}^{-1} \text{ cm}^{-2} \text{ keV}^{-1}$ , the low- and high-energy spectral indices  $\alpha$  and  $\beta$ , and the  $\nu F_\nu$  peak energy  $E_{\text{peak}}$ .

### The Comptonized (Comp) Model

The second model considered is a low-energy power-law with an exponential high-energy cutoff. It is equivalent to the Band model without a high-energy power-law, namely  $\beta \rightarrow -\infty$ , and has the form

$$f_{Comp}(E) = A \left( \frac{E}{100 \text{ keV}} \right)^\alpha \exp\left(-\frac{E(2 + \alpha)}{E_{\text{peak}}}\right). \quad (5.3)$$

The model is so named because in the special case  $\alpha = -1$  it represents the Comptonized spectrum from a thermal medium; however,  $\alpha$  is kept as a free parameter here. More details regarding both spectral models can be found in Kaneko et al. (2006).

## 5.4 Spectral Analysis Results

The results of the comprehensive time-integrated spectral analysis performed herein are presented in Table 5.6, for each burst. The model adopted for the spectral fit and the spectral analysis parameters  $E_{\text{peak}}$ ,  $\alpha$  and  $\beta$  are given in columns 2–4. Column 5 and 6 give the photon flux (in photons  $\text{s}^{-1} \text{cm}^{-2}$ ) an energy flux (in  $\text{erg s}^{-1} \text{cm}^{-2}$ ) calculated in the standard NaI energy range 8–1000 keV. The quality of fit in terms of CSTAT over degrees-of-freedom (DOF) is listed in column 7. For each burst, the fluence was calculated by multiplying the energy flux by the duration of the time interval selected for the spectral analysis (which is reported in columns 8 and 9 of Table 5.1). This calculation was performed in 5 different energy bands, namely (i.) the standard NaI energy range 8–1000 keV; (ii.) the complete GBM energy range 8 keV–40 MeV; (iii.) the BGO energy range (not overlapping with the NaI one) 1–40 MeV; (iv.) the standard BATSE trigger energy 50–300 keV; and (v.) the complete BATSE energy range 20–2000 keV. The two latter energy intervals were chosen in order to be able to make comparison with previous GRB samples, like the BATSE bright burst one (Kaneko et al., 2006). Results for the fluence calculation (in  $\text{erg cm}^{-2}$ ) for each burst are listed in Table 5.7.

In the time-integrated spectral analysis presented in Table 5.6, the Band model is preferred over the Comptonized one in 30 out of 56 cases, i.e. for those fits resulting in significant improvements ( $\Delta\text{CSTAT} > 6$ ) for the additional DOF. This assures that the spectra have a well-identifiable high-energy power-law component. Short bursts (with  $T_{90} < 2$  s) are usually best fit by a Comptonized model. Only six out of 20 short GRBs are best fit by the Band model. Three of those are the brightest bursts, which are currently under investigation by Guiriec et al. (2010) for the presence of an extra power-law component in the GBM data<sup>1</sup>. In my analysis, the fit with the extra-component does not imply a significant improvement in the CSTAT over the simple Band model. This may be mainly due to differences in the detector's selection and in the time-interval selection.

<sup>1</sup>In the case of GRB 090510, the extra-component is already discussed in §4.2.

## 5. BGO–BRIGHT GRBS

**Table 5.6:** Summary of time–integrated spectral fit results for 56 GRBs

Name	Model	$E_{\text{peak}}$ (keV)	$\alpha$	$\beta$	Photon Flux ( $\text{ph s}^{-1} \text{cm}^{-2}$ ) (8–1000 keV)	Energy Flux ( $\text{ergs}^{-1} \text{cm}^{-2}$ ) (8–1000 keV)	CSTAT/DOF
080723.557	Band	231 (+10 −9)	−0.88 (±0.02)	−2.49 (+0.10 −0.15)	8.62 (±0.05)	(1.25±0.01)·10 <sup>−6</sup>	398/236
080723.985	Comp	439 (±20)	−0.95 (±0.03)	—	3.88 (±0.04)	(7.38±0.11)·10 <sup>−7</sup>	506/359
080725.541	Comp	1708 (+750 −500)	−0.89 (+0.14 −0.11)	—	5.6 (±0.4)	(1.80±0.10)·10 <sup>−6</sup>	355/356
080802.386	Comp	669 (+300 −150)	−0.81 (+0.18 −0.16)	—	4.5 (±0.3)	(1.20±0.10)·10 <sup>−6</sup>	394/356
080807.993	Comp	791 (+260 −170)	−1.01 (+0.07 −0.06)	—	1.67 (±0.04)	(3.81±0.13)·10 <sup>−7</sup>	577/481
080816.989	Comp	1750 (+190 −180)	−0.42 (+0.08 −0.07)	—	4.86 (±0.17)	(2.47±0.08)·10 <sup>−6</sup>	400/357
080817.161	Band	473 (+24 −22)	−0.91 (±0.02)	−2.51 (+0.13 −0.17)	8.80 (±0.05)	(1.80±0.02)·10 <sup>−6</sup>	507/361
080825.593	Band	174 (±8)	−0.64 (±0.04)	−2.31 (+0.08 −0.10)	10.19 (±0.07)	(1.49±0.02)·10 <sup>−6</sup>	429/357
080905.499	Comp	604 (+200 −130)	−0.29 (+0.28 −0.23)	—	3.93 (±0.24)	(1.47±0.10)·10 <sup>−6</sup>	398/361
080906.212	Band	149 (±9)	−0.49 (±0.07)	−2.28 (+0.10 −0.12)	6.97 (±0.08)	(1.01±0.02)·10 <sup>−6</sup>	522/479
080916.009	Band	563 (±30)	−1.03 (+0.02 −0.01)	−2.24 (+0.07 −0.09)	7.48 (±0.04)	(1.48±0.01)·10 <sup>−6</sup>	486/358
080925.775	Band	137 (+9 −8)	−0.98 (+0.05 −0.04)	−2.22 (+0.07 −0.09)	5.28 (±0.05)	(5.82±0.10)·10 <sup>−7</sup>	441/359
081006.604	Comp	818 (+340 −210)	−0.43 (+0.28 −0.22)	—	1.83 (±0.12)	(7.3±0.5)·10 <sup>−7</sup>	390/362
081009.690	Band	78.77 (+12 −10)	−0.59 (+0.18 −0.16)	−1.93 (+0.06 −0.08)	2.66 (±0.05)	(3.11±0.10)·10 <sup>−7</sup>	476/358
081012.045	Comp	753 (+300 −160)	−0.44 (+0.23 −0.20)	—	3.95 (±0.20)	(1.50±0.08)·10 <sup>−6</sup>	368/355
081024.891	Comp	2231 (+1300 −900)	−1.02 (+0.13 −0.11)	—	3.09 (±0.25)	(8.8±0.7)·10 <sup>−7</sup>	347/359
081101.532	Comp	498 (+30 −28)	−0.69 (±0.04)	—	7.18 (±0.11)	(1.82±0.03)·10 <sup>−6</sup>	360/360
081105.614	Comp	456 (+180 −90)	0.77 (+0.90 −0.70)	—	3.4 (±0.3)	(1.55±0.21)·10 <sup>−6</sup>	379/360
081110.601	Comp	549 (+100 −80)	−1.12 (+0.05 −0.04)	—	3.26 (±0.06)	(5.77±0.14)·10 <sup>−7</sup>	587/358
081121.858	Band	163 (+20 −16)	−0.48 (+0.13 −0.11)	−1.97 (+0.06 −0.07)	4.36 (±0.10)	(7.46±0.13)·10 <sup>−7</sup>	403/356
081122.520	Band	177 (+20 −18)	−0.62 (+0.09 −0.08)	−2.26 (+0.14 −0.25)	5.40 (±0.09)	(8.18±0.20)·10 <sup>−7</sup>	467/361
081125.496	Band	165 (±9)	−0.45 (±0.06)	−2.56 (+0.14 −0.20)	13.10 (±0.14)	(1.91±0.03)·10 <sup>−6</sup>	412/354
081126.899	Comp	357 (+40 −30)	−0.93 (+0.06 −0.05)	—	2.25 (±0.04)	(3.85±0.12)·10 <sup>−7</sup>	381/360

Table 5.6: (continued)

Name	Model	$E_{\text{peak}}$ (keV)	$\alpha$	$\beta$	Photon Flux ( $\text{ph s}^{-1} \text{cm}^{-2}$ ) (8–1000 keV)	Energy Flux ( $\text{erg s}^{-1} \text{cm}^{-2}$ ) (8–1000 keV)	CSTAT/DOF
081129.161	Band	208 <sup>(+30)</sup> <sub>(-25)</sub>	-0.89 ( $\pm 0.07$ )	-2.05 <sup>(+0.09)</sup> <sub>(-0.14)</sub>	4.58 ( $\pm 0.07$ )	(6.77 $\pm 0.13$ ) $\cdot 10^{-7}$	434/356
081207.680	Band	429 <sup>(+30)</sup> <sub>(-28)</sub>	-0.67 ( $\pm 0.03$ )	-2.11 <sup>(+0.08)</sup> <sub>(-0.09)</sub>	2.54 ( $\pm 0.02$ )	(6.21 $\pm 0.07$ ) $\cdot 10^{-7}$	501/356
081209.981	Band	1271 ( $\pm 400$ )	-0.72 <sup>(+0.15)</sup> <sub>(-0.10)</sub>	-2.37 <sup>(+0.36)</sup> <sub>(-0.73)</sub>	10.9 ( $\pm 0.4$ )	(3.93 $\pm 0.14$ ) $\cdot 10^{-6}$	360/356
081215.784	Band	458 ( $\pm 13$ )	-0.71 ( $\pm 0.02$ )	-2.36 <sup>(+0.04)</sup> <sub>(-0.05)</sub>	31.00 ( $\pm 0.13$ )	(7.43 $\pm 0.04$ ) $\cdot 10^{-6}$	519/356
081216.531	Band	1253 ( $\pm 230$ )	-0.81 <sup>(+0.07)</sup> <sub>(-0.05)</sub>	-2.8 <sup>(+0.5)</sup> <sub>(-1.2)</sub>	8.20 ( $\pm 0.23$ )	(2.68 $\pm 0.08$ ) $\cdot 10^{-6}$	445/358
081224.887	Comp	419 ( $\pm 12$ )	-0.71 ( $\pm 0.02$ )	—	12.37 ( $\pm 0.07$ )	(2.79 $\pm 0.03$ ) $\cdot 10^{-6}$	428/358
081226.509	Comp	368 <sup>(+130)</sup> <sub>(-80)</sub>	-0.50 <sup>(+0.25)</sup> <sub>(-0.20)</sub>	—	5.4 ( $\pm 0.4$ )	(1.27 $\pm 0.13$ ) $\cdot 10^{-6}$	436/360
081231.140	Band	232 <sup>(+24)</sup> <sub>(-22)</sub>	-1.07 ( $\pm 0.04$ )	-2.26 <sup>(+0.14)</sup> <sub>(-0.24)</sub>	4.26 ( $\pm 0.04$ )	(5.58 $\pm 0.09$ ) $\cdot 10^{-7}$	491/358
090102.122	Comp	431 <sup>(+14)</sup> <sub>(-13)</sub>	-0.61 ( $\pm 0.03$ )	—	6.59 ( $\pm 0.05$ )	(1.61 $\pm 0.02$ ) $\cdot 10^{-6}$	376/356
090131.090	Band	58.4 <sup>(+5)</sup> <sub>(-4)</sub>	-1.19 <sup>(+0.08)</sup> <sub>(-0.07)</sub>	-2.29 <sup>(+0.06)</sup> <sub>(-0.07)</sub>	9.83 ( $\pm 0.08$ )	(6.80 $\pm 0.11$ ) $\cdot 10^{-7}$	326/236
090217.206	Band	582 ( $\pm 40$ )	-0.92 ( $\pm 0.03$ )	-2.8 <sup>(+0.3)</sup> <sub>(-0.9)</sub>	3.96 ( $\pm 0.04$ )	(8.87 $\pm 0.12$ ) $\cdot 10^{-7}$	525/357
090219.074	Comp	173 <sup>(+80)</sup> <sub>(-40)</sub>	-0.6 <sup>(+0.6)</sup> <sub>(-0.5)</sub>	—	5.1 ( $\pm 0.7$ )	(6.4 $\pm 0.9$ ) $\cdot 10^{-7}$	240/239
090227.310	Comp	1052 <sup>(+230)</sup> <sub>(-180)</sub>	-0.93 ( $\pm 0.06$ )	—	1.69 ( $\pm 0.05$ )	(4.59 $\pm 0.12$ ) $\cdot 10^{-7}$	391/360
090227.772	Band	1954 ( $\pm 80$ )	-0.41 <sup>(+0.27)</sup> <sub>(-0.26)</sub>	-3.23 <sup>(+0.20)</sup> <sub>(-0.26)</sub>	77.2 ( $\pm 1.0$ )	(4.03 $\pm 0.05$ ) $\cdot 10^{-5}$	406/359
090228.204	Band	767 ( $\pm 30$ )	-0.26 ( $\pm 0.04$ )	-3.7 <sup>(+0.4)</sup> <sub>(-0.5)</sub>	87.3 ( $\pm 1.1$ )	(3.76 $\pm 0.05$ ) $\cdot 10^{-5}$	380/361
090305.052	Comp	898 <sup>(+150)</sup> <sub>(-120)</sub>	-0.51 <sup>(+0.11)</sup> <sub>(-0.10)</sub>	—	5.19 ( $\pm 0.17$ )	(2.02 $\pm 0.06$ ) $\cdot 10^{-6}$	392/360
090308.734	Comp	625 <sup>(+60)</sup> <sub>(-50)</sub>	-0.50 <sup>(+0.09)</sup> <sub>(-0.08)</sub>	—	6.19 ( $\pm 0.18$ )	(2.02 $\pm 0.06$ ) $\cdot 10^{-6}$	511/479
090323.002	Band	530 <sup>(+30)</sup> <sub>(-24)</sub>	-0.81 ( $\pm 0.02$ )	-2.42 <sup>(+0.09)</sup> <sub>(-0.12)</sub>	5.56 ( $\pm 0.04$ )	(1.33 $\pm 0.01$ ) $\cdot 10^{-6}$	568/237
090328.401	Band	657 ( $\pm 40$ )	-0.93 ( $\pm 0.02$ )	-2.44 <sup>(+0.14)</sup> <sub>(-0.19)</sub>	6.16 ( $\pm 0.06$ )	(1.44 $\pm 0.02$ ) $\cdot 10^{-6}$	534/360
090328.713	Comp	2026 <sup>(+680)</sup> <sub>(-520)</sub>	-0.96 ( $\pm 0.07$ )	—	13.9 ( $\pm 0.6$ )	(4.13 $\pm 0.20$ ) $\cdot 10^{-6}$	376/356
090424.592	Band+eff	158 ( $\pm 4$ )	-1.00 ( $\pm 0.02$ )	-2.86 <sup>(+0.12)</sup> <sub>(-0.15)</sub>	21.82 ( $\pm 0.09$ )	(2.27 $\pm 0.02$ ) $\cdot 10^{-6}$	558/357
090425.377	Comp	200 <sup>(+50)</sup> <sub>(-30)</sub>	-1.61 ( $\pm 0.04$ )	—	4.77 ( $\pm 0.07$ )	(3.83 $\pm 0.13$ ) $\cdot 10^{-7}$	409/239
090429.753	Comp	1233 <sup>(+630)</sup> <sub>(-380)</sub>	-1.07 <sup>(+0.09)</sup> <sub>(-0.08)</sub>	—	5.72 ( $\pm 0.25$ )	(1.36 $\pm 0.06$ ) $\cdot 10^{-6}$	356/360
090510.016	Band	4400 <sup>(+400)</sup> <sub>(-380)</sub>	-0.79 ( $\pm 0.03$ )	-2.81 <sup>(+0.28)</sup> <sub>(-0.40)</sub>	21.9 ( $\pm 0.5$ )	(8.86 $\pm 0.17$ ) $\cdot 10^{-6}$	345/359

## 5. BGO-BRIGHT GRBS

Table 5.6: (continued)

Name	Model	$E_{\text{peak}}$ (keV)	$\alpha$	$\beta$	Photon Flux ( $\text{ph s}^{-1} \text{cm}^{-2}$ ) (8–1000 keV)	Energy Flux ( $\text{ergs}^{-1} \text{cm}^{-2}$ ) (8–1000 keV)	CSTAT/DOF
090528.516	Band	180 $\begin{smallmatrix} (+12) \\ (-11) \end{smallmatrix}$	-1.09 ( $\pm 0.03$ )	-2.29 $\begin{smallmatrix} (+0.09) \\ (-0.13) \end{smallmatrix}$	6.33 ( $\pm 0.05$ )	(7.26 $\pm$ 0.01) $\cdot$ 10 <sup>-6</sup>	528/357
090529.564	Comp	243 $\begin{smallmatrix} (+26) \\ (-22) \end{smallmatrix}$	-1.17 ( $\pm 0.04$ )	–	7.00 ( $\pm 0.10$ )	(8.11 $\pm$ 0.23) $\cdot$ 10 <sup>-7</sup>	425/359
090531.775	Comp	1682 $\begin{smallmatrix} (+370) \\ (-320) \end{smallmatrix}$	-0.62 $\begin{smallmatrix} (+0.12) \\ (-0.10) \end{smallmatrix}$	–	3.54 ( $\pm 0.17$ )	(1.50 $\pm$ 0.07) $\cdot$ 10 <sup>-6</sup>	477/360
090617.208	Band	543 $\begin{smallmatrix} (+200) \\ (-150) \end{smallmatrix}$	-0.26 $\begin{smallmatrix} (+0.26) \\ (-0.20) \end{smallmatrix}$	-1.93 $\begin{smallmatrix} (+0.18) \\ (-0.24) \end{smallmatrix}$	12.5 ( $\pm 0.5$ )	(4.59 $\pm$ 0.23) $\cdot$ 10 <sup>-6</sup>	516/483
090618.353	Band+eff	164 ( $\pm 3$ )	-1.05 ( $\pm 0.01$ )	-2.52 ( $\pm 0.033$ )	36.66 ( $\pm 0.12$ )	(3.97 $\pm$ 0.02) $\cdot$ 10 <sup>-6</sup>	354/232
090620.400	Band	154 $\begin{smallmatrix} (+7) \\ (-6) \end{smallmatrix}$	-0.30 $\begin{smallmatrix} (+0.06) \\ (-0.05) \end{smallmatrix}$	-2.53 $\begin{smallmatrix} (+0.11) \\ (-0.13) \end{smallmatrix}$	6.78 ( $\pm 0.07$ )	(1.01 $\pm$ 0.02) $\cdot$ 10 <sup>-6</sup>	446/359
090621.922	Comp	310 $\begin{smallmatrix} (+90) \\ (-60) \end{smallmatrix}$	-0.2 $\begin{smallmatrix} (+0.4) \\ (-0.3) \end{smallmatrix}$	–	4.0 ( $\pm 0.4$ )	(9.8 $\pm$ 1.4) $\cdot$ 10 <sup>-7</sup>	389/360
090623.107	Band	366 $\begin{smallmatrix} (+50) \\ (-46) \end{smallmatrix}$	-0.59 ( $\pm 0.07$ )	-2.32 $\begin{smallmatrix} (+0.22) \\ (-0.5) \end{smallmatrix}$	2.09 ( $\pm 0.04$ )	(4.88 $\pm$ 0.12) $\cdot$ 10 <sup>-7</sup>	405/356
090626.189	Band	154 $\begin{smallmatrix} (+11) \\ (-9) \end{smallmatrix}$	-1.11 ( $\pm 0.03$ )	-2.12 $\begin{smallmatrix} (+0.04) \\ (-0.05) \end{smallmatrix}$	11.50 ( $\pm 0.06$ )	(1.29 $\pm$ 0.01) $\cdot$ 10 <sup>-6</sup>	380/240

## 5.4. Spectral Analysis Results

**Table 5.7:** Summary of the fluence calculation in different energy bands for 56 GRBs

Name	Energy Fluence (erg cm <sup>-2</sup> )				
	(8–1000 keV)	(8–40000 keV)	(1–40 MeV)	(50–300 keV)	(20–2000 keV)
080723.557	$(7.52 \pm 0.07) \cdot 10^{-5}$	$(1.00 \pm 0.05) \cdot 10^{-4}$	$(2.54 \pm 0.42) \cdot 10^{-5}$	$(3.98 \pm 0.03) \cdot 10^{-5}$	$(8.09 \pm 0.13) \cdot 10^{-5}$
080723.985	$(3.61 \pm 0.05) \cdot 10^{-5}$	$(4.02 \pm 0.09) \cdot 10^{-5}$	$(4.01 \pm 0.47) \cdot 10^{-6}$	$(1.59 \pm 0.02) \cdot 10^{-5}$	$(3.89 \pm 0.08) \cdot 10^{-5}$
080725.541	$(8.06 \pm 0.45) \cdot 10^{-7}$	$(1.90 \pm 0.35) \cdot 10^{-6}$	$(1.09 \pm 0.35) \cdot 10^{-6}$	$(2.27 \pm 0.13) \cdot 10^{-7}$	$(1.30 \pm 0.09) \cdot 10^{-6}$
080802.386	$(3.82 \pm 0.32) \cdot 10^{-7}$	$(4.92 \pm 0.95) \cdot 10^{-7}$	$(1.09 \pm 0.73) \cdot 10^{-7}$	$(1.37 \pm 0.11) \cdot 10^{-7}$	$(4.66 \pm 0.70) \cdot 10^{-7}$
080807.993	$(8.58 \pm 0.29) \cdot 10^{-6}$	$(1.20 \pm 0.14) \cdot 10^{-5}$	$(3.42 \pm 1.10) \cdot 10^{-6}$	$(3.10 \pm 0.08) \cdot 10^{-6}$	$(1.09 \pm 0.08) \cdot 10^{-5}$
080816.989	$(2.85 \pm 0.09) \cdot 10^{-6}$	$(8.00 \pm 0.59) \cdot 10^{-6}$	$(5.13 \pm 0.60) \cdot 10^{-6}$	$(5.68 \pm 0.21) \cdot 10^{-7}$	$(5.33 \pm 0.18) \cdot 10^{-6}$
080817.161	$(4.61 \pm 0.04) \cdot 10^{-5}$	$(7.21 \pm 0.33) \cdot 10^{-5}$	$(2.57 \pm 0.36) \cdot 10^{-5}$	$(1.96 \pm 0.01) \cdot 10^{-5}$	$(5.44 \pm 0.06) \cdot 10^{-5}$
080825.593	$(3.75 \pm 0.04) \cdot 10^{-5}$	$(5.56 \pm 0.30) \cdot 10^{-5}$	$(1.80 \pm 0.28) \cdot 10^{-5}$	$(2.04 \pm 0.02) \cdot 10^{-5}$	$(4.13 \pm 0.08) \cdot 10^{-5}$
080905.499	$(9.37 \pm 0.64) \cdot 10^{-7}$	$(1.13 \pm 0.15) \cdot 10^{-6}$	$(1.86 \pm 1.02) \cdot 10^{-7}$	$(3.03 \pm 0.19) \cdot 10^{-7}$	$(1.11 \pm 1.11) \cdot 10^{-6}$
080906.212	$(7.20 \pm 0.15) \cdot 10^{-6}$	$(1.08 \pm 0.10) \cdot 10^{-5}$	$(3.61 \pm 0.86) \cdot 10^{-6}$	$(3.95 \pm 0.05) \cdot 10^{-6}$	$(7.95 \pm 0.29) \cdot 10^{-6}$
080916.009	$(7.49 \pm 0.07) \cdot 10^{-5}$	$(1.48 \pm 0.08) \cdot 10^{-4}$	$(7.24 \pm 0.76) \cdot 10^{-5}$	$(3.01 \pm 0.02) \cdot 10^{-5}$	$(9.19 \pm 0.11) \cdot 10^{-5}$
080925.775	$(1.80 \pm 0.03) \cdot 10^{-5}$	$(2.75 \pm 0.22) \cdot 10^{-5}$	$(9.39 \pm 1.92) \cdot 10^{-6}$	$(9.13 \pm 0.11) \cdot 10^{-6}$	$(1.92 \pm 0.06) \cdot 10^{-5}$
081006.604	$(1.59 \pm 0.10) \cdot 10^{-6}$	$(2.28 \pm 0.41) \cdot 10^{-6}$	$(6.82 \pm 3.48) \cdot 10^{-7}$	$(4.47 \pm 0.30) \cdot 10^{-7}$	$(2.14 \pm 0.28) \cdot 10^{-6}$
081009.690	$(1.02 \pm 0.03) \cdot 10^{-5}$	$(2.28 \pm 0.29) \cdot 10^{-5}$	$(1.26 \pm 0.25) \cdot 10^{-5}$	$(4.63 \pm 0.10) \cdot 10^{-6}$	$(1.17 \pm 0.06) \cdot 10^{-5}$
081012.045	$(1.34 \pm 0.07) \cdot 10^{-6}$	$(1.83 \pm 0.24) \cdot 10^{-6}$	$(4.76 \pm 1.97) \cdot 10^{-7}$	$(3.98 \pm 0.22) \cdot 10^{-7}$	$(1.74 \pm 0.18) \cdot 10^{-6}$
081024.891	$(5.60 \pm 0.43) \cdot 10^{-7}$	$(1.55 \pm 0.45) \cdot 10^{-6}$	$(9.89 \pm 4.48) \cdot 10^{-7}$	$(1.64 \pm 0.12) \cdot 10^{-7}$	$(9.06 \pm 0.83) \cdot 10^{-7}$
081101.532	$(1.59 \pm 0.03) \cdot 10^{-5}$	$(1.81 \pm 0.05) \cdot 10^{-5}$	$(2.16 \pm 0.29) \cdot 10^{-6}$	$(6.38 \pm 0.09) \cdot 10^{-6}$	$(1.77 \pm 0.05) \cdot 10^{-5}$
081105.614	$(2.98 \pm 0.40) \cdot 10^{-7}$	$(3.13 \pm 0.54) \cdot 10^{-7}$	$(1.41 \pm 1.75) \cdot 10^{-8}$	$(1.01 \pm 0.12) \cdot 10^{-7}$	$(3.13 \pm 0.54) \cdot 10^{-7}$
081110.601	$(8.72 \pm 0.21) \cdot 10^{-7}$	$(1.05 \pm 0.06) \cdot 10^{-5}$	$(1.78 \pm 0.42) \cdot 10^{-6}$	$(3.59 \pm 0.07) \cdot 10^{-6}$	$(9.88 \pm 0.45) \cdot 10^{-6}$
081121.858	$(1.60 \pm 0.03) \cdot 10^{-5}$	$(3.71 \pm 0.32) \cdot 10^{-5}$	$(2.10 \pm 0.30) \cdot 10^{-5}$	$(7.84 \pm 0.13) \cdot 10^{-6}$	$(1.94 \pm 0.05) \cdot 10^{-5}$
081122.520	$(7.20 \pm 0.18) \cdot 10^{-7}$	$(1.12 \pm 0.14) \cdot 10^{-5}$	$(4.01 \pm 1.32) \cdot 10^{-6}$	$(3.86 \pm 0.07) \cdot 10^{-6}$	$(8.05 \pm 0.35) \cdot 10^{-6}$
081125.496	$(1.79 \pm 0.03) \cdot 10^{-5}$	$(2.23 \pm 0.14) \cdot 10^{-5}$	$(4.45 \pm 1.12) \cdot 10^{-6}$	$(1.05 \pm 0.01) \cdot 10^{-5}$	$(1.90 \pm 0.05) \cdot 10^{-5}$
081126.899	$(9.82 \pm 0.31) \cdot 10^{-7}$	$(1.04 \pm 0.05) \cdot 10^{-5}$	$(6.00 \pm 1.71) \cdot 10^{-7}$	$(4.71 \pm 0.09) \cdot 10^{-6}$	$(1.01 \pm 0.04) \cdot 10^{-5}$
081129.161	$(1.33 \pm 0.03) \cdot 10^{-5}$	$(2.67 \pm 0.29) \cdot 10^{-5}$	$(1.34 \pm 0.29) \cdot 10^{-5}$	$(6.41 \pm 0.11) \cdot 10^{-6}$	$(1.54 \pm 0.05) \cdot 10^{-5}$
081207.680	$(6.23 \pm 0.07) \cdot 10^{-5}$	$(1.41 \pm 0.10) \cdot 10^{-4}$	$(7.87 \pm 0.97) \cdot 10^{-5}$	$(2.59 \pm 0.02) \cdot 10^{-5}$	$(7.87 \pm 0.12) \cdot 10^{-5}$
081209.981	$(1.51 \pm 0.05) \cdot 10^{-6}$	$(4.35 \pm 0.65) \cdot 10^{-6}$	$(2.83 \pm 0.65) \cdot 10^{-6}$	$(4.11 \pm 0.17) \cdot 10^{-7}$	$(2.33 \pm 0.14) \cdot 10^{-6}$
081215.784	$(5.51 \pm 0.03) \cdot 10^{-5}$	$(9.63 \pm 0.22) \cdot 10^{-5}$	$(4.10 \pm 0.23) \cdot 10^{-5}$	$(2.29 \pm 0.01) \cdot 10^{-5}$	$(6.67 \pm 0.04) \cdot 10^{-5}$
081216.531	$(3.08 \pm 0.09) \cdot 10^{-6}$	$(6.94 \pm 0.92) \cdot 10^{-6}$	$(3.84 \pm 0.92) \cdot 10^{-6}$	$(8.89 \pm 0.28) \cdot 10^{-7}$	$(4.63 \pm 0.22) \cdot 10^{-6}$
081224.887	$(3.47 \pm 0.03) \cdot 10^{-5}$	$(3.76 \pm 0.05) \cdot 10^{-5}$	$(2.84 \pm 0.21) \cdot 10^{-6}$	$(1.54 \pm 0.01) \cdot 10^{-5}$	$(3.68 \pm 0.05) \cdot 10^{-5}$
081226.509	$(4.08 \pm 0.42) \cdot 10^{-7}$	$(4.26 \pm 0.54) \cdot 10^{-7}$	$(1.79 \pm 1.63) \cdot 10^{-8}$	$(1.94 \pm 0.14) \cdot 10^{-7}$	$(4.20 \pm 0.54) \cdot 10^{-7}$
081231.140	$(1.77 \pm 0.03) \cdot 10^{-5}$	$(2.78 \pm 0.30) \cdot 10^{-5}$	$(1.00 \pm 0.29) \cdot 10^{-5}$	$(8.81 \pm 0.12) \cdot 10^{-6}$	$(1.95 \pm 0.06) \cdot 10^{-5}$
090102.122	$(3.01 \pm 0.03) \cdot 10^{-5}$	$(3.28 \pm 0.05) \cdot 10^{-5}$	$(2.55 \pm 0.22) \cdot 10^{-6}$	$(1.31 \pm 0.01) \cdot 10^{-5}$	$(3.23 \pm 0.05) \cdot 10^{-5}$
090131.090	$(2.11 \pm 0.03) \cdot 10^{-5}$	$(2.75 \pm 0.12) \cdot 10^{-5}$	$(6.39 \pm 0.93) \cdot 10^{-6}$	$(9.17 \pm 0.13) \cdot 10^{-6}$	$(1.98 \pm 0.05) \cdot 10^{-5}$
090217.206	$(3.10 \pm 0.04) \cdot 10^{-5}$	$(4.56 \pm 0.38) \cdot 10^{-5}$	$(1.45 \pm 0.42) \cdot 10^{-5}$	$(3.68 \pm 0.07) \cdot 10^{-5}$	$(3.68 \pm 0.07) \cdot 10^{-5}$
090219.074	$(4.07 \pm 0.59) \cdot 10^{-7}$	$(4.08 \pm 0.59) \cdot 10^{-7}$	$(3.12 \pm 8.32) \cdot 10^{-10}$	$(2.74 \pm 0.32) \cdot 10^{-7}$	$(3.92 \pm 0.57) \cdot 10^{-7}$
090227.310	$(9.81 \pm 0.26) \cdot 10^{-7}$	$(1.62 \pm 0.17) \cdot 10^{-5}$	$(6.33 \pm 1.62) \cdot 10^{-6}$	$(3.17 \pm 0.09) \cdot 10^{-6}$	$(1.37 \pm 0.08) \cdot 10^{-5}$
090227.772	$(8.71 \pm 0.11) \cdot 10^{-5}$	$(3.12 \pm 0.08) \cdot 10^{-5}$	$(2.24 \pm 0.08) \cdot 10^{-5}$	$(1.67 \pm 0.02) \cdot 10^{-6}$	$(1.71 \pm 0.02) \cdot 10^{-5}$
090228.204	$(6.02 \pm 0.08) \cdot 10^{-5}$	$(8.90 \pm 0.32) \cdot 10^{-6}$	$(2.85 \pm 0.30) \cdot 10^{-6}$	$(1.64 \pm 0.03) \cdot 10^{-6}$	$(7.92 \pm 0.16) \cdot 10^{-6}$

## 5. BGO–BRIGHT GRBS

**Table 5.7:** (continued)

Name	Energy Fluence (erg cm <sup>-2</sup> )				
	(8–1000 keV)	(8–40000 keV)	(1–40 MeV)	(50–300 keV)	(20–2000 keV)
090305.052	(2.33±0.07)·10 <sup>-6</sup>	(3.55±0.30)·10 <sup>-6</sup>	(1.21±0.28)·10 <sup>-6</sup>	(6.49±0.23)·10 <sup>-7</sup>	(3.24±0.18)·10 <sup>-6</sup>
090308.734	(3.10±0.09)·10 <sup>-6</sup>	(3.82±0.20)·10 <sup>-6</sup>	(6.95±1.51)·10 <sup>-7</sup>	(1.06±0.04)·10 <sup>-6</sup>	(3.71±0.17)·10 <sup>-6</sup>
090323.002	(9.51±0.09)·10 <sup>-5</sup>	(1.65±0.08)·10 <sup>-4</sup>	(6.92±0.79)·10 <sup>-5</sup>	(3.77±0.28)·10 <sup>-5</sup>	(1.16±0.01)·10 <sup>-4</sup>
090328.401	(4.42±0.05)·10 <sup>-5</sup>	(8.01±0.49)·10 <sup>-5</sup>	(3.58±0.49)·10 <sup>-5</sup>	(1.65±0.01)·10 <sup>-5</sup>	(5.50±0.07)·10 <sup>-5</sup>
090328.713	(7.93±0.38)·10 <sup>-7</sup>	(2.08±0.31)·10 <sup>-6</sup>	(1.28±0.29)·10 <sup>-6</sup>	(2.28±0.10)·10 <sup>-7</sup>	(1.29±0.07)·10 <sup>-6</sup>
090424.592	(4.47±0.03)·10 <sup>-5</sup>	(4.97±0.11)·10 <sup>-5</sup>	(4.93±0.89)·10 <sup>-6</sup>	(2.55±0.01)·10 <sup>-5</sup>	(4.40±0.06)·10 <sup>-5</sup>
090425.377	(1.53±0.05)·10 <sup>-5</sup>	(1.60±0.08)·10 <sup>-5</sup>	(6.97±3.12)·10 <sup>-7</sup>	(7.04±0.14)·10 <sup>-6</sup>	(1.40±0.07)·10 <sup>-5</sup>
090429.753	(1.04±0.05)·10 <sup>-6</sup>	(1.77±0.32)·10 <sup>-6</sup>	(8.10±3.15)·10 <sup>-7</sup>	(3.13±0.15)·10 <sup>-7</sup>	(1.38±0.11)·10 <sup>-6</sup>
090510.016	(3.97±0.08)·10 <sup>-6</sup>	(2.76±0.12)·10 <sup>-5</sup>	(2.36±0.12)·10 <sup>-5</sup>	(9.04±0.17)·10 <sup>-7</sup>	(7.93±0.17)·10 <sup>-6</sup>
090528.516	(4.39±0.01)·10 <sup>-4</sup>	(6.04±0.45)·10 <sup>-5</sup>	(2.09±0.40)·10 <sup>-5</sup>	(2.00±0.02)·10 <sup>-5</sup>	(4.27±0.11)·10 <sup>-5</sup>
090529.564	(8.98±0.25)·10 <sup>-6</sup>	(8.32±0.30)·10 <sup>-6</sup>	(2.18±0.71)·10 <sup>-7</sup>	(4.23±0.06)·10 <sup>-6</sup>	(7.80±0.29)·10 <sup>-6</sup>
090531.775	(1.44±0.06)·10 <sup>-6</sup>	(3.88±0.55)·10 <sup>-6</sup>	(2.42±0.56)·10 <sup>-6</sup>	(3.38±0.16)·10 <sup>-7</sup>	(2.61±0.14)·10 <sup>-6</sup>
090617.208	(1.03±0.05)·10 <sup>-6</sup>	(3.34±0.56)·10 <sup>-6</sup>	(2.45±0.58)·10 <sup>-6</sup>	(2.94±0.13)·10 <sup>-7</sup>	(1.31±0.08)·10 <sup>-6</sup>
090618.353	(1.79±0.01)·10 <sup>-4</sup>	(2.23±0.03)·10 <sup>-4</sup>	(4.41±0.24)·10 <sup>-5</sup>	(9.63±0.04)·10 <sup>-5</sup>	(1.83±0.01)·10 <sup>-4</sup>
090620.400	(1.48±0.02)·10 <sup>-5</sup>	(1.87±0.10)·10 <sup>-5</sup>	(3.94±0.86)·10 <sup>-6</sup>	(8.79±0.10)·10 <sup>-6</sup>	(1.58±0.04)·10 <sup>-5</sup>
090621.922	(3.75±0.54)·10 <sup>-7</sup>	(3.82±0.54)·10 <sup>-7</sup>	(5.41±7.30)·10 <sup>-9</sup>	(2.02±0.17)·10 <sup>-7</sup>	(3.79±0.54)·10 <sup>-7</sup>
090623.107	(2.05±0.05)·10 <sup>-5</sup>	(3.54±0.59)·10 <sup>-5</sup>	(1.48±0.59)·10 <sup>-5</sup>	(9.23±0.14)·10 <sup>-6</sup>	(2.45±0.10)·10 <sup>-5</sup>
090626.189	(7.79±0.06)·10 <sup>-5</sup>	(1.34±0.05)·10 <sup>-4</sup>	(5.57±0.45)·10 <sup>-5</sup>	(3.78±0.03)·10 <sup>-5</sup>	(8.52±0.10)·10 <sup>-5</sup>

### 5.4.1 Spectral Parameter Distribution

Distributions of the spectral parameters are shown in Figure 5.10 and 5.11. In both figures, the low–energy index  $\alpha$  (*top panels*), high–energy index  $\beta$  (*middle panels*) and  $E_{\text{peak}}$  (*bottom panels*) distributions are plotted for 56 time–integrated spectra (“All”, *black histogram*).

*Blue* and *red histograms* in the *left panels* of Figure 5.10 represent the distributions of 40 long and 16 short GRBs, respectively. Short bursts tend to have harder  $\alpha$  and higher  $E_{\text{peak}}$  values. Furthermore, only five GRBs are best fitted by a Band model (*middle panel*), and in three cases  $\beta < -2.9$ . The distributions of bursts belonging to the MAIN, BEST and GOLD samples are shown in the *right panels* with *light blue*, *green* and *orange histograms*. As previously mentioned, the GOLD sample mainly comprises short GRBs. Bursts with the more constrained parameters usually belong to the BEST and GOLD samples.

The *grey histograms* in Figure 5.11 represent the spectral parameter distributions of 342 bursts from the BEST<sup>2</sup> sample of Kaneko et al. (2006), which comprises 350 bright GRBs observed with BATSE ( $\sim 30$  keV–2 MeV). This spectral catalog is the most comprehensive study of spectral properties of GRB prompt emission to date and represents a perfect sample for comparing with GBM burst’s properties. For better comparison, the GBM distributions are rescaled (*right y-axis*). While the two  $\beta$  distributions looks similar, differences appear in the  $\alpha$  and  $E_{\text{peak}}$  distributions. After one year of operations, GBM detected a sample of bright bursts which tend to have harder  $\alpha$  and higher  $E_{\text{peak}}$  values than what was observed in 10 years by the BATSE instruments.

Another way to interpret the spectral parameter distributions is to plot each parameter against the total energy fluence measured in the standard NaI and BGO energy bands, i.e. 8–1000 keV (Figure 5.12) and 1–40 MeV (Figure 5.13). Also in this case, the distributions of short and long bursts is shown in the panels on the *left*, while the three samples (MAIN, BEST and GOLD) are shown in the *right panels*.

Let’s firstly consider Figure 5.12. The low–energy index  $\alpha$  tends to get harder for increasing fluence values, while bursts with lower fluence, mostly short bursts, have steeper spectra with lower  $\beta$  values. For those values uncertainties are also greater. These short, low–fluence bursts also show higher  $E_{\text{peak}}$  values (*bottom histograms*), while long, high–fluence bursts tend to have softer  $E_{\text{peak}}$  values.

The corresponding plots in the 1–40 MeV range in Figure 5.13 comprise only those bursts where the fluence in the BGO energy range could be reasonably constrained. Results for all spectral parameters are similar to those in the NaI energy band. A detailed statistical analysis of the distributions presented in this chapter will be summarized in a forthcoming paper (Bissaldi et al., 2010).

The comparison with BATSE bright bursts was made in the standard BATSE energy range of 20 keV–2 MeV and is shown in Figure 5.14. From the spectral parameter distributions it becomes immediately evident that the two samples were selected following different criteria. The BATSE sample comprises more GRBs with higher fluence than the GBM one. In fact, only 17 out of 342 bright bursts are short ones, which represents only a  $\sim 5\%$ . With 15 short GRBs out 56 selected bright bursts ( $\sim 30\%$ ), GBM confirms to have detect many more short and bright bursts than BATSE did.

---

<sup>2</sup>Kaneko et al. (2006) designated the model with the more constrained parameters as the best–fit (BEST) model

## 5. BGO-BRIGHT GRBS

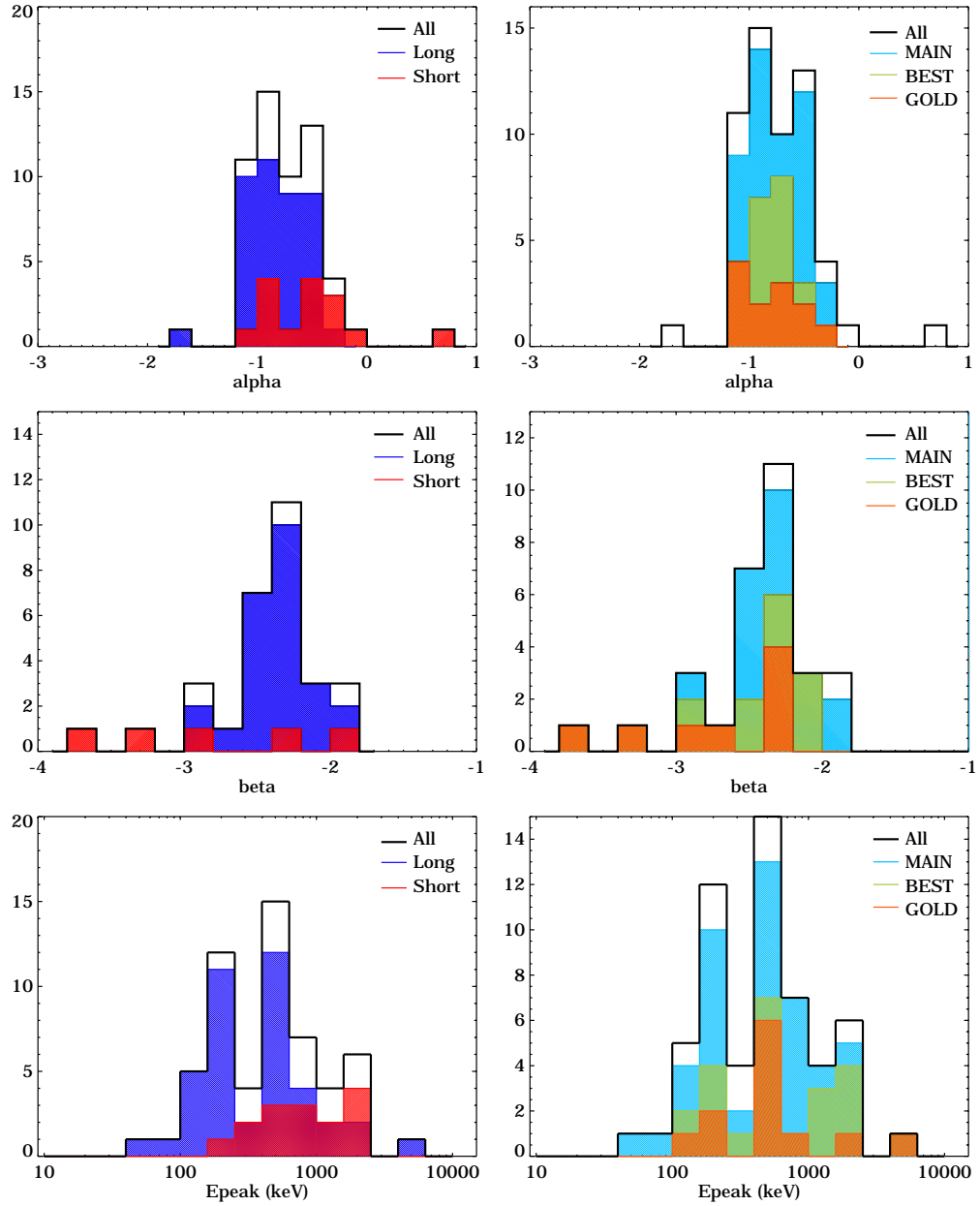


**Figure 5.10:** Low-energy index  $\alpha$  (top panels), high-energy index  $\beta$  (middle panels) and  $E_{\text{peak}}$  (bottom panels) distribution of time-integrated spectra from 56 bright GRBs (“All”, black histogram). Blue and red histograms in the left panels represent the distributions of 40 long and 16 short GRBs, respectively. The distributions of bursts belonging to the MAIN, BEST and GOLD samples is shown in the right panels with light blue, green and orange histograms

### 5.4.1. Spectral Parameter Distribution

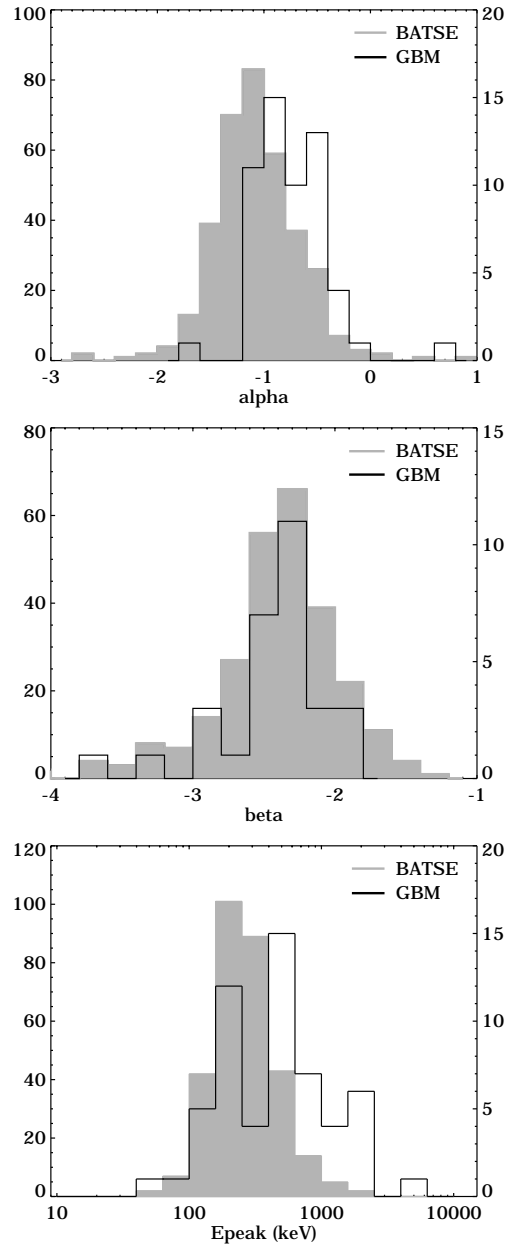


**Figure 5.11:** Low-energy index  $\alpha$  (*top panels*), high-energy index  $\beta$  (*middle panels*) and  $E_{\text{peak}}$  (*bottom panels*) distributions of time-integrated spectra from 342 BATSE and 56 GBM bright bursts. The GBM parameter distributions follow the right y-axis

## 5. BGO-BRIGHT GRBS

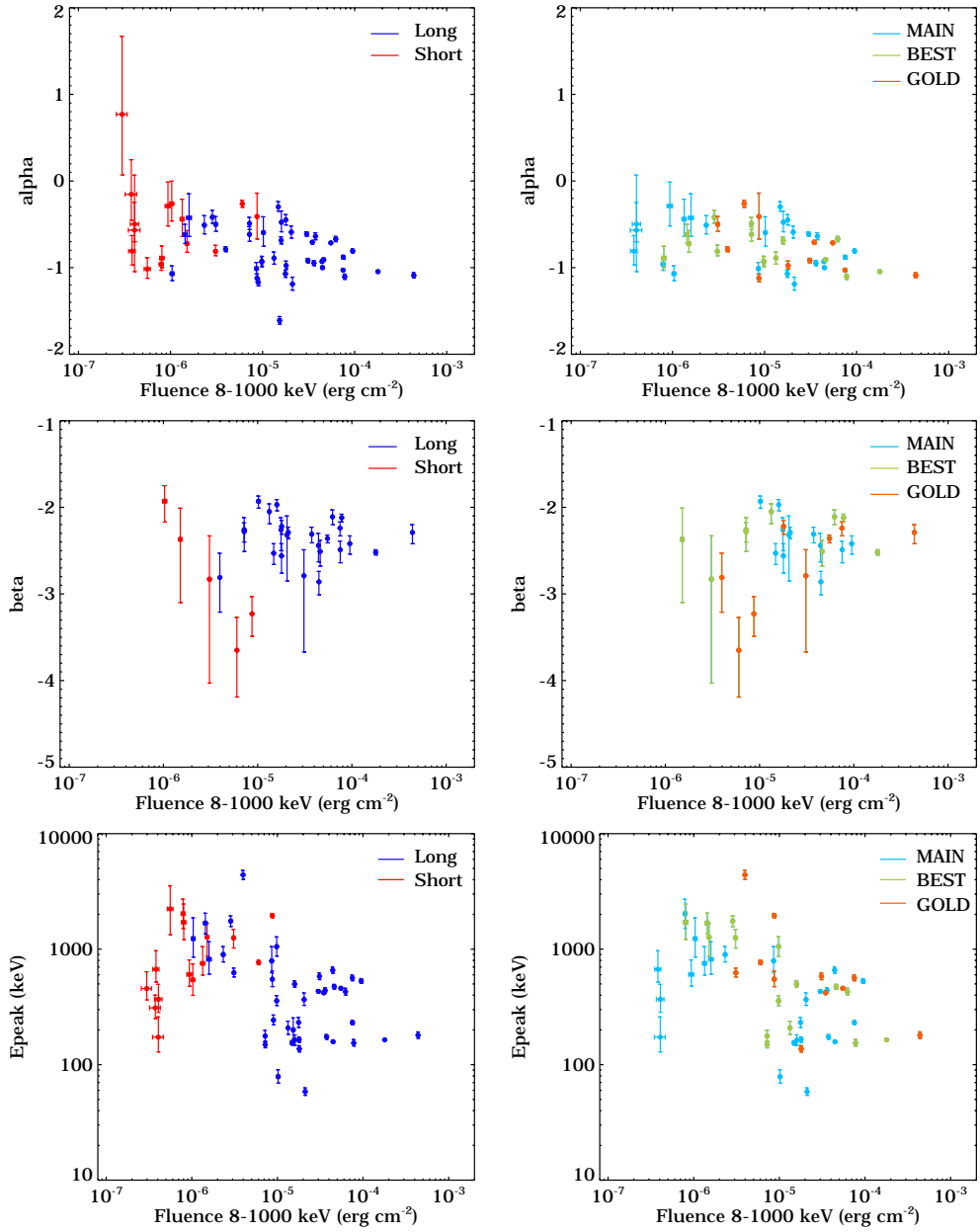


**Figure 5.12:** Distribution of spectral parameter vs. energy fluence calculated in the NaI (8–1000 keV) energy range. *Top panel:*  $\alpha$  distribution; *middle panel:*  $\beta$  distribution; *bottom panel:*  $E_{\text{peak}}$  distribution. Color code same as in Figure 5.10

### 5.4.1. Spectral Parameter Distribution

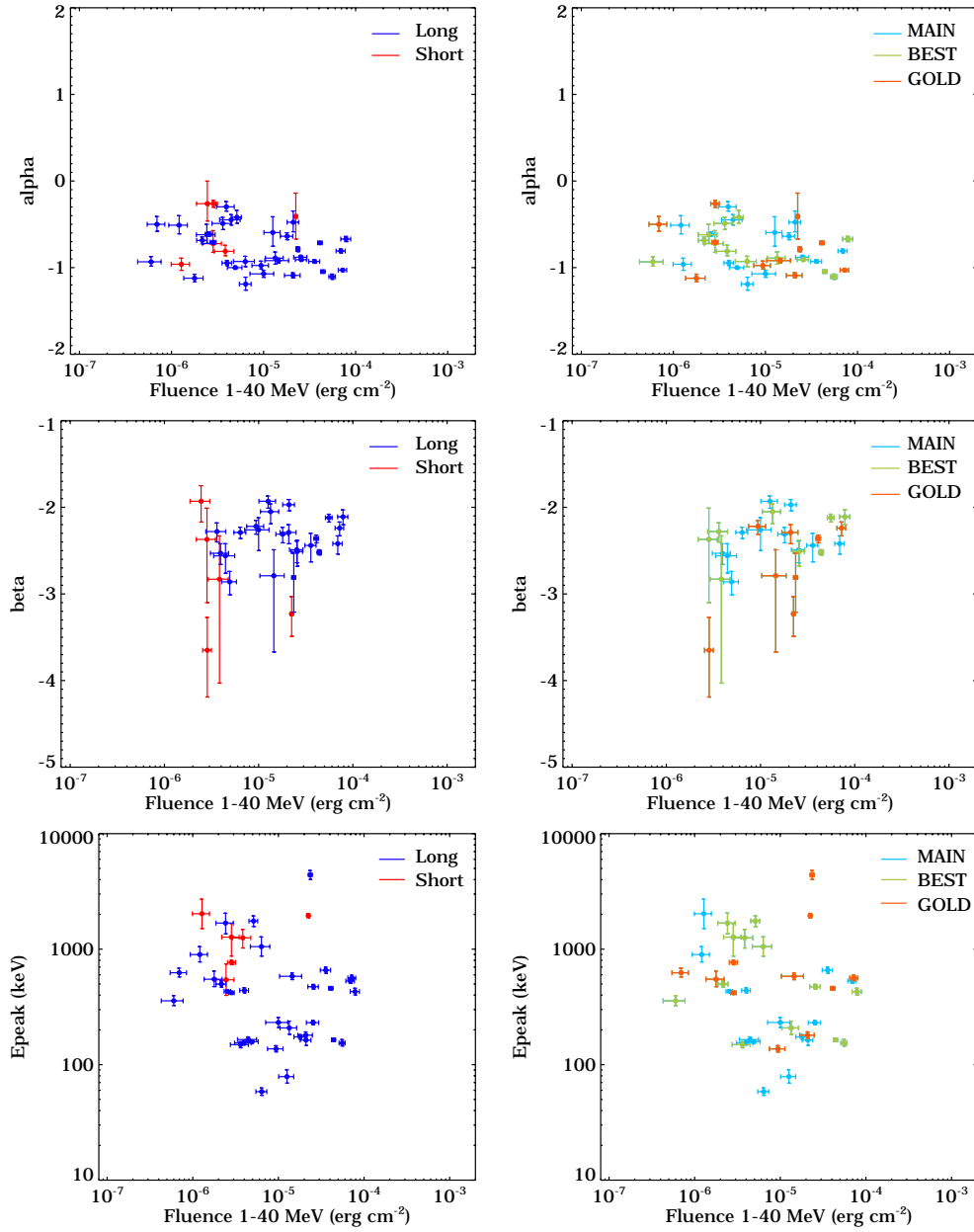


**Figure 5.13:** Distribution of spectral parameter vs. energy fluence calculated in the BGO (1–40 MeV) energy range. *Top panel:*  $\alpha$  distribution; *Middle panel:*  $\beta$  distribution; *Bottom panel:*  $E_{\text{peak}}$  distribution. Color code same as in Figure 5.10

## 5. BGO-BRIGHT GRBS

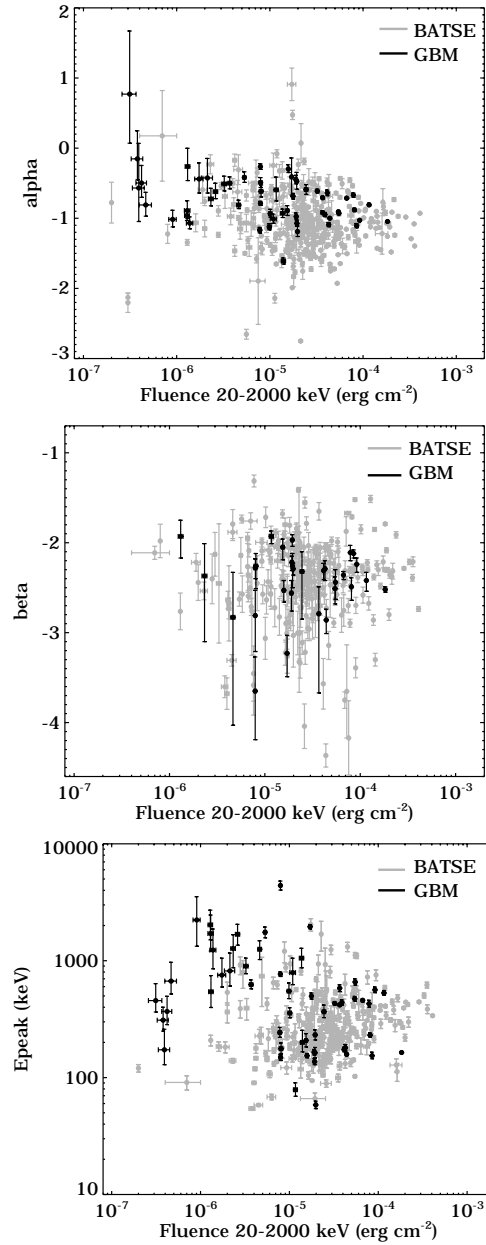


**Figure 5.14:** Distribution of spectral parameter vs. energy fluence calculated in the BATSE (20–2000 keV) energy range. *Top panel:*  $\alpha$  distribution; *middle panel:*  $\beta$  distribution; *bottom panel:*  $E_{\text{peak}}$  distribution. Color code same as in Figure 5.11

### 5.4.1. Spectral Parameter Distribution

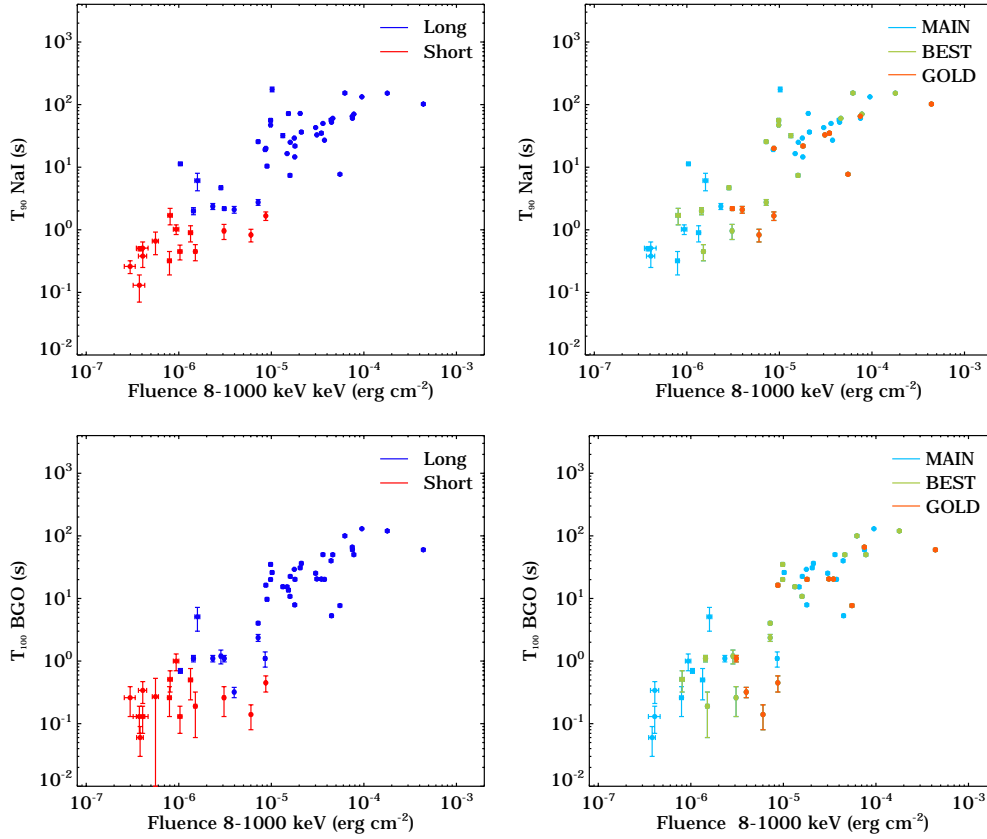


**Figure 5.15:** Burst durations measured in NaI and BGO vs. energy fluence in the 8–1000 keV energy band. *Top panel:* NaI duration; *Bottom panel:* BGO duration. Color code same as in Figure 5.10

The distribution of  $T_{90}$  measured in NaI and BGO versus energy fluence in the 8–1000 keV band is shown in Figure 5.15. These representations nicely emphasize how short bursts tend to have lower fluence than long ones and that high fluence corresponds to longer durations.

The distribution of hardness ratio versus  $T_{90}$  is shown in Figure 5.16. The hardness ratio is defined by the ratio of counts in the BGO vs. NaI energy ranges, namely  $[1000\text{--}40000]/[8\text{--}1000]$  (all in keV). As previously shown in Figure 1.5 in the first chapter for 222 BATSE bursts, one can see that shorter bursts tend to have harder spectra than the long ones.

Finally, Figures 5.17 and 5.18 show the peak photon flux and energy fluence distribution calculated in different energy bands for all 56 time-integrated spectra. The peak photon flux and fluence distributions are given in the NaI and BGO energy bands, namely 8–1000 keV and 1–40 MeV (*pink and purple histograms*).

## 5. BGO–BRIGHT GRBS

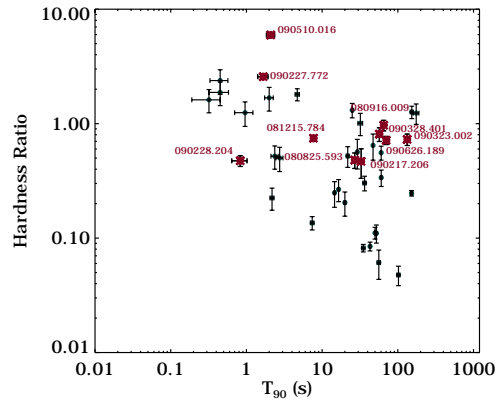


**Figure 5.16:** Distribution of hardness ratio versus  $T_{90}$  for 56 bright GBM bursts. The hardness ratio is defined by the ratio of counts in the BGO vs. NaI energy ranges, namely  $[1000-40000]/[8-1000]$ . Bursts fully or marginally detected by the LAT are marked with *dark red crosses*

The fluence distribution is additionally given in the 50–300 keV and 20–2000 keV energy bands (*ligh blue and teal blue histograms*). The peak photon flux distribution in the 8–1000 keV energy band is smoothly distributed around  $10 \text{ ph s}^{-1} \text{ cm}^{-2}$ , while the distribution in the 1–40 MeV energy band is clustered around  $1 \text{ ph s}^{-1} \text{ cm}^{-2}$ , with a tail of  $\sim 10$  more energetic bursts showing a peak photon flux  $> 1 \text{ ph s}^{-1} \text{ cm}^{-2}$ . GRBs with a statistically uncertain peak photon flux (error larger than 30%) were excluded from the histogram. The fluence distributions (see Figure 5.18) calculated in those energy bands highlight the same behavior. The fluence calculated in the 8–1000 keV energy band (*right panel*) has its distribution maximum around  $10^{-5} \text{ erg cm}^{-2}$ . This is also seen in the distribution calculated

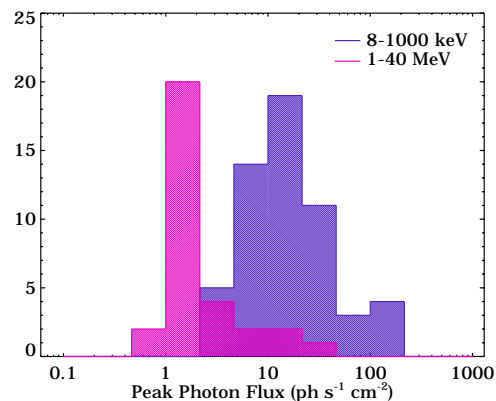


**Figure 5.17:** Peak photon flux distribution calculated in different energy bands for 56 time-integrated spectra

## 5.4.2. Correlation Among Spectral Parameters

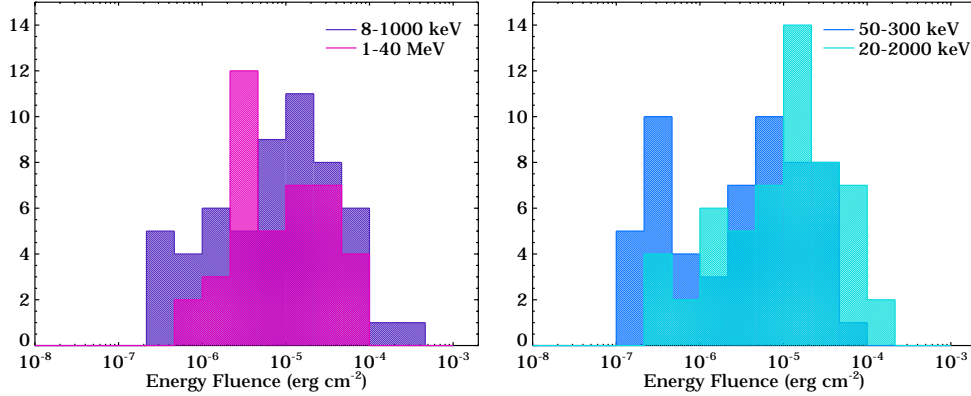


**Figure 5.18:** Energy fluence distributions calculated in different energy bands for 56 time-integrated spectra

in the 20-2000 keV band (*right panel*), while the 50–300 keV fluence distribution shows a sort of bimodality.

## 5.4.2 Correlation Among Spectral Parameters

Empirical correlations among spectral parameters have been previously found with smaller samples either within individual bursts or for collections of time-resolved parameters. By calculating the Spearman rank-order correlation coefficients and the associated significance probabilities, Kaneko et al. (2006) found no indication of global correlations among the time-integrated spectral parameters, while strong correlation was seen among the time-resolved spectral parameters. Moreover, they note that it is best to look for parameter correlations within individual bursts in order to eliminate possible effects due to cosmological redshift that varies from burst to burst.

Since no time-resolved spectral analysis was performed in this work, the correlation analysis was limited to a short comparison of the low- and high-energy spectral parameters against  $E_{\text{peak}}$  and against each other. Figure 5.19 shows scatter plots for  $E_{\text{peak}}-\alpha$  (*top panel*),  $E_{\text{peak}}-\beta$  (*middle panel*) and  $\alpha-\beta$  (*bottom panel*). Again, plots on the *left* and on the *right* show the distribution of short-long bursts and of the three BGO samples, respectively. Even by eye, no evidence of correlation is seen in any distribution. A comparison with the BATSE BEST bursts is shown in Figure 5.20. The only slight hint of possible correlation is marginally visible in the  $E_{\text{peak}}-\beta$  scatter plot, in which  $\beta$  decreases with increasing  $E_{\text{peak}}$ , however a rigorous statistical analysis is needed in order to be conclusive.

## 5. BGO-BRIGHT GRBS

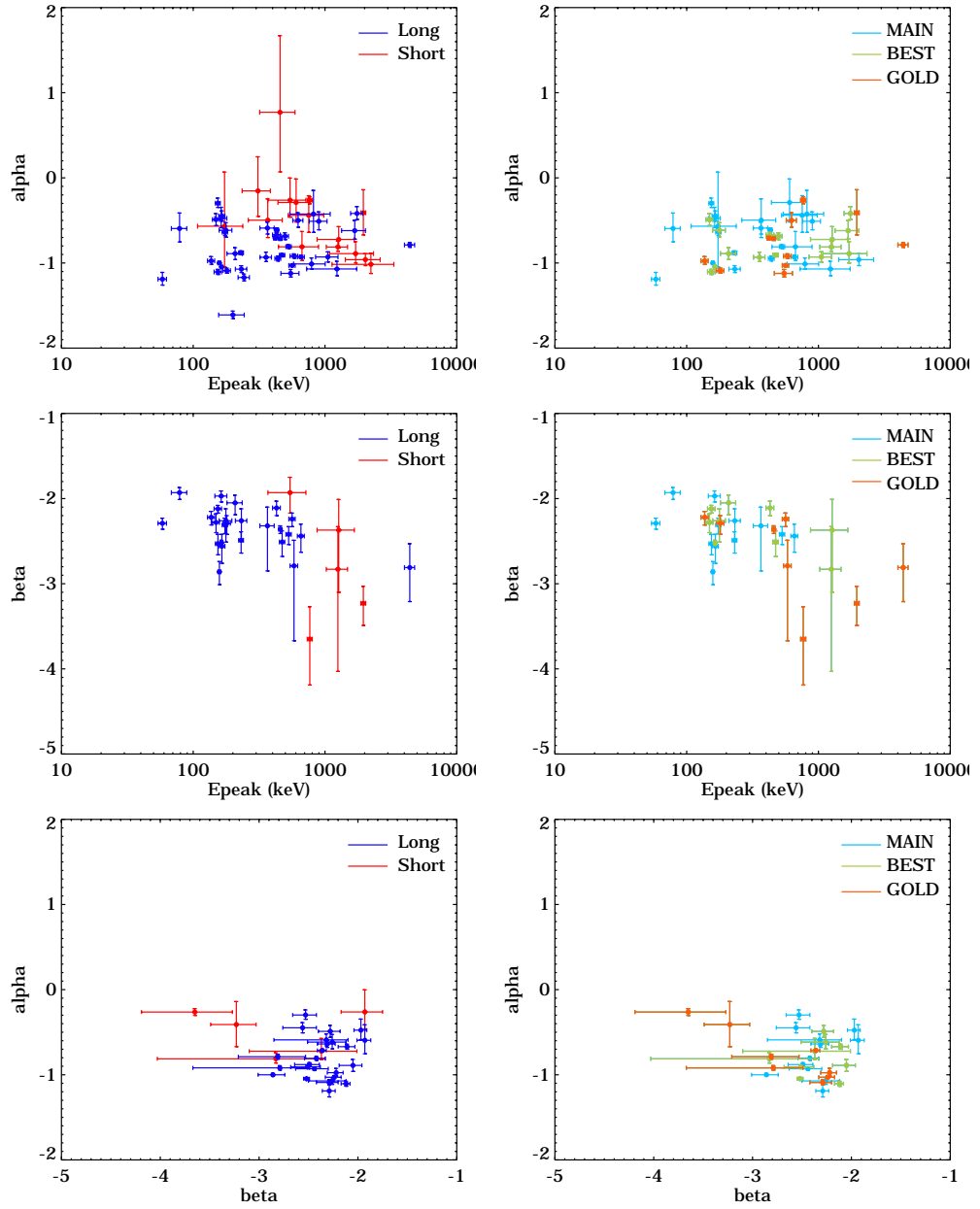


**Figure 5.19:** Scatter plot of spectral parameter pairs: *Top panel:*  $E_{\text{peak}}-\alpha$ ; *Middle panel:*  $E_{\text{peak}}-\beta$ ; *Bottom panel:*  $\alpha-\beta$ ; Color code same as in Figure 5.10

## 5.4.2. Correlation Among Spectral Parameters

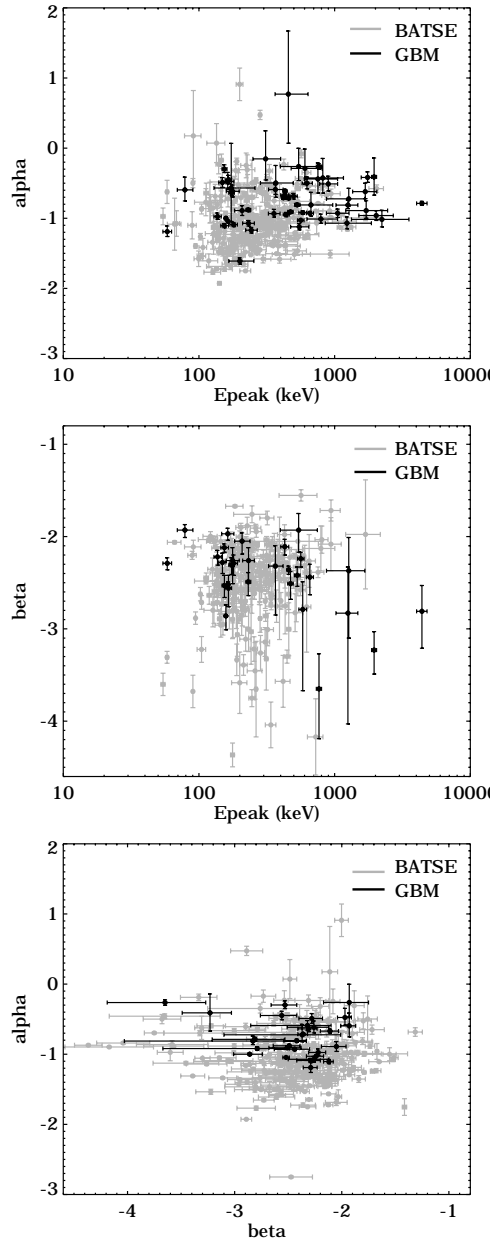


**Figure 5.20:** Scatter plot of spectral parameter pairs for 342 bright BATSE bursts and 56 bright GBM bursts. *Top panel:*  $E_{\text{peak}}-\alpha$ ; *Middle panel:*  $E_{\text{peak}}-\beta$ ; *Bottom panel:*  $\alpha-\beta$ ; Color code same as in Figure 5.11

### GRB Energy Relationships

As briefly discussed in §1.3.3, it has recently been shown, that the Amati relation may suffer from strong selection effects and is inconsistent with a larger set of GRB data obtained with BATSE (Nakar & Piran, 2005a; Band & Preece, 2005). Responding to the results, Ghirlanda et al. (2005) argued that taking into account the intrinsic scatter of the relation, the BATSE bursts may still be consistent with this relation. This claim, however, has also been challenged (Nakar & Piran, 2005b). The inconsistency of BATSE bursts with the Amati relation was tested by Nakar & Piran (2005a) by studying the ratio  $E_{\text{peak}}^2/E_{\text{iso}}$ , through which it is possible to place a limit in the observed  $E_{\text{peak}}$  and energy fluence values, i.e. a limit on observable quantities without involving any redshift measurements.

The conversion of the Amati relation into an energy ratio is nicely described in Band & Preece (2005). Starting from Equation 1.6, the relation can be expressed as:

$$E_{p,r} = C_1 \left( \frac{E_{\text{iso}}}{10^{52} \text{erg}} \right)^{\eta_1}, \quad (5.4)$$

where  $E_{p,r}$  is the peak energy for the “fluence spectrum” (the spectrum averaged over the entire burst) in the burst frame, and  $E_{\text{iso}}$  is the burst energy if the observed flux were emitted in all directions. Friedman & Bloom (2005) find  $C_1 = 95 \pm 11$  and  $\eta_1 = 0.50 \pm 0.04$ . Similarly, the Ghirlanda relation can be expressed as:

$$E_{p,r} = C_2 \left( \frac{E_\gamma}{10^{51} \text{erg}} \right)^{\eta_2}, \quad (5.5)$$

where  $E_\gamma$  is total energy actually radiated. The values obtained by Friedman & Bloom (2005) are  $C_2 = 512 \pm 15$  and  $\eta_2 = 0.70 \pm 0.07$ .

The peak energy in the observer’s frame is

$$E_{p,obs} = E_{p,r}/(1 + z), \quad (5.6)$$

where  $z$  is the burst’s redshift. The isotropic energy is

$$E_{\text{iso}} = \frac{4\pi S_\gamma d_L^2}{1 + z} \quad (5.7)$$

where  $S_\gamma$  is the bolometric fluence and  $d_L$  is the luminosity distance. The total energy radiated is

$$E_\gamma = E_{\text{iso}}(1 - \cos\theta_j) = f_B E_{\text{iso}}, \quad (5.8)$$

## 5.4.2. Correlation Among Spectral Parameters

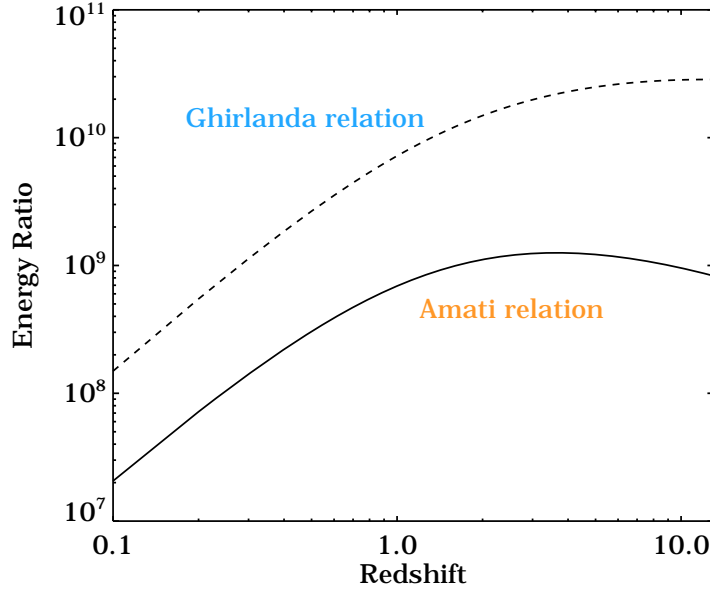


**Figure 5.21:** Predicted value of the Amati relation energy ratio  $E_{p,obs}^2/S_\gamma$  (*dashed curve*) and Ghirlanda relation energy ratio  $E_{p,obs}^{1.43}/[f_B S_\gamma]$  (*solid curve*) as a function of redshift

where  $\theta_j$  is the jet opening angle and  $f_B$  is the beaming fraction, which is determined observationally from modeling the evolution of the afterglow.

The Amati relation implies

$$\xi_1 = \frac{E_{p,obs}^2}{S_\gamma} = \frac{4\pi d_L^2 C_1^2}{[10^{52} \text{ erg}] (1+z)^3} = A_1(z) \quad , \quad (5.9)$$

and the Ghirlanda relation implies

$$\xi_2 = \frac{E_{p,obs}^{1.429}}{S_\gamma} = f_B \frac{4\pi d_L^2 C_2^{1.429}}{[10^{51} \text{ erg}] (1+z)^{2.429}} = f_B A_2(z) \quad . \quad (5.10)$$

Since  $f_B = (1 - \cos \theta_j)$  ranges between 0 and 1,  $A_2(z)$  is the upper limit to the  $\xi_2$  ratio.  $\xi_1$  and  $\xi_2$  are used as the observed ratios and  $A_1(z)$  and  $A_2(z)$  as theoretical functions of  $z$ .

Assuming a standard cosmology with  $\Omega_m = 0.3$ ,  $\Omega_\Lambda = 0.7$ , and  $H_0 = 70$  Mpc/km/s, the results can be represented as in Figure 5.21, which shows  $A_1(z)$  (*upper curve*) and  $A_2(z)$  (*lower curve*), respectively. As pointed out by Nakar & Piran (2005a), observed values of  $\xi_1$  that exceed the maximum value of  $A_1(z)$ , in this case  $1.1 \times 10^9$ , cannot satisfy the Amati relation. Similarly, observed values of  $\xi_2$

## 5. BGO–BRIGHT GRBS

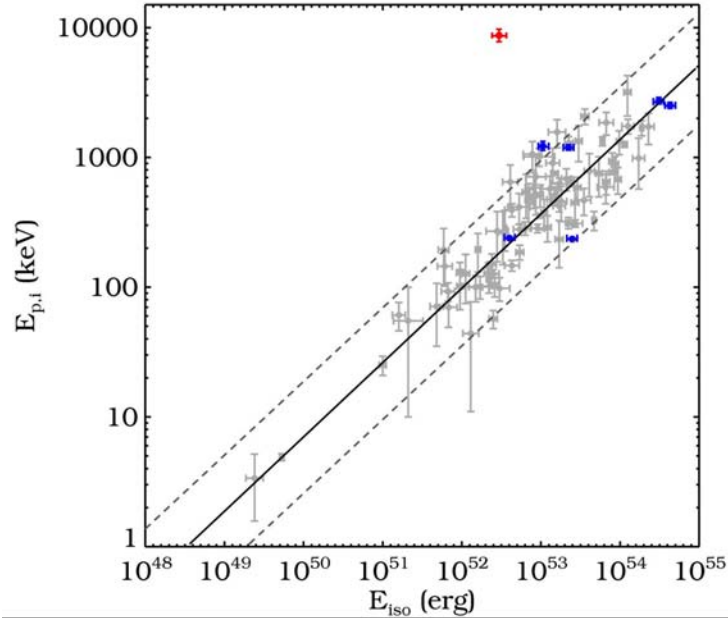


**Figure 5.22:** Distribution of the rest frame  $E_{\text{peak}}$  vs.  $E_{\text{iso}}$  calculated in the 1 keV–10 MeV energy range. The Amati relation is shown as a *black curve*. The *dashed lines* correspond to the best-fit power-law and the  $\pm 2\sigma$  dispersion region of the  $E_{p,i}$ – $E_{\text{iso}}$  correlation derived by Amati et al. (2008). Short and long GBM bursts with known redshift are indicated with *red* and *blue dots*

that exceed the maximum value of  $A_2(z) = 2.9 \times 10^{10}$  cannot satisfy the Ghirlanda relation. Since  $A_1(z)$  and  $A_2(z)$  are both 0 at  $z = 0$ , both ratios do not have useful lower bounds. In reality the two relations have a dispersion that may not only result from errors in the measured energies, and the maximum values of the ratios may be slightly greater. An example plot for the BATSE  $E_{\text{peak}}$ –fluence distribution can be found in chapter 1 (see Figure 1.15).

As was already claimed by Band & Preece (2005), also Kaneko et al. (2006) find that a large fraction of GRBs ( $\sim 88\%$ ) are not consistent with the Amati relation. Nonetheless, in a subsequent study, Ghirlanda et al. (2005) showed that only 1.4% of a large sample (442) of BATSE bursts do not fulfill the  $3\sigma$  limit allowed for the relation. They concluded that equation 5.4 had to be considered as a temporary estimate of the  $E_{\text{peak}}$ – $E_{\text{iso}}$  correlation with an uncertainty likely due to the still small number of GRBs with known redshift in 2005. As a matter of fact, also Band & Preece (2005) underline the importance of having a larger sample of bursts with redshift in order to test these relations conclusively. In a forthcoming paper (Bissaldi et al., 2010), I plan to further investigate the  $E_{\text{peak}}$ –fluence plane, and in particular the allowed  $3\sigma$  limit (as shown in Figure 5 of Ghirlanda

et al., 2005), based on a larger sample of GBM bursts (i. e. the official GBM first catalog).

The Amati relation itself was tested also for those bursts included in the BGO–bright burst sample with a firm redshift measurement. This was possible in 7 cases, namely for six long bursts (GRB 080916C at  $z = 4.35$ ; GRB 090102 at  $z = 1.55$ ; GRB 090323 at  $z = 3.57$ ; GRB 090328 at  $z = 0.74$ ; GRB 090424 at  $z = 0.54$ ; and GRB 090618 at  $z = 0.54$ ;) and for one short burst (GRB 090510 at  $z = 0.90$ ). The distribution of the rest frame  $E_{\text{peak}}$  vs.  $E_{\text{iso}}$  calculated in the 1 keV–10 MeV energy range is shown in Figure 5.22. The Amati relation is shown as a *black curve*, while the *dashed lines* correspond to the best–fit power–law and the  $\pm 2\sigma$  dispersion region of the  $E_{\text{peak}}-E_{\text{iso}}$  correlation derived by Amati et al. (2008). In this representation, long bursts (*blue dots*) seem to follow the  $E_{\text{peak}}-E_{\text{iso}}$  correlation, as was recently pointed out by Amati et al. (2010), the only outlier being the short burst GRB 090510 (*red dot*), as expected.

## 5. BGO-BRIGHT GRBS

---

# Conclusions

After the successful launch of the *Fermi* mission and the proper activation of its instruments, the 14 GBM detectors started to collect scientific data. The spectral overlap of the two BGO detectors (0.2 to 40 MeV) with the LAT lower limit of  $\sim 20$  MeV opens a promising epoch of investigation of the high-energy prompt and afterglow GRB emission in the yet poorly explored MeV–GeV energy region.

On ground, the angular and energy response of each GBM detector was calibrated using various radioactive sources between 14.4 keV and 4.4 MeV. The channel–energy relations, energy resolutions, on– and off–axis effective areas of the single detectors were determined. Additional calibration measurements were performed for NaI detectors at PTB/BESSY below 60 keV and for BGO detectors at SLAC above 5 MeV, thus covering the whole GBM energy domain. As already mentioned in chapter 3, further calibration measurements at system level and after integration onto the spacecraft were carried out. All those measurements crucially contribute to the validation of Monte Carlo simulations of the direct GBM detector response. The response as a function of photon energy and direction is finally captured in a Direct Response Matrix (DRM) database, allowing the determination of the true gamma-ray spectrum from the measured data. The results reported in this thesis directly contribute to the DRM final determination, and they fully follow physical expectations. It is also worth noting that all detectors behave the same within statistics.

The GBM detectors will play an important role in the GRB field in the next decade. The unprecedented synergy between the GBM and the LAT allows to observe burst spectra covering  $\sim 7$  decades in energy. During the first year and a half of the *Fermi* mission, 14 GRBs were already jointly detected by both instruments, as extensively described in chapter 4. Moreover, simultaneous observations by the large number of gamma-ray burst detectors operating in the *Fermi* era are complementing each other. The GBM detectors fit in this overall picture by providing a higher trigger energy range (50–300 keV) than e. g. *Swift*-BAT (15–150 keV)

## CONCLUSIONS

---

and a spectral coverage up to 40 MeV.

The number of GRBs detected by LAT above 100 MeV still represents a minority with respect to the total number of GRBs observed by GBM. Therefore, calculations of LAT upper limits become very interesting. These are mainly based on the brightest and hardest bursts detected by GBM inside the LAT field-of-view. In chapter 5, I presented a selection methodology and successive spectral analysis of a well-defined sample of bursts which have a strong signal in the GBM BGO detectors. The spectral analysis parameters of the selected BGO-sample are currently used as a starting point for the first LAT upper-limit paper. Moreover, criteria for determining the burst relevance in terms of a possible LAT detection, which are mainly based on the BGO count rate, were also developed. The best burst candidates are clearly those showing significant emission above 1 MeV. The possibility of integrating these selection criteria as automatized analysis tools in the GBM analysis software is currently under discussion. This will hopefully help during BA shifts for alerting the LAT team in case of potentially interesting events, thus allowing a more rapid alert of other space- and ground-based telescopes, too.

Further statistical analysis of the spectral parameter distributions presented in chapter 5 will be summarized in a forthcoming paper, which will also include an investigation of the  $E_{\text{peak}}$ -fluence plane and of the Amati and Ghirlanda relations. It is worth noting that this work can be considered as a precursor of detailed studies, which will be based on a much larger sample of GRBs (i. e. the official GBM catalogs). This will mainly depend on the mission's lifetime, which is planned to be five years, but will hopefully be extended to 10 years or more. Larger GRB samples, better locations and greater multiwavelength follow-up observations will shed light on the still unknown properties of those extremely energetic events.

# Bibliography

- Abdo, A. A., et al., 2009a, *ApJ*, **707**, 580
- Abdo, A. A., et al., 2009b, *Science*, **323**, 1688
- Abdo, A. A., et al., 2010b, *ApJ*, **712**, 558
- Abdo, A. A., et al., 2009d, *Nature*, **462**, 331
- Abdo, A. A., et al., 2009e, *ApJ*, **706**, 138
- Abdo, A. A., et al., 2010a, *ApJ in preparation*
- Abdo, A. A., et al., 2010c, *ApJ in preparation*
- Agostinelli, S., et al., 2003, *NIMPA*, **506**, 250
- Albert, J., et al., 2006, *ApJ*, **614**, L9
- Amati, L., et al., 2002, *A&A*, **390**, 81
- Amati, L., et al., 2007, *A&A*, **463**, 913
- Amati, L., et al., 2008, *MNRAS*, **391**, 577
- Amati, L., 2010, *Venice GRB Conf. Proc. in press*
- Amelino-Camelia et al., 1998, *Nature*, **395**, 525
- Asano, K., Guiriec, S., and Mészáros, P., 2009, *ApJ*, **705**, 191
- Arnaud, K. A., 1996, *ASP Conf. Proc.*, **101**, 17
- Atkins, R., et al., 2000, *ApJ*, **533**, L119
- Atteia, J.-L., et al., 1995, *Ap&SS*, **231**, 471
- Atwood, W. B., 1994, *NIMPA*, **342**, 302
- Atwood, W. B., et al., 2007, *Aph*, **28**, 422
- Atwood, W. B., et al., 2009, *ApJ*, **697**, 1071
- Band, D., et al., 1993, *ApJ*, **413**, 281
- Band, D., and Preece, R. D., 2005, *ApJ*, **627**, 319
- Band, D. 2008, *AIP Conf. Proc.*, **1000**, 121
- Band, D., et al., 2009, *ApJ*, **701**, 1673

## BIBLIOGRAPHY

---

- Baring, M. G., and Harding, A. K., 1997, *ApJ*, **491**, 663
- Barraud, C., et al., 2003, *A&A*, **400**, 1021
- Barthelmy, S., et al., 1998, *AIP Conf. Proc.*, **428**, 99
- Barthelmy, S., et al., 2005, *Space Science Reviews*, **120**, 143
- Barthelmy, S., et al., 2005, *Nature*, **438**, 994
- Barthelmy, S., et al., 2009, *AIP Conf. Proc.*, **1133**, 3
- Berger, E., et al., 2003, *Nature*, **426**, 154
- Berger, E., et al., 2005, *ApJ*, **634**, 501
- Bhat, P. N., et al., 1992, *Nature*, **359**, 217
- Bildstein, L., et al., 1997, *ApJS*, **113**, 367
- Bissaldi, E., et al., 2007, *A&A*, **471**, 585B
- Bissaldi, E., 2009, *GCN* **9933**
- Bissaldi, E., and Connaughton, V., 2009, *GCN* **9866**
- Bissaldi, E., et al., 2009a, *ExA*, **24**, 47
- Bissaldi, E., et al., 2009b, *GCN* **9972**
- Bissaldi, E., 2010a, *Venice GRB Conf. Proc. in press*
- Bissaldi, E., 2010b, *SciNeGHE Conf. Proc. in press*
- Bissaldi, E., et al., 2010, *in preparation*
- Bloom, J. S., et al., 1998, *ApJ*, **508**, 21
- Bloom, J. S., et al., 2001, *ApJ*, **554**, 678
- Bouvier, A., et al., 2008, *GCN* **8183**
- Briggs, M. S., 1996, *AIP Conf. Proc.*, **384**, 133
- Briggs, M. S., et al., 1999a, *ApJ*, **524**, 82
- Briggs, M. S., et al., 1999b, *ApJS*, **122**, 503
- Briggs, M. S., et al., 2009, *AIP Conf. Proc.*, **1133**, 40
- Briggs, M. S., et al., 2010, *JGR in press*
- Burrows, D. N., et al., 2005, *Science*, **309**, 1833
- Burrows, D. N., et al., 2005, *SSRv*, **120**, 165
- Campana, S., et al., 2006, *Nature*, **442**, 1008
- Carlson, P., et al., 1996, *NIMPA*, **376**, 271
- Cash, W., 1979, *ApJ*, **228**, 939)
- Cavallo, G., and Rees, M. J., 1978, *MNRAS*, **183**, 359
- Cenko, S. B., et al., 2009, *GCN* **9053**

- Chandra, P., and Frail, D. A., 2009, *GCN* **9889**
- Chornock, R., et al., 2009, *GCN* **9028**
- Cline, T. L., et al., 1973, *ApJ*, **185**, 1
- Cline, T. L., et al., 1980, *ApJL*, **237**, 1
- Colgate, S. A., 1968, *Can. J. Phys.*, **46**, 476
- Connaughton, V., and Briggs, M. S., 2008, *GCN* **8408**
- Connaughton, V., et al., 2010, *Venice Conf. Proc. in press*
- Costa, E., et al., 1997, *Nature*, **387**, 783
- Crider, A., et al., 1997, *ApJL*, **479**, 39
- Cucchiara, A., et al., 2009a, *GCN* **9873**
- Cucchiara, A., et al., 2009b, *GCN* **10031**
- Cutini, S., Vasileiou, V., and Chiang, J., 2009, *GCN* **9077**
- Cwiok, M., et al., 2008, *GCN* **7445**
- de Palma, F., Bregeon, J., and Tajima, H., 2009a, *GCN* **9867**
- de Palma, F., et al., 2009b, *GCN* **9872**
- de Palma, F., et al., 2009c, *GCN* **10163**
- Dermer, C. D., Chiang, J., and Böttcher, M., 1999, *ApJ*, **513**, 656
- Dermer, C. D., and Atoyan, A., 2006, *New J. Phys.*, **8**, 122
- de Ugarte Postigo, A., et al., 2008, *GCN* **8089**
- Dingus, B. L., 1995, *Ap&SS*, **231**, 187
- Dingus, B. L., Catelli, J. R., and Schneid, E. J., 1998, *AIP Conf. Proc.*, **428**, 349
- Dingus, B. L., et al., 2001, *AIP Conf. Proc.*, **558**, 383
- Dingus, B. L., 2003, *AIP Conf. Proc.*, **662**, 240
- Djorgovski, S. G., et al., 1999, *GCN* **289**
- Eichler, D., et al., 1989, *Nature*, **340**, 126
- Engelkemeir, D., 1956, *Rev. Sci. Instrum.*, **27**, 589
- Evans, P. A., et al., 2008, *GCN* **8086**
- Fenimore, E. E., Epstein, R. I. and Ho, C., 1993a, *A&AS*, **97**, 59
- Fenimore, E. E., et al., 1993b, *Nature*, **366**, 40
- Finke, J. D., Razzaque, S., and Dermer, C. D., 2009, *arXiv: 0905.1115*
- Finger, M. H., et al., 2009, *Fermi Symposium, eConf Proc.*
- Fishman, G. J., et al., 1989, *Proc. CGRO Science Workshop*, **2**, 30
- Fishman, G. J., et al., 1994, *ApJS*, **92**, 229

## BIBLIOGRAPHY

---

- Ford, L. A., et al., 1995, *ApJ*, **439**, 307
- Frail, D. A., et al., 1994, *ApJL*, **437**, 43
- Frail, D. A., et al., 1997, *Nature*, **389**, 263
- Frail, D. A., et al., 2000, *AIP Conf. Proc.*, **526**, 298
- Frail, D. A., et al., 2009, *GCN* **9060**
- Franceschini, A., Rodighiero, G., and Vaccari, M., 2008, *A&A*, **487**, 837
- Friedman, A. S., and Bloom, J. S., 2005, *ApJ*, **627**, 1
- Galama, T. J., et al., 1998, *Nature*, **395**, 670
- GBM Science Investigation and Technical Description, 1999,  
from <http://gammaray.msfc.nasa.gov/gbm/publications/proposal/>
- Gehrels, N., et al., 2004, *ApJ*, **611**, 1005
- Gehrels, N., 2006, *AIP Conf. Proc.*, **836**, 14
- Ghirlanda, G., Ghisellini, G., and Lazzati, D. 2004, *ApJ*, **616**, 331
- Ghirlanda, G., et al., 2005, *MNRAS*, **361**, 10
- Ghirlanda, G., Ghisellini, G., and Nava, L., 2009, *arXiv: 0909.0016*
- Gilmore, R. C., et al., 2009, *MNRAS*, **399**, 1694
- Giuliani, A., et al., 2008, *A&A*, **491**, 25
- Giuliani, A., et al., 2010, *ApJ*, **708**, 84
- GLAST Science Brochure, 2001, Document ID: 20010070290;  
Report Number: NAS 1.83:9-107-GSFC, NASA/NP-2000-9-107-GSFC
- Goldstein, A., and van der Horst, A. J., 2008, *GCN* **8245**
- Gonzalez, M. M., et al., 2003, *Nature*, **424**, 749
- Goodman, J., 1986, *ApJL*, **308**, 47
- Goodman, J., 1997, *NewA*, **2**, 449
- Görner, W., et al., 2001, *NIMPA*, **467**, 703
- Gorosabel, J., et al., 2004, *A&A*, **427**, 87
- Gotz, D., et al., 2003, *GCN* **2459**
- Greiner, J., et al., 2009a, *ApJ*, **693**, 1610
- Greiner, J., et al., 2009b, *A&A*, **498**, 89
- Guiriec, S., Connaughton, V., and Briggs, M. S., 2009, *GCN* **9336**
- Guiriec, S., et al., 2010, *ApJ in preparation*
- Harris, M., and Share, G., 1998, *ApJ*, **494**, 724
- Harrison, F., et al., 2009, *GCN* **9043**

- Harmon, B. A., et al., 2002, *ApJS* **138**, 149
- Heise, J., et al., 2001, *GRBA Conf. Proc.*, **16**
- Heise, J., et al., 2003, *AIP Conf. Proc.*, **662**, 229
- Hjorth, J., et al., 2003, *Nature*, **423**, 847
- Holland, S. T., and Page, K. L., 2008, *GCN* **8095**
- Hoover, A. S., et al., 2008, *AIP Conf. Proc.*, **1000**, 565
- Horack, J. M., 1991, *NASA Reference Publication*, **1268**
- Hunag, Y. F., Dai, Z. G., and Lu, T., 2002, *MNRAS*, **332**, 735
- Hurley, K., et al., 1994, *Nature*, **372**, 652
- Iredale, P., 1961, *NIMPA*, **11**, 336
- Jakobsson, P., et al., 2006, *A&A*, **447**, 897
- Jin, Z. P., and Wei, D. M., 2004, *Chin.J.Astron.Astrophys.*, **4**, 473
- Kaneko, Y., et al., 2006, *ApJSS*, **166**, 298
- Kaneko, Y., et al., 2008, *ApJ*, **677**, 1168
- Kaneko, Y., et al., 2010, *arXiv: 0911.4636*
- Katz, J. I., 1994, *ApJL*, **432**, 107
- Kawai, N., et al., 1999, *A&AS*, **138**, 563
- Kennea, J. A., et al., 2009a, *GCN* **9024**
- Kennea, J. A., et al., 2009b, *GCN* **9045**
- Kennea, J. A., and Stratta, G., 2009, *GCN* **9868**
- von Kienlin, A., et al., 2003, *A&A*, **411**, 299
- von Kienlin, A., et al., 2004, *SPIE Conf. Proc.*, **5488**, 763
- von Kienlin, A., et al., 2007, *AIP Conf. Proc.*, **921**, 576
- von Kienlin, A., 2009a, *GCN* **8902**
- von Kienlin, A., 2009b, *GCN* **9579**
- Kippen, R. M., 2004, *NewA*, **48**, 221
- Kippen, R. M., et al., 2007, *AIP Conf. Proc.*, **921**, 590
- Klebesadel, R. W., Strong, I. B. and Olson, R. A., 1973, *ApJ*, **182**, L85
- Kneiske, T. M., et al., 2004, *A&A*, **413**, 807
- Knoll, G. F., Radiation detection and measurement, 1989, *John Wiley and Sons*,  
**3rd edition**
- Kobayashi, S., Ryde, F., and MacFadyen, A., 2002, *ApJ*, **577**, 302
- Kouveliotou, C., et al., 1993, *ApJ*, **413**, L101

## BIBLIOGRAPHY

---

- Kouveliotou, C., et al., 1994, *ApJ*, **422**, 59
- Krimm, H. A., et al., 2009, *ApJ*, **704**, 1405
- Krolik, J. H., and Pier, E. A., 1991, *ApJ*, **373**, 277
- Krumrey, M., et al., 2006, *NIMPA*, **568**, 364
- Kumar, P., and Barniol Duran, R., 2009, *arXiv: 0905.2417*
- Lamb, D. Q., 1984, *AIP Conf. Proc.*, **115**, 512
- Lederer, C. M., and Shirley, V. S., Table of isotopes, 1978, *Wiley-Interscience*, **7th edition**
- Li, Z., and Waxman, E., 2006, *ApJ*, **651**, 328
- Liang, E. W., Dai, Z. G., and Wu, X. F., 2004, *ApJ*, **606**, L29
- Lichti, G., et al., 1996, *SPIE Conf. Proc.*, **2806**, 217
- Link, B., Epstein, R. I., and Priedhorsky, W. C., 1993, *ApJ*, **408**, L81
- Lithwick, Y., and Sari, R., 2001, *ApJ*, **555**, 540
- Lloyd, N. M., and Petrosian, V., 1999, *ApJ*, **511**, 550
- Lloyd, N. M., and Petrosian, V., 2000, *ApJ*, **543**, 722
- Lloyd, N. M., Petrosian, V., and Mallozzi, R. S., 2000, *ApJ*, **534**, 227
- MacFadyen, A., and Woosley, S., 1999, *ApJ*, **524**, 262
- Malesani, D., et al., 2004, *ApJ*, **609**, 5
- Malesani, D., et al., 2009, *GCN* **9942**
- Mallozzi, R. S., Preece, R. D. and Briggs, M. S., *RMFIT, A Light Curve and Spectral Analysis Tool*, ©2005 Robert D. Preece, University of Alabama in Huntsville
- Mazets, E. P., et al., 1981a, *Nature*, **290**, 378
- Mazets, E. P., et al., 1981b, *Ap&SS*, **80**, 3
- McBreen, S. et al., 2006, *A&A*, **455**, 433
- McBreen, S., and Chaplin, V., 2009, *GCN* **10115**
- McEnery, J., et al., 2008, *GCN* **8684**
- McEnery, J., et al., 2009a, *GCN* **9044**
- McEnery, J., et al., 2009b, *GCN* **9985**
- McGlynn, S., et al., 2007, *A&A*, **466**, 895
- Meegan, C. A., et al., 1992, *Nature*, **355**, 143
- Meegan, C. A., et al., 2008, *GCN* **8100**
- Meegan, C. A., et al., 2009, *ApJ*, **702**, 791

- Mészáros, P., and Rees, M. J., 1992, *ApJ*, **397**, 570
- Mészáros, P., and Rees, M. J., 1993, *ApJ*, **405**, 278
- Mészáros, P., Rees, M. J., and Papathanassiou, H., 1994, *ApJ*, **432**, 181
- Mészáros, P., and Rees, M. J., 1997, *ApJ*, **476**, 232
- Mészáros, P., and Rees, M. J., 2000, *ApJ*, **530**, 292
- Mészáros, P., et al., 2002, *ApJ*, **578**, 812
- Mészáros, P., 2002, *Ann. Rev. of A.&A.*, **40**, 137
- Metcalf, L., et al., 2003, *A&A*, **407**, 791
- Metzger, M. R., et al., 1997, *Nature*, **387**, 878
- Michelson, P. F., 1996, *SPIE Conf. Proc.*, **2806**, 31
- Modjaz, M., et al., 2006, *ApJ*, **645**, 21
- Moiseev, A. A., et al., 2007, *APh*, **27**, 339
- Morselli, A., 2002, *Memorie della Società Astronomica Italiana*, **73**, 1199
- Moszynski, M., et al., 2002, *NIMPS*, **484**, 259
- Murakami, T., et al., 1988, *Nature*, **335**, 234
- Nakamura, T., 1999, *ApJL*, **522**, 101
- Nakar, E., and Piran, T., 2005a, *MNRAS*, **360**, 73
- Nakar, E., and Piran, T., 2005b, *arXiv: 0503517*
- Natarajan, P. et al., 2005, *MNRAS*, **364**, L8
- Norris, J. P. et al., 1986, *ApJ*, **301**, 213
- Norris, J. P. et al., 1996, *ApJ*, **459**, 393
- Norris, J. P., and Bonnell, J., 2006, *ApJ*, **643**, 266
- Nousek, J. A., et al., 2006, *ApJ*, **642**, 389
- O'Brien, P. T., et al., 2006, *NJPh*, **8**, 121
- Oates, S. R., 2009, *GCN* **9048**
- Ohno, M., et al., 2009a, *GCN* **8903**
- Ohno, M., et al., 2009b, *GCN* **9021**
- Ohno, M., et al., 2009c, *GCN* **9334**
- Olivares, F., et al., 2009, *GCN* **9874**
- Omodei, N., 2008, *GCN* **8407**
- Omodei, N., et al., 2009, *GCN* **9350**
- Paciesas, W. S., et al., 1999, *ApJSS*, **122**, 465
- Paczynski, B., 1986, *ApJ*, **308**, L43

## BIBLIOGRAPHY

---

- Paczynski, B., 1991, *Acta Astron.*, **41**, 157
- Page, K. L., Willingale, R., Bissaldi, E., et al., 2009, *MNRAS*, **400**, 134
- Pandey, S. B., et al., 2009, *GCN* **9878**
- Patat, F., et al., 2001, *ApJ*, **555**, 900
- Pe'er, A., et al., 2007, *ApJL*, **664**, L1
- Pelassa, V., et al., 2010, *Fermi Symposium, eConf Proc.*, *arXiv: 1002.2617*
- Perley, D., Kleiser, I. K. W., and Rex, J. M., 2009, *GCN* **9870**
- Piron, F., et al., 2009, *GCN* **9584**
- Preece, R. D., et al., 1996, *ApJ*, **473**, 310
- Preece, R. D., 2008, *GCN* **8678**
- Prescott, J. R. and Narayan, G. H., 1969, *NIMPA*, **75**, 51
- Prochaska, J. X., et al., 2003, *GCN* **2482**
- Prochaska, J. X., Chen, H., and Bloom, J. S., 2006, *ApJ*, **648**, 95
- Prochaska, J. X., et al., 2008, *GCN* **8083**
- Quilligan, F., et al., 2002, *A&A*, **385**, 377
- Racusin, J. L., et al., 2008, *GCN* **7427**
- Ramirez-Ruiz, E., and Fenimore, E. E., 2000, *ApJ*, **539**, 712
- Rau, A., et al., 2005, *A&A*, **438**, 1175
- Rau, A., Connaughton, V., and Briggs, M. S., 2009a, *GCN* **9057**
- Rau, A., et al., 2009b, *GCN* **9353**
- Rau, A., 2009, *GCN* **9983**
- Razzaque, S., Dermer, C. D., and Finke, J. D., 2009, *arXiv: 0908.0513*
- Rees, M. J., 1995, *PASP*, **107**, 1176
- Rees, M. J., and Mészáros, P., 2005, *ApJ*, **628**, 847
- Riesemeier, H., et al., 2005, *X-Ray Spectrometry*, **34**, 160
- Roming, P., et al., 2005, *SSRv*, **120**, 95
- Rossi, A., et al., 2008, *A&A*, **491**, L29
- Ruderman, M., 1975, *New York Academy Sciences Annals*, **262**, 243
- Ryde, F., 2004, *ApJ*, **614**, 827
- Rykoff, E. S., 2008, *GCN* **8084**
- Sakamoto, T., et al., 2004, *ApJ*, **602**, 875
- Sakamoto, T., et al., 2008a, *GCN* **8082**
- Sakamoto, T., et al., 2008b, *GCN* **8101**

- Sakamoto, T., et al., 2009, *ApJ*, **693**, 922
- Sari, R., et al., 1998, *ApJ*, **497**, 17
- Sari, R., and Piran, T., 1999, *A&ASS*, **138**, 537
- Sari, R., and Esin, A. A., 2001, *ApJ*, **548**, 787
- Savaglio, S., 2010, *IAU Conf. Proc. in press*
- Schoenberg, I. J., 1946, *Quart. Appl. Math.*, **4**, 45-99
- Schötzig, U., and Schrader, H., 1998, *PTB-Ra-16/5*
- Schneid, E. J., et al., 1993, *A&A*, **255**, L13
- Schneid, E. J., et al., 1994, *ApJ*, **453**, 95
- Sommer, M., et al., 1994, *ApJ*, **422**, L63
- Stamatikos, M., Sakamoto, T., and Band, D.L., 2008, *AIP Conf. Proc.*, **1065**, 59
- Stamatikos, M., 2009, *arXiv: 0907.3190*
- Stanek, K. Z., et al., 2003, *ApJ*, **591**, L17
- Stecker, F. W., Malkan, M. A., and Scully, S. T., 2006, *ApJ*, **648**, 774
- Steinle, H., et al., 2007, *AIP Conf. Proc.*, **921**, 572
- Stratta, G., D'Elia, V., and Perri, M., 2009, *GCN* **9876**
- Strong, I. B., and Klebesadel, R. W., 1976, *Scientific American*, **235**, 66
- Swenson, C. A., and Stratta, G., 2009, *GCN* **9877**
- Tagliaferri, G., et al., 2005, *Nature*, **436**, 985
- Tajima, H., et al., 2008, *GCN* **8246**
- Tanvir, N. R., et al., 2008, *GCN* **7569**
- Tavani, M., 1996, *ApJ*, **466**, 768
- Tavani, M., et al., 2006, *SPIE Conf. Proc.*, **6266**, 626603
- Tavani, M., et al., 2008, *NIMPS*, **588**, 52
- Thompson, D. J., et al., 1993, *ApJSS*, **86**, 629
- Thompson D. J., and Thompson, T. E., 2003, *GLAST Technical Document*, **LATPR-1967**
- Thompson, A., and Vaughan, D., 2001, X-ray Data Booklet, Lawrence Berkeley National Laboratory
- Ubertini, P., et al., 2003, *A&A*, **411**, 131
- Uehara, T., Takahashi, H., and McEnery, J., 2009, *GCN* **9934**
- Updike, A. C., et al., 2009, *GCN* **9026**
- van der Horst, A. J., and Connaughton, V., 2008, *GCN* **8141**

## BIBLIOGRAPHY

---

- van der Horst, A. J., Connaughton, V., and Briggs, M. S., 2008, *GCN* **8184**
- van der Horst, A. J., Goldstein, A., 2008, *GCN* **8278**
- van der Horst, A. J., et al., 2009a, *GCN* **9035**
- van der Horst, A. J., et al., 2009b, *GCN* **9883**
- van der Horst, A. J., et al., 2010, *arXiv: 0911.5544v1*
- van Paradijs, J., et al., 1997, *Nature*, **386**, 686
- van Paradijs, J., Kouveliotou, C., and Wijers, R. A. M. J., 2000, *ARA&A*, **38**, 379
- Vanderspek, R., et al., 1999, *A&AS*, **138**, 565
- Vaughan, S., et al., 2004, *ApJ*, **603**, 5
- Vaughan, S., et al., 2006, *ApJ*, **638**, 920
- Vedrenne, G., et al., 2003, *A&A*, **411**, 63
- Vrba, F. J., Hartmann, D. H., and Jennings, M. C., 1995, *ApJ*, **446**, 115
- Wallace, M. S., et al., 2007, *AIP Conf. Proc.*, **921**, 580
- Wang, X., Li, Z., and Mészáros, P., 2006, *ApJ*, **641**, L89
- Waxman, E., 1997, *ApJL*, **485**, 5
- Wilson-Hodge, C. A., et al., 2009, *Fermi Symposium, eConf Proc.*
- Wijers, R. A. M. J., Rees, M. J., and Mészáros, P., 1997, *MNRAS*, **288**, L51
- Woosley, S. E., 1993, *ApJ*, **405**, 273
- Woosley, S. E., and Loeb, A., 1995, *ApJ*, **453**, 583
- Woosley, S. E., Eastman, R. G., and Schmidt, B. P., 1999, *ApJ*, **516**, 788
- Woosley, S. E., Zhang, W., and Heger, A., 2003, *ESO Astrophysics Symposia*, 87
- Yamazaki, R., Ioka K., and Nakamura, T., 2002, *ApJ*, **571**, L31
- Yamazaki, R., Ioka K., and Nakamura, T., 2004, *COSPAR Conf. Proc.*, **35**, 3284
- Zhang, B., and Mészáros P., 2002, *ApJ*, **581**, 1236